University of Central Florida
STARS

Electronic Theses and Dissertations, 2004-2019

2014

The effect of electron-hole pairs in semiconductor and topological insulator nanostructures on plasmon resonances and photon polarizations.

Hari Paudel
University of Central Florida

Part of the Physics Commons
Find similar works at: https://stars.library.ucf.edu/etd
University of Central Florida Libraries http://library.ucf.edu

This Doctoral Dissertation (Open Access) is brought to you for free and open access by STARS. It has been accepted for inclusion in Electronic Theses and Dissertations, 2004-2019 by an authorized administrator of STARS. For more information, please contact STARS@ucf.edu.

STARS Citation
Paudel, Hari, "The effect of electron-hole pairs in semiconductor and topological insulator nanostructures on plasmon resonances and photon polarizations." (2014). *Electronic Theses and Dissertations, 2004-2019*. 4737.
https://stars.library.ucf.edu/etd/4737

Showcase of Text, Archives, Research & Scholarship

THE EFFECT OF ELECTRON-HOLE PAIRS IN SEMICONDUCTOR AND TOPOLOGICAL INSULATOR NANOSTRUCTURES ON PLASMON RESONANCES AND PHOTON POLARIZATIONS

by

HARI P. PAUDEL
B.Sc., Tribhuvan University, Kathmandu 2002
M.Sc., Tribhuvan University, Kathmandu 2006

A dissertation submitted in partial fulfillment of the requirements
for the degree of Doctor of Philosophy
in the Department of Physics
in the College of Sciences
at the University of Central Florida
Orlando, Florida

Summer Term
2014

Major Professor: Michael N. Leuenberger

© 2014 Hari P. Paudel

ABSTRACT

The generation of electron-hole pairs in materials has great importance. In direct bandgap semiconductor materials, the mechanism of radiative recombination of electron-hole pairs leads to the emission of photons, which is the basis of Light Emitting Diodes (LEDs). The excitation of electron-hole pairs by absorption of photons is the active process in photodiodes, solar cells, and other semiconductor photodetector devices. In optoelectronic devices such as optical switches which are based on transmission and reflection of the photons, electron-hole pairs excitation is a key for the device performance. Diodes and transistors are also great discoveries in electronics which rely on the generation and recombination of electron-hole pairs at p-n junctions. In three-dimensional topological insulators (3D TIs) materials nanostructures excitation of electron-hole pairs can be utilized for the quantum memory, quantum information and quantum teleportation. In two-dimensional (2D) layered materials like graphene, MoS_2, $MoSe_2$, WS_2 and WSe_2 generation and recombination of electron hole pairs is main process at p-n junctions, infrared detectors and sensors.

This PhD thesis is concerned with the physics of different types of electron-hole pairs in various materials, such as wide-bandgap semiconductors, 3D topological insulators, and plasmonic excitations in metallic nanostructures. The materials of interest are wide bandgap semiconductors such as TiO_2 , 3D TIs such as $Pb_{1-x}Sn_xTe$ and the 2D layered materials such as MoS_2 and MoO_3. We study the electronic and optical properties in bulk and nanostructures and find applications in the area of semiclassical and quantum information processing. One of the interesting applications we focus in this thesis is shift in surface plasmon resonance due to reduction in index of refraction of surrounding dielectric environment which in turns shifts the wavelength of surface plasmon resonance up to 125 nm for carrier density of $10^{22}/\mathrm{cm}^3$. Employing this effect, we present a model of a light controlled plasmon switching using a hybrid metal-dielectric heterostructures.

In 3D TIs nanostructures, the time reversible spin partners in the valence and conduction band can be coupled by a left and a right handed circular polarization of the light. Such coupling of light with electron-hole pair polarization provides an unique opportunity to utilize 3D TIs in quantum information processing and spintronics devices. We present a model of a 3D TI quantum dot made of spherical core-bulk heterostructure. When a 3D TI QD is embedded inside a cavity, the single-photon Faraday rotation provides the possibility to implement optically mediated quantum teleportation and quantum information processing with 3D TI QDs, where the qubit is defined by either an electron-hole pair, a single electron spin, or a single hole spin in a 3D TI QD.

Due to excellent transport properties in single and multiple layers of 2D layered materials, several efforts have demonstrated the possibility to engineer electronic and optoelectronic devices based on MoS_2. In this thesis, we focus on theoretical and experimental study of electrical property and photoluminescence tuning, both in a single-layer of MoS_2. We present theoretical analysis of experimental results from the point of view of stability

of MoO_3 defects in MoS_2 single layer and bandstructures calculation. In experiment, the electrical property of a single layer of MoS_2 can be tuned from semiconducting to insulating regime via controlled exposure to oxygen plasma. The quenching of photoluminescence of a single sheet of MoS_2 has also been observed upon exposure to oxygen plasmas. We calculate the direct to indirect band gap transitions by going from MoS_2 single sheet to MoO_3 single sheet during the plasma exposure, which is due to the formation of MoO_3 rich defect domains inside a MoS_2 sheet.

To my mother and late father

ACKNOWLEDGMENTS

I would like to thank my supervisor Prof. Michael N. Leuenberger. Without him it would have been impossible to complete this thesis. I learned most of my knowledge in physics from him. Whenever I was stuck in a problem, discussions with him used to be truly inspirational moments which filled my sails with wind. I enjoyed freedom to choose problems of my interest, which is one of the most wonderful privileges for a graduate student. It is not only the physics I learned from Prof. Leuenberger but also the values that are essential to fit a student in the scientific communities.

At this point, I would like to acknowledge the financial support provided by the National Science Foundation (NSF) under grant numbers ECCS-0901784 and ECCS-1128597 and the financial support provided by the Airforce Office of Scientific Research (AFOSR) under grant number FA9550-09-1-0450.

The members in our research group were very helpful. I would like to thank Dr. Mikhail (Misha) Erementchouk and Dr. Volodymr Turkowski for their valuable suggestion during my PhD. Misha was always so helpful whenever I had questions. A special word of gratitude goes to Prof. Rahman, the UCF physics chair, whose advice and suggestions always kept me hungry for physics. She is a truly inspirational person. I would also like to acknowledge Prof. Saha for being my committee member and so helpful to complete

my thesis. My sincere gratitude also goes to Prof. Gesquiere for kindly agreeing to be my external committee member.

During my PhD carrier at UCF, I was lucky to be taught by a group of bright faculty members. At this moment, I would like to remember Prof. Klemm whose courses in condensed matter physics became a milestone in understanding several aspects in my research. I would like to thank all professors at UCF who established a sense of physics in my life.

Last but not least I thank my wife Sapana. Without her constant support, it would have been difficult me to succeed in my PhD. I would like also to thank my family who always supported me for my study.

TABLE OF CONTENTS

LIST OF FIGURES xiv

LIST OF TABLES xxv

CHAPTER 1 INTRODUCTION 1

- 1.1 Light-matter Interaction 7
- 1.2 Electron-hole pairs and surface plasmons in metallic structures 10
- 1.3 Electron-hole pairs and excitons in wide bandgap semiconductors 13
- 1.4 Topological insulators in two and three dimensions 16
  - 1.4.1 Edge states and quantum Hall effect 17
  - 1.4.2 Z_2 Topological insulators 20
  - 1.4.3 Quantum spin Hall insulator 22
  - 1.4.4 3D topological insulators 24

1.5 Electron-hole pairs generation in 3D topological insulators 25

1.6 Two-dimensional layered materials 26

1.7 Methodology of using density functional theory to describe electron-hole pairs 28

1.8 Goal of this thesis 31

1.9 Organization of thesis 33

CHAPTER 2 SURFACE PLASMONS AND PLASMONICS 36

2.1 Introduction 36

2.2 Objective 38

2.3 Surface plasmon resonances in hybrid metal-semiconductor heterostructures 41

2.4 Electronic and optical properties of TiO_2 46

2.5 Plasmon resonance shifts and plasmonic switching 56

CHAPTER 3 THREE DIMENSIONAL TOPOLOGICAL INSULATOR QUANTUM DOT 61

3.1 Background 61

3.2 Model Based on Dirac Equation 66

3.3 Bound States of the Weyl Fermions 71

3.4 Optical Excitations 80

3.5 Faraday Effect for 3D TI QDs 87

3.6 Quantum Memory with 3D TI QDs 91

3.7 Single-Photon Faraday Effect for 3D TI QDs 97

3.8 Quantum Teleportation and Quantum Computing with 3D TI QDs 101

3.8.1 Photon polarization - e-h pair polarization entanglement 102

3.8.2 Photon polarization - electron spin entanglement 107

3.9 Conclusions 109

CHAPTER 4 TOPOLOGICAL INSULATORS WITH BULK GEOMETRY 111

4.1 Introduction 111

4.2 Model based on Dirac equation 119

4.3 Helicity operator 122

4.4 Optical transition matrix elements 125

4.5 Bandstructure calculation 133

4.6 Faraday Effect for 3D TIs 135

4.7 Conclusion 151

CHAPTER 5 TRANSMISSION FROM THE MULTILAYER OF THREE DIMENSIONAL TOPOLOGICAL INSULATORS: A TRANSFER MATRIX METHOD . . . 152

5.1 Introduction 152

5.2 Transfer matrix method 155

5.3 Transmission through 3D TI multilayers 158

CHAPTER 6 TWO DIMENSIONAL LAYERED MATERIALS 162

6.1 Introduction 162

6.2 Electrical property tuning of MoS_2 single sheet 163

  6.2.1 Results from the experiments 163

  6.2.2 Theoretical calculation 166

6.3 Photoluminescence tuning of MoS_2 single sheet 171

CHAPTER 7 CONCLUSIONS 178

APPENDIX A FERMION DOUBLING THEOREM IN 3D TI QD 181

A.1 Calculation of the Wronskian 182

A.2 Limiting form of Bessel functions 182

A.3 The fermion doubling theorem 183

APPENDIX B BOUNDARY CONDITIONS IN 3D TI SLAB 189

B.1 Solutions of the Maxwell Equations and the Boundary Conditions 190

APPENDIX C 2D LAYERED MATERIALS: EXPERIMENTAL AND THEORETICAL METHODS 193

C.1 Experimental method 194

C.2 Theoretical method 194

C.3 Theoretical calculation of resistance 195

LIST OF REFERENCES 197

LIST OF FIGURES

Figure 1.1 Atomic level splitting into bands as the atoms are brought together. When the atoms are far apart levels are discrete and N-fold degenerate. As they come closer the discrete levels form bands. 3

Figure 1.2 **a**, The bandstructure in the independent electron picture, and **b**, the Coulombic interaction between the electron and hole: excitonic effect. **c**, a conceptual picture of the periodic envelope function extent of the Frenkel and Mott excitons. 15

Figure 1.3 Dispersion relation for Kramers degenerate points at $\mathit{\Gamma}_a = 0$ and $\mathit{\Gamma}_b = \pi/a$. The number of Fermi surface crossing the Fermi Level is even in **a,** and odd in **b**. The bulk valence and conduction bands are also shown. 21

Figure 1.4 Interface modes in 2D quantum spin Hall insulator (QSHI) interfaced with trivial insulator. Weak and strong topological insulators, **a** and **b.** 23

Figure 1.5 A single sheet of MoS_2 (**a**), and MoO_3 (**b**). 27

Figure 2.1 Scheme of dynamically controlled plasmon excitation in a nanoshell. (a) The probe pulse excites plasmons on the surface of silver at a resonance frequency. The pump pulse generates electron-hole pairs in the semiconductor changing its dielectric function. The plasmon resonance frequency is now blue-shifted because of the changed dielectric environment. (b) A pump pulse with energy at band gap or above generates electron-hole pairs in the semiconductor. In quasi Fermi equilibrium, electrons and holes are settled at the bottom and top of the conduction and valence band, respectively, with the different quasi Fermi levels. 40

Figure 2.2 Ag core dielectric shell nanostructure with the dielectric function ε_1 for the Ag core, ε_2 for the TiO_2 shell and ε_3 for the embedding medium. The size of the nanoshell is 15 nm. 42

Figure 2.3 Local field enhancement factor at different positions in the shell portion of the nanoshell. The radius of the inner core is 3.5 nm. The magnitude of the local field factor decreases with increasing distance from the center of the nanoshell. Smallest peak to largest peak calculated, respectively, at positions $r = 7$, 6, 5 and 4 nm. 44

Figure 2.4 Local field enhancement factor at different shell thickness on the surface of the nanoshell. The resonance peak is blue shifted with decreasing shell thickness. Peaks are for 4, 3, 2 and 1 nm shell thickness, respectively, from right to left. 45

Figure 2.5 Bandstructure calculated using VASP. 48

Figure 2.6 Imaginary part of dielectric function for polarization parallel (green line) and perpendicular (blue line) to the electric field vector. 50

Figure 2.7 Real part of dielectric function for polarization parallel (green line) and perpendicular (blue line) to the electric field vector. 51

Figure 2.8 Parallel component of change in imaginary part of dielectric function. . 54

Figure 2.9 Perpendicular component of change in imaginary part of dielectric function. 55

Figure 2.10 Local field enhancement factor on the surface of a nanoshell of 3.5 nm silver core coated with 4 nm TiO_2 at different densities of excitation for parallel polarization of the incident light. At higher densities, the resonance peak is gradually blue shifted. 58

Figure 2.11 Light-controlled SPP switch. Propagation of surface plasmon-polariton in a chain of nanoshells of two types: a nanoshell with silver (light blue color) core coated with TiO_2 (yellow color) embedded in PMMA and nanoshells with GaN (no color) core coated with silver embedded in GaN . Nanoshells are separated by a distance a. This structure acts as a grating necessary to supply momentum for efficient coupling. Probed surface plasmons propagate across the chain because the excitation gap matches exactly in all nanoshells. The pump pulse generates electron-hole pairs in TiO_2. This results in a blue shift of plasmon resonances. 60

Figure 3.1 A heterostructure spherical core-bulk 3D TI QD with a single interface. **a**. The arrows indicate the infinite size of the host. The core and bulk host can be chosen as PbTe and $Pb_{0.31}Sn_{0.69}Te$ or vice versa. **b**. The potential $\Delta(r)$ binds Weyl fermions at the interface. The energy of the bound interface states depends on the size of the QD and the strength of the potential. As an example, two bound states at the interface are shown with energies $+\varepsilon$ and $-\varepsilon$ (short dashed lines) for a QD of size r_0 =2 nm. 63

Figure 3.2 Plot of Eq. (4.7) showing the intersections of the monotonically decreasing $F(z)$ (solid lines) with the constants (black dashed lines). Intersection at $z = 0$ gives the minimum threshold of the size of a QD to have two bound states, one positive and one negative energy state, for a given confining potential. For a larger QD, multiple bound states exist, corresponding to multiple intersection points. The intersection points A, B and C are example points where we evaluate the wavefunctions. The energy of the bound states are determined by the relation $z = \lambda r_o$. 70

Figure 3.3 Spatial dependence of f_- and f_+ inside and outside the QD calculated for the intersection point A shown in Figure 3.2. The QD has size $r_0 = 2$ nm. The solid horizontal lines represent the energy eigenvalues $\varepsilon_\pm = \pm 0.8\Delta_o$. 77

Figure 3.4 Spatial dependence of f_- and f_+ inside and outside the QD calculated for the intersection points B and C shown in Figure 3.2. The QD has size $r_0 = 3.5$ nm. The horizontal solid lines represent the energy eigenvalues $\varepsilon_\pm = \pm 0.91\Delta_o$ at point B and the horizontal dotted lines represent the energy eigenvalues $\varepsilon_\pm = \pm 0.48\Delta_o$ at point C. . 78

Figure 3.5 Optical transitions between the states $\kappa = 1$ and $\kappa = 2$ in 3D TI QD. Transitions are vertical. The transitions between $\left|\Phi^{\kappa=1}_{\frac{1}{2},\pm\frac{1}{2}}\right\rangle$ and $\left|\Phi^{\kappa=2}_{\frac{3}{2},\pm\frac{1}{2}}\right\rangle$ are coupled to the linear polarization of the incoming photons, while the transitions between $\left|\Phi^{\kappa=1}_{\frac{1}{2},\pm\frac{1}{2}}\right\rangle$ and $\left|\Phi^{\kappa=2}_{\frac{3}{2},\mp\frac{1}{2}}\right\rangle$ couple to $\sigma^\mp$ polarizations and the transitions between $\left|\Phi^{\kappa=1}_{\frac{1}{2},\pm\frac{1}{2}}\right\rangle$ and $\left|\Phi^{\kappa=2}_{\frac{3}{2},\pm\frac{3}{2}}\right\rangle$ couple to $\sigma^\pm$ polarizations of the light. 82

Figure 3.6 This is one possible level configuration that can be used for the implementation of the quantum memory. 92

Figure 3.7 This is another possible level configuration that can be used for the implementation of the quantum memory. 94

Figure 3.8 (a) The incident photon can be either σ^+ or σ^- polarized. The initial level configuration is the one shown in Figure 3.6. (b) If the photon is σ^+ polarized, an e-h pair with +1 polarization is created, which can be probed using off-resonant linearly polarized light that acquires a negative Faraday rotation angle through virtual excitation of an e-h pair and virtual recombinations of the present e-h pair. (c) If the photon is σ^- polarized, an e-h pair with -1 polarization is created, which can be probed using off-resonant linearly polarized light that acquires a positive Faraday rotation angle through virtual excitation of an e-h pair and virtual recombinations of the present e-h pair. (d) After the probing, the e-h pair relaxes into the ground state configuration. 95

Figure 3.9 This is one possible level configuration that can be used for the implementation of the quantum Faraday rotation, where the quantum information is stored in form of an electron (a) in the spin up state or (b) in the spin down state. (a) A single spin up electron is probed by using off-resonant linearly polarized photon that acquires a positive Faraday rotation angle through virtual excitation of e-h pairs. (b) A single spin down electron is probed by using off-resonant linearly polarized photon that acquires a negative Faraday rotation angle through virtual excitation of e-h pairs. 104

Figure 3.10 This is another possible level configuration that can be used for the implementation of the quantum Faraday rotation, where the quantum information is stored in form of a hole (a) in the spin up state or (b) in the spin down state. (a) A single spin up hole is probed by using off-resonant linearly polarized photon that acquires a positive Faraday rotation angle through virtual excitation of e-h pairs. (b) A single spin down hole is probed by using off-resonant linearly polarized photon that acquires a negative Faraday rotation angle through virtual excitation of e-h pairs. 106

Figure 4.1 (a) Band inversion in between two end members in $\mathrm{Pb}_{1-x}\mathrm{Sn}_x\mathrm{Te}$. (b) Energy spectrum of the inverted contact. The solid lines are Weyl states and dashed lines are additional branches that appear for contact thickness $l > l_o$. 112

Figure 4.2 Brillouin zone for rocksalt type crystal with space group $\mathrm{Fm\bar{3}m}$. There are four inequivalent L points at the center of the faces on the surface of the Brillouin zone. The growth direction is along [111] and is chosen to point along the z-axis. With the appropriate level of doping by Sn atoms in PbTe, band gap goes to zero at L point with a linear excitation energy that traces out a cone in the 2D Fermi surface parallel to the face of Brillouin zone that is perpendicular to the growth direction 115

Figure 4.3 Transparency region for the optical excitation of the Weyl fermion. The light yellow color (online) represents the filled Fermi sea of the electrons. The zero energy is defined by the apex of the Dirac cone. **a** With the photon energy of $\hbar\omega \geq 2E_F$ a Weyl fermion can be excited. There are no transitions for a photon energy below $2E_F$. The Fermi level is measured from the zero of the energy. **b** The Fermi level can be shifted below the

Dirac node by applying a gate voltage $V_g \geq E_F$. Then a Weyl fermion can be excited with a photon energy of $\hbar\omega \geq |E_F|$. 118

Figure 4.4 Effect of Rashba spin-orbit coupling. Spin vector $\boldsymbol{S}^{(-)}$ ($\tilde{\boldsymbol{S}}^{(-)}$) in the L^- band and spin vector $\boldsymbol{S}^{(+)}$ ($\tilde{\boldsymbol{S}}^{(+)}$) in the L^+ band are perpendicular to both the z-axis and $\boldsymbol{p}_\perp$ ($\tilde{\boldsymbol{p}}_\perp$) for Weyl interface states (Weyl Kramers partner states). (a) and (b) ((c) and (d)) correspond to positive (negative) eigenenergy. 123

Figure 4.5 The interband transitions for the spin selection rules in 3D TIs. The Dirac cone represents the component of the Weyl states. The interband transitions occur between positive and negative energy solutions. The helicity of the band is represented by $h = +1/2$ ($h = -1/2$) for the positive energy solution (negative energy solution). 128

Figure 4.6 Spin selection rules in 3D TIs. The states are labeled with $\phi_{\pm}^{L^{\pm}}$. The transitions are vertical conserving the spin's direction. The direction of the momentum is shown along x-axis (a) in which case the polarization of the light couples the spin pointing along y-axis and along y-axis (b) in which case the polarization of the light couples the spin pointing along x-axis. In each case the spin points perpendicular to the momentum (see Figure 4.5). 131

Figure 4.7 Bulk bandstructure of $\mathrm{Pb}_{1-x}\mathrm{Sn}_x\mathrm{Te}$ at $x = 0.375$ doping level including spin-orbit coupling. The crossing has been reported around $x = 0.35$. In the supercell Brillouin zone bands are folded from the neighboring Brillouin zones into the first Brillouin zone [(a) and (b)]. A small band gap of 1.8 meV appears at the Γ point of the supercell Brillouin zone, which corresponds to the band gap minimum at the L point in the primitive cell Brillouin zone after unfolding, as shown in **c**. L_{SC} and L_{PC} are L points in the supercell Brillouin zone and the primitive cell Brillouin zone, respectively. The solid green color peaks in (c) denotes the spectral functions. Bands of opposite parity nearly cross at around 67 meV below the Fermi level at the L point where a single Dirac point is observed (d). 134

Figure 4.8 **a**. A slab of thickness $d = 10$ nm of 3D TI material $\mathrm{Pb}_{1-x}\mathrm{Sn}_x\mathrm{Te}$ is sandwiched by PbTe with thickness t. This structure can have Weyl fermions at the interface with zero bandgap at one of the L point in the Brillouin zone while the rest of the L points have non-zero bandgaps due to the interactions between the L valleys of the two interfaces. **b**. Solutions inside and outside the material can be found by dividing the geometry into five different regions, I, II, III, IV and V with the fields E_I, E_{II}, E_{III}, E_{IV} and E_V, . 136

Figure 4.9 Illustration of the diagonal, $|D\rangle$ and anti-diagonal, $|A\rangle$ polarization in a Poincare sphere. $\langle\hat{\sigma}_x\rangle$, $\langle\hat{\sigma}_y\rangle$ and $\langle\hat{\sigma}_z\rangle$ are the expectation values of the Pauli matrices $\sigma_x = \begin{pmatrix} 0 & 1 \\ 1 & 0 \end{pmatrix}$, $\sigma_y = \begin{pmatrix} 0 & -i \\ i & 0 \end{pmatrix}$ and $\sigma_z = \begin{pmatrix} 1 & 0 \\ 0 & -1 \end{pmatrix}$, respectively. $|\sigma_x\rangle$ and $|\sigma_y\rangle$ represent the x- and y-polarization states and $|\sigma_+\rangle$ and $|\sigma_-\rangle$ represent the left and right circular polarization states of the photon 148

Figure 4.10 Transmittance and the Faraday rotation angle are plotted as a function of thickness t and wavelength λ for the geometry shown in Figure 4.8. In **a** and **b** we choose $T_r = T_p = 1$ ps, while in **c** and **d** we choose $T_r = T_p/10 = 1$ ps. For **a** and **c** the wavelength is $\lambda = 9.97\,\mu m$, which corresponds to a detuning energy of 10 meV. For **b** and **d** the thickness is $t = 1.72\,\mu m$. The width of the transparency region of the excitation of Weyl fermion is 134 meV, as calculated from the bandstructure as shown in Figure 4.7. 150

Figure 5.1 **a**, 3D TI layers stacked on top of each other to make a multilayer heterostructure consisting of PbTe/$Pb_{0.31}Sn_{0.69}Te$/PbTe. There are Weyl fermions at each interface that give rise to the large value of the surface conductivity. **b**, The multilayer system can be solved by using a transfer matrix method. In each layer there is a reflected and a transmitted field. The interface conductivity is modeled to be proportional to a delta function, which corresponds to the trapping of the Weyl fermions at each interface. 155

Figure 5.2 A gate voltage V_g can be applied to shift the Fermi level in a controlled way. 157

Figure 5.3 Transmittance plotted as a function of the number of unit cell (number of AB stacking). Transmittance decreases as the number of interface layers increases. Each layer has a width of $d \approx 10$ nm along the growth direction. 160

Figure 6.1 (a) and (b) Optical micrograph and AFM image of a single layer MoS_2 flake exfoliated on Si/SiO_2 substrate. (c) Raman spectrum of the single layer MoS_2. (d) Gate dependence of the source drain current (ID) after different plasma exposure time. (e) Effect of plasma exposure on the on-current (at $V_G = 40$ V) and mobility of the single layer MoS_2 device (These results were obtained by Dr. Khandaker's group). 164

Figure 6.2 (a) I_D vs V_{DS} characteristics curve for the single layer MoS_2 device after different plasma exposure time. (b) Resistance of the device as a function of plasma exposure time. The green line is the linear fit of the logarithmic resistance as a function of exposure duration. (c) Raman spectra of pristine MoS_2 (red) and plasma etched MoS_2 (green) obtained with a 532 nm excitation wavelength. 165

Figure 6.3 A single sheet of (a) MoS_2 and (b) MoO_3. (c) Side and (d) top view of the optimized structure of MoS_2 with a single O atom (red) replaced by a single S atom (yellow) in the unit cell. (e) Top and (e) side view of the optimized structure of MoS_2 with three S atoms replaced by three O atoms in a 2x2 supercell, where it is evident that the covalent bonds form between one of the Molybdenum atoms (cyan) and the three O atoms forming a stable MoO_3 defect 168

Figure 6.4 Single-layer MoS_2 characterization. (a) Optical, (b) AFM image and height profile, (c) Raman spectrum, (d) photoluminescence (PL) spectrum of exfoliated single-layer MoS_2 on Si/SiO_2 substrate. 172

Figure 6.5 (a) PL spectrum of single-layer MoS_2 as function of plasma-treated time. PL spectra of pristine flake shows strong response of the monolayer (red) and gradual PL quenching appears after treatment (t1 to t8). (b) PL intensity ratio (peak A1/peak B1) is plotted with respect to exposure time. 174

Figure 6.6 Band structure of (a) pristine single-layer MoS_2, (b) single-layer MoS_2 with one S atom replaced by one O atom, (c) single-layer MoS_2 with three S atoms replaced by three

O atoms, and (d) a single-layer of MoO_3. Single layer of MoS_2 has direct bandgap at K point (a). The replacement of an S atom by an O atom changes the positions of the band extrema (b,c). The d-bands of MoS2 at the band extrema are more hole type at the K point (a). The red arrows indicate the direct bandgap and blue arrows indicate the indirect bandgap . 175

Figure A.1 Two antipodal points on the surface of the sphere defined by the QD are identified as the Dirac cones of opposite helicity. One point lies on the northern hemisphere, while its antipodal point lies on the southern hemisphere. The currents flowing along the latitudes can be imagined as angular momentum states of a 3D TI QD in the continuum limit. At the antipodal points momenta (red arrows) point in opposite $\hat{\varphi}$ direction to each other while spins (blue arrows) point in the same $\hat{\theta}$ direction, where $\hat{\theta}$ and $\hat{\varphi}$ are the spherical angular unit vectors. Hence, they have opposite chirality. This satisfies the fermion doubling theorem. 188

Figure C.1 Schematic of MoS_2–EMSC heterojunction when treated with oxygen plasma. 196

LIST OF TABLES

Table 3.1 ϕ_- and ϕ_+ components 73

CHAPTER 1
INTRODUCTION

Since the discovery of Bohr's semiclassical theory of atom, it has been well-known that electrons are permitted to circulate around the nucleus in a certain number of close orbits. Along with motion of the electrons, these orbits around the nucleus are quantized in discrete numbers, as given by the famous Bohr quantization relation, $n\lambda = 2\pi r$, where n an is integer. λ and r are, respectively, the de Broglie's wavelength and radius of the orbit. Many fascinating phenomena in solid state physics rely on the quantization of the electronic motion and the electron's circular orbit around the nucleus. The quantized quantities are always characterized by quantum numbers. These numbers uniquely identify the properties of electrons and atoms in physics, and are the consequence of symmetries and boundary conditions present in the physical system.

For example, in the hydrogen atom an electron experiences a spherically symmetric potential due to the nucleus, which in turn provides a centrifugal force to keep the electron in circular orbits. The consequence of the periodic boundary condition of the closed orbits is that the electronic properties, such as the energy of the electron, are quantized with quantum numbers such as n, l, m_l, and so on. Each energy level is specified by a particular value of the quantum numbers. The lowest possible energy state, which is determined by the zero-point energy, defines the ground state of the electron. When two or more atoms of the same or different species bind together to form a molecule, the atomic orbitals from different atom hybridize with each other to form molecular orbitals with bonding and antibonding states. This means that the molecular orbitals are made of linear combinations of atomic orbitals, which is the basis for the Linear Combination of Atomic Orbitals (LCAO) method.

A statistically large number ($\sim 10^{23}$) of atoms bind together to form a solid. A solid can have several symmetries, one of which is the translation symmetry due to the periodic arrangements of atoms in a lattice. A simple band theory relies on the translation symmetry of the solid. When many atoms are brought together to form a solid, the atomic orbitals from the neighboring atoms hybridize with each other. Electrons are subjected to a periodic potential $V(\mathbf{r}) = V(\mathbf{r} + a)$, where $\mathbf{r}$ is the position vector of an electron and a is the lattice constant. This leads to a compact and a continuous structure of orbitals in the form of bands as shown in Figure 1.1. At 0 K, below the Fermi energy all the bands are occupied by electrons. Above the Fermi energy all the bands are empty. For materials like semiconductors, The Fermi energy lies between two bands. The energy separation between these two bands is called the bandgap. The bands around the Fermi level are usually derived from the valence orbitals of the atoms. Metals are zero bandgap materials because the Fermi level lies inside a band, and therefore the electrons can be accelerated with an infinitesimally small bias voltage. In contrast, semiconductors are materials with bandgaps ranging from several hundreds of meV to a few eV. Thus, an excitation energy exceeding the bandgap is required to generate mobile electrons in intrinsic semiconductor materials.

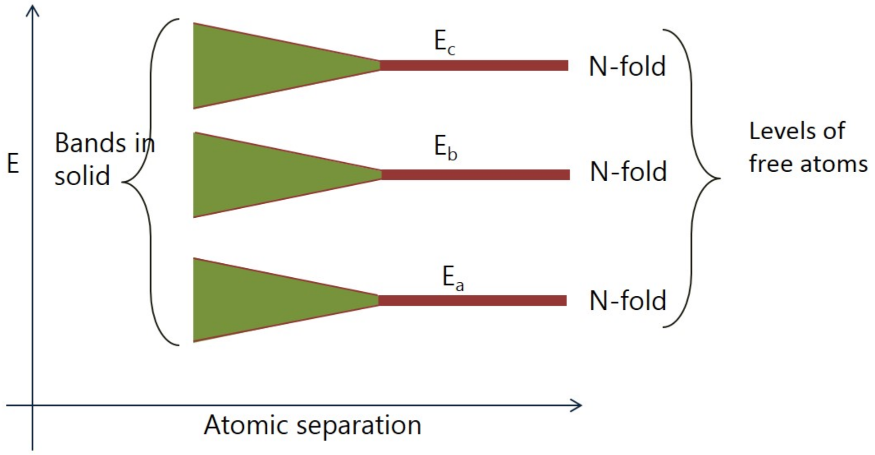

Figure 1.1: Atomic level splitting into bands as the atoms are brought together. When the atoms are far apart levels are discrete and N-fold degenerate. As they come closer the discrete levels form bands.

The bandgap in a solid has a significant role in modern electronic and optoelectronic devices. The semiconductor technology relies on the excitation of electrons and holes at band extrema across the bandgap. At zero temperature in a semiconductor the valence band is completely occupied and separated from the conduction band by an energy gap of magnitude E_g. At room temperature the occupation of the conduction band is proportional to a factor $e^{-\beta E_g/2} \sim 10^{-9}$, where $\beta = 1/k_B T$ and k_B is the Boltzmann constant. The thermal excitation provides an exponentially growing number of charge carriers with exponential increase in the conductivity with rising temperature, in contrast to metals where electron-electron and electron-phonon scattering reduces the conductivity as temperature rises. If the bandgap is below 1 eV, the thermal effect is more pronounced as the carriers can be excited due to thermal excitation. The semiconductor crystal is transparent for incident light with photon energy below E_g. Photons with energy above E_g are absorbed with efficiency according to the strength of the light-matter interaction. This process creates a large number of electron and holes (carriers) in the semiconductor. Carrier generation leads to quasi-equilibrium nonlinearities. The process drives the whole semiconductor into non-equilibrium dynamics, but the carriers are locally in quasi-equilibrium in their respective bands. The generated electron-hole pairs are thermalized at each band before they undergo [1] non-radiative Auger and radiative recombination. The laser pump pulse excites electrons in the picosecond regime and electrons acquire an electronic temperature T_e which can be much higher than the lattice temperature T_l, depending on laser pulse energy. In several hundreds of femtoseconds to a few picoseconds after excitation, electrons lose energy by electron-phonon and electron-electron scattering process, thereby thermalizing in the conduction band. The same happens to holes in the valence band. The experiment shows that carriers are cooled to the lattice temperature on a timescale of the order of 100 picoseconds. [2] Due to the principle of energy minimization, thermalized electrons and holes in quasi-equilibrium occupy the available states from the bottom of the conduction band and the top of the valence band, respectively, so that the energetically lowest states are occupied first. These generated free electron-hole pairs can alter the index of refraction of the materials. Due to Pauli's exclusion principle, further excitation of the carriers are suppressed if the lowest conduction bands are filled, which causes a decrease in the rate of absorption of photons.

The generation of electron-hole pairs in materials has great importance. In direct bandgap semiconductor materials, the mechanism of radiative recombination of electron-hole pairs leads to the emission of photons, which is the basis of Light Emitting Diodes (LEDs). In photodiodes, solar cells, and other semiconductor photodetector devices the excitation of electron-hole pairs by absorption of photons is the active process. In optoelectronic devices such as optical switches which are based on transmission and reflection of the photons, electron-hole pairs excitation is a *key* for the device performance. Diodes and transistors are also great discoveries in electronics which rely on the generation and recombination of electron-hole pairs at p-n junctions. A semiconductor heterostructures and semiconductor-metal heterostructures can form barrier regions due to charges redistribution or due to band misalignments. The working mechanism of devices that implement such heterostructures can be well understood by studying the dynamics of the electrons and holes across the barrier.

In 2D materials like graphene, electron-hole pairs can be excited around the Dirac point. An electron in a sheet of graphene has a linear excitation spectrum around the Dirac point. The Fermi level can be tuned using a gate voltage.[3] An electron at the valence band absorbs an energy $\hbar\omega \geq 2\,|E_F|$, where E_F is the Fermi level measured from the Dirac point, and is excited to the conduction band leaving a hole behind. Small band-gap semiconductors usually have large electron-hole recombination rates due to Coulomb scattering. Due to linear excitation, and energy and momentum conservation requirement, the Coulomb scattering in graphene is restricted so that electron-hole recombination time can be much larger than 1 picosecond for electron-hole densities smaller than 10^{12}cm^{-2}.[4] The recombination rate is mainly dominated by the Auger process. Graphene has large optical phonon energy (196 meV).[5] Light absorption in graphene is universal[6], $\mathcal{P}_{graphene} = \pi\alpha$, where α is the fine structure constant.

Like in graphene, 3D topological insulator (3D TI) materials such as Bi_2Te_3, Bi_2Se_3, $Bi_{1-x}Sb_x$ and $Pb_{1-x}Sn_xTe$ are also characterized by the presence of linear excitation energy at band crossing point after which they enter into the topological regime.[7] These materials are metallic on the surface due to the presence of gapless surface/interface states, but insulators in the bulk.[8, 9, 10, 11] The electron's spin is locked in perpendicular direction to the momentum due to the Rashba spin-orbit coupling.[12] In graphene it is the pseudo-spin that is locked to the momentum, pointing either in the same or in the opposite direction. The spin-orbit coupling in graphene is negligibly small. Therefore the real spin is not locked to the momentum direction in graphene. In topological insulators, time reversal symmetry, leading to Kramers degeneracy, protects the surface states, which form Kramers pairs, from back scattering off non-magnetic impurities. The interband and intraband transitions obey strict optical selection rules that govern the low energy excitation of the electron-hole pairs around the Dirac point on the surface. In 3D TIs nanostructures, the Kramers partners in the valence and conduction band can be coupled by a left (σ_-) and a right (σ_+) handed circular polarization of the light. Such coupling of light with electron-hole pair polarization provides the unique opportunity to utilize 3D TIs in quantum information processing and spintronics devices. There is an electron-hole symmetry in the linear excitation spectrum of 3D TIs, which is in contrast to the electorn-hole dispersion in a semiconductor, where electron and hole have different masses. In Bi_2Te_3 film with thickness exceeding 6 quintuple layers (QLs), the low energy absorption of photons by the gapless states always occurs with photon energy ranging from 0 to 0.3 eV. Due to two Dirac cones from up and down surfaces, which provide two real spins, the absorption is half of the one in graphene[4], $\mathcal{P}_{gapless} = \frac{\pi}{2}\alpha$. In less than 6 QLs, the case would be different as the gap is opened due to interaction between the states from the opposite surfaces, and therefore, the absorption becomes gap dependent.

1.1 Light-matter Interaction

An electron in the ground energy level can be excited to a higher-energy level by means of the absorption of a photon of energy matching the energy separation between the two levels. In atoms, the valence electrons are loosely bound. They can be easily excited to higher levels. Similarly, in a molecule electrons occupying the valence molecular orbitals are loosely bound and can be excited with a small amount of energy. In a solid, electrons occupying the bands around the Fermi level are more loosely bound than those occupying the bands lying deeply below the Fermi level. In insulators the bandgap is wide and energy needed to excite valence electrons close to the Fermi level is much larger than in semiconductors. In metals, in principle, no energy is needed to excite the electrons as the bandgap is zero.

Let us consider a perfect crystal. The Hamiltonian of the system can be written as

$$\begin{aligned} H \;&=\; \sum_i \frac{p_i^2}{2m} + \sum_j \frac{P_j^2}{2M_j} + \frac{1}{2}\sum_{j',j}{}' \frac{Z_j Z_{j'} e^2}{4\pi\varepsilon_o \left|\mathbf{R}_j - \mathbf{R}_{j'}\right|} \\ &\quad -\sum_{j,i} \frac{Z_j e^2}{4\pi\varepsilon_o \left|\mathbf{r}_i - \mathbf{R}_{j'}\right|} + \frac{1}{2}\sum_{j,i}^{\;\prime} \frac{e^2}{4\pi\varepsilon_o \left|\mathbf{r}_i - \mathbf{r}_{j'}\right|}, \end{aligned} \tag{1.1}$$

where $\mathbf{r_i}$ denotes the position of the ith electron, $\mathbf{R}_j$ is the position of the jth nucleus, Z_j is the atomic number of the nucleus, $\mathbf{p}_i$ and $\mathbf{P}_j$ are the momentum operators of the electrons and nuclei, respectively. $\sum'$ denotes the summation over pairs of indices which are not identical. The quantum mechanical solution for such a large number of electrons is formidable. We need some approximations to solve this problem. The first approximation is that we separate electrons into two groups: valence and core electrons. Since the core electrons are localized near the nuclei we can combine them with the nuclei to make ion cores. The second approximation is called the Born-Oppenheimer approximation. The frequencies of the ionic vibration in a solid are less than 10^{13} s^{-1}, while in a typical semiconductor with a gap of 1 eV the electronic frequencies are of the order of 10^{15} s^{-1}. Thus, for the electrons the ions appear to be at rest, i.e. the ions cannot follow the motion of the electrons, which is the basis for the Born-Oppenheimer approximation. Consequently, the electronic motion in Equation 4.1 can be separated from the ionic motion. The electronic Hamiltonian H_e reads

$$H_e = \sum_i \frac{p_i^2}{2m} + \frac{1}{2}\sum_{i,i'}{}' \frac{e^2}{4\pi\varepsilon_o \left|\mathbf{r}_i - \mathbf{r}_{i'}\right|} - \sum_{i,j} \frac{Z_j e^2}{4\pi\varepsilon_o \left|\mathbf{r}_i - \mathbf{R}_{jo}\right|}, \tag{1.2}$$

where R_{jo} is the ion's position frozen at the equilibrium.

The diagonalization of Hamiltonian H_e is almost impossible for a semiconductor where the density of the electrons is $> 10^{23}/\text{cm}^3$. To circumvent this problem we make a mean field approximation. Under this approximation, every electron experiences the same average potential $V(\mathbf{r})$. Therefore, the Hamiltonian describing the motion of each electron will be identical and is given by

$$\mathcal{H}_o = \frac{p^2}{2m} + V(\mathbf{r}). \tag{1.3}$$

When the electron is placed in an external electromagnetic field, the electron's momentum $\mathbf{p}$ behaves as $\mathbf{p} \longrightarrow \mathbf{p} + e\mathbf{A}(\mathbf{r}, t)/c$, where $\mathbf{A}(\mathbf{r}, t)$ is the vector potential of the electromagnetic field and c is the velocity of light. Due to *gauge invariance,* the choice of $\mathbf{A}(\mathbf{r}, t)$ is not unique. We can choose a Coulomb gauge in which $\Phi(\mathbf{r}, t) = 0$ and $\nabla \cdot \mathbf{A}(\mathbf{r}, t) = 0$, where $\Phi(\mathbf{r}, t)$ is a scalar potential. Equation 4.3 can be written as

$$\mathcal{H}_e = \frac{(\mathbf{p} + e\mathbf{A}/c)^2}{2m} + V(\mathbf{r}). \tag{1.4}$$

Since $\nabla \cdot \mathbf{A}(\mathbf{r}, t) = 0$ we have $(e/2mc)\, \mathbf{p} \cdot \mathbf{A}$=$(e/2mc)\, \mathbf{A} \cdot \mathbf{p}$. The quadratic term in $\mathbf{A}$ can be neglected for the calculation of linear optical properties. Using this assumption, Equation 3.4 can be written as

$$\mathcal{H}_e = \mathcal{H}_o + \mathcal{H}_{eR}, \tag{1.5}$$

where $\mathcal{H}_{eR} = \frac{e}{mc}\mathbf{A}.\mathbf{p}$ describes the interaction of radiation with a Bloch electron. In the limit when the wave vector of the electromagnetic radiation is small compared to the lattice constant, $\mathcal{H}_{eR} = \frac{e}{mc}\mathbf{A}.\mathbf{p}$ is equivalent to $\mathcal{H}_{eR} = (-e)\mathbf{r} \cdot \mathbf{E}$, where $\mathbf{E}$ is the electric field. This is called the electric dipole approximation. Both forms of $\mathcal{H}_{eR}$ neglect the quadratic term in the field. In $\mathcal{H}_{eR} = (-e)\mathbf{r} \cdot \mathbf{E}$ the Lorentz force has been neglected. This means there is no quadratic term in the field as the Lorentz force depends on $\mathbf{v} \times \mathbf{B}$, and $\mathbf{v}$ behaves as

E, so $\mathbf{v} \times \mathbf{B}$ is quadratic in the field. The advantage of using the form $\mathcal{H}_{eR} = \frac{e}{mc}\mathbf{A}.\mathbf{p}$ in semiconductors is that in the $\mathbf{k} \cdot \mathbf{p}$ method the matrix elements of the electron wave vector enter directly. The matrix elements of the electron's wave vector enter in many important optical properties of the materials, such as e.g. the dielectric function of the materials.

1.2 Electron-hole pairs and surface plasmons in metallic structures

When an electron in the valence band absorbs a photon with energy $\hbar\omega \geq E_g$, it is excited to the conduction band. During this process it creates a hole in the valence band. In semiconductors, the Coulomb interaction between the electron and the hole creates a bound system called the exciton. In metals, unlike semiconductors, the situation is different. The metal has a Fermi level that lies in conduction band. Therefore, there are free carriers on the metal's surface which move under the influence of ion cores. In a sodium atom, for example, the valence electron is in a 3s state and in sodium metal this becomes a conduction electron in a 3s conduction band. The alkali metals such as lithium, potassium, cesium, and rubidium have free electrons in their conduction bands. The collection of such electrons is called a free electron Fermi gas.

The classical properties of the metal can be explained by a simple *plasma model,* where a gas of free electrons of number density n moves against a homogeneous background of positive ion cores. For alkali metals this model works up to the ultraviolet regime, while for the noble metals the model is limited due to the interband transitions that occur at visible frequencies. The holes in valence bands are filled by the free carrier absorption which are the intraband transitions. The classical plasma model does not incorporate the electron-electron interaction and the notion of the effective mass from the band theory. Free electrons subjected to the external electric field **E** oscillate with a frequency ω. The oscillations damps with a characteristic collision frequency of $\gamma = 1/\tau$, where τ is the relaxation time of the free electrons (τ is in the order of 10^{-14} s in metal). The equation of motion of the free electron gas can be written as

$$m\ddot{\mathbf{x}} + m\gamma\dot{\mathbf{x}} = -e\mathbf{E}. \tag{1.6}$$

Using a harmonic dependence of the field as $\mathbf{E}(t) = \mathbf{E}_o e^{-i\omega t}$, the solution of Eq. (4.6) can be written as $\mathbf{x}(t) = \mathbf{x}_o e^{-i\omega t}$. So, we obtain $\mathbf{x}(t) = \frac{e}{m(\omega^2+i\gamma\omega)}\mathbf{E}(t)$. The polarization **P** is given by $\mathbf{P} = -ne\mathbf{x} = -\frac{ne^2}{m(\omega^2+i\gamma\omega)}\mathbf{E}$. The electric displacement vector **D** can be written as $\mathbf{D} = \varepsilon_o\mathbf{E} + \mathbf{P}$ (in SI unit), where ε_o is the permittivity of free space. We also have $\mathbf{D} = \varepsilon_o\varepsilon(\omega)\mathbf{E}$, where $\varepsilon(\omega)$ is the frequency dependent dielectric function. Therefore, $\varepsilon(\omega)$ can be written as

$$\varepsilon(\omega) = 1 - \frac{\omega_p^2}{\omega^2 + i\gamma\omega}, \tag{1.7}$$

where $\omega_p^2 = \frac{ne^2}{\varepsilon_o m}$ is called the plasma frequency of free electron gas. For the noble metals such as gold (Au), silver (Ag) and copper (Cu), there is a residual polarization due to the positive background of the ion cores the effect of which can be incorporated by writing Eq. (4.7) as

$$\varepsilon(\omega) = \varepsilon_\infty - \frac{\omega_p^2}{\omega^2 + i\gamma\omega} \tag{1.8}$$

This model, while being able to explain the behavior of the dielectric function for the alkali metals, fails to explain the dielectric function for the noble metals. Au has at least two interband transitions occurring at the wavelength of 470 nm and 330 nm. [13] These interband transitions are not described by Eq. (4.8). The Lorentz oscillator of the form $\frac{A_i}{\omega_i^2-\omega^2-i\gamma_i\omega}$ can be added to model each interband transition in Eq. (4.8). Other improved models such as the Drude-critical model and the L4 model can be used to circumvent this drawback.[14] The above model is also known as the Drude model for free electron gas.

The coherent oscillations of the free electron density described by Eq. (4.8) on the positive background of the ion cores are known as plasmons. In noble metals these coherent oscillations are disturbed by the interband transitions that occur at the visible frequencies. The plasmons can be well described within classical electrodynamics by solving Maxwell's equations. Using Maxwell's equation it is not difficult to show that for longitudinal waves $\varepsilon(\mathbf{K},\omega) = 0$ and for transverse waves $K^2 = \varepsilon(\mathbf{K},\omega)\frac{\omega^2}{c^2}$. For large frequency close to ω_p, $\omega\tau \gg 1$, we get $\varepsilon(\omega) = 1 - \frac{\omega_p^2}{\omega^2}$. This is the plasma oscillations for the undamped free electrons. For the noble metals interband transitions alter the situation. Combining the above relations we obtain that $\omega^2 = \omega_p^2 + K^2c^2$. The $\omega > \omega_p$ is the transparency regime of the metal and supports the propagation of the transverse modes. For $\omega < \omega_p$, the metal does not support the propagation of the transverse modes. For $K = 0$, i.e. for the long wavelength limit, we obtain $\omega = \omega_p$ and hence $\varepsilon(\omega) = 0$. The quanta of such oscillations are known as the volume plasmons. The metal volume plasmon energy is in the range of 5 to 15 eV.

The excitations of the quantum of the electron's oscillations on the metal-dielectric interface are known as surface plasmons. Surface plasmons can be coupled with the propagating electromagnetic waves at the interface and evanescently confined in the perpendicular direction. These are the surface plasmon polaritons which are characterized in terms of their dispersion and spatial profile together with the field confinement. The resonance energy of the surface plasmons at the metal dielectric interface depends on several parameters such as geometry, compositions, and surrounding dielectric environment.

1.3 Electron-hole pairs and excitons in wide bandgap semiconductors

In metals, valence electrons are treated as a free electron gas with the background of positive ion cores. The interband transitions from d bands in noble metals create holes which are filled by the free carrier absorption. In semiconductor crystals, the plasma model usually fails due to lack of free electrons in the intrinsic (undoped) regime. The generated electrons and holes are subjected to the periodic potential. As a result, when they travel over a distance of few lattice spacings their motion is affected. Their masses also appear to be different than the masses of the free electron or the free hole, and the new masses are taken as the effective masses. The electron and hole have different effective masses. As an example, the effective mass of electron in germanium is $m^* = 0.041\, m_o$, where m_o is free electron mass. Due to the difference in effective masses, an electron has a sharper dispersion of bands than a hole.

Electrons in semiconductors can be excited in two ways: **a**, an electron in the valence band is excited to the conduction band by absorbing a photon with energy $\hbar\omega \geq E_g$ (interband transition) and **b**, an electron is excited within the valence or within the conduction band by absorbing a photon of energy $\hbar\omega$ (intraband transition). The interband transition creates a hole in the valence band. The hole can be filled either by a free carrier absorption (phonon assisted transition) or by recombining with the excited electrons. A laser excites an electron in semiconductors in few picoseconds. The electron relaxes to the bottom of the conduction by thermalization process (carrier-carrier scattering and carrier-phonon scattering) in time of few picoseconds to about 100 nanoseconds.[1] In about 100 nanoseconds to 1 microsecond, the electron recombines with a hole either by Auger or radiative recombination. In several hundreds microseconds, thermal and structural effects may appear in the semiconductor crystal due to ablation, thermal diffusion, or re-solidification.

If we ignore the effect of Coulomb interaction between an excited electron and a hole, the pair is called the free electron-hole pair. In reality, Coulomb interaction is always present, which may modify the electronic and optical properties of the materials. Consider a bandstructure of a semiconductor as shown in Figure 1.2 **a** with full valence band and an empty conduction band. There are no allowed states in the bandgap. Now consider the case with one electron in the conduction band and one hole in the valence band as shown in Figure 1.2 **b**. We now have an additional Coulomb interaction between the electron and the hole. The electron-hole system coupled through the Coulomb interaction is called the exciton.

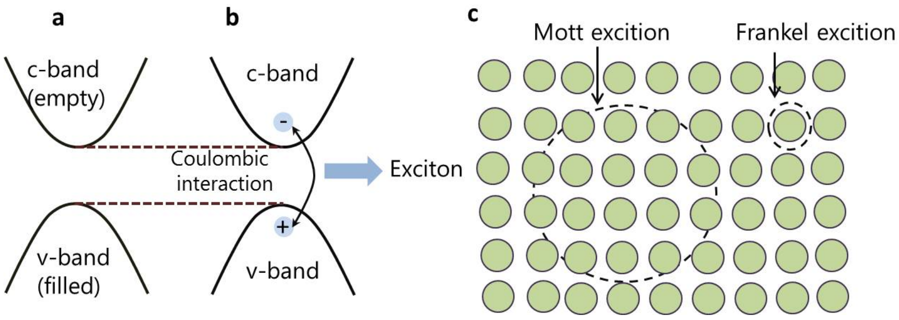

Figure 1.2: **a**, The bandstructure in the independent electron picture, and **b**, the Coulombic interaction between the electron and hole: excitonic effect. **c**, a conceptual picture of the periodic envelope function extent of the Frenkel and Mott excitons.

There are two types of exciton in general depending on the spatial extension of the envelope function: Frenkel excitons and Mott excitons. Frenkel excitons are excitions with envelope function confined to just a few unit cells, while the Mott excitions have envelope functions spread over several unit cells. In effective mass theory both excitions can be described by the following equation,

$$\left[-\frac{\hbar^2}{2m_e^*}\nabla_e^2 - \frac{\hbar^2}{2m_h^*}\nabla_h^2 - \frac{e^2}{4\pi\varepsilon\left|\mathbf{r}_e - \mathbf{r}_h\right|}\right]\psi_{ex} = E\psi_{ex}. \tag{1.9}$$

Here m_e^* and m_h^* are the effective masses, respectively, for the electron and the hole. ψ_{ex} is the excitonic wave function. This is a two-body problem and can be reduced to one body problem by defining $\mathbf{r} = \mathbf{r}_e - \mathbf{r}_h$, $\mathbf{k} = \frac{m_e^*\mathbf{k}_e + m_h^*\mathbf{k}_h}{m_e^* + m_h^*}$, $\mathbf{R} = \frac{m_e^*\mathbf{r}_e + m_h^*\mathbf{r}_h}{m_e^* + m_h^*}$ and $\mathbf{K} = \mathbf{k}_e - \mathbf{k}_h$. The

Hamiltonian of the system is

$$H = \frac{\hbar^2 K^2}{2(m_e^* + m_h^*)} + \left\{ \frac{\hbar^2 k^2}{2m_r^*} - \frac{e^2}{4\pi\varepsilon\, |\mathbf{r}|} \right\}, \tag{1.10}$$

where m_r^* is the reduced mass of electron and hole. The first term in Eq. (3.18) has the plane wave solution in the center of mass system and has the form $\psi_{cm} = e^{i\mathbf{K}.\mathbf{R}}$ while the second term can be solved in a similar way to the problem of the hydrogen atom. The complete solution can be written as $\psi_{n\,\mathbf{K}_{ex}} = e^{i\mathbf{K}_{ex}.\mathbf{R}} F_n\left(\mathbf{r}\right) \phi_c\left(\mathbf{r}_c\right) \phi_v\left(\mathbf{r}_h\right)$, where $F_n\left(\mathbf{r}\right)$ is the envelope function that satisfies the second term in Equation 3.18. $\phi_c\left(\mathbf{r}_c\right)$ and $\phi_v\left(\mathbf{r}_h\right)$ represent the bandedge states of the electron and hole, respectively. The excitonic energy levels are given by

$$E_{n\,\mathbf{K}_{ex}} = E_n + \frac{\hbar^2 K^2}{2(m_e^* + m_h^*)}, \tag{1.11}$$

where n is an integer and $E_n = -\frac{m_r^* e^4}{2(4\pi\varepsilon)^2\hbar^2}\frac{1}{n^2}$. The second term in Equation 1.11 is simply the kinetic energy of electon-hole's center of mass. The excitonic levels appear slightly below the bandgap. The typical values of E_1 are 2-6 meV for most semiconductors.

1.4 Topological insulators in two and three dimensions

On the basis of charge flow, materials can be divided mainly into insulators, semiconductors, and conductors. If we analyze materials going into their electronic levels, amazingly, a semiconductor can be found to behave like a metal on its surface and a metal can be found to behave like an insulator. A metal can become insulating if repulsive interactions localize the electrons, which leads to a strongly correlated Mott insulator. A disordered system can also become insulating due to back-scattering events. In some materials an electron behaves very differently from others in external electric and magnetic fields. The behavior of electrons are deeply related to the symmetry in those materials. In addition, temperature is another controlling factor that determines the behavior of electrons. At low temperature when the system spontaneously loses one of the symmetries present at high temperature, it acquires an ordered state. The energy dominates over the entropy. As an example, a magnet breaks the time-reversal symmetry and the rotational symmetry in spin space. Their transport properties also change drastically. Landau symmetry breaking theory can provides insight in such order states. However, in 1980 the ordered state beyond the symmetry breaking was observed which could not be explained by Landau symmetry breaking theory.[15] After that many theoretical and experimental attempts have been done to understand such unusual property of the electron. Here we briefly discuss the physics behind this interesting effect.

1.4.1 Edge states and quantum Hall effect

The experimental and theoretical understandings of the quantum Hall states in condensed matter physics have been established since the 1980's.[15, 16] Such states occur when an electron confined in a two dimensional plane is placed in a strong magnetic filed. The electron's orbit is quantized with the cyclotron frequency ω_c. The quantized Landau levels are given by $E_n = \hbar\omega_c \left(n + \frac{1}{2}\right)$. The Hall conductivity σ_{xy} is also quantized: $\sigma_{xy} = Ne^2/\hbar$,

N being the number of filled Landau levels. The difference between a quantum Hall system and a trivial insulator is determined by topology.[17] A 2D bandstructure is a mapping of a wave vector $\mathbf{k}$ in a 2D Brillouin zone (which is a torus) to the Bloch Hamiltonian $\mathcal{H}(\mathbf{k})$. In gapped insulators, two equivalent classes of $\mathcal{H}(\mathbf{k})$ can be deformed continuously from one to another without closing the gap, and bandstructures can be classified in terms of these classes. The integer quantity $n \in \mathbb{Z}$, where $\mathbb{Z}$ is the integer domain, that distinguishes these different classes is called Chern invariant. The Chern invariant can be understood in terms of Berry phase associated with the Bloch wave function $u_m(\mathbf{k})$ in Brillouin zone. When $u_m(\mathbf{k})$ changes adiabatically in parameter space (here $\mathbf{k}$-space), it acquires a Berry phase γ_m which is given by the line integral of the quantity $\mathcal{A} = i \langle u_m | \nabla_{\mathbf{k}} | u_m \rangle$ around a closed path. There is a Berry flux $\mathcal{B}_m = \nabla \times \mathcal{A}_m$ associated with the closed path. The Chern number is given by $n_m = (1/2\pi) \int d^2\mathbf{k}\mathcal{B}_m$. This is a quantized quantity. The total Chern number $n = \sum\limits_{m}^{N} n_m$ over all the occupied bands is invariant regardless of the degeneracies present in the system. This explains that even if the Hamiltonian $\mathcal{H}(\mathbf{k})$ is smoothly deformed, the total Chern number associated with the system remains unchanged. This is why the quantization of σ_{xy} is so robust under deformation.

A fundamental consequence of topological classification of gapped insulators is that it predicts the presence of gapless states at the interfaces. The topological invariant of the system changes as we pass the gapless point in surface bandstructures. This identifies the two phases of matter in contact to each other, say quantum Hall state ($n = 1$) and vacuum ($n = 0$), which forms an interface. The quantum Hall states occur as the cyclotron motion of the electrons undergoes skipping orbits at the surface. Such electronic states are *chiral*. This means the propagation is along one direction along the edges. These chiral states are safe from the backscattering events as no states are available to make a U-turn.

To elucidate this fact further, we consider an interface with quantum Hall state and vacuum perpendicular to y-axis. If the topological invariant of the system has to change from $n = 1$ to $n = 0$, inevitably, the gap vanishes at the edge of the two-dimensional system. At this point, it is instructive to consider a low energy Hamiltonian for quantum Hall system as developed by Ludwig et al.[18] They showed that the low energy effective Hamiltonian can be written as $H_i = v_F\left(\sigma_x k_x + \sigma_y k_y\right) + m_i \sigma_z$, where v_F is the Fermi velocity, σ_i are the Pauli matrices, m_i is the effective mass in ith band. We can model the interface assuming $m \longrightarrow m\left(y\right)$ such that $m_1 > 0$ (quantum Hall state) and $m_2 < 0$ (vacuum). Since the gapless states are at the edges, we can write $m_1\left(y\right) = -m_{10} \arctan\left(y\right)$. At $y = 0$, m_1 goes to zero. The effective Hamiltonian has a simple solution, $\Psi\left(x,\, y\right) = C e^{i k_x x} e^{(1/v_F)\int_0^y dy^i m_1(y^{'})} \begin{pmatrix} 1 \\ 1 \end{pmatrix}$, where C is the normalization constant. This shows that wave function is localized along y direction, whereas it is a plane wave in x direction. The energy eigenvalue for the gapless mode is $E = \hbar v_F k_x$. By means of bosonization a representation in the form of one-dimensional right and left movers along the edges can be found.[18]

1.4.2 Z_2 Topological insulators

In quantum Hall states, the time reversal (TR) symmetry is broken because the applied magnetic field is odd under the TR operation. There is a new topological class that occurs in a zero applied magnetic field but with a strong spin-orbit coupling. This class is protected by the TR symmetry. To understand that, it is essential to know how the TR operator Θ affects spin under operation. This operator is defined as $\Theta = e^{(i\pi S_y/\hbar)}K$, where S_y is the spin operator and K is the complex conjugation. For electrons, $\Theta^2 = -1$. This tells us that Bloch Hamiltonian $\mathcal{H}(\mathbf{k})$ that respects TR symmetry, $\Theta^{-1}\mathcal{H}(\mathbf{k})\,\Theta = \mathcal{H}(-\mathbf{k})$, is at least two fold degenerate on the surfaces. This is known as Kramers theorem. In the absence of spin-orbit interaction Kramers degeneracy is the degeneracy between up and down spin. Consider the 2D bandstructures in Figure 1.3, plotted for half of the Brillouin zone, $0 > k_x > \pi/a$.

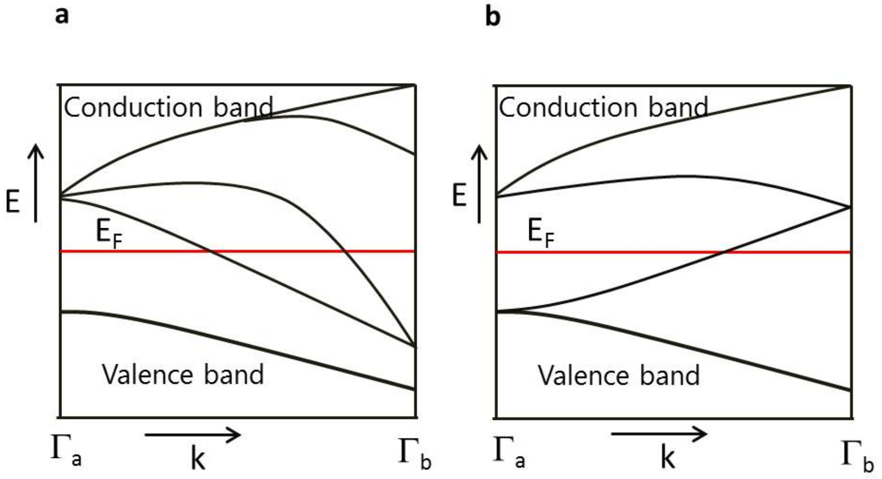

Figure 1.3: Dispersion relation for Kramers degenerate points at $\mathit{\Gamma}_a = 0$ and $\mathit{\Gamma}_b = \pi/a$. The number of Fermi surface crossing the Fermi Level is even in **a,** and odd in **b**. The bulk valence and conduction bands are also shown.

Two halves of the Brillouin zone are mirror images of each other, as required by TR symmetry. From the Kramers theorem the points $\mathit{\Gamma}_a = 0$ and $\mathit{\Gamma}_b = \pi/a$ are two-fold degenerate. In Figure 1.3 **a** edge states cross the Fermi level at two points, whereas in **b** there is only one edge that crosses the Fermi level. In the case of two crossings, edge states are pushed out of the gap due to scattering, leading to a trivial insulator, whereas in the case of a single crossing we get a nontrivial topological insulator. This topological nature of the bands can be understood by introducing one more topological invariant with two possible values: $\nu = 0$ and $\nu = 1$ [10], in addition to the previously introduced topological invariant n. ν is also called the Z_2 topological invariant. This new invariant distinguishes weak topological insulators from strong topological insulators. Each band intersecting the

Fermi level at k_x has a Kramers pair at $-k_x$. The number N_k of Kramers pairs intersecting the Fermi level is related to the changes in the Z_2 invariants as $N_k = \Delta\nu \bmod 2$. The Z_2 invariant ν can be calculated in different ways. In a system which conserves spins along the z direction, i.e. S_z is conserved, the difference $n_\sigma = \left(n_\downarrow - n_\uparrow\right)/2$ defines the Z_2 invariant as $v\nu = n_\sigma \bmod 2$.[19]

1.4.3 Quantum spin Hall insulator

In 2006, Bernevig, Hughes, and Zhang predicted that the transverse spin Hall conductivity is quantized in a system which respects the TR symmetry.[20] Subsequently, Kronig et. al in 2007 observed the quantized spin Hall conductivity effect in HgCdTe quantum well.[21] This effect is called quantum spin Hall effect (QSHE). Consider a system with strong spin-orbit coupling. The Hamiltonian decouples into two copies of the Haldane model[22] (a model for quantum Hall states), one for up spin, the other one for down spin. The quantum Hall conductivity is zero but the quantum spin Hall conductivity σ^s_{xy} is quantized and is given by $\sigma^s_{xy} = e/2\pi$. The quantum spin Hall states are the gapless modes at edges. Figure 1.4 shows the interface modes in a quantum spin Hall insulator (QSHI).

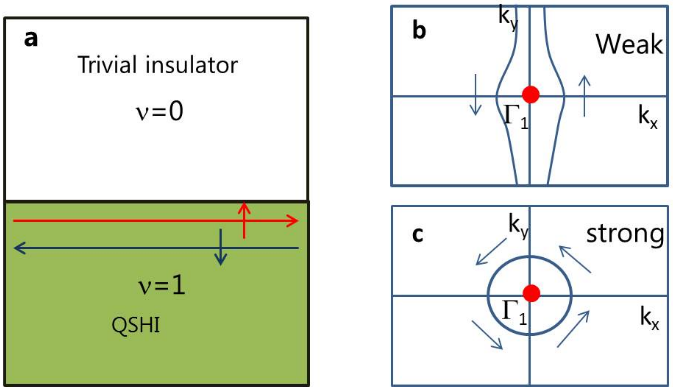

Figure 1.4: Interface modes in 2D quantum spin Hall insulator (QSHI) interfaced with trivial insulator. Weak and strong topological insulators, **a** and **b.**

The QSH states are *helical,* which means spin tracks the direction of the momentum. The spin and momentum are locked in perpendicular direction as required by the spin-orbit coupling. The spin up component propagates in opposite direction to that of the spin down component. Thus, there are two spin channels. Each channel is reserved for the flow of a particular type of spin. This is analogous to a half of a trivial 1D conductor. Such states cannot be localized even in presence of strong disorder, in contrast to ordinary conducting states where the effect of Anderson localizations cannot be ignored. Therefore, the edge states transport is always ballistic in QSHI.

1.4.4 3D topological insulators

QSHI are 2D topological insulators. In 2007, Moore and Balents [23] along with other research groups generalized the 2D topological insulators into 3D topological insulators. In 2008, Hsieh et. al[24]. experimentally observed the existence of the 3D topological nature of the QSHI in $\mathrm{Bi}_{1-x}\mathrm{Sb}_x$. In subsequent years, materials such as $\mathrm{Bi_2Te_3}$ and $\mathrm{Bi_2Se_3}$ were also experimentally found to be 3D topological insulators.[25] The 3D topological insulators are characterized by four Z_2 invariants $\nu_o : \nu_1, \nu_2, \nu_3$. The value of the invariant ν_o classifies whether the 3D topological insulator is weak ($\nu_o = 0$) or strong ($\nu_o = 1$) as shown in Figure 1.4 **a** and **b.** A weak topological insulator can be realized with a stack of 2D quantum spin Hall insulator layers, where the helical edge modes leads to anisotropic surface modes. In such a setup the indices ν_1, ν_2 and ν_3 are defined as Miller indices describing the orientation of the layers. The Fermi surface is cut an odd number of times between $\mathit{\Gamma}_a = 0$ and $\mathit{\Gamma}_b = \pi/a$, but no closed Fermi surface exists. These modes, unlike the 2D helical modes, are not protected by TR symmetry. A strong topological insulator is not a simple generalization of 2D QSHI. The Fermi circle encloses an odd number of Dirac point. Due to TR symmetry, the state with $\mathbf{k}$ and $-\mathbf{k}$ are Kramers partners and back-scattering from one to another is always prohibited. An electron circling around a Dirac point always acquires a Berry phase of π as its spin rotates by 2π. A strong 3D topological insulator can be described by a low energy Dirac Hamiltonian, $\mathcal{H} = -i\hbar v_F \boldsymbol{\sigma} \cdot \nabla$, where $\boldsymbol{\sigma}$ are the in plane Pauli matrices. Eigen functions are localized on the 2D plane and exponentially decay in z direction. The localization length is around few nanometers. Within $k \cdot p$ approximation, the band crossing can be described by the two-band Dirac Hamiltonian. This results in two coupled equations for low energy modes with free particle like solutions in plane and exponentially decaying solutions in perpendicular direction. Those modes are called *Weyl* modes since they satisfies the Weyl equation.

1.5 Electron-hole pairs generation in 3D topological insulators

There is an important difference between graphene and 3D TIs from the physics point of view. The helicity operator in the graphene is given by $h_{\text{gra}} = -\left(1/\left|p_{\perp}\right|\right) \boldsymbol{\sigma} \cdot \boldsymbol{p}$, whereas in 3D TIs the helicity operator is given by $h_{\text{TI}} = \left(1/\left|p_{\perp}\right|\right) \beta \left(\boldsymbol{\sigma}_{\perp} \times \boldsymbol{p}_{\perp}\right) \cdot \hat{\boldsymbol{z}}$, where β is the Dirac β-matrix. The root of this difference lies in the spin-orbit coupling. Due to the strong spin-orbit coupling in 3D TIs, the electron spin points always in perpendicular direction to its momentum. A pristine graphene monolayer has a very small spin-orbit coupling and therefore the (real) spin-momentum locking is absent. Usually 3D TIs are compounds or alloys with heavy elements, so spin-orbit coupling is large in 3D TIs. The electron spin lies in the plane of the 2D Fermi surface encircling the Dirac point. Low energy excitations around the Dirac point can be obtained by the absorption of photons with energy $\hbar\omega \geq 2\left|E_F\right|$. Electron-hole pair generation is driven by strict spin selection rules. The interband coupling of low energy modes is basically controlled by the matrix elements of the Dirac α-matrix and the intraband coupling is driven by the matrix element of momentum matrix under dipole approximation. A photon traveling along x direction can excite a spin pointing along the y direction, and vice versa. Due to the presence of the strong spin-orbit coupling in 3D TI the induced spin polarization relaxes on a time scale of the momentum scattering. As calculated in Ref. [26], the spin polarization decays rapidly within a time of the order of T_2 =0.01–0.1 ps, which results in loss of spin coherence. The large anisotropic dielectric constant ($\varepsilon \sim$50-200) tells that the Coulomb interaction is strongly reduced in 3D TIs.[27] This leads to a weak coupling between the generated electron and hole. Thus it is a good approximation to assume that electron-hole pairs do not form bound excitons in 3D TIs.

1.6 Two-dimensional layered materials

The experimental discovery of two-dimensional (2D) sheets of graphene by mechanical exfoliation from a layered solid and their unique mechanical, electrical, and optical properties attracted many scientists and engineers in the area of physics, engineering, and chemistry. These scientific efforts gave rise to the possibility of harvesting other 2D materials from layered solids.[28, 29, 30] In addition to graphene, several 2D layered materials with a possibility of single sheet exfoliation have been experimentally found. Examples of 2D layered materials include graphene, transition metal dichalcogenides (TMDs) (MX_2; M= transition metal from group IV, V or VI such as Mo, W and X=S, Se, Te), transition metal oxides (TMOs), layered double hydroxides (LDHs), ultrathin layers of wurtzite materials (such as AlN, BeO, GaN, ZnO, and ZnS), MXenes, silicene, germanene, and other compounds such as the topological insulators ($Bi_2Te_3$3, Bi_2Se_3). Novel 2D materials present new opportunities in materials science, physics, chemistry, and engineering that are impossible to obtain from their bulk counterpart. Molybdenum disulphide (MoS_2), for example, a transition metal dichalcogenides (TMDC), is an indirect band gap semiconductor in the bulk form. However, when it is exfoliated to single layer, it becomes a direct bandgap semiconductor.[31] It also provides an opportunity to tune the band gap varying the number of layers of MoS_2.

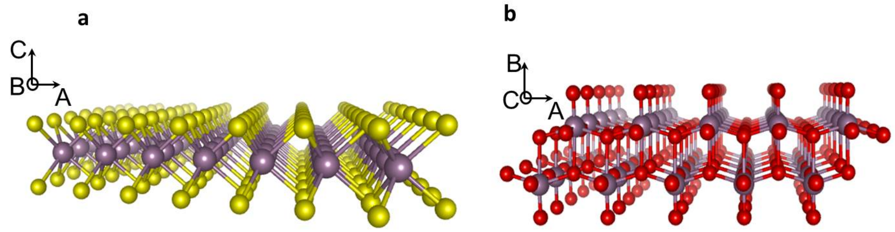

Figure 1.5: A single sheet of MoS_2 (**a**), and MoO_3 (**b**).

As an example, Figure 1.5 shows a single sheet of MoS_2 and MoO_3 where Mo atoms are sandwiched by the S atoms with honeycomb lattice structure and single sheet of MoO_3 with orthorhombic layered structure. In both cases, weak van der Waal bonds connect different layers stacking along c (MoS_2) and along b (MoO_3) direction.

The 2D layered materials are potential candidates for the development of field effect transistor (FET) and other optoelectronic devices. A FET based on single layer of MoS_2 has current switching of up to 10^8 with a mobility of 250 cm^2/Vs. In experiment, fabrication of such quantum devices requires semiconductor-insulator-semiconductor heterojunction. Their operation relies on the resonant tunneling of the carriers across the barriers. It is desirable to laterally align the heterostructures and create a pattern of insulating regions in a controlled manner on 2D layered materials such as MoS_2 rather than a vertical stacking of materials. The insulating regions form barriers, which could be made of defected domains. In experiment, such devices can be fabricated by treating MoS_2 with energetic oxygen plasmas which knock out sulfur atoms and create MoO_3 reach domains. MoO_3 has a higher band gap than MoS_2, leading to insulating regions for the carrier flow. One of the theoretical understandings necessary in such experiments is to confirm the formation of MoO_3. This can be studied by using DFT calculations of electronic structures of MoS_2 and MoO_3.

1.7 Methodology of using density functional theory to describe electron-hole pairs

In order to understand the material properties, we need to obtain and analyze the electronic structure of the materials. To calculate the electronic structure of materials, first principles computational methods can be used. The density functional theory (DFT) is one of the computational methods which is widely used to study the electronic structure and optical properties of the bulk and nanostructures of the materials. DFT is based on the Hohenberg-Kohn theorems.[32] There are two theorems by Hohenberg and Kohn. The first theorem states that the external potential $V(\mathbf{r})$ is determined within a trivial adaptive constant by the electronic density $n(\mathbf{r})$ and the second theorem states that the exact ground state is the global minimum value of functional of $n(\mathbf{r})$. Consequently, the ground state energy can be written as $E\left[n\left(\mathbf{r}\right)\right] = T\left[n\right] + V_{ext}\left[n\right] + V_{e-e}\left[n\right]$, where $T\left[n\right]$ is the kinetic energy of the non interacting system, $V_{ext}\left[n\right]$ is the interaction with external potential and $V_{e-e}\left[n\right]$ is the electron-electron interaction potential. Using the Hohenberg-Kohn theorems, we minimize the total energy of the system with respect to the orbitals in order to obtain the density $n\left(\mathbf{r}\right)$. This leads to a effective single particle Kohn-Sham equation which is written as

$$\left[-\frac{1}{2}\nabla^2 + V_{eff}\left(\mathbf{r}\right)\right]\phi_i = \varepsilon_i\phi_i, \tag{1.12}$$

where ϕ_i are the single particle Khon-Sham orbitals, $n_i = \sum\limits_i \left|\phi_i\right|^2$, $V_{eff}\left(\mathbf{r}\right) = v_{ext} + V_H + \delta E_{XC}/\delta n$, v_{ext} is the kernel of $V_{ext}\left[n\right]$, V_H is the Hatree potential and $\delta E_{XC}/\delta n$ is the exchange correlation energy. ε_i are the single particle energies. Here the main problem is to know the exchange-correlation term $\delta E_{XC}/\delta n_{XC}$ that produces the exact ground state of the system. The determination of the exchange-correlation energy is a difficult many-body problem even for homogeneous electron gas. The exchange-correlation is usually obtained by fitting theory with the experiments or more accurate Quantum Monte-Carlo (QMC) method. One of the widely used methods in DFT is the local density approximation (LDA) where the single-particle exchange-correlation energy depends only on local coordinates of a given particle. This method is acceptable for the homogeneous gas; however, it fails to describe accurately many electronic properties such as dissociation energy of molecule, adsorption energy of atoms and molecules on solid surfaces, some magnetic properties, etc. The generalized gradient approximation (GGA) can be used to circumvent some of the problems with LDA.[33] In addition, on-site Coulomb interaction U can be included in

LDA and GGA to get better results for transition metals. More improved versions of the DFT approximations, such as the muffin tin approximation (MTA), the augmented plane wave method (APW), and the projected augmented wave method (PAW) can be used to get better results of electronic and optical properties. The GW approximation is further improved method which is based on the solution to the quasiparticle equation (multi-particle problem). It is based on the Green's function formalism and the linear response theory, and it is designed for the calculation of excited states.

DFT can be used to calculate the bandstructures and absorption properties of the materials. Although the gaps are underestimated, it is a useful tool to calculate the types of gaps, band characters, band topology and density of states, and compare them with the experimental results to get further insight. The ground and excited states wave function can also be calculated to obtain the transition dipole matrix elements: $\langle \mathbf{e} \cdot \mathbf{P}_{c,v} \rangle = \frac{1}{\Omega} \int \Psi^*_{c,\mathbf{k}'} \mathbf{e} \cdot i\hbar \nabla \Psi_{v,\mathbf{k}} d\mathbf{r}$. The wave function $\Psi_{v,\mathbf{k}}$ and $\Psi_{c,\mathbf{k}}$ can be written in terms of Bloch functions $u_{\mathbf{k}}(\mathbf{r})$ which carry the information about the crystal symmetry. The matrix element then can be used to determine the absorption properties of the materials. Bloch functions can be directly calculated using first principle computational packages. There are several packages where DFT is implemented. Examples are the Vienna ab initio Simulation Package (VASP), Quantum Expresso, Quantumwise (atomistic toolkit), and Siesta.

1.8 Goal of this thesis

The projects in this thesis focus on the study of electron-hole pair generation in bulk and nanostructures of different materials. The materials of interest are wide bandgap semiconductors such as TiO_2, 3D TIs such as $Pb_{1-x}Sn_xTe$, and the 2D layered materials such as MoS_2 and MoO_3. We study the electronic and optical properties in bulk and nanostructures, and find applications in the area of semiclassical and quantum information processing. In wide band gap semiconductors, several interesting applications arise from electron-hole pair polarization. One of the interesting applications we focus on in this thesis is a shift in surface plasmon resonance due to the reduction in index of refraction of the surrounding dielectric environment. A change in index of refraction occurs when there is a decrease in absorption of the incoming stream of photons due to the Pauli exclusion principle. A shift up to 125 nm in wavelength of surface plasmon resonance is found. Employing this effect, we also present a model of a light controlled plasmon switching using a hybrid metal-dielectric heterostructures.

This thesis also covers electron-hole polarization in 3D TI materials, where we consider surfaces, interfaces, heterostructures, and nanostructures of $Pb_{1-x}Sn_xTe$. A detailed study on electronic and optical properties of both bulk and nanostructures of 3D TIs are systematically presented. Nanostructures of 3D TIs are of special interest due to amplification of the effect coming from those exotic surface states. We present a model of a quantum dot (QD) consisting of a spherical core-bulk heterostructure made of 3D TI materials, such as

$PbTe/Pb_{0.31}Sn_{0.69}Te$, with bound massless and helical Weyl states existing at the interface and being confined in all three dimensions. The number of bound states can be controlled by tuning the size of the QD and the magnitude of the core and bulk energy gaps, which is determined by the confining potential. We propose the implementation of quantum spin memory and quantum information processing in QDs of a few nanometers, where the qubit is defined by either an electron-hole pair, a single electron spin, or a single hole spin in a 3D TI QD. A giant Faraday effect is presented also for a 3D TI slab. The strict optical selection rules are employed to calculate the Faraday effect due to Pauli exclusion principle in a pump-probe setup using a 3D TI double interface of a $PbTe/Pb_{0.31}Sn_{0.69}Te/PbTe$ heterostructure. The Faraday rotation angle exhibits oscillations as a function of probe wavelength and thickness of the heterostructure. The maxima in the Faraday rotation angle are of the order of millirads.

The 2D layered materials such as MoS_2, $MoSe_2$, WTe_2, WS_2 and WSe_2 show important advantages over graphene in terms of their electronic and optical properties due to the presence of nonzero bandgaps. These materials are layered materials with weak interlayer van der Waals bonds. A single sheet of MoS_2 has direct band gap 1.8 eV. Due to excellent transport properties in single and multiple layers, several efforts have demonstrated the possibility to engineer electronic and optoelectronic devices based on MoS_2 . In this thesis, we focus on two different tasks using single layer MoS_2 from experimental and theoritical point of view: **a**, study of electrical property tuning, and **b**, photoluminescence tuning, both in a single-layer of MoS_2 via oxygen plasma treatment. Both tasks have been done in collaboration with the Dr. Saiful Khondaker's research group who have performed the experiments on the current-voltage (I-V) characteristics, x-ray photoelectron spectroscopy (XPS) and Raman spectroscopy measurements. Our task here is to provide the theoretical analysis for the stability of MoO_3 defects inside MoS_2 single sheet and their bandstructures using DFT. The electrical property of a single layer of MoS_2 can be tuned from semiconducting to insulating regime via controlled exposure to oxygen plasma. The quenching of photoluminescence of a single sheet of MoS_2 has also been observed upon exposure to oxygen plasmas. We calculate the direct to indirect band gap transitions by going from MoS_2 single sheet to MoO_3 single sheet during the plasma exposure, which is due to the formation of MoO_3 rich defect domains inside a MoS_2 sheet.

1.9 Organization of thesis

The thesis is organized as follows. Chapter II is focused on the study of the surface plasmons where we present our results on the surface plasmon resonance shift. Chapter III and IV are dedicated to 3D TIs in heterostructures and QD nanostructures where we provide interesting applications for the Faraday effect and quantum information processing. Chapter V is focused on analytical calculations for the transmission from a stack of 3D TI materials. In Chapter VI we present the results for defect engineering and tuning of the transport property in MoS_2 single sheet. We provide both theoretical and experimental evidence of the MoO_3 defect formation during the exposure of MoS_2 single sheet in oxygen plasma. Chapter VII is dedicated to the absorption calculations for ATPMS/FA/TiO_2 for a thin film. Here we also present the experimental results for photocurrent generation.

We provide here the list of publications resulting from the work presented in this PhD thesis. Preprints are available on the Los Alamos National Laboratory server http://lanl.arxiv.org/.

- Hari P. Paudel, **Michael N. Leuenberger**, Light-controlled plasmon switching using hybrid metal-semiconductor nanostructures,
  Nano Lett. 12, 2690 (2012).

- Hari P. Paudel, **Michael N. Leuenberger**, Three-dimensional topological insulator quantum dot for optically controlled quantum memory and quantum computing,
  Phys. Rev. B **88**, 085316-1 to 085316-17 (2013).

- Hari P. Paudel, **Michael N. Leuenberger**, Giant Faraday effect due to Pauli exclusion principle in 3D topological insulators,
  J. Phys. Cond. Mat. Fast Track Comm. **26**, 082201 (2014).

- Hari P. Paudel, **Michael N. Leuenberger**, Faraday effect due to Pauli exclusion principle in 3D topological insulator nanostructures,
  Proc. SPIE 9123, Quantum Information and Computation XII, 91230E (May 28, 2014).

- Muhammad R Islam, Narae Kang, Udai Bhanu, Hari P. Paudel, Mikhail Erementchouk, Laurene Tetard, **Michael N. Leuenberger**, and Saiful I. Khondaker, Electrical property tuning via defect engineering of single layer MoS2 by oxygen plasma, Nanoscale, published online, soon to be published in print (2014).

- Narae Kang, Hari P. Paudel, **Michael N. Leuenberger**, Laurene Tetard, and Saiful I. Khondaker, Photoluminescence Tuning in Single-layer MoS2 via Oxygen Plasma Treatment,

  Submitted; see arXiv:1405.0646 (2014).

CHAPTER 2
SURFACE PLASMONS AND PLASMONICS

2.1 Introduction

Electromagnetic properties of metal-dielectric interfaces have attracted vast amount of resarch efforts. Ever since the work of Mie [34] for small particles and Ritchie [35] for flat interfaces, wide spectrum of scientists ranging from physists, chemists, material scientists to biologists are involdved to explore underlying phenomenon and their potential applications in practical life. In such structure under the right circumstances a light waves propagting at metal-dielectric interface induce a resonant interaction between mobile electrons and light wave at the metal surface. This results a generation of density waves called surface plasmons (SPs) that propagate along the interface like a ripples across the surface of water. SPs help to concentrate and channel light using subwavelength structures.[36, 37] In metallic nanostructures much smaller than the wavelength of light, SPs are used to enhance the signal in surface-enhanced Raman spectroscopy (SERS), which allows for the detection of a single molecule.[38] SPs generated at metal-dielectric interface can be utilized to carry information in microprocessors faster than electronics transistor in current use.[39] Plasmonics can encode more information than currently possible in conventional electronics.[40] Use of optically excited plasmons as a tunable frequency source that can be mixed with a laser frequency through Raman scattering enables dynamical shifting of the wavelength of light in a control manner.[41] In the experiment of Fluegel and co-workers,[42] the wavelength of the signal beam undergoing inelastic Raman scattering downshifted by 13-15 nm. This experiment demonstrates an approach to achieve larger wavelength shifts of an optical data using low pump powers. Plasmonics can also be exploited in optical tweezers to confine nanoparticles to small dimensions.[43] Grigorenko[44] and Juan[45] made electromagnetically coupled gold pillars in which localized surface plasmons offer better trapping of nanometer-sized objects.

Recently, a method to achieve coupling between light and matter was proposed.[46] There was a strong coupling between the optical field associated with plasmon modes on conducting nanowires with emitters. Such a system also provided a remarkable optical nonlinearity resulting from the interaction between individual photons.[47] A similar model where a one-dimensional array of nanoshells replaces the nanowires can be thought of as an efficient optical switch. In this model, plasmon excitations are dynamically controlled by varying the nanoshell dielectric environment. A chain of nanoshells with fixed separation from each other can support surface plasmon polaritons (SPPs). This is a light-controlled SPP switch. Plasmonic switches are ultrafast and have high on/off contrast ratio.[48]

The optical resonances of a nanoshell exhibit an enhanced sensitivity to its local dielectric environment relative to a solid nanoparticle.[49] In particle ensembles, additional shifts are noticed due to electromagnetic interaction between localized plasmon modes. In the case of dimers, plasmons can be viewed as bonding and antibonding combinations, whose shift follow $\frac{1}{d^3}$ interaction between two classical dipoles.[50] Under the dipolar approximation, with $d \ll \lambda$, near-field interaction with $\frac{1}{d^3}$ dependence dominates and a particle array can be described as point dipoles interacting via their near field.[51] Transport of energy along such an array is the key to transmit information in plasmonics.[52, 53]

A recent experiment showed all-optical control of a single plasmonic nanoantenna - ITO hybrid, which relies on the ITO free-carrier nonlinearity that modifies the plasmon resonance.[54] A method to realize dynamically reconfigurable plasmon antennas has been proposed.[55] This is based on engineering of the plasmon dispersion relations, relying on the possibility that the host index can be changed by means of liquid crystals or other phase-changing materials.

2.2 Objective

In this work, we present the proof of concept of a method to control the spectrum for the surface plasmon modes in a spherical silver-TiO_2 core-shell nanoparticle by varying the dielectric function of TiO_2 through excitation of electron-hole pairs in TiO_2. The underlying concept is that the frequency of the surface plasmon mode on the metal surface is sensitive to its dielectric environment. Our spherical nanoparticle consists of a spherical metallic core of a few nanometers in size and an outer spherically symmetric shell made of semiconducting material. A pump laser pulse of energy equal to the band gap or above generates electron-hole pairs in the semiconducting material, which leads to a decrease in absorption (bleaching) due to Pauli blocking, thereby altering the dielectric function of the semiconducting shell.

The resulting blue shift in the frequency of the surface plasmon can be measured by means of a probe laser pulse that excites the surface plasmon mode at the altered plasmon resonance frequency.

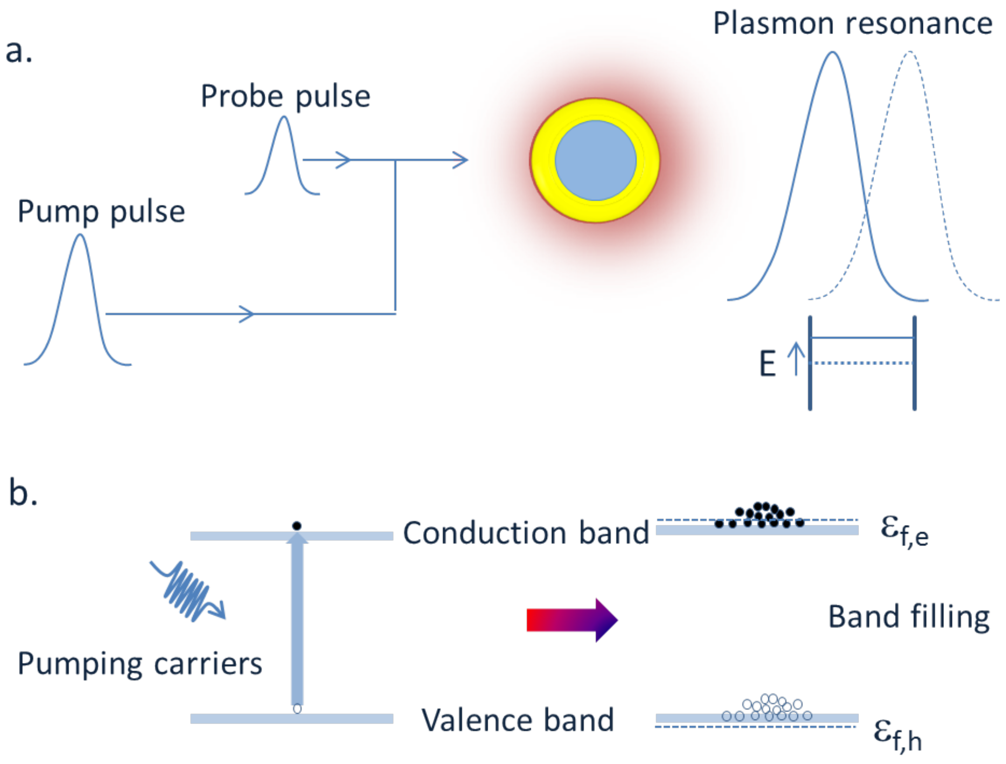
a.
Plasmon resonance
Probe pulse
Pump pulse
E
b.
Conduction band
$\varepsilon_{f,e}$
Band filling
Pumping carriers
Valence band
$\varepsilon_{f,h}$

Figure 2.1: Scheme of dynamically controlled plasmon excitation in a nanoshell. (a) The probe pulse excites plasmons on the surface of silver at a resonance frequency. The pump pulse generates electron-hole pairs in the semiconductor changing its dielectric function. The plasmon resonance frequency is now blue-shifted because of the changed dielectric environment. (b) A pump pulse with energy at band gap or above generates electron-hole pairs in the semiconductor. In quasi Fermi equilibrium, electrons and holes are settled at the bottom and top of the conduction and valence band, respectively, with the different quasi Fermi levels.

In Figure 2.1, we show a scheme of our model where our pump-probe technique is used. The model shows the dynamic control over the plasmon resonances by varying the dielectric function of the semiconducting shell. The frequency of the probe pulse must be below the band gap of the semiconducting shell in order to avoid generation of electron-hole pairs when probing the surface plasmon mode. Therefore, we chose TiO_2, which has a large band gap of 3.0 eV, and for the metal core we chose silver, which allows for surface plasmons with energy below 3.0 eV. Another advantage of TiO_2 is its large dielectric function, which leads to excitons that have a Bohr radius much smaller than the size of our nanoparticle. This allows us to use bulk values for the excitonic properties in the TiO_2 shell. Let us describe these effects now in more detail.

2.3 Surface plasmon resonances in hybrid metal-semiconductor heterostructures

The surface plasmon resonance of a nanoshell depends on the curvatures of outer and inner shell surfaces. A metallic core dielectric nanoshell with inner metal core of radius r_1 and outer dielectric shell of radius r_2 exhibits plasmon resonance at a frequency depending on the aspect ratio $\frac{r_1}{r_2}$ (see Figure 2.2). The plasmon modes are shifted if the nanoparticle is coated with dielectric materials. The shift depends on the relative size of the shell and the nanoparticle as well as on the surrounding medium. It has been shown that with increasing shell thickness, the local field enhancement factor peak decreases and either red shifts nonlinearly for $\varepsilon_2 > \varepsilon_3$, or blue shifts nonlinearly for $\varepsilon_3 > \varepsilon_2$, where $\varepsilon_2$and ε_3 are dielectric functions of shell and surrounding materials, respectively.[56] The local field enhancement factor increases strongly in the vicinity of the metal surface. The enhancement is weaker on the surface of the embedding medium.

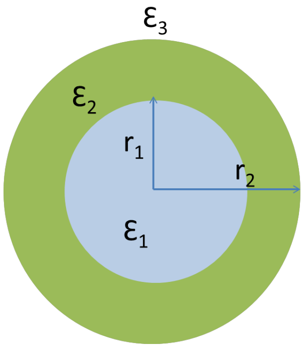

Figure 2.2: Ag core dielectric shell nanostructure with the dielectric function ε_1 for the Ag core, ε_2 for the TiO_2 shell and ε_3 for the embedding medium. The size of the nanoshell is 15 nm.

The enhancement of the local electric field in different regions of the nanoshell is different due to the screening field in the presence of the dielectric environment. For a nanoparticle size much smaller than the wavelength of the incident light, local field enhancement factors are well approximated by quasi-static theory. The polarization of the nanoparticle oscillates like a dipole with polarization proportional to the incident field. Under such condition electrostatic solutions are obtained by solving Laplace's equation. The treatment can be found in ref AverittHalas:1999. The solutions that we are using in our method are given by

$$\begin{aligned}
E_1 &= \frac{9\varepsilon_2\varepsilon_3}{\varepsilon_2\varepsilon_a + 2\varepsilon_3\varepsilon_b} E_o(\cos\theta\hat{r} - \sin\theta\hat{\theta}) && (2.1)\\
E_2 &= \frac{3\varepsilon_3}{\varepsilon_2\varepsilon_a + 2\varepsilon_3\varepsilon_b}\Big[\{(\varepsilon_1 + 2\varepsilon_2) \\
&\quad + 2(\varepsilon_1 - \varepsilon_2)\left(\frac{r_1}{r}\right)^3\Big\} E_o\cos\theta\hat{r} \\
&\quad - \left\{(\varepsilon_1 + 2\varepsilon_2) - (\varepsilon_1 - \varepsilon_2)\left(\frac{r_1}{r}\right)^3\right\} \\
&\quad E_o\sin\theta\hat{\theta}\Big] && (2.2)\\
E_3 &= \{2\frac{\varepsilon_2\varepsilon_a - \varepsilon_3\varepsilon_b}{\varepsilon_2\varepsilon_a + 2\varepsilon_3\varepsilon_b}\left(\frac{r_2}{r}\right)^3 + 1\}E_o\cos\theta\hat{r} \\
&\quad + \{\frac{\varepsilon_2\varepsilon_a - \varepsilon_3\varepsilon_b}{\varepsilon_2\varepsilon_a + 2\varepsilon_3\varepsilon_b}\left(\frac{r_2}{r}\right)^3 - 1\}E_o\sin\theta\hat{\theta} && (2.3)
\end{aligned}$$

where

$$\begin{aligned}
\varepsilon_a &= \varepsilon_1\{1 + 2\left(\frac{r_1}{r_2}\right)^3\} + 2\varepsilon_2\{1 - \left(\frac{r_1}{r_2}\right)^3\} && (2.4)\\
\varepsilon_b &= \varepsilon_1\{1 - \left(\frac{r_1}{r_2}\right)^3\} + \varepsilon_2\{2 + \left(\frac{r_1}{r_2}\right)^3\} && (2.5)
\end{aligned}$$

In eqs (2.1) - (2.3), E_1, E_2 and E_3 are the electric fields in the core, shell and embedding medium, respectively, and E_o is the incident electric field. The angle θ is an angle between the direction of polarization and the scattered field direction, and ε_1 is dielectric function of the core. Various analytic models have been proposed in an attempt to account accurately for the dielectric function of the noble metals, such as Ag and Au. Au has comparatively simple surface chemistry compared to Ag; however due to the presence of interband transitions (at least two transitions at 470 nm and 330 nm) in Au, optical properties are more difficult to present in the visible and near-ultraviolet region with an analytic model.

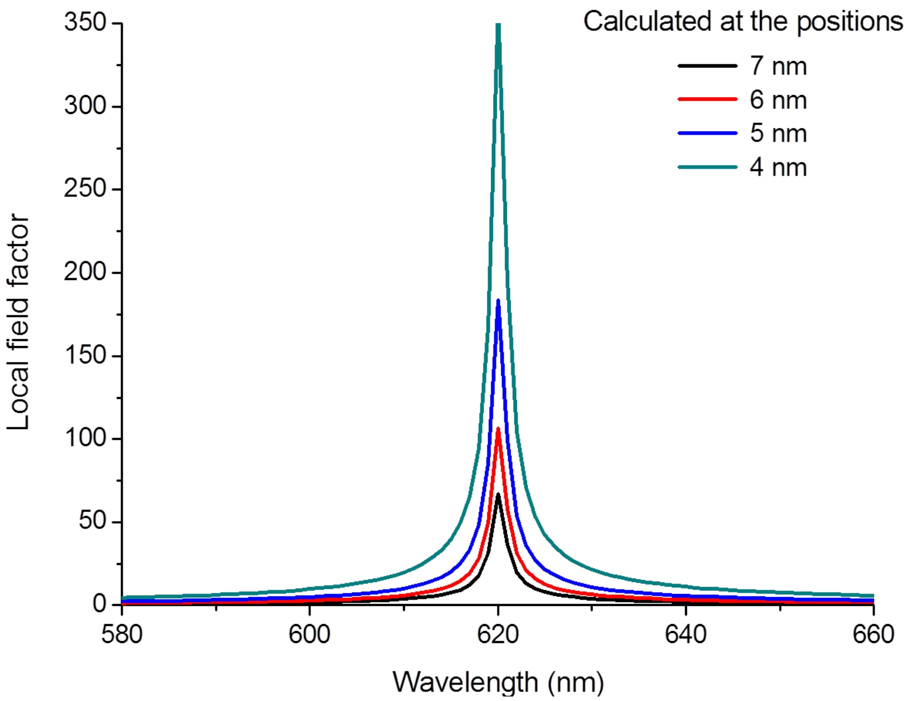

Figure 2.3: Local field enhancement factor at different positions in the shell portion of the nanoshell. The radius of the inner core is 3.5 nm. The magnitude of the local field factor decreases with increasing distance from the center of the nanoshell. Smallest peak to largest peak calculated, respectively, at positions $r = 7$, 6, 5 and 4 nm.

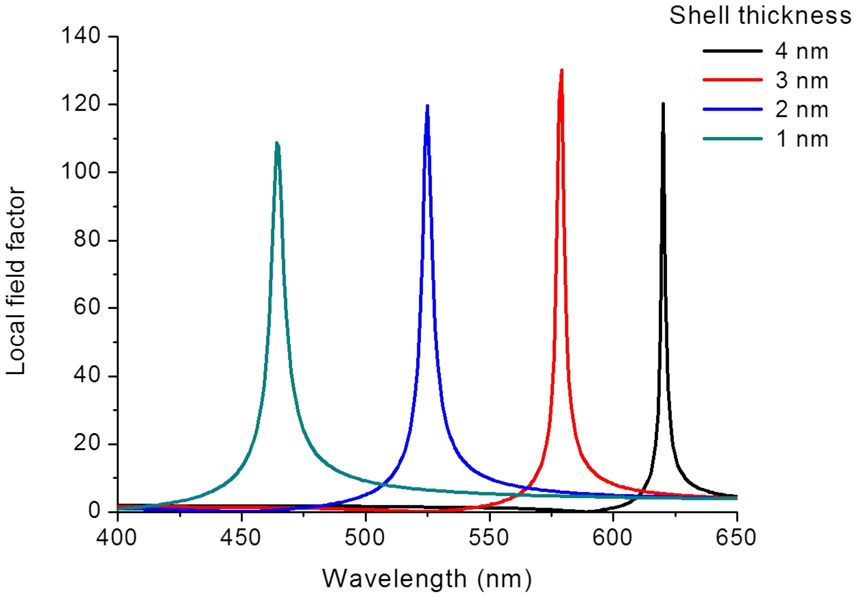

Figure 2.4: Local field enhancement factor at different shell thickness on the surface of the nanoshell. The resonance peak is blue shifted with decreasing shell thickness. Peaks are for 4, 3, 2 and 1 nm shell thickness, respectively, from right to left.

For particular frequencies, metals possess a negative real part of $\varepsilon(\omega)$ and very low loss. The negative real part of $\varepsilon(\omega)$ is linked to plasmons and plasmon resonances. The magnitude of the ratio of outgoing field to incident field is given by the local field enhancement factor. These factors along the incident field polarization are plotted in Figures 2.3 and 2.4 at different positions inside the shell and on the surface of the shell, respectively, using $\varepsilon(\omega)$ from Drude-critical point model.[14] The results show that there is significant decrease in the enhancement intensity as we go deeper into the shell. If we decrease the shell thickness, the resonance peak on the shell surface gradually blue shifts. The shift is very sensitive to the shell thickness. So, we can easily tune the resonances to a wide range of frequencies.

2.4 Electronic and optical properties of TiO_2

The dynamic control over the plasmon resonances would be interesting for their potential application to plasmonic switches. Our main idea is to change the dielectric environment in such a model so that there is a shift in plasmon resonance wavelength. An accurate picture of this model requires the study of the electronic and the optical properties of the material. We calculate the necessary electronic and optical properties of TiO_2 in the rutile phase and compare them with experiments. It has been reported that TiO_2 has an effective electron mass, m_e^*, between 5 and 13 m_e.[57, 58] Such a heavy mass results in an excitonic Bohr radius between 0.75 and 1.9 nm and exciton ionization energy of 4 meV. It also has been reported that quantum size effects in colloidal nanoparticles occur when $d < 3$ nm.[59, 60] So, for a nanostructure of few nanometers in size, we are far away from the strong confinement limit and expect properties similar to those of bulk.

In Figure 2.5, we show our calculated band structure within the first Brillouin zone obtained by means of VASP (Vienna ab initio Simulation Package) in the framework of density functional theory (DFT) using the generalized gradient approximation with ultrasoft pseudopotentials.[61] The tightly bound O 2s bands are 16.355 eV below the top of the valence band, zero of the energy is at the top of the valence band. The experimental value from Auger spectroscopy is 16-18 eV.[62] The bandwidth of the O 2s band is 1.699 eV. The upper valence band is primarily due to the O 2p states with bandwidth of 5.626 eV, the experimental value is in the range of 5-6 eV.[63] The lower conduction band is primarily due to Ti 3d states with bandwidth of 7.800 eV. The band gap is calculated to be 1.649 eV, whereas the experimental band gap is 3.0 eV in rutile structure.[57] The relative positions of the bands are in good agreement with experiments and previously calculated results.[64, 65] The DFT band gaps are inherently small due to the lack of integer discontinuity of the exchange-correlation energy derivative (the well-know band gap problem of DFT). Correction is often done by adopting a scissor operator that rigidly shifts the conduction band up relative to the valence band. It is important to note that we calculated the transition dipole matrix elements $\mathbf{P}_{c,v}$ in the momentum representation. Therefore $\mathbf{P}_{c,v}$ do not depend on the value of the band gap.

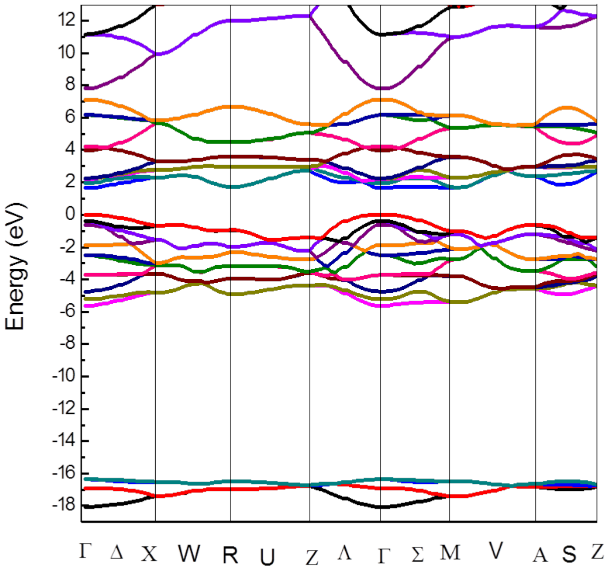

Figure 2.5: Bandstructure calculated using VASP.

The optical properties of a material can be studied by calculating the imaginary part of the dielectric function, $\varepsilon(\omega)$, which can be obtained using Fermi's golden rule and is given by

$$\begin{aligned} \mathrm{Im}(\varepsilon(\omega)) &= \frac{4\pi^2 e^2}{m^2\omega^2}\sum_{k,c,v} |\mathbf{e}\cdot\mathbf{P}_{c,v}|^2 f((E_v(\mathbf{k}))\,[1-f(E_c(\mathbf{k}))] \\ &\quad \times\delta(E_c(\mathbf{k})-E_v(\mathbf{k})-\hbar\omega) \qquad (2.6) \end{aligned}$$

where $\mathbf{e}$ is the direction of incident field polarization. $E_c(\mathbf{k})$ and $E_v(\mathbf{k})$ are energies of the conduction and valence band, respectively. The quantities $f(E_v(\mathbf{k}))$ and $f(E_c(\mathbf{k}))$ are occupation probabilities of a state $\mathbf{k}$ in the valence and conduction band, respectively. In the material with no laser excitation the valence band is occupied and the conduction band is empty. We can set $f(E_c(\mathbf{k}))$ to be zero and $f(E_v(\mathbf{k}))$ to be one. Both the intraband and interband transitions are included in eq 2.6. The intraband transitions are mostly important in metals. Indirect transitions are due to scattering off phonons and are expected to give small contribution to the dielectric function.[66] The dipole matrix element is given by

$$\langle \mathbf{e} \cdot \mathbf{P}_{c,v} \rangle = \tfrac{1}{\Omega} \int \Psi^*_{c,\mathbf{k}'} \mathbf{e} \cdot i\hbar \nabla \Psi_{v,\mathbf{k}} d\mathbf{r} \tag{2.7}$$

For the periodic system this can be written as

$$\langle \mathbf{e} \cdot \mathbf{P}_{c,v} \rangle = \tfrac{\hbar}{\Omega} \sum_{\mathbf{G}} a^*_{\mathbf{k},c}(\mathbf{G}) a_{\mathbf{k},v}(\mathbf{G}) \mathbf{e} \cdot (\mathbf{G} + \mathbf{k}) \tag{2.8}$$

where the transitions are supposed to be vertical. The quantities $a_{\mathbf{k},c}$ and $a_{\mathbf{k},v}$ are expansion coefficients in the periodic part of Bloch functions. These coefficients are directly obtained from VASP in our calculation. $\mathbf{G}$ is a reciprocal lattice vector and Ω is the volume of the unit cell.

Because of the anisotropic nature of the tetragonal cell structure of the rutile lattice, optical properties depend strongly on the direction of the incoming light polarization. We resolve real and imaginary part of the dielectric function of this material in direction perpendicular and in direction parallel to the light polarization, as shown in Figure 2.6 and 2.7. The real part has been obtained using Kramers-Kronig relations. A good approximation of the delta function at all frequencies in the eq 2.6 can be obtained using a Gaussian wave packet which gives the best match with the experimental spectra. A Lorentzian could be used instead but due to the longer tail of the Lorentzian, absorption decreases rapidly in the low frequency regime. Calculated spectra are convoluted with a Gaussian with full width at half maximum (fwhm) of 0.30 eV. Results are in good agreement with the experiment of Cardona and Harbeke.[67]

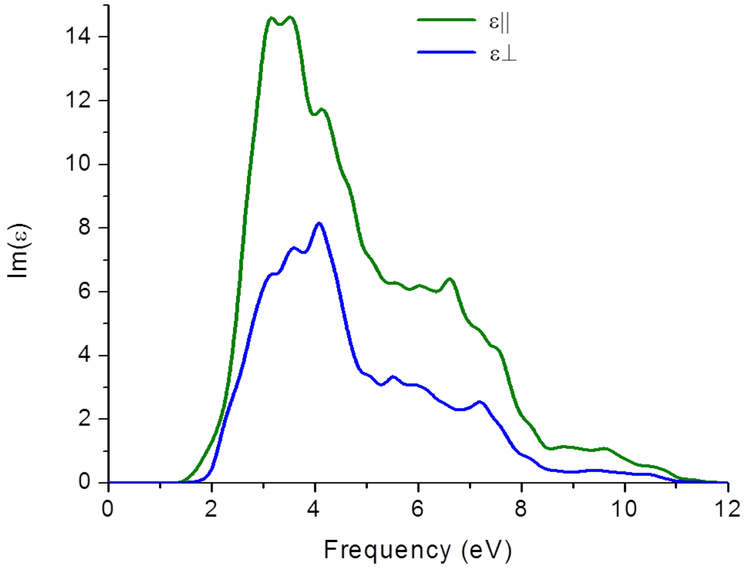

Figure 2.6: Imaginary part of dielectric function for polarization parallel (green line) and perpendicular (blue line) to the electric field vector.

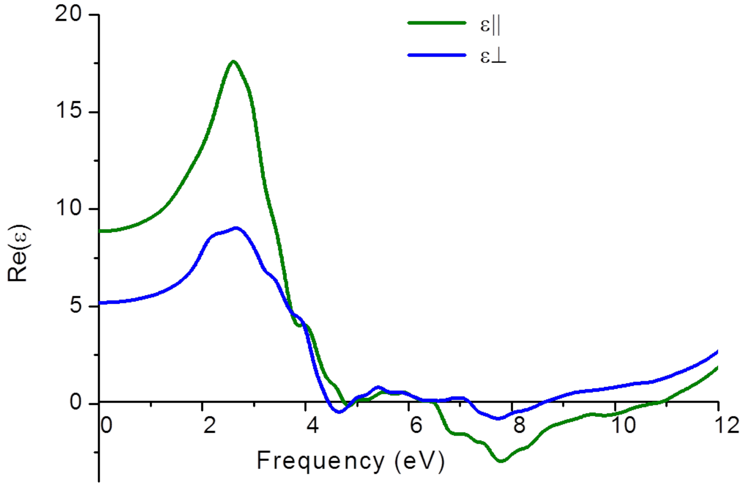

Figure 2.7: Real part of dielectric function for polarization parallel (green line) and perpendicular (blue line) to the electric field vector.

The imaginary part of the dielectric function can be altered temporarily by the real carriers generated by the pump pulse.The carrier gneration leads to a quasi-equilibrium nonlinearity in the semiconductor. The generated carriers are thermalized at the top and bottom of the valence and conduction bands according to the principle of energy minimization. There is a window of time before the generated carriers recombine to each other. The lifetime of a single electron-hole pair in an excited 12 nm size TiO_2 colloidal particle is reported to be (30 ±15) nanoseconds.[60]

Under high intensity light illumination photoexcited electron density ($\triangle n$) and hole density ($\triangle p$) are created with $\triangle n = \triangle p$. Generated electrons and holes have their respective quasi Fermi energies E_f^c and E_f^v. These energies are determined from the quasi-Fermi distribution function $f(E_c) = 1/(1+e^{\beta[E_c(\mathbf{k})-E_f^c]})$ for the electrons and $f(E_v) = 1/(1 + e^{\beta[E_v(\mathbf{k})-E_f^v]})$ for the holes. The chemical potentials in $f(E_c)$ and $f(E_v)$ are determined using $n_i = \int f(E_i)D(E_i)dE_i$ for the excited carrier density, where $D(E_i)$ is the density of states. In order to obtain a change in the optical spectrum for the dielectric function, we need to generate a large number of electron-hole pairs which block further absorption due to the Pauli exclusion principle and due to the lack of carriers for certain transitions.

In Figures 2.8 and 2.9, we show our calculations of the change in both the parallel and perpendicular components of $\mathrm{Im}(\varepsilon)$ for different densities of excited carriers. After the excitation, the value of $\mathrm{Im}(\varepsilon)$ is decreased for all densities we choose. Because the low-lying conduction bands and the high-lying valence bands are occupied after pumping of the electron-hole pairs, the absorption of further incoming photons is suppressed. This effect is called photobleaching. We also calculated the contribution to the dielectric function due to two-photon absorption, which may occur due to the symmetry-allowed transitions of electrons from the lower conduction bands to the upper conduction bands. Our results show that this two-photon contribution is small. The net change in $\mathrm{Im}(\varepsilon)$ is therefore negative. For $10^{18}/\mathrm{cm}^3$ excitation density, the change in peak value of $\mathrm{Im}(\varepsilon)$ is not noticeable in the parallel component, but there is a 13% shift of the peak corresponding to an energy of 2.24 eV in the perpendicular component. For $10^{19}/\mathrm{cm}^3$ the peak value of $\mathrm{Im}(\varepsilon)$ is shifted by 52% corresponding to 1.96 eV in the parallel component and 26% corresponding to 2.24 eV in the perpendicular component, while for $10^{20}/\mathrm{cm}^3$ the peak shifts by 35% corresponding to 2.32 eV and 48% corresponding to 2.24 eV in the parallel and perpendicular components, respectively. For even higher excitations of $10^{21}/\mathrm{cm}^3$ and $5 \times 10^{21}/\mathrm{cm}^3$, the peak for the parallel component shifts by 67% corresponding to 2.71 eV and by 95% corresponding to 3.06 eV, respectively, and the peak for the perpendicular component shifts by 59% corresponding to 2.76 eV and by 95% corresponding to 3.06 eV, respectively. The onset of the negative change starts at 1.50 eV for the parallel component and at 1.87 eV for the perpendicular component.

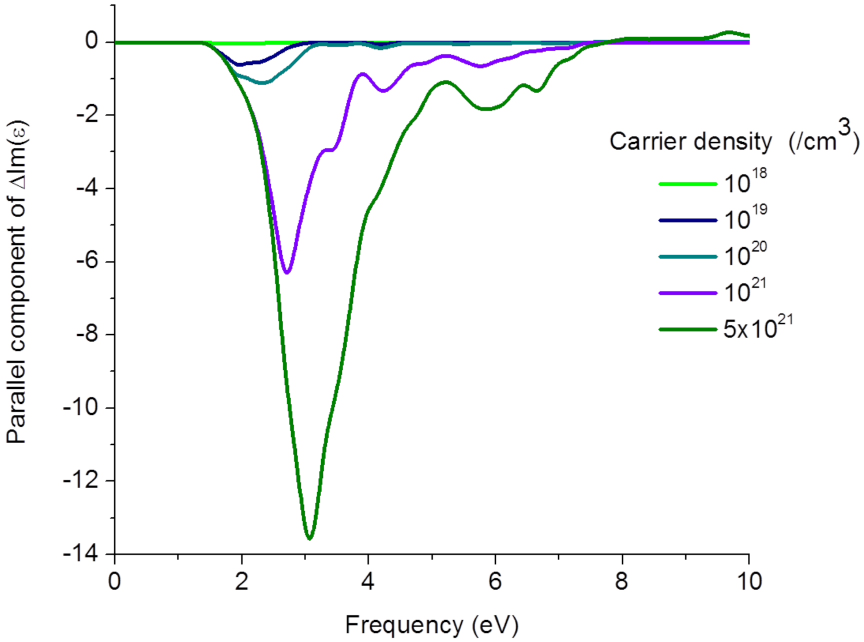

Figure 2.8: Parallel component of change in imaginary part of dielectric function.

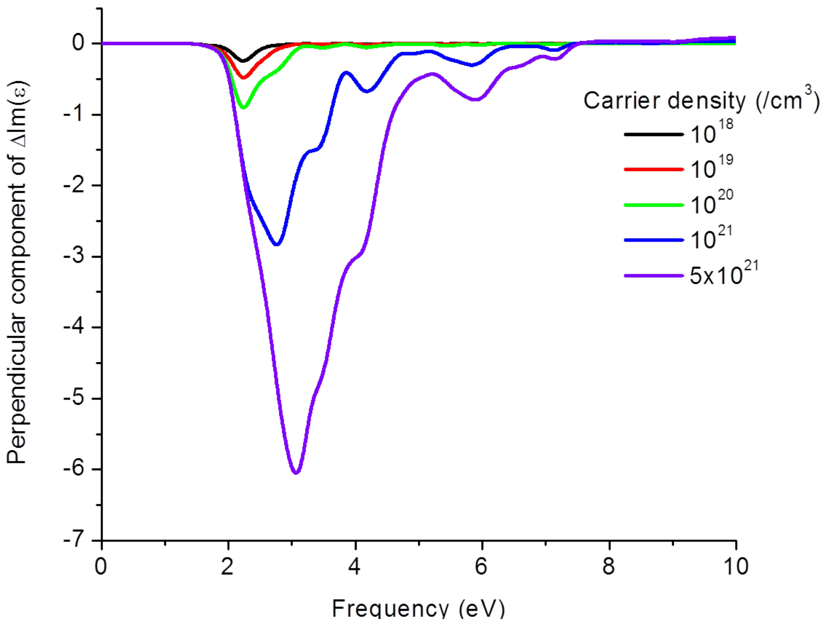

Figure 2.9: Perpendicular component of change in imaginary part of dielectric function.

It is evident that the onset of the absorption is blue shifting as we increase the density of the excitation. This is because the filling of the bands results in a gradual bleaching of the absorption in the vicinity of the band gap. For higher densities of excited electron-hole pairs, the Pauli blocking is stronger and the lack of carriers for certain transitions is larger and thus the bleaching is higher. In our calculation, we did not account for the Coulomb interaction, which would give exciton effects for frequencies below the band gap. Calculating the blue shift for higher densities of excited electron-hole pairs is not necessary, because at around $10^{22}/\mathrm{cm}^3$ the material starts to melt.[68]

2.5 Plasmon resonance shifts and plasmonic switching

The change in the dielectric function induces many important phenomena. The change in dielectric function of the TiO_2 in the nanoshell (as shown in Figure 2.2) provides a new dielectric environment for the surface plasmon resonance induced in the metallic core. Surface plasmon resonances in the silver core dielectric nanoshell can be easily tuned below the exciton resonances of the TiO_2. The pump laser pulse excites electrons from the valence band to the conduction band in TiO_2 causing change in the dielectric function. The probe laser pulse working at surface plasmon resonance frequency excites plasmons on the surface of the silver. This frequency is in the transparency regime of TiO_2 and can pass through the outer shell of the nanostructure. A typical plasmon resonance frequency in silver nanoshell occurs around 2.0 eV (620 nm), depending on the geometry of the nanoshell structure. In an experiment, this plasmon mode can be excited with a probe pulse of energy 2.0 eV or above. The pumping of the electron-hole pairs does not depend on the band gap. Generated electron-hole pairs that lead to change in index of refraction are determined by the strength of the transition dipole matrix elements. Our calculated dipole matrix elements are very accurate as can be seen from the accuracy of calculated absorption spectra (Figures 2.6 and 2.7). Therefore our proposed experimental model is reliable irrespective of the band gap underestimation in TiO_2.

As shown in Figure 2.10, without any electron-hole pair excitation resonance occurs at 620 nm. For $10^{18}/cm^3$ excitation, the conduction band is occupied by the generated electrons, thereby changing slightly the dielectric environment. Now the SP appears in a changed surrounding, which blue shifts the resonance by 5 nm. At $10^{19}/\mathrm{cm}^3$ and $10^{20}/\mathrm{cm}^3$, the shift is 9 and 13 nm, respectively, with respect to the nonexcited nanoparticle. For higher density, $10^{21}/\mathrm{cm}^3$ and $5 \times 10^{21}/\mathrm{cm}^3$, the plasmon resonance is blue shifted by 55 nm and 126 nm, respectively. It is interesting to see that even at low densities of $10^{18}/\mathrm{cm}^3$ the blue shift is large enough to be measured. The fwhm of the plasmon resonance lines are calculated to be 3 nm for the unexcited structure to 8 nm for $5 \times 10^{21}/\mathrm{cm}^3$ excitations. The first resonance peak for $10^{18}/\mathrm{cm}^3$ excitation lies at 5 nm from the resonance peak for the unexcited structure.

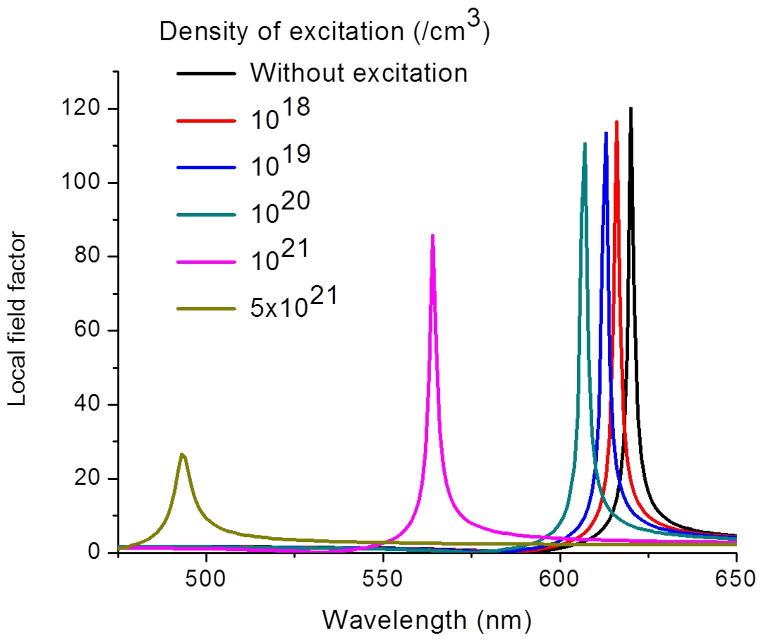

Figure 2.10: Local field enhancement factor on the surface of a nanoshell of 3.5 nm silver core coated with 4 nm TiO_2 at different densities of excitation for parallel polarization of the incident light. At higher densities, the resonance peak is gradually blue shifted.

We calculate the excitonic Rabi frequency from the interaction energy, $H_I = (e/m)p_{cv}A_o$ where p_{cv} is the magnitude of momentum matrix element between valence band and conduction band and A_o is the magnitude of the vector potential. At $k = 0$, our calculated p_{cv} at minimum band gap is 3.3×10^{-25} Js/m. Assuming a cavity of approximately the size of wavelength of the pump laser pulse and the power of the laser pulse of 100 mW, the interaction energy is around 16 meV. This gives rise to a switching time, the inverse of the Rabi frequency, of 41 fs.

In summary, the plasmon resonance peak shifts due to a change in dielectric environment. We calculated the shift in a silver core TiO_2 nanoshell. We showed that it is possible to dynamically control the shift by varying the dielectric function of TiO_2. We calculated the band structure and the absorption spectra of TiO_2; both are in good agreement with the reported experimental results. Generation of electron-hole pairs leads to a change in absorption due to Pauli blocking and lack of carriers for certain transitions. The magnitude of the change varies for different densities of excited electron-hole pairs. The spectra are blue-shifted for increasing carrier density. At the density $10^{18}/\text{cm}^3$ the spectrum is blue shifted by 5 nm and the blue shift increases at higher densities. For $5 \times 10^{21}/\text{cm}^3$ density, the blue shift is 126 nm, which can easily be measured in an experiment. Using the mechanism of the dynamic control over the plasmon resonances we developed the concept of a plasmonic switch that can be much faster than conventional electronic switches for the purpose of controlling data transfer in future computer processors based on plasmonics.

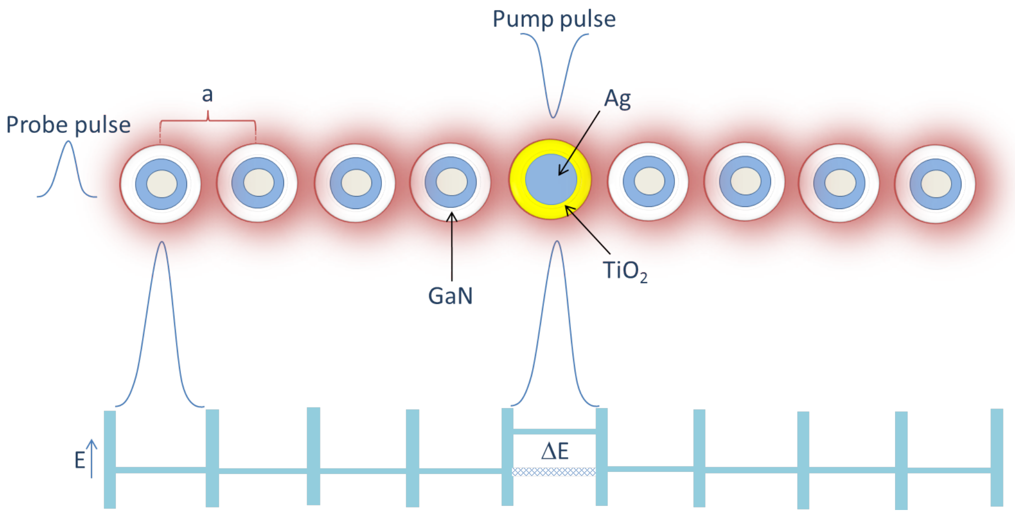

Figure 2.11: Light-controlled SPP switch. Propagation of surface plasmon-polariton in a chain of nanoshells of two types: a nanoshell with silver (light blue color) core coated with TiO_2 (yellow color) embedded in PMMA and nanoshells with GaN (no color) core coated with silver embedded in GaN . Nanoshells are separated by a distance a. This structure acts as a grating necessary to supply momentum for efficient coupling. Probed surface plasmons propagate across the chain because the excitation gap matches exactly in all nanoshells. The pump pulse generates electron-hole pairs in TiO_2. This results in a blue shift of plasmon resonances.

CHAPTER 3
THREE DIMENSIONAL TOPOLOGICAL INSULATOR QUANTUM DOT

3.1 Background

3D TIs are narrow-bandgap materials with topologically protected gapless surface/interface states that are characterized by the linear spectrum of massless Weyl fermions.[69, 7] In such materials, the spins of the Kramers pairs are locked at a right angle to their momenta on the Fermi surface due to spin-orbit coupling,[70, 24, 9, 25, 71, 72] which can be used for spin current generation.[73, 74, 75] The surface states are protected by time reversal symmetry, leading to suppression of backscattering from edges and nonmagnetic impurities.[69, 7, 10, 76, 71] Such states are of great importance in low-power opto-spintronics.[77, 73] Decoherence can be circumvented by highly polarized spin states with helical spin texture,[70, 78, 76, 79] leading to a phase coherence length of several hundred nanometers in nanostructures.[80, 81]

In 3D TI nanostructures the special properties of topologically protected surface states of TIs are amplified because of the large surface-to-volume ratio. In addition, the chemical potential can be electrically tuned using a gate voltage. For example, the coherent propagation of the Weyl electrons around the perimeter of a nanoribbon provides excellent evidence of the topological nature of the surface states in TI nanostructures.[81] Experiments on both the physical and chemical synthesis of TI nanostructures have been done recently to understand their transport properties at the nanoscale.[82, 83, 84] Recently, in a TI QD with tunable barriers based on ultrathin Bi_2Se_3 films, Coulomb blockade with around 5 meV charging energy was observed.[85]

So far, a theoretical study of electronic properties of 2D helical states occurring at nanoscale of 3D TIs, such as in QDs, is still lacking. In this article, we present the study of bound Weyl states that are confined at the interface of a spherical core-bulk heterostructure QD made of 3D TI materials such as $Pb_{1-x}Sn_xTe$. We show that at the interface massless Weyl fermions are confined in all three dimensions. The directions of spin and momentum are tangent to the surface of the QD. Remarkably, their inherent spin-momentum locking property exists even in a QD. Because of the linear dispersion there is a mirror symmetry in the energy spectrum between positive and negative energy states, in contrast to topologically trivial semiconductors. We demonstrate that this symmetry in energy spectrum is preserved for the QD spectrum.

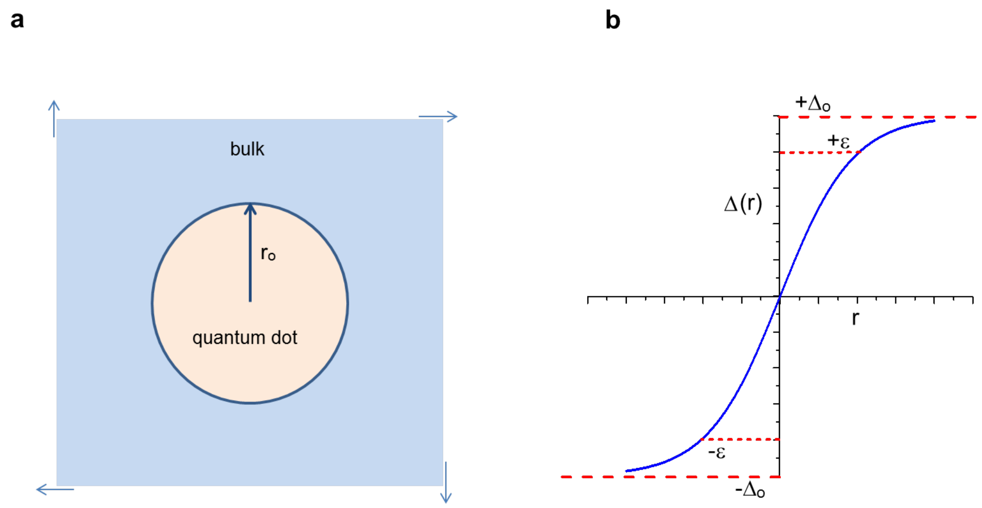

Figure 3.1: A heterostructure spherical core-bulk 3D TI QD with a single interface. **a**. The arrows indicate the infinite size of the host. The core and bulk host can be chosen as PbTe and $Pb_{0.31}Sn_{0.69}Te$ or vice versa. **b**. The potential $\Delta(r)$ binds Weyl fermions at the interface. The energy of the bound interface states depends on the size of the QD and the strength of the potential. As an example, two bound states at the interface are shown with energies $+\varepsilon$ and $-\varepsilon$ (short dashed lines) for a QD of size r_0 =2 nm.

Several methods have been proposed to implement optically controlled quantum memory and optically mediated quantum computing with topologically trivial QDs. Quantum memories have been recently reviewed in [86]. A recent review on optically controlled quantum computing with electron spins can be found in [87]. Optically controlled single-electron spin memory has been experimentally demonstrated using GaAs QDs[88] and InGaAs QDs.[89] Exciton memory has been implemented experimentally in a semiconductor nanopost.[90] For the purpose of using a hole spin as quantum memory or qubit, high coherence of hole spins in InGaAs QDs has been experimentally shown.[91] Ref. [92] demonstrates experimentally that a single spin can be read out using Faraday rotation. Schemes for optically controlled two-qubit interaction have been proposed that are based on the exchange of virtual photons inside a cavity,[93] the optical RKKY interaction and[94] dipole-dipole interaction,[95] Substantial experimental progress has been made to implement optically controlled electron spin state preparation,[92] hole spin state preparation,[96] single-spin readout,[97] dephasing protection,[98] two-qubit gate,[99, 100] two QD-spin entanglement[101] and spin-photon entanglement.[102]

In Refs. [103, 104] we developed the method of the Faraday rotation of a single photon due to the Pauli exclusion principle occurring on a topologically trivial QD. Our proposed method can be used for entangling remote excitons, electron spins, and hole spins. We showed that this entanglement can be used for the implementation of optically mediated quantum teleportation and quantum computing. Our ideas and methods have been copied in Ref. [105].

Here we show that classical and single-photon Faraday rotation due to the Pauli exclusion principle in a 3D TI QD occur due to strict optical selection rules satisfied by both interband and intraband transitions that depend on the polarization of electron-hole pairs. Based on this finding we propose that 3D TI QDs can be used as quantum memory and for the implementation of optically mediated quantum teleportation and quantum computing. First, we propose that a single e-h pair in a 3D TI QD can be used as a quantum memory.

The information is stored in form of the polarization state of the e-h pair. In order to be able to read out this information multiple times, we develop the method of Faraday rotation of a classical electromagnetic field due to Pauli exclusion principle in a 3D TI QD. Second, we propose that the polarization of a single e-h pair, a single electron spin, or a single hole spin can be used as a qubit in a 3D TI QD for the implementation of optically mediated quantum teleportation and quantum computing. We develop the method of single-photon Faraday rotation in a 3D TI QD, which creates the entanglement between a single photon and a qubit on the 3D TI QD. This entanglement is the resource for the implementation of quantum teleportation and quantum computing.

In wide bandgap semiconductor QDs optical inter- and intraband transitions are energetically separated because the bandgap is typically much larger than the QD level spacing.[106] In contrast to that, we show that in 3D TI QDs inter- and intraband transitions combine because of the vanishing bandgap at band crossing. The resulting large dipole moment of up to 450 Debye provides the possibility to reach the strong-coupling regime for a cavity quality factor of $Q \approx 10^4$ in the infrared wavelength regime of around 10 μm.

The paper is organized as follows. In Sec. 3.2 we present the analytical derivation of the Weyl solution of the radial Dirac equation using Greens function technique at the bulk-quantum dot interface. The resulting eigenvalues and eigenfunctions are analyzed in the Sec. 3.3. The Sec. 3.4 is devoted to the evaluation of the optical transition matrix elements and the discussion on them. We also discuss on the potential applications of our results. In Sec. 3.5 we explain the Faraday rotation effect achieve in the 3D TI QD. The application of the 3D TI QD as a quantum memory is explained in the Sec. 3.6. where we also explain the Stark energy shift that can be used to achieve clean selection rules for the excitation of a single electron-hole (e-h) pair. The Sec. 3.7 and 3.8 are devoted to the detailed description of the single-photon Faraday effect, where we show that a single e-h pair, a single electron, or a single hole can be used as a qubit to implement optically mediated quantum teleportation and quantum computing with 3D TI QDs. In this section, different possible level configurations of the Weyl states are shown to achieve the Faraday rotation effect.

3.2 Model Based on Dirac Equation

In Figure 3.1 we show the model of our spherically symmetric 3D TI QD of a core-bulk structure with a single interface at radius $r = r_0$. This core-bulk structure consists, for example, of an inner core of PbTe and an outer bulk of $\mathrm{Pb_{0.31}Sn_{0.69}Te}$ with bandgaps of 0.187 and -0.187 eV, respectively, or vice versa, so that Weyl fermions are generated at the interface. Here we used the bandgap formula provided in Ref. 24 for determining x. Note that the band crossing happens in $\mathrm{Pb}_{1-x}\mathrm{Sn}_x\mathrm{Te}$ at $x = 0.35$ at 4 K. The Weyl fermions are subjected to the spherically symmetric potential $\Delta(r)$ (Figure 3.1 (b)).

To understand the properties of a 3D TI QD, we start with the Dirac Hamiltonian within the $\mathbf{k} \cdot \mathbf{p}$ approximation.[107] Neglecting the far band terms, we have

$$H = v_\parallel \alpha_z \hat{p}_z + v_\perp \boldsymbol{\alpha}_\perp \cdot \hat{\mathbf{p}} + \beta \Delta \tag{3.1}$$

where $\boldsymbol{\alpha} = \begin{pmatrix} 0 & \boldsymbol{\sigma} \\ \boldsymbol{\sigma} & 0 \end{pmatrix}$ are the Dirac $\boldsymbol{\alpha}$- matrices, $\boldsymbol{\sigma}$ are the Pauli matrices, $\beta = \begin{pmatrix} 1 & 0 \\ 0 & -1 \end{pmatrix}$ is the Dirac β-matrix, and $\hat{\mathbf{p}}$ is the momentum operator. The component of the Fermi velocities $v_\perp$and $v_\parallel$ in angular and radial direction are determined by the $v_\perp = P_\perp/m_0$ and $v_\parallel = P_\parallel/m_0$ respectively, where $P_\perp$ and $P_\parallel$ are the interband matrix elements. $m_0 = 9.10938188 \times 10^{-31}$ kg is the free electron mass. $\Delta(\mathbf{r}) = \varepsilon_g(\mathbf{r})/2$ is the gap energy parameter.

Assuming spherical symmetry for the 3D TI QD, $\Delta(r)$ depends on the radial coordinate only which breaks the crystal symmetry in radial direction and has the symmetry $\Delta(r - r_0) = -\triangle(r_0 - r)$, where r_0 is the radius of the QD. Therefore, the angular parts are separated from the radial part of the Dirac Hamiltonian (4.1). Thus, we can follow the derivation of the solution for the central-force problem of a hydrogen atom in relativistic quantum mechanics.[108] The eigenfunctions of H are four-component spinors $\Phi = \begin{bmatrix} \phi_- \\ \phi_+ \end{bmatrix} = \begin{bmatrix} f_-(r)\mathcal{Y}_{jl_-}^{m_j} \\ if_+(r)\mathcal{Y}_{jl_+}^{m_j} \end{bmatrix}$, where $f_-$and f_+ are the radial functions and $\mathcal{Y}_{jl_-}^{m_j}$ and $\mathcal{Y}_{jl_+}^{m_j}$ are the normalized spin-angular functions corresponding to the L_- and L_+ band, respectively, such as in $\mathrm{Pb}_{1-x}\mathrm{Sn}_x\mathrm{Te}$. After eliminating the angular parts, the radial part of the Dirac Hamiltonian (4.1) takes the form

$$H = \begin{pmatrix} \Delta(r) & -v_\parallel \hbar\left(\frac{d}{dr} - \frac{\kappa}{r}\right) \\ v_\parallel \hbar\left(\frac{d}{dr} + \frac{\kappa}{r}\right) & -\Delta(r) \end{pmatrix} \tag{3.2}$$

where $v_\parallel = 2.24 \times 10^5$ m/s for $\mathrm{Pb}_{1-x}\mathrm{Sn}_x\mathrm{Te}$ and $\kappa = \pm\left(j + \frac{1}{2}\right)$ is a nonzero positive or negative integer, j being the total angular momentum quantum number. For given κ, it is known from relativistic quantum mechanics that the angular momenta l_- and l_+ for

ϕ_- and ϕ_+ are determined by the relations $-\kappa = j\,(j+1) - l_-\,(l_- + 1) + 1/4$ and $\kappa = j\,(j+1) - l_+\,(l_+ + 1) + 1/4$, respectively. By solving $H^2\Phi = \varepsilon^2\Phi$, we obtain

$$\left(r^2\frac{d^2}{dr^2} + 2r\frac{d}{dr}\right)F_\mp - \left(\lambda^2 r^2 + \kappa\,(\kappa \pm 1)\right)F_\mp = \beta r^2\frac{d\Delta}{dr}F_\pm \tag{3.3}$$

where $F_\pm = rf_\pm$, $\beta = 1/v_\parallel\hbar$ and $\lambda = \beta\sqrt{(\Delta_0^2 - \varepsilon^2)}$. λ behaves like a wave vector $\mathbf{k}$ whose allowed quantized values determine the particle's energy levels. In a flat geometry of a thin layer of a 3D TI, $\Delta\,(z)$ can be chosen to be $\Delta\,(z) = \Delta\,(\infty)\tanh\,(z/l)$.[109, 110] We adopt a similar potential along the radial direction of the form $\Delta(r^{'}) = \Delta_o sgn(r^{'} - r_o)$. Hence, the source term in Eq. (4.3) is $\mathcal{F}_\pm\left(r^{'}\right) = 2\Delta_o\beta F_\pm\,(r_o)\,r^{'2}\delta\left(r^{'} - r_o\right)$. Eqs. (4.3) can be solved by using the corresponding differential equation for the Green's function, i.e.

$$\left[\frac{d}{dr}\left(r^2\frac{d}{dr}\right) - \left(\lambda^2 r^2 + \kappa\,(\kappa \pm 1)\right)\right]G_\mp = \delta\left(r - r^{'}\right) \tag{3.4}$$

The solutions regular at $r = 0$ with outgoing wave behavior at $r \to \infty$ are the product of spherical modified Bessel functions of the order κ for G_- and of the order $\kappa - 1$ for G_+, i.e. $G_-\left(r,\, r^{'},\, \lambda\right) = C_-\mathcal{I}_\kappa\,(\lambda r_<)\,\mathcal{K}_\kappa\,(\lambda r_>)$, $G_+\left(r,\, r^{'},\, \lambda\right) = C_+\mathcal{I}_{\kappa-1}\,(\lambda r_<)\,\mathcal{K}_{\kappa-1}\,(\lambda r_>)$, where $r_<$ $(r_>)$ is the smaller (larger) of r and $r^{'}$. The functions $\mathcal{I}\,(\lambda r)$ and $\mathcal{K}\,(\lambda r)$ are, respectively, the first and the second kind of modified spherical Bessel functions, and $C_\mp$ are the normalization constants. These constants are determined by the discontinuity in slope implied by the delta function in Eq. (3.4). Integration is performed at the interface of the QD along the radial direction: $\left[r^2\frac{dG_\mp}{dr}\right]_{r^{'}-\eta}^{r^{'}+\eta} = 1$, where η is an infinitesimal quantity with $\eta > 0$. For $r = r^{'} + \eta$, $r_> = r$, $r_< = r^{'}$ and for $r = r^{'} - \eta$, $r_> = r^{'}$, $r_< = r$. Consequently, the normalization constants are $C_- = 1/\lambda r_0^{'2}W_\kappa$ and $C_+ = 1/\lambda r_o^{'2}W_{\kappa-1}$, where

$W_\kappa = \left[\mathcal{I}_\kappa\left(\lambda r'\right)\mathcal{K}'_\kappa\left(\lambda r\right) - \mathcal{I}'_\kappa\left(\lambda r\right)\mathcal{K}_\kappa\left(\lambda r'\right)\right]_{r=r'}$ and

$W_{\kappa-1} = \left[\mathcal{I}_{\kappa-1}\left(\lambda r'\right)\mathcal{K}'_{\kappa-1}\left(\lambda r\right) - \mathcal{I}'_{\kappa-1}\left(\lambda r\right)\mathcal{K}_{\kappa-1}\left(\lambda r'\right)\right]_{r=r'}$ are the Wronskians of $\mathcal{I}\left(\lambda r\right)$ and $\mathcal{K}\left(\lambda r\right)$, respectively, for κ and $\kappa-1$ order, and $\mathcal{I}'\left(\lambda r\right)$ and $\mathcal{K}'\left(\lambda r\right)$ are derivatives of the Bessel functions. The Wronskian of two linearly independent functions is proportional to $1/r^2$ for Sturm-Liouville type equations such as Eq. (3.4) (see the App. A.1). The solutions of Eqs. (4.3) are $F_\mp = \int G_\mp\left(r,\, r',\, \lambda\right)\mathcal{F}_\pm(r')dr' = 2\Delta_o\beta\int G_\mp\left(r,\, r',\, \lambda\right)F_\pm\left(r_o\right)r'^2\delta\left(r' - r_o\right)dr'$, i.e.

$$F_-\left(r\right) = 2\Delta_o\beta F_+\left(r_o\right)\mathcal{I}_\kappa\left(\lambda r_<\right)\mathcal{K}_\kappa\left(\lambda r_>\right)/\lambda W_\kappa \tag{3.5}$$

$$F_+\left(r\right) = 2\Delta_o\beta F_-\left(r_o\right)\mathcal{I}_{\kappa-1}\left(\lambda r_<\right)\mathcal{K}_{\kappa-1}\left(\lambda r_>\right)/\lambda W_{\kappa-1} \tag{3.6}$$

where $r_<$ ($r_>$) is now the smaller (larger) of r and r_0. A transcendental equation is obtained by solving Eqs. (4.5) and (4.6) is evaluated at $r = r_0$,

$$\left[z\mathcal{I}_\kappa\left(z\right)\mathcal{K}_\kappa\left(z\right)\right]\left[z\mathcal{I}_{\kappa-1}\left(z\right)\mathcal{K}_{\kappa-1}\left(z\right)\right] = 1/4\Delta_o^2\beta^2 r_o^2 \tag{3.7}$$

where $z = \lambda r_0$. In Figure 3.2, we show the plot of Eq. (4.7) where the function $F\left(z\right)$ is defined as $F\left(z\right) = \left[z\mathcal{I}_\kappa\left(z\right)\mathcal{K}_\kappa\left(z\right)\right]\left[z\mathcal{I}_{\kappa-1}\left(z\right)\mathcal{K}_{\kappa-1}\left(z\right)\right]$.

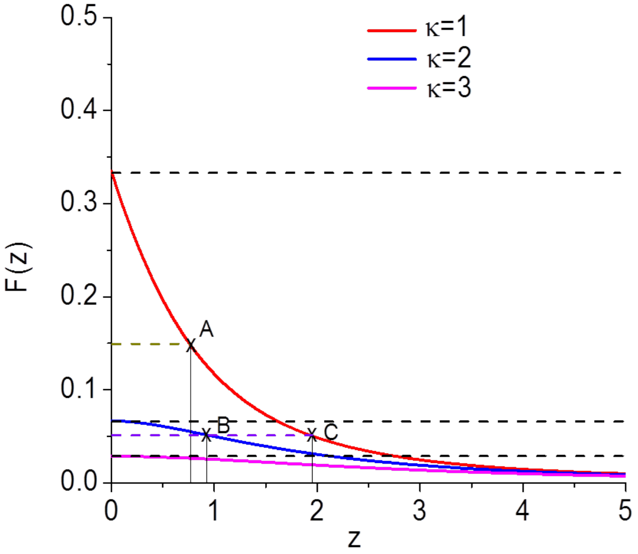

Figure 3.2: Plot of Eq. (4.7) showing the intersections of the monotonically decreasing $F(z)$ (solid lines) with the constants (black dashed lines). Intersection at $z = 0$ gives the minimum threshold of the size of a QD to have two bound states, one positive and one negative energy state, for a given confining potential. For a larger QD, multiple bound states exist, corresponding to multiple intersection points. The intersection points A, B and C are example points where we evaluate the wavefunctions. The energy of the bound states are determined by the relation $z = \lambda r_o$.

3.3 Bound States of the Weyl Fermions

Each term in the square bracket on the left hand side of Eq. (4.7) is a monotonically decreasing function of z (for $z > 0$), with maximum value of $1/(2\kappa+1)$ for κ^{th} order term and $1/(2\kappa-1)$ for $(\kappa-1)^{th}$ order term occurring at $z = 0$ (see the App. A.2). Therefore, their product has a maximum value of $1/(4\kappa^2-1)$ at $z = 0$ and is equal to $1/4\Delta_o^2\beta^2 r_o^2$. Since $F(z)$ is a monotonically decreasing function, for each κ, there is at most a single solution given by the intersection of $F(z)$ with the constant $1/4\Delta_o^2\beta^2 r_o^2$ (dashed line and solid line in Figure 3.2). The critical limit for having a single solution is determined by the intersection at the maximum value of $F(z)$, which occurs at $z = 0$. This means that there exists a single solution of Eq. (4.7) for each κ as long as the condition $1/4\Delta_o^2\beta^2 r_o^2 \leq 1/(4\kappa^2-1)$ is satisfied. Figure 3.2 shows the plot of the first three different values of κ, $\kappa = 1$ (red), 2 (blue) and 3 (pink), each a monotonically decreasing line (solid line) is cut by a horizontal line (dashed line) at most one time. Since $\lambda = \beta\sqrt{(\Delta_0^2 - \varepsilon^2)}$, each single solution gives rise to two bound states with same magnitude but opposite sign of energy, giving rise to the mirror symmetry in the energy spectrum. Indeed, this makes sense since Weyl fermions are massless at zero band gap with the linear dispersion relation. Note that there is no radial quantum number because in general a Dirac potential allows only for a single positive-energy and a single negative-energy solution in radial direction.

As the size of the QD grows, it is filled with more and more bound states (see Figure 3.2) where for smaller value of $F(z)$, a horizontal dashed line makes multiple cuts at different values of the energy (i.e. z) for different κ. For negative κ, the solutions diverge at the origin and are therefore physically not valid. This result has profound implications because the sign of κ determines whether $\mathbf{j}$ is parallel or antiparallel to the spin $\mathbf{s}$ (see Ref. 48). Since κ is only allowed to be positive, only one spin orientation with respect to $\mathbf{j}$ is permitted. This corresponds to the spin locking effect, which is a hallmark of 3D TIs. This allows us to write down the more specific form of the spin-angular functions, i.e.

$$\begin{aligned}\mathcal{Y}_{jl_-}^{m_j} &= -\sqrt{\frac{l_- - m_j + \frac{1}{2}}{2l_- + 1}} Y_{l_-}^{m_j - \frac{1}{2}} \begin{bmatrix} 1 \\ 0 \end{bmatrix} \\ &\quad + \sqrt{\frac{l_- + m_j + \frac{1}{2}}{2l_- + 1}} Y_{l_-}^{m_j + \frac{1}{2}} \begin{bmatrix} 0 \\ 1 \end{bmatrix} \end{aligned} \tag{3.8}$$

$$\begin{aligned}\mathcal{Y}_{jl_+}^{m_j} &= \sqrt{\frac{l_+ + m_j + \frac{1}{2}}{2l_+ + 1}} Y_{l_+}^{m_j - \frac{1}{2}} \begin{bmatrix} 1 \\ 0 \end{bmatrix} \\ &\quad + \sqrt{\frac{l_+ - m_j + \frac{1}{2}}{2l_+ + 1}} Y_{l_+}^{m_j + \frac{1}{2}} \begin{bmatrix} 0 \\ 1 \end{bmatrix} \end{aligned} \tag{3.9}$$

where $l_- = j + \frac{1}{2}$ and $l_+ = j - \frac{1}{2}$.

The condition $1/4\Delta_o^2\beta^2 r_o^2 = 1/(4\kappa^2 - 1)$ determines the lower limit of the size of the QD to hold two bound interface states, a positive and a negative energy state, for a given value of the confining potential strength. The critical QD size depends on the Fermi velocities and band gaps of the 3D TI materials. In $\mathrm{Pb}_{1-x}\mathrm{Sn}_x\mathrm{Te}$, $\Delta_o = 0.0935$ eV, half of the band gap of PbTe. Choosing $v_{\parallel} = 2.24 \times 10^5$m/s,[110] results in a critical QD size of $r_0 = 1.4$ nm for $\kappa = 1$ at $z = 0$. Similarly for $\kappa = 2$ at $z = 0$, the critical QD size for $\mathrm{Pb}_{1-x}\mathrm{Sn}_x\mathrm{Te}$ is

$r_0 = 3$ nm. The energy of the bound states are determined from $z = \lambda r_o$, which gives a very shallow energy level of $\varepsilon = \pm\Delta_o$ for $z = 0$.

Table 3.1: ϕ_- and ϕ_+ components

ϕ_-			ϕ_+		
κ	l_-	j	κ	l_+	j
1	1	1/2	1	0	1/2
2	2	3/2	2	1	3/2
3	3	5/2	3	2	5/2
4	4	7/2	4	3	7/2

For a given value of κ, quantum numbers characterizing the wavefunctions ϕ_- and ϕ_+ can be determined. For $\kappa = 1$, 2, 3 and 4, the possible combination of the quantum numbers are shown in Table 3.1 for both spinors ϕ_- and ϕ_+. Here we observe that the ϕ_- component is characterized by the spin being antiparallel to its angular momentum, whereas the ϕ_+ component is characterized by the spin being parallel to its angular momentum. We show now how to identify the Kramers pairs. According to Kramers theorem, which applies to a time-reversal invariant system, a spin 1/2 state is at least twofold degenerate on the surface of a 3D TI. Hence, we obtain the following examples of Kramers pairs. For $\kappa = 1$, the 4-spinor state with $m_{\frac{1}{2}} = \frac{1}{2}$,

$$\begin{aligned}
\Phi^{\kappa=1}_{\frac{1}{2},\frac{1}{2}} &= \begin{bmatrix} f_-(r)\mathcal{Y}^{\frac{1}{2}}_{\frac{1}{2}1} \\ if_+(r)\mathcal{Y}^{\frac{1}{2}}_{\frac{1}{2}0} \end{bmatrix} \\
&= \begin{bmatrix} f_-(r)\left(-\sqrt{\frac{1}{3}}Y^0_1\begin{bmatrix}1\\0\end{bmatrix} + \sqrt{\frac{2}{3}}Y^1_1\begin{bmatrix}0\\1\end{bmatrix}\right) \\ if_+(r)Y^0_0\begin{bmatrix}1\\0\end{bmatrix} \end{bmatrix}
\end{aligned} \tag{3.10}$$

has as Kramers partner the 4-spinor state with $m_{\frac{1}{2}} = -\frac{1}{2}$,

$$\begin{aligned}
\Phi^{\kappa=1}_{\frac{1}{2},-\frac{1}{2}} &= \begin{bmatrix} f_-(r)\mathcal{Y}^{-\frac{1}{2}}_{\frac{1}{2}1} \\ if_+(r)\mathcal{Y}^{-\frac{1}{2}}_{\frac{1}{2}0} \end{bmatrix} \\
&= \begin{bmatrix} f_-(r)\left(-\sqrt{\frac{2}{3}}Y^{-1}_1\begin{bmatrix}1\\0\end{bmatrix} + \sqrt{\frac{1}{3}}Y^0_1\begin{bmatrix}0\\1\end{bmatrix}\right) \\ if_+(r)Y^0_0\begin{bmatrix}0\\1\end{bmatrix} \end{bmatrix}
\end{aligned} \tag{3.11}$$

For $\kappa = 2$, the 4-spinor state with $m_{\frac{3}{2}} = \frac{3}{2}$,

$$\begin{aligned} \Phi^{\kappa=2}_{\frac{3}{2},\frac{3}{2}} &= \begin{bmatrix} f_-(r)\mathcal{Y}^{\frac{3}{2}}_{\frac{3}{2}2} \\ if_+(r)\mathcal{Y}^{\frac{3}{2}}_{\frac{3}{2}1} \end{bmatrix} \\ &= \begin{bmatrix} f_-(r)\left(-\sqrt{\frac{1}{5}}Y^1_2\begin{bmatrix}1\\0\end{bmatrix} + \sqrt{\frac{4}{5}}Y^2_2\begin{bmatrix}0\\1\end{bmatrix}\right) \\ if_+(r)Y^1_1\begin{bmatrix}1\\0\end{bmatrix} \end{bmatrix} \end{aligned} \tag{3.12}$$

has as Kramers partner the 4-spinor with $m_{\frac{3}{2}} = -\frac{3}{2}$,

$$\begin{aligned} \Phi^{\kappa=2}_{\frac{3}{2},-\frac{3}{2}} &= \begin{bmatrix} f_-(r)\mathcal{Y}^{-\frac{3}{2}}_{\frac{3}{2}2} \\ if_+(r)\mathcal{Y}^{-\frac{3}{2}}_{\frac{3}{2}1} \end{bmatrix} \\ &= \begin{bmatrix} f_-(r)\left(-\sqrt{\frac{4}{5}}Y^{-2}_2\begin{bmatrix}1\\0\end{bmatrix} + \sqrt{\frac{1}{5}}Y^{-1}_2\begin{bmatrix}0\\1\end{bmatrix}\right) \\ if_+(r)Y^{-1}_1\begin{bmatrix}0\\1\end{bmatrix} \end{bmatrix} \end{aligned} \tag{3.13}$$

For $\kappa = 2$, the 4-spinor state with $m_{\frac{3}{2}} = \frac{1}{2}$,

$$\Phi^{\kappa=2}_{\frac{3}{2},\frac{1}{2}} = \begin{bmatrix} f_-(r)\mathcal{Y}^{\frac{1}{2}}_{\frac{3}{2}2} \\ if_+(r)\mathcal{Y}^{\frac{1}{2}}_{\frac{3}{2}1} \end{bmatrix} = \begin{bmatrix} f_-(r)\left(-\sqrt{\frac{2}{5}}Y^0_2\begin{bmatrix}1\\0\end{bmatrix} + \sqrt{\frac{3}{5}}Y^1_2\begin{bmatrix}0\\1\end{bmatrix}\right) \\ if_+(r)\left(\sqrt{\frac{2}{3}}Y^0_1\begin{bmatrix}1\\0\end{bmatrix} + \sqrt{\frac{1}{3}}Y^1_1\begin{bmatrix}0\\1\end{bmatrix}\right) \end{bmatrix} \tag{3.14}$$

has as Kramers partner the 4-spinor with $m_{\frac{3}{2}} = -\frac{1}{2}$,

$$\Phi^{\kappa=2}_{\frac{3}{2},-\frac{1}{2}} = \begin{bmatrix} f_-(r)\mathcal{Y}^{-\frac{1}{2}}_{\frac{3}{2}2} \\ if_+(r)\mathcal{Y}^{-\frac{1}{2}}_{\frac{3}{2}1} \end{bmatrix} = \begin{bmatrix} f_-(r)\left(-\sqrt{\frac{3}{5}}Y^{-1}_2\begin{bmatrix}1\\0\end{bmatrix} + \sqrt{\frac{2}{5}}Y^0_2\begin{bmatrix}0\\1\end{bmatrix}\right) \\ if_+(r)\left(\sqrt{\frac{1}{3}}Y^{-1}_1\begin{bmatrix}1\\0\end{bmatrix} + \sqrt{\frac{2}{3}}Y^0_1\begin{bmatrix}0\\1\end{bmatrix}\right) \end{bmatrix} \tag{3.15}$$

In general, the number of Kramers pairs is determined by the spin multiplicity for each m_j value.

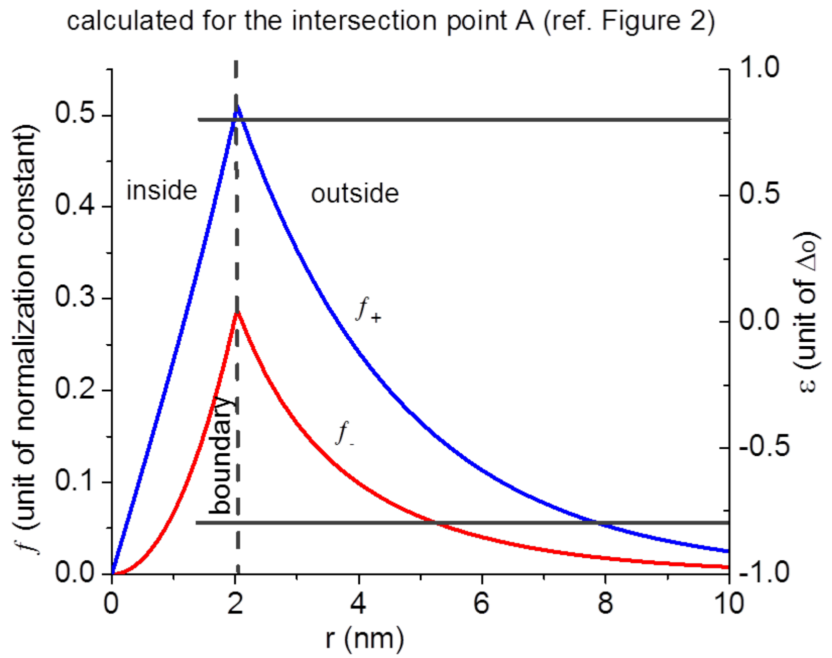

Figure 3.3: Spatial dependence of f_- and f_+ inside and outside the QD calculated for the intersection point A shown in Figure 3.2. The QD has size $r_0 = 2$ nm. The solid horizontal lines represent the energy eigenvalues $\varepsilon_\pm = \pm 0.8\Delta_o$.

In Figs. 3.3 and 3.4 we show the spatial wavefunctions of the f_- and f_+ components inside and outside the QD made of the core-bulk heterostructure PbTe/Pb$_{0.31}$Sn$_{0.69}$Te. The Figure 3.3 shows the example of the intersection point A and the Figure 3.4 shows the example of the intersection points B and C (points A, B and C are shown in Figure 3.2). Since the 4-spinors must be continuous at the boundary, also each of the 2-spinor components must be continuous, i.e. $f_-^{in} = f_-^{out}$ and $f_+^{in} = f_+^{out}$ at the QD surface. The horizontal solid and short dashed lines in the figures represent the energy eigenvalues, respectively, at the intersection point A, corresponding to $r_0 = 2$ nm, and at the intersection point B and C, corresponding to $r_0 = 3.5$ nm. Eigenvalues are $\varepsilon_\pm = \pm 0.80\Delta_o$ at point A, $\varepsilon_\pm = \pm 0.91\Delta_o$ at point B, and $\varepsilon_\pm = \pm 0.48\Delta_o$ at point C.

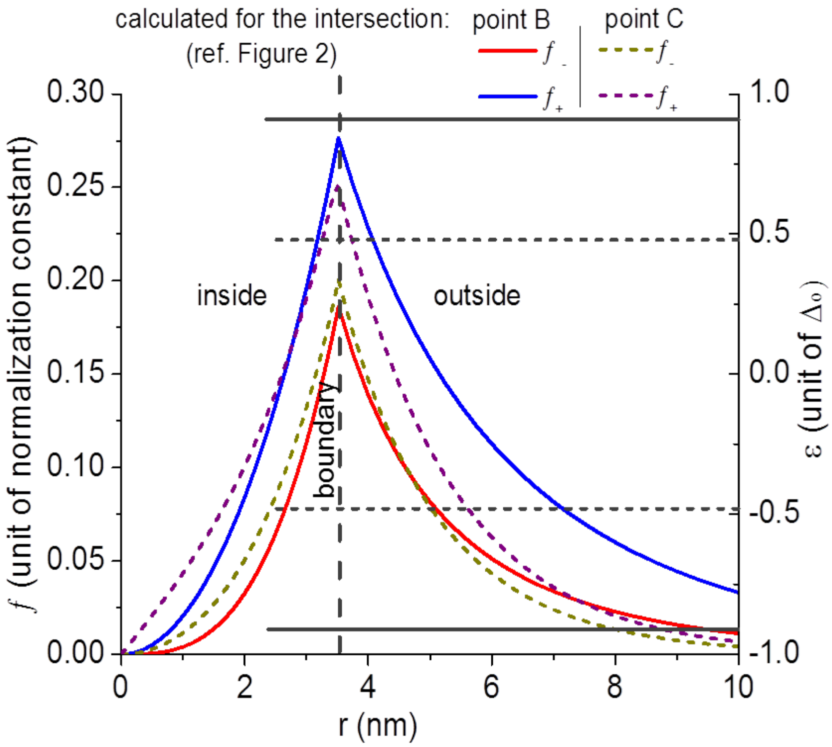

Figure 3.4: Spatial dependence of f_- and f_+ inside and outside the QD calculated for the intersection points B and C shown in Figure 3.2. The QD has size $r_0 = 3.5$ nm. The horizontal solid lines represent the energy eigenvalues $\varepsilon_\pm = \pm 0.91\Delta_o$ at point B and the horizontal dotted lines represent the energy eigenvalues $\varepsilon_\pm = \pm 0.48\Delta_o$ at point C.

In order to show that the solutions correspond to Weyl fermions, we perform an expansion of Eq. (4.7) for large z to obtain the energy eignenvalues in the continuum limit.

Using the second order in the expansion of the spherical modified Bessel functions for $z \to \infty$ (see the App. A.2), we get

$$\frac{1}{2z}\left[1-\frac{2\kappa\left(\kappa+1\right)}{\left(2z\right)^2}\right]\times\frac{1}{2z}\left[1-\frac{2\kappa\left(\kappa-1\right)}{\left(2z\right)^2}\right]=1/4\Delta_o^2\beta^2r_o^2. \tag{3.16}$$

This can be written as

$$\varepsilon^4-\varepsilon^2\Delta_o^2+\frac{\Delta_o^2\kappa^2}{\beta^2r_o^2}=0 \tag{3.17}$$

which results in the energy eigenvalues for the electron and hole,

$$\varepsilon_{\pm}=\pm\kappa v_{\parallel}\hbar/r_o. \tag{3.18}$$

This corresponds to the linear spectrum of free massless Dirac fermions, i.e. free Weyl fermions on a sphere. This means that the energy splittings between the trapped Weyl states in the quantum dot result from the confinement of the Weyl fermions on a sphere. The solution in Eq. (3.18) corresponds to the eigenspectra found in Ref. [111] for zero magnetic field and without quantum confinement effects.

In the continuum limit, the Nielsen-Ninomiya fermion doubling theorem [112, 113, 114] is satisfied by the pairs of Dirac cones positioned at antipodal points of the sphere defined by the surface of the QD (see App. A.3 for details). However, for a general finite QD radius r_o the eigenstates are bound and have a discrete energy spectrum. Since the Nielsen-Ninomiya fermion doubling theorem is valid only for continuum states, it does not apply to the bound Weyl fermions in a 3D TI QD with finite radius r_o.

3.4 Optical Excitations

The $\mathbf{k}\cdot\mathbf{p}$ Hamiltonian contains also a quadratic term in the momenta,[107] namely

$$H_q = \begin{pmatrix} \frac{(p_z+eA_z)^2}{2m_\parallel^-} + \frac{(\mathbf{p}_\perp+e\mathbf{A}_\perp)^2}{2m_\perp^-} & 0 \\ 0 & \frac{(p_z+eA_z)^2}{2m_\parallel^+} + \frac{(\mathbf{p}_\perp+e\mathbf{A}_\perp)^2}{2m_\perp^+} \end{pmatrix}, \tag{3.19}$$

where $m_\parallel^\mp$ and $m_\perp^\mp$ are the longitudinal and transverse effective masses of the $L^\mp$ bands, respectively. Through minimal coupling the quadratic term leads to a linear term in the momentum, which we need to take into account. Hence, in the presence of electromagnetic radiation, the total Hamiltonian for the Dirac particle is given by

$$\begin{aligned} H_{tot} &= v_\parallel \alpha_z \left(\hat{p}_z + eA_z\right) + v_\perp \boldsymbol{\alpha}_\perp \cdot \left(\hat{\mathbf{p}} + e\mathbf{A}_\perp\right) + \beta\Delta - e\hat{\mathbf{r}}\cdot\mathbf{E} \\ &= \begin{pmatrix} \Delta - e\hat{\mathbf{r}}\cdot\mathbf{E} & v_\parallel\sigma_z\left(\hat{p}_z + eA_z\right) + v_\perp\boldsymbol{\sigma}_\perp\cdot\left(\hat{\mathbf{p}} + e\mathbf{A}_\perp\right) \\ v_\parallel\sigma_z\left(\hat{p}_z + eA_z\right) + v_\perp\boldsymbol{\sigma}_\perp\cdot\left(\hat{\mathbf{p}} + e\mathbf{A}_\perp\right) & -\Delta - e\hat{\mathbf{r}}\cdot\mathbf{E} \end{pmatrix} \end{aligned} \tag{3.20}$$

where $A = (A_z,\ \boldsymbol{A}_\perp)$ is the vector potential, $\mathbf{E} = \partial\mathbf{A}/\partial t$ in the Coulomb gauge, and we made use of the equivalence between $(e/m)\mathbf{A}\cdot\mathbf{p}$ and $-e\hat{\mathbf{r}}\cdot\mathbf{E}$.[108] We identify the interaction Hamiltonian as

$$\begin{aligned} H_{int} &= ev_\parallel\alpha_z A_z + ev_\perp\boldsymbol{\alpha}_\perp\cdot\boldsymbol{A}_\perp - e\hat{\mathbf{r}}\cdot\mathbf{E} \\ &= \begin{pmatrix} -e\hat{\mathbf{r}}\cdot\mathbf{E} & ev_\parallel\sigma_z A_z + ev_\perp\boldsymbol{\sigma}_\perp\cdot\mathbf{A}_\perp \\ ev_\parallel\sigma_z A_z + ev_\perp\boldsymbol{\sigma}_\perp\cdot\mathbf{A}_\perp & -e\hat{\mathbf{r}}\cdot\mathbf{E} \end{pmatrix} \end{aligned} \tag{3.21}$$

It will turn out that both interband and intraband transitions contribute. It is important to note that $v_\parallel = P_\parallel/m_0$ and $v_\perp = P_\perp/m_0$ include the Kane interband matrix elements $\mathbf{P} =$

$\left\langle u^{\mp}_{\mathbf{k}_{\mathrm{f}}} \left| \hat{\mathbf{P}} \right| u^{\pm}_{\mathbf{k}_{\mathrm{I}}} \right\rangle$, where $u^{\mp}_{\mathbf{k}}$ are the Bloch's functions for the $L^{\mp}$ bands. This means that the interband transitions are governed by the interband Hamiltonian $H_{inter} = ev_{\parallel}\alpha_z A_z + ev_{\perp}\boldsymbol{\alpha}_{\perp} \cdot \boldsymbol{A}_{\perp}$, where the Dirac $\boldsymbol{\alpha}$- matrices couple the L^- band with the L^+ band. The Hamiltonian $H_{intra} = -e\hat{\mathbf{r}} \cdot \mathbf{E}$ accounts for intraband transitions with $\hat{\mathbf{r}}$ operating on the envelope wavefunctions only. H_{intra} is proportional to the identity in 4-spinor space and therefore couples the L^- band to itself and the L^+ band to itself. Thus the interband Hamiltonian H_{inter} and the intraband Hamiltonian H_{intra} are not equivalent in this description. On the one hand, H_{inter} gives rise to interband transitions because it contains the Kane interband matrix elements $P_{\perp}$ and $P_{\parallel}$. On the other hand, H_{intra} gives rise to intraband transitions because the electric dipole operator $e\hat{\mathbf{r}}$ operates on the envelope wavefunctions. Remarkably, both terms lead to the same strict optical selection rules and add up to a combined optical matrix element, as shown below. This enhancement of the optical matrix element is a feature of the 3D TI QD. In contrast, in a wide-bandgap semiconductor QD the interband and intraband transitions are energetically separated, i.e. interband transitions occur typically around the bandgap energy, whereas intraband transitions occur around the energy level separation due to the confinement of the QD. [106]

Figure 3.5 shows the possible transitions between the states $\kappa = 1$ and $\kappa = 2$. It is to be noted that there is a complete symmetry in the solutions in the sense that a κ state can be chosen from either the positive- or the negative-energy solutions.

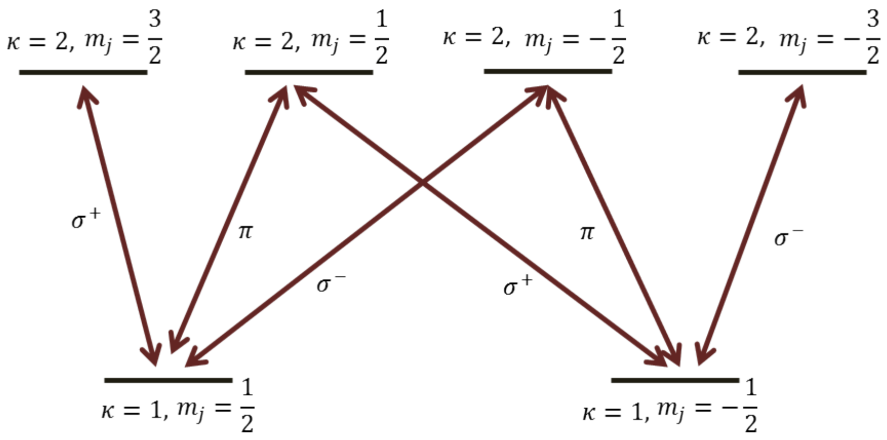
$\kappa = 2,\ m_j = \frac{3}{2}$
$\kappa = 2,\ m_j = \frac{1}{2}$
$\kappa = 2,\ m_j = -\frac{1}{2}$
$\kappa = 2,\ m_j = -\frac{3}{2}$
σ^+
π
σ^-
σ^+
π
σ^-
$\kappa = 1,\ m_j = \frac{1}{2}$
$\kappa = 1,\ m_j = -\frac{1}{2}$

Figure 3.5: Optical transitions between the states $\kappa = 1$ and $\kappa = 2$ in 3D TI QD. Transitions are vertical. The transitions between $\left|\Phi^{\kappa=1}_{\frac{1}{2},\pm\frac{1}{2}}\right\rangle$ and $\left|\Phi^{\kappa=2}_{\frac{3}{2},\pm\frac{1}{2}}\right\rangle$ are coupled to the linear polarization of the incoming photons, while the transitions between $\left|\Phi^{\kappa=1}_{\frac{1}{2},\pm\frac{1}{2}}\right\rangle$ and $\left|\Phi^{\kappa=2}_{\frac{3}{2},\mp\frac{1}{2}}\right\rangle$ couple to $\sigma^{\mp}$ polarizations and the transitions between $\left|\Phi^{\kappa=1}_{\frac{1}{2},\pm\frac{1}{2}}\right\rangle$ and $\left|\Phi^{\kappa=2}_{\frac{3}{2},\pm\frac{3}{2}}\right\rangle$ couple to $\sigma^{\pm}$ polarizations of the light.

The optical matrix elements are given by

$$\begin{aligned}\left\langle \phi_f \left| H_{int} \right| \phi_I \right\rangle =& ev_{\parallel} \left\langle \phi_f \left| \alpha_z \right| \phi_I \right\rangle A_z \\ &+ ev_{\perp} \left\langle \phi_f \left| \boldsymbol{\alpha}_{\perp} \right| \phi_I \right\rangle \cdot \boldsymbol{A}_{\perp} \\ &- e \left\langle \phi_f \left| \hat{\mathbf{r}} \right| \phi_I \right\rangle \cdot \mathbf{E} \end{aligned} \tag{3.22}$$

The incoming photon's wavelength is much larger than the dot size. Therefore, the transitions are vertical, which means $\mathbf{A} = (A_{x0}, A_{y0}, A_{z0})e^{i\mathbf{q}\cdot\mathbf{r}} \approx (A_{x0}, A_{y0}, A_{z0})$ can be used, yielding the electric dipole approximation. The transition energies $\hbar\omega_0 = \varepsilon_{\kappa=2} - \varepsilon_{\kappa=1}$ are large compared with the room temperature $k_BT = 25$ meV and the Coulomb charging energy of about 5 meV.[85] For the control of the number of electrons and holes in the 3D TI QD it is necessary to work at low temperatures of around 1 K.

As an example, here we consider transitions between the states $\kappa = 1$ (at point C) and $\kappa = 2$ (at point B). The matrix elements of the Dirac-α matrix are given by

$$\langle \Phi_f \left| \boldsymbol{\alpha} \right| \Phi_I \rangle = \left\langle \phi_-^{\kappa=2} \left| \boldsymbol{\sigma} \right| \phi_+^{\kappa=1} \right\rangle + \left\langle \phi_+^{\kappa=2} \left| \boldsymbol{\sigma} \right| \phi_-^{\kappa=1} \right\rangle \tag{3.23}$$

The matrix elements of $\hat{\mathbf{r}}$ are given by

$$\langle \phi_f \left| \hat{\mathbf{r}} \right| \phi_I \rangle = \left\langle \phi_-^{\kappa=2} \left| \hat{\mathbf{r}} \right| \phi_-^{\kappa=1} \right\rangle + \left\langle \phi_+^{\kappa=2} \left| \hat{\mathbf{r}} \right| \phi_+^{\kappa=1} \right\rangle \tag{3.24}$$

The spherical harmonics can be determined using the Table 3.1. In order to obtain optical selection rules for circular polarizations, it is useful to express the scalar products of the interband and the intraband Hamiltonian in the form $\mathbf{e} \cdot \boldsymbol{\alpha} = \mathbf{e}_z \alpha_z + \mathbf{e}_- \alpha_+ + \mathbf{e}_+ \alpha_-$ and $\mathbf{e} \cdot \hat{\mathbf{r}} = \mathbf{e}_z \hat{z} + \mathbf{e}_- \hat{r}_+ + \mathbf{e}_+ \hat{r}_-$, respectively, where $\mathbf{e}_\pm = \left(\mathbf{e}_x \pm i \mathbf{e}_y \right) / \sqrt{2}$ are the unit vectors of circular polarizations, $\alpha_\pm = \left(\alpha_x \pm i \alpha_y \right) / \sqrt{2}$, and $\hat{r}_\pm = \left(\hat{x} \pm i \hat{y} \right) / \sqrt{2} = -\sqrt{\frac{4\pi}{3}} r Y_1^{\pm 1}$. Using our spinor states $|\phi_\mp\rangle$ and radial wavefunction functions $|f_\mp\rangle$ we obtain the following nonzero matrix elements for $\boldsymbol{\alpha}$:

$$\begin{aligned}
\left\langle \Phi^{\kappa=2}_{\frac{3}{2},\pm\frac{1}{2}} \left|\alpha_z\right| \Phi^{\kappa=1}_{\frac{1}{2},\pm\frac{1}{2}} \right\rangle &\overset{\pi}{=} \left\langle \phi^{\kappa=2}_{+,\frac{3}{2},\pm\frac{1}{2}} \left|\sigma_z\right| \phi^{\kappa=1}_{-,\frac{1}{2},\pm\frac{1}{2}} \right\rangle \\
&= \frac{2\sqrt{2}}{3} i \left\langle f_+ \mid f_- \right\rangle \qquad (3.25) \\
\left\langle \Phi^{\kappa=2}_{\frac{3}{2},-\frac{1}{2}} \left|\alpha_-\right| \Phi^{\kappa=1}_{\frac{1}{2},+\frac{1}{2}} \right\rangle &\overset{\sigma^-}{=} \left\langle \phi^{\kappa=2}_{+,\frac{3}{2},-\frac{1}{2}} \left|\sigma_-\right| \phi^{\kappa=1}_{-,\frac{1}{2},+\frac{1}{2}} \right\rangle \\
&= \frac{2}{3} i \left\langle f_+ \mid f_- \right\rangle \qquad (3.26) \\
\left\langle \Phi^{\kappa=2}_{+,\frac{3}{2},+\frac{1}{2}} \left|\alpha_+\right| \Phi^{\kappa=1}_{-,\frac{1}{2},-\frac{1}{2}} \right\rangle &\overset{\sigma^+}{=} \left\langle \phi^{\kappa=2}_{+,\frac{3}{2},+\frac{1}{2}} \left|\sigma_+\right| \phi^{\kappa=1}_{-,\frac{1}{2},-\frac{1}{2}} \right\rangle \\
&= -\frac{2}{3} i \left\langle f_+ \mid f_- \right\rangle \qquad (3.27) \\
\left\langle \Phi^{\kappa=2}_{\frac{3}{2},+\frac{3}{2}} \left|\alpha_+\right| \Phi^{\kappa=1}_{\frac{1}{2},+\frac{1}{2}} \right\rangle &\overset{\sigma^+}{=} \left\langle \phi^{\kappa=2}_{+,\frac{3}{2},+\frac{3}{2}} \left|\sigma_+\right| \phi^{\kappa=1}_{-,\frac{1}{2},+\frac{1}{2}} \right\rangle \\
&= -\frac{2}{\sqrt{3}} i \left\langle f_+ \mid f_- \right\rangle \qquad (3.28) \\
\left\langle \Phi^{\kappa=2}_{+,\frac{3}{2},-\frac{3}{2}} \left|\alpha_-\right| \Phi^{\kappa=1}_{-,\frac{1}{2},-\frac{1}{2}} \right\rangle &\overset{\sigma^-}{=} \left\langle \phi^{\kappa=2}_{+,\frac{3}{2},-\frac{3}{2}} \left|\sigma_-\right| \phi^{\kappa=1}_{-,\frac{1}{2},-\frac{1}{2}} \right\rangle \\
&= \frac{2}{\sqrt{3}} i \left\langle f_+ \mid f_- \right\rangle \qquad (3.29)
\end{aligned}$$

For $\hat{\mathbf{r}}$ we obtain the following nonzero matrix elements:

$$\begin{aligned}
\left\langle \Phi^{\kappa=2}_{\frac{3}{2},+\frac{1}{2}} \left|\hat{z}\right| \Phi^{\kappa=1}_{\frac{1}{2},+\frac{1}{2}} \right\rangle &\overset{\pi}{=} \sqrt{\frac{2}{15}} \left\langle f_- Y_2^0 \right| \hat{z} \left| f_- Y_1^0 \right\rangle \\
&\quad + \sqrt{\frac{6}{15}} \left\langle f_- Y_2^1 \right| \hat{z} \left| f_- Y_1^1 \right\rangle \\
&\quad + \sqrt{\frac{2}{3}} \left\langle f_+ Y_1^0 \right| \hat{z} \left| f_+ Y_0^0 \right\rangle, \qquad (3.30) \\
\left\langle \Phi^{\kappa=2}_{\frac{3}{2},-\frac{1}{2}} \left|\hat{z}\right| \Phi^{\kappa=1}_{\frac{1}{2},-\frac{1}{2}} \right\rangle &\overset{\pi}{=} \sqrt{\frac{6}{15}} \left\langle f_- Y_2^{-1} \right| \hat{z} \left| f_- Y_1^{-1} \right\rangle \\
&\quad + \sqrt{\frac{2}{15}} \left\langle f_- Y_2^0 \right| \hat{z} \left| f_- Y_1^0 \right\rangle \\
&\quad + \sqrt{\frac{2}{3}} \left\langle f_+ Y_1^0 \right| \hat{z} \left| f_+ Y_0^0 \right\rangle, \qquad (3.31)
\end{aligned}$$

$$\begin{aligned}\left\langle \Phi^{\kappa=2}_{\frac{3}{2},-\frac{1}{2}} \left|\hat{r}_-\right| \Phi^{\kappa=1}_{\frac{1}{2},+\frac{1}{2}} \right\rangle &\overset{\sigma^-}{=} \sqrt{\frac{3}{15}} \left\langle f_- Y_2^{-1} \right| \hat{r}_- \left| f_- Y_1^0 \right\rangle \\ &+\sqrt{\frac{4}{15}} \left\langle f_- Y_2^{0} \right| \hat{r}_- \left| f_- Y_1^1 \right\rangle \\ &+\sqrt{\frac{1}{3}} \left\langle f_+ Y_1^{-1} \right| \hat{r}_- \left| f_+ Y_0^0 \right\rangle , \qquad (3.32)\\ \left\langle \Phi^{\kappa=2}_{\frac{3}{2},+\frac{1}{2}} \left|\hat{r}_+\right| \Phi^{\kappa=1}_{\frac{1}{2},-\frac{1}{2}} \right\rangle &\overset{\sigma^+}{=} \sqrt{\frac{4}{15}} \left\langle f_- Y_2^{0} \right| \hat{r}_+ \left| f_- Y_1^{-1} \right\rangle \\ &+\sqrt{\frac{3}{15}} \left\langle f_- Y_2^{1} \right| \hat{r}_+ \left| f_- Y_1^0 \right\rangle \\ &+\sqrt{\frac{1}{3}} \left\langle f_+ Y_1^{1} \right| \hat{r}_+ \left| f_+ Y_0^0 \right\rangle , \qquad (3.33)\end{aligned}$$

$$\begin{aligned}\left\langle \Phi^{\kappa=2}_{\frac{3}{2},+\frac{3}{2}} \left|\hat{r}_+\right| \Phi^{\kappa=1}_{\frac{1}{2},+\frac{1}{2}} \right\rangle &\overset{\sigma^+}{=} \sqrt{\frac{1}{15}} \left\langle f_- Y_2^{1} \right| \hat{r}_+ \left| f_- Y_1^0 \right\rangle \\ &+\sqrt{\frac{8}{15}} \left\langle f_- Y_2^{2} \right| \hat{r}_+ \left| f_- Y_1^1 \right\rangle \\ &+ \left\langle f_+ Y_1^{1} \right| \hat{r}_+ \left| f_+ Y_0^0 \right\rangle , \qquad (3.34)\\ \left\langle \Phi^{\kappa=2}_{\frac{3}{2},-\frac{3}{2}} \left|\hat{r}_-\right| \Phi^{\kappa=1}_{\frac{1}{2},-\frac{1}{2}} \right\rangle &\overset{\sigma^-}{=} \sqrt{\frac{8}{15}} \left\langle f_- Y_2^{-2} \right| \hat{r}_- \left| f_- Y_1^{-1} \right\rangle \\ &+\sqrt{\frac{1}{15}} \left\langle f_- Y_2^{-1} \right| \hat{r}_- \left| f_- Y_1^0 \right\rangle \\ &+ \left\langle f_+ Y_1^{-1} \right| \hat{r}_- \left| f_+ Y_0^0 \right\rangle , \qquad (3.35)\end{aligned}$$

where $\sigma_+ = \left(\sigma_x + i\sigma_y\right)/\sqrt{2} = \begin{pmatrix} 0 & \sqrt{2} \\ 0 & 0 \end{pmatrix}$, $\sigma_- = \left(\sigma_x - i\sigma_y\right)/\sqrt{2} = \begin{pmatrix} 0 & 0 \\ \sqrt{2} & 0 \end{pmatrix}$, and the normalization and orthogonality condition $\int\limits_{\Omega} d\Omega Y^{*m',l'}\left(\Omega\right) Y^{m,l}\left(\Omega\right) = \delta_{l'l}\delta_{m'm}$ have been used. All other matrix elements are zero.

The transition energy difference between the states $\kappa = 1$ (at point C) and $\kappa = 2$ (at point B) is $0.43\Delta_o$ and $1.39\Delta_o$ within the same energy solution and between the negative and positive energy solutions, respectively (see Figure 3.4). For $\Delta_o = 93.5$ meV (half of the band gap of PbTe), the corresponding wavelengths are $31\,\mu m$ and $9.5\,\mu m$. Consider the transitions as shown in Figure 4.5. We find that the z-component of the matrix element gives rise to π-transitions with $\kappa = 2,\, m_j = 1/2 \longleftrightarrow \kappa = 2,\, m_j = 1/2$ and with $\kappa = 2,\, m_j = -1/2 \longleftrightarrow \kappa = 1, m_j = -1/2)$. Thus, these π-transitions are coupled to light polarized linearly in z-direction. The $x - iy$- and $x + iy$-components of the matrix element give rise to the σ^+ transition with $\kappa = 2,\; m_j = +1/2 \longleftrightarrow \kappa = 1,\; m_j = -1/2$ and with $\kappa = 2,\; m_j = 3/2 \longleftrightarrow \kappa = 1,\; m_j = 1/2$ and to the σ^- transition with $\kappa = 2,\; m_j = -1/2 \longleftrightarrow \kappa = 1,\; m_j = +1/2$ and with $\kappa = 2, m_j = -3/2 \longleftrightarrow \kappa = 1, m_j = -1/2$. Thus, σ^+ and σ^- transitions couple to the components of corresponding circular polarization of the light. We can take advantage of these strict optical selection rules to implement the semi-classical and quantum Faraday effect shown below. The overlap integrals $\langle f_+ \left(\kappa = 2\right) \mid f_- \left(\kappa = 1\right)\rangle$ and $\langle f_- \left(\kappa = 2\right) \mid f_+ \left(\kappa = 1\right)\rangle$ for the transitions between the points B and C are evaluated to be 0.31 and 0.24, respectively. The Kane energy, $E_p = 2P_\perp^2/m_o$, is calculated to be 7.3 eV which is about 3 times smaller than the Kane energy value of 22.7 eV for GaAs.[115, 116] The smaller Kane energy here is due to the fact that the Fermi velocity is an order of magnitude smaller than the Fermi velocity in GaAs. The polarization matrix elements of $\hat{r}_\mp$ accounts for the strength of the in-plane intraband transitions at the band crossing. We calculate the magnitude of the matrix elements for $\sigma^\mp$ transitions and find that $e\left|\left\langle \Phi^{\kappa=2}_{\frac{3}{2},-\frac{1}{2}} \left|\hat{r}_-\right| \Phi^{\kappa=1}_{\frac{1}{2},+\frac{1}{2}} \right\rangle\right| = e\left|\left\langle \Phi^{\kappa=2}_{\frac{3}{2},+\frac{1}{2}} \left|\hat{r}_+\right| \Phi^{\kappa=1}_{\frac{1}{2},-\frac{1}{2}} \right\rangle\right| = 128$ Debye and $e\left|\left\langle \Phi^{\kappa=2}_{\frac{3}{2},+\frac{3}{2}} \left|\hat{r}_+\right| \Phi^{\kappa=1}_{\frac{1}{2},+\frac{1}{2}} \right\rangle\right| = e\left|\left\langle \Phi^{\kappa=2}_{\frac{3}{2},-\frac{3}{2}} \left|\hat{r}_-\right| \Phi^{\kappa=1}_{\frac{1}{2},-\frac{1}{2}} \right\rangle\right| = 221$ Debye. For the π transitions we find the magnitude of the matrix elements as, $e\left|\left\langle \Phi^{\kappa=2}_{\frac{3}{2},+\frac{1}{2}} \left|\hat{z}\right| \Phi^{\kappa=1}_{\frac{1}{2},+\frac{1}{2}} \right\rangle\right| = e\left|\left\langle \Phi^{\kappa=2}_{\frac{3}{2},-\frac{1}{2}} \left|\hat{z}\right| \Phi^{\kappa=1}_{\frac{1}{2},-\frac{1}{2}} \right\rangle\right| = 181$ Debye.

3.5 Faraday Effect for 3D TI QDs

In Refs. [103, 104, **?**, 117, 118] we showed that the single-photon Faraday rotation cannot only be used for quantum spin memory but also for quantum teleportation and quantum computing with wide-bandgap semiconductor QDs. In Ref. citeThompson:2009 we showed that the conditional Faraday rotation can be used for optical switching of classical information. In Ref. [119] we proposed a single-photon Mach-Zehnder interferometer for quantum networks based on the single-photon Faraday effect. In Ref. [120] a single spin in a wide-bandgap semiconductor QD was detected using the Faraday rotation. In order to implement these applications with 3D TI QDs, we need strict optical selection rules for the circular polarization of the photons. Since, indeed, for 3D TI QDs we obtain strict optical selection rules for circular polarization of photons, we suggest that it is possible to implement quantum memory, quantum teleportation and quantum computing using the single-photon Faraday rotation in 3D TI QDs. In order to prove this conjecture, we derive the Faraday effect for 3D TI QDs. For the derivation of the Faraday effect for a classical laser beam due to Pauli exclusion principle we are going to follow Ref. [**?**]. In Sec. 3.7 we are going to derive also the Faraday effect for a single photon using quantum optical calculations, where we use Ref. [121].

In order to simplify the notation, we write the light-matter interaction Hamiltonian as $H_{int} = ev\boldsymbol{\alpha} \cdot \boldsymbol{A} - e\hat{\mathbf{r}} \cdot \mathbf{E}$. Without loss of generality, the anisotropy coming from the band velocity can be introduced back into the solutions at a later time. Since the incident light is a plane wave with wavevector $\mathbf{q}$ and frequency ω and the electric field component is $E = -\partial \boldsymbol{A}/\partial t$, the interaction Hamiltonian reads

$$\begin{aligned} H_{int} &= \frac{ePE_0}{im_0\omega}\left(e^{i(\mathbf{q}\cdot\mathbf{r}-\omega t)} - e^{-i(\mathbf{q}\cdot\mathbf{r}-\omega t)}\right)\boldsymbol{e}\cdot\boldsymbol{\alpha} \\ &\quad -eE_0\left(e^{i(\mathbf{q}\cdot\mathbf{r}-\omega t)} + e^{-i(\mathbf{q}\cdot\mathbf{r}-\omega t)}\right)\boldsymbol{e}\cdot\hat{\mathbf{r}} \end{aligned} \tag{3.36}$$

where $P = m_0 v$ is the Kane interband matrix element. The transition rate for a single 3D TI QD can then be calculated using Fermi's golden rule,

$$\begin{aligned} W_{fI} &= \frac{2\pi}{\hbar}\left(eE_0\right)^2 \left|\langle\Phi_f|\,\frac{P}{im_0\omega}\boldsymbol{e}\cdot\boldsymbol{\alpha} + \boldsymbol{e}\cdot\hat{\mathbf{r}}\,|\Phi_I\rangle\right|^2 \\ &\quad \times f\left(\varepsilon_I\right)\left[1 - f\left(\varepsilon_f\right)\right]\delta\left(\varepsilon_f - \varepsilon_I \mp \hbar\omega\right) \end{aligned} \tag{3.37}$$

where $f\left(\varepsilon\right) = \left[\exp\left(\frac{\varepsilon-\varepsilon_F}{k_B T}\right) + 1\right]$ is the Fermi-Dirac distribution function, ε_F is the Fermi energy, $|\Phi_I\rangle$ denotes the initial Weyl state, $|\Phi_f\rangle$ denotes the final Weyl state, and the - sign in front of $\hbar\omega$ corresponds to absorption and the + sign to emission. Thus, the absorption of energy per spin state is $\mathcal{P} = \hbar\omega\sum_{I,f} W_{fI}$. Comparing with the total power $\mathcal{P} = 2\sigma_1 V E_0^2$ dissipated in the system of volume V, where $\sigma = \sigma_1 + i\sigma_2$ is the complex conductivity, and including absorption and emission, it follows that the real part of the conductivity is given by

$$\begin{aligned} \sigma_1 &= \frac{\pi e^2\omega}{V}\sum_{I,f}\left|\langle\Phi_f|\,\frac{P}{im_0\omega}\boldsymbol{e}\cdot\boldsymbol{\alpha} + \boldsymbol{e}\cdot\hat{\mathbf{r}}\,|\Phi_I\rangle\right|^2 \\ &\quad \times\left[f\left(\varepsilon_I\right) - f\left(\varepsilon_f\right)\right]\delta\left(\varepsilon_f - \varepsilon_I - \hbar\omega\right) \end{aligned} \tag{3.38}$$

which can be written in terms of the oscillator strengths

$f_{fI} = (2m_0\omega_{fI}/\hbar)\left|\langle\Phi_f|\,\frac{P}{im_0\omega}\boldsymbol{e}\cdot\boldsymbol{\alpha}+\boldsymbol{e}\cdot\hat{\mathbf{r}}\,|\Phi_I\rangle\right|^2$ as

$$\sigma_1(\omega) = \frac{\pi e^2}{2m_0 V}\sum_{fI} f_{fI}\left[f(\varepsilon_I) - f(\varepsilon_f)\right]\delta(\varepsilon_f - \varepsilon_I - \hbar\omega) \tag{3.39}$$

Using the relation $\epsilon_r = 1 + \frac{i}{\omega\epsilon_0}\sigma$, where ϵ_0 is the free-space permittivity, between the complex conductivity and the complex dielectric function $\epsilon_r = \epsilon_1 + i\epsilon_2$ and taking advantage of the Kramers-Kronig relations the complex dielectric function is given by

$$\epsilon_r(\omega) = 1 - \frac{e^2}{\epsilon_0 m_0 V}\sum_{fI}\frac{f_{fI}\left[f(\varepsilon_I) - f(\varepsilon_f)\right]}{\left(\omega^2 - \omega_{fI}^2\right) + i\gamma\omega} \tag{3.40}$$

In order to describe the Faraday rotation, we need to consider only the states $\left|\Phi^{\kappa=1}_{\frac{1}{2},\pm\frac{1}{2}}\right\rangle$, $\left|\Phi^{\kappa=2}_{\frac{3}{2},\pm\frac{1}{2}}\right\rangle$, and $\left|\Phi^{\kappa=2}_{\frac{3}{2},\pm\frac{3}{2}}\right\rangle$ coupled by circular polarized light (see Figure 3.5). We denote their energy difference by $\hbar\omega_0 = \varepsilon_{\kappa=2} - \varepsilon_{\kappa=1}$. Defining the the quantity

$$\begin{aligned} M_{f;I} &= \left|\left\langle\Phi^{\kappa=2}_f\right|\frac{P}{im_0\omega}\boldsymbol{e}\cdot\boldsymbol{\alpha}+\boldsymbol{e}\cdot\hat{\mathbf{r}}\left|\Phi^{\kappa=1}_I\right\rangle\right|^2 \\ &\quad \times\left[f(\varepsilon_I) - f(\varepsilon_f)\right] \end{aligned} \tag{3.41}$$

we can rewrite the complex dielectric function as

$$\begin{aligned} \epsilon_r(\omega) &= \epsilon_{QD}(\omega) - \frac{2e^2\rho\omega}{\epsilon_0\hbar}\left\{\frac{M_{\frac{3}{2},+\frac{3}{2};\frac{1}{2},+\frac{1}{2}} + M_{\frac{3}{2},-\frac{3}{2};\frac{1}{2},-\frac{1}{2}}}{(\omega^2-\omega_0^2)+i\gamma\omega}\right. \\ &\quad \left. + \frac{M_{\frac{3}{2},+\frac{1}{2};\frac{1}{2},-\frac{1}{2}} + M_{\frac{3}{2},-\frac{1}{2};\frac{1}{2},+\frac{1}{2}}}{[\omega^2 - (\omega_0 + \Delta_S/\hbar)^2] + i\gamma\omega}\right\} \end{aligned} \tag{3.42}$$

where Δ_S is the Stark energy shift (see below) and γ is the line boardening. Summation over the other states is included in $\epsilon_{QD}(\omega)$, which is the dielectric function of $\mathrm{Pb_{0.63}Sn_{0.37}Te}$, corresponding to the material at the interface. $\rho = 1/V$ is the 3D TI QD density. This expression can be split into a component of the dielectric function for the σ^+ polarization,

$$\begin{aligned}\epsilon_+(\omega) &= \epsilon_{QD}(\omega) - \frac{2e^2\rho\omega}{\epsilon_0\hbar}\left\{\frac{M_{\frac{3}{2},+\frac{3}{2};\frac{1}{2},+\frac{1}{2}}}{(\omega^2-\omega_0^2)+i\gamma\omega}\right. \\ &\qquad \left. + \frac{M_{\frac{3}{2},+\frac{1}{2};\frac{1}{2},-\frac{1}{2}}}{[\omega^2-(\omega_0+\Delta_S/\hbar)^2]+i\gamma\omega}\right\} \end{aligned} \tag{3.43}$$

and a component of the dielectric function for the σ^- polarization,

$$\begin{aligned}\epsilon_-(\omega) &= \epsilon_{QD}(\omega) - \frac{2e^2\rho\omega}{\epsilon_0\hbar}\left\{\frac{M_{\frac{3}{2},-\frac{3}{2};\frac{1}{2},-\frac{1}{2}}}{(\omega^2-\omega_0^2)+i\gamma\omega}\right. \\ &\qquad \left. + \frac{M_{\frac{3}{2},-\frac{1}{2};\frac{1}{2},+\frac{1}{2}}}{[\omega^2-(\omega_0+\Delta_S/\hbar)^2]+i\gamma\omega}\right\} \end{aligned} \tag{3.44}$$

Consequently, the indices of refraction for $\sigma^\pm$ polarizations of the light are given by $n_\pm = \sqrt{\epsilon_\pm}$. Assuming that the length of the material is L, the Faraday rotation can now be understood by considering the electric component of the plane wave after passing through the material at position $z = L$,

$$\begin{aligned}\mathbf{E}(z=L) &= \frac{E_0}{\sqrt{2}}\left(e^{ik_-L}\mathbf{e}_+ + e^{ik_+L}\mathbf{e}_-\right)e^{-i\omega t} \\ &= E_0\left(\cos\frac{\Delta n\omega L}{c}\mathbf{e}_x + \sin\frac{\Delta n\omega L}{c}\mathbf{e}_y\right) \\ &\quad \times e^{i\left(kL-\omega t+(n-1)\frac{\omega L}{c}\right)} \end{aligned} \tag{3.45}$$

where $\mathbf{e}_\pm = (\mathbf{e}_x \pm i\mathbf{e}_y)/\sqrt{2}$ are the circular polarization unit vectors, $n = (n_+ + n_-)/2$ is the average index of refraction, c is the speed of light in vacuum, and $\Delta n = n_+ - n_-$ is the difference in index of refraction between σ^+ and σ^- circular polarization. Thus, the Faraday rotation angle is given by

$$\vartheta = \frac{\Delta n\omega L}{2c}. \tag{3.46}$$

This formula shows that the Faraday rotation angle depends on the populations of the states $\left|\Phi^{\kappa=1}_{\frac{1}{2},\pm\frac{1}{2}}\right\rangle$, $\left|\Phi^{\kappa=2}_{\frac{3}{2},\pm\frac{1}{2}}\right\rangle$, and $\left|\Phi^{\kappa=2}_{\frac{3}{2},\pm\frac{3}{2}}\right\rangle$, as determined by the Fermi functions, which can be used in the quasi-equilibrium, i.e. when the time is much smaller than the electron-hole recombination time. A similar Faraday effect has already been successfully used to experimentally detect a single spin inside a GaAs QD.[120]

3.6 Quantum Memory with 3D TI QDs

Let us first describe the quantum memory with 3D TI QDs. In order to obtain the maximum Faraday effect, it is possible to apply an oscillating electric field $\mathbf{E}(t)$ pointing in z-direction, which splits the $\left|\Phi^{\kappa=2}_{\frac{3}{2},\pm\frac{1}{2}}\right\rangle$ states from the $\left|\Phi^{\kappa=2}_{\frac{3}{2},\pm\frac{3}{2}}\right\rangle$ states due to the optical Stark effect (see Figure 3.6). The coupling to the electric field is described by the relativistic Stark Hamiltonian

$$H_S = \begin{pmatrix} -ezE_z e^{i\omega_S t} & ev_\parallel \sigma_z A_z \\ ev_\parallel \sigma_z A_z & -ezE_z e^{i\omega_S t} \end{pmatrix}, \tag{3.47}$$

where $E_z(t) = E_S\left(e^{i\omega_S t} + e^{-i\omega_S t}\right)$ and thus $A_z(t) = \frac{iE_S}{\omega_S}\left(e^{i\omega_S t} - e^{-i\omega_S t}\right)$. In second-order perturbation theory we obtain the quadratic Stark effect. The only nonzero contributions come from the matrix element coupling the $\left|\Phi^{\kappa=2}_{\frac{3}{2},+\frac{1}{2}}\right\rangle$ state to the $\left|\Phi^{\kappa=1}_{\frac{1}{2},+\frac{1}{2}}\right\rangle$ state, and from the matrix element coupling the$\left|\Phi^{\kappa=2}_{\frac{3}{2},-\frac{1}{2}}\right\rangle$ state to the $\left|\Phi^{\kappa=1}_{\frac{1}{2},-\frac{1}{2}}\right\rangle$ state. This yields the Stark energy shift

$$\begin{aligned}\Delta_S &= e^2 E_S^2 \frac{\left|\left\langle \Phi^{\kappa=1}_{\frac{1}{2},+\frac{1}{2}} \right| \frac{P}{im_0\omega_S}\alpha_z + z \left| \Phi^{\kappa=2}_{\frac{3}{2},+\frac{1}{2}} \right\rangle\right|^2}{\hbar(\omega_0-\omega_S)} \\ &= e^2 E_S^2 \frac{\left|\left\langle \Phi^{\kappa=1}_{\frac{1}{2},-\frac{1}{2}} \right| \frac{P}{im_0\omega_S}\alpha_z + z \left| \Phi^{\kappa=2}_{\frac{3}{2},-\frac{1}{2}} \right\rangle\right|^2}{\hbar(\omega_0-\omega_S)} \end{aligned} \tag{3.48}$$

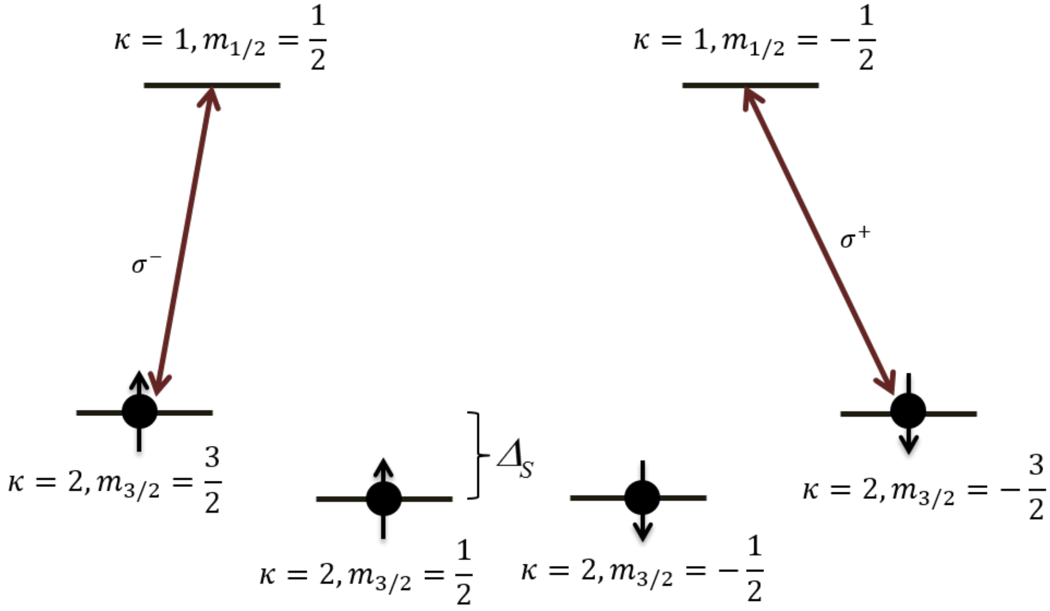
$\kappa = 1, m_{1/2} = \frac{1}{2}$
$\kappa = 1, m_{1/2} = -\frac{1}{2}$
σ^-
σ^+
Δ_S
$\kappa = 2, m_{3/2} = \frac{3}{2}$
$\kappa = 2, m_{3/2} = \frac{1}{2}$
$\kappa = 2, m_{3/2} = -\frac{1}{2}$
$\kappa = 2, m_{3/2} = -\frac{3}{2}$

Figure 3.6: This is one possible level configuration that can be used for the implementation of the quantum memory.

The Stark energy shift can be determined by applying an oscillating electric field whose amplitude is measured along z-direction. The amplitude of the electric field can be calculated as $|E_S| = \sqrt{2\mathcal{S}n/A\epsilon_o c}$, where $\mathcal{S}$ is the power of the laser, n is the index of refraction of the medium through which the light propagates and A is the area of the aperture of the laser source. A laser power of 50 mW with energy $\hbar\omega_S = 30\,meV$ and area of the aperture of $1\,\mu m^2$ in a medium with $n = 5.7$ (for $\mathrm{Pb_{0.68}Sn_{0.32}Te}$ at room temperature) can produce an electric field of 1.46×10^7 V/m. Using the Fermi velocity of $v_\parallel = 2.24 \times 10^5$ m/s to calculate P, our calculations show that the matrix element in Eq. (4.39) is $e\left|\left\langle \Phi^{\kappa=1}_{\frac{1}{2},+\frac{1}{2}} \right| \frac{P}{im_0\omega_S}\alpha_z + z \left| \Phi^{\kappa=2}_{\frac{3}{2},+\frac{1}{2}} \right\rangle\right| = 410$ Debye. With the transition energy difference of $\hbar\omega_0 = 130$ meV we get a Stark energy shift of $\Delta_S = 14$ meV.

It has already been shown experimentally that single-electron loading is possible in 3D TI QDs. [85] We focus on two possible level configurations due to the electron-hole symmetry in 3D TI QDs:

1. Figure 3.6 shows the first level configuration where the electron states are given by the s-like states $\left|\Phi^{\kappa=1}_{\frac{1}{2},\pm\frac{1}{2}}\right\rangle$ and the hole states are given by the p-like states $\left|\Phi^{\kappa=2}_{\frac{3}{2},\pm\frac{1}{2}}\right\rangle$ and $\left|\Phi^{\kappa=2}_{\frac{3}{2},\pm\frac{3}{2}}\right\rangle$.
2. Figure 3.7 shows the second level configuration where the electron states are given by the p-like states $\left|\Phi^{\kappa=2}_{\frac{3}{2},\pm\frac{1}{2}}\right\rangle$ and $\left|\Phi^{\kappa=2}_{\frac{3}{2},\pm\frac{3}{2}}\right\rangle$ and the hole states are given by the s-like states $\left|\Phi^{\kappa=1}_{\frac{1}{2},\pm\frac{1}{2}}\right\rangle$.

Only due to the symmetry between positive- and negative-energy solutions in a 3D TI QD it is possible to choose either of these two level configurations.

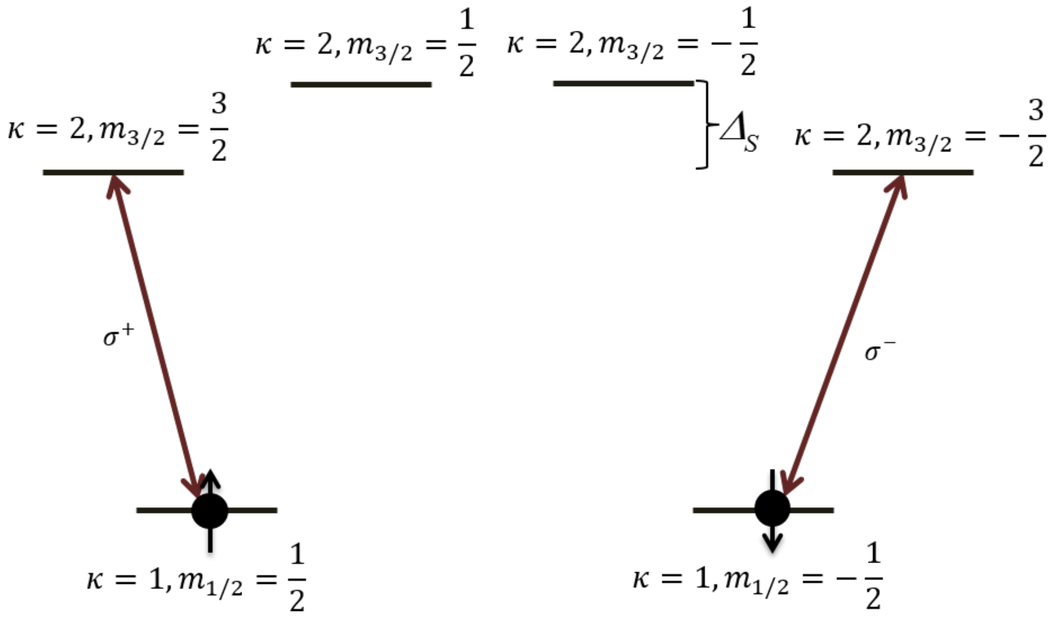
$\kappa = 2, m_{3/2} = \frac{1}{2}$
$\kappa = 2, m_{3/2} = -\frac{1}{2}$
$\kappa = 2, m_{3/2} = \frac{3}{2}$
Δ_S
$\kappa = 2, m_{3/2} = -\frac{3}{2}$
σ^+
σ^-
$\kappa = 1, m_{1/2} = \frac{1}{2}$
$\kappa = 1, m_{1/2} = -\frac{1}{2}$

Figure 3.7: This is another possible level configuration that can be used for the implementation of the quantum memory.

Then, using the optical selection rules shown in Figure 3.5, we can use σ^+ polarized light to create an e-h pair with polarization +1, as shown in Figure 3.6. This corresponds to writing the information +1 on the 3D TI QD. Alternatively, we can use σ^- circularly polarized light to create an e-h pair with polarization -1, as shown in Figure 3.6. This corresponds to writing the information -1 on the 3D TI QD.

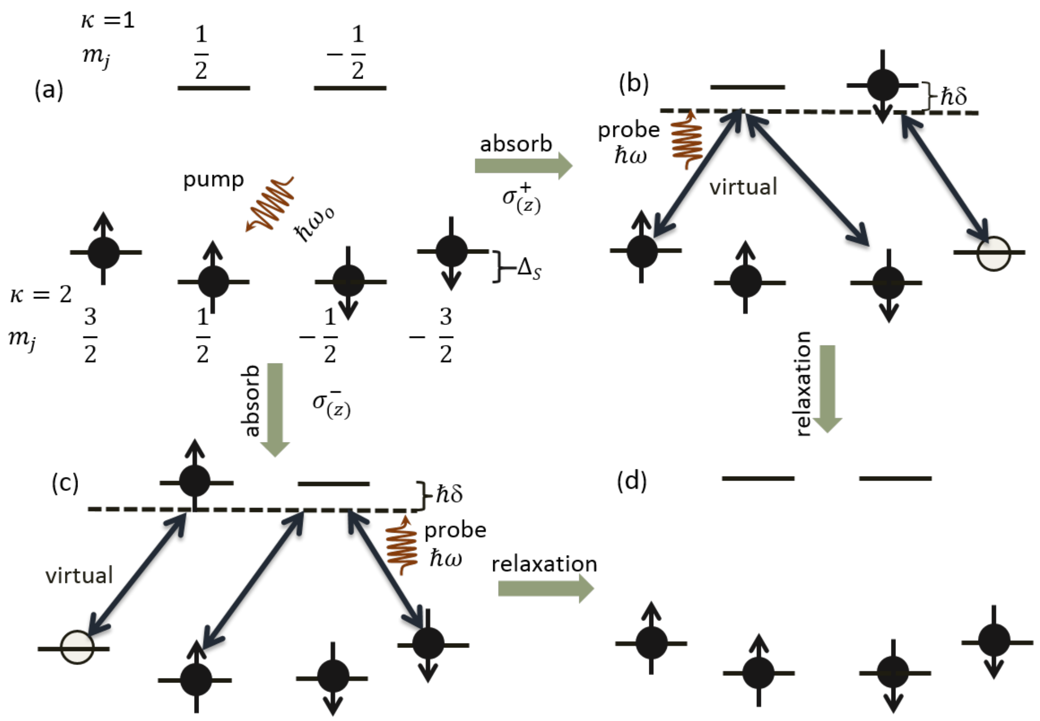
(a)
κ =1
m_j
1/2
−1/2
pump
ħω₀
κ = 2
m_j
3/2
1/2
−1/2
−3/2
Δ_S
absorb
σ⁺(z)
(b)
ħδ
probe
ħω
virtual
relaxation
absorb
σ⁻(z)
(c)
ħδ
virtual
probe
ħω
relaxation
(d)

Figure 3.8: (a) The incident photon can be either σ^+ or σ^- polarized. The initial level configuration is the one shown in Figure 3.6. (b) If the photon is σ^+ polarized, an e-h pair with +1 polarization is created, which can be probed using off-resonant linearly polarized light that acquires a negative Faraday rotation angle through virtual excitation of an e-h pair and virtual recombinations of the present e-h pair. (c) If the photon is σ^- polarized, an e-h pair with -1 polarization is created, which can be probed using off-resonant linearly polarized light that acquires a positive Faraday rotation angle through virtual excitation of an e-h pair and virtual recombinations of the present e-h pair. (d) After the probing, the e-h pair relaxes into the ground state configuration.

If we want to read out the information several times before the electron-hole recombination, we can take advantage of the Faraday effect due to the Pauli exclusion principle. For this method, we apply a π-pulse of circularly polarized light, thereby writing the information +1 or -1 as shown in Figure 3.8. For +1 polarization, the Fermi functions, corresponding to populations in quasi-equilibrium, are $f\left(\varepsilon_{\frac{1}{2},+\frac{1}{2}}\right) = 0$, $f\left(\varepsilon_{\frac{1}{2},-\frac{1}{2}}\right) = 1$, $f\left(\varepsilon_{\frac{3}{2},+\frac{3}{2}}\right) = 1$, $f\left(\varepsilon_{\frac{3}{2},+\frac{1}{2}}\right) = 1$, $f\left(\varepsilon_{\frac{3}{2},-\frac{1}{2}}\right) = 1$ and $f\left(\varepsilon_{\frac{3}{2},-\frac{3}{2}}\right) = 0$. For -1 polarization, the Fermi functions, corresponding to populations in quasi-equilibrium, are $f\left(\varepsilon_{\frac{1}{2},+\frac{1}{2}}\right) = 1$, $f\left(\varepsilon_{\frac{1}{2},-\frac{1}{2}}\right) = 0$, $f\left(\varepsilon_{\frac{3}{2},+\frac{3}{2}}\right) = 0$, $f\left(\varepsilon_{\frac{3}{2},+\frac{1}{2}}\right) = 1$ $f\left(\varepsilon_{\frac{3}{2},-\frac{1}{2}}\right) = 1$ and $f\left(\varepsilon_{\frac{3}{2},-\frac{3}{2}}\right) = 1$. Since the off-resonant interaction does not destroy the quantum state on the 3D TI QD, the information can be read out several times before recombination. These results are in complete agreement with the quantum-optical calculations shown below.

Let us assume that σ^+ polarized pump pulse of energy $\hbar\omega_0$ excites an e-h pair with polarization +1 from the state $\left|\Phi^{\kappa=2}_{\frac{3}{2},-\frac{3}{2}}\right\rangle$ to the state $\left|\Phi^{\kappa=1}_{\frac{1}{2},-\frac{1}{2}}\right\rangle$ in the level configuration shown in Figure 3.6. Then a linearly polarized probe pulse of energy $\hbar\omega$ with certain detuning energy is applied to read it out. There are three virtual transitions that can occur while probing, one σ^- transition: $\left|\Phi^{\kappa=2}_{\frac{3}{2},\frac{3}{2}}\right\rangle \longleftrightarrow \left|\Phi^{\kappa=1}_{\frac{1}{2},+\frac{1}{2}}\right\rangle$ and two σ^+ transitions: $\left|\Phi^{\kappa=1}_{\frac{3}{2},-\frac{3}{2}}\right\rangle \longleftrightarrow \left|\Phi^{\kappa=2}_{\frac{1}{2},-\frac{1}{2}}\right\rangle$ and $\left|\Phi^{\kappa=2}_{\frac{3}{2},-\frac{1}{2}}\right\rangle \longleftrightarrow \left|\Phi^{\kappa=1}_{\frac{1}{2},+\frac{1}{2}}\right\rangle$. The matrix elements are evaluated to be $M_{\frac{3}{2},\pm\frac{3}{2};\frac{1}{2},\pm\frac{1}{2}} = \mp 8.07 \times 10^{-18}$ m^2 and $M_{\frac{3}{2},-\frac{1}{2};\frac{1}{2},+\frac{1}{2}} = -2.67 \times 10^{-18}$ m^2. The sign of the matrix elements $M_{f,I}$ is determined by the Fermi functions. The corresponding dipole moments are 454 Debye and 261 Debye. For a quantitative estimate, we choose a transition energy gap between the negative and positive energy solution of $\hbar\omega_o = 130\, meV$, a linearly polarized probe pulse with detuning energy of $\hbar\delta = 1$ meV and a cavity photon with a bandwidth of $\hbar\gamma = 100\,\mu$eV.[122, 120] We further assume that there is a single QD in a slab material of length $L = 0.1\,\mu$m. With these values for our 3D TI QD of size 3.5 nm we obtain the real part of the Faraday rotation angle of $\vartheta_{+1} = -624\,\mu$rad. This Faraday rotation angle is well above the angle value that has been measured for the experimental detection of a single spin in GaAs QDs.[120] A similar calculation can be done for σ^- polarized pump pulse that excites an e-h pair with polarization -1 from the state $\left|\Phi^{\kappa=2}_{\frac{3}{2},+\frac{3}{2}}\right\rangle$ to the state $\left|\Phi^{\kappa=1}_{\frac{1}{2},+\frac{1}{2}}\right\rangle$. Due to the symmetry of the positive- and negative-energy solutions in 3D TI QDs, a large variety of level configurations can be considered to achieve the Faraday effect.

The largest dipole moment of 452 Debye is one order of magnitude larger than the typical value of 75 Debye for GaAs QDs,[123] and two orders of magnitude larger than the typical value of a few Debye for atoms.[124] This large strength of the coupling of infrared light to 3D TI QDs can partially compensate the weak overlap of the photon with the 3D TI QD, which is due to the wavelength of the infrared light being so much larger than the size of the 3D TI QD.

3.7 Single-Photon Faraday Effect for 3D TI QDs

Let us consider a 3D TI QD in the level configuration shown in Figure 3.6 inside a cavity. We define $c_{1\pm}$, $c_{2\pm}$ and $c_{3\pm}$ as the annihilation operators of the states $\left|\Phi^{\kappa=2}_{\frac{3}{2},\pm\frac{1}{2}}\right\rangle$, $\left|\Phi^{\kappa=2}_{\frac{3}{2},\pm\frac{3}{2}}\right\rangle$, and $\left|\Phi^{\kappa=1}_{\frac{1}{2},\pm\frac{1}{2}}\right\rangle$, respectively. Then the Jaynes-Cummings model[121] gives rise to the

Hamiltonian $H = H_p + H_{QD} + H_{p-QD}$, where

$$\begin{aligned}
H_p &= \hbar\omega_c \left(a_+^\dagger a_+ + a_-^\dagger a_-\right), && (3.49)\\
H_{QD} &= \sum_{j=1}^{3} \hbar\omega_j \left(c_{j+}^\dagger c_{j+} + c_{j-}^\dagger c_{j-}\right), &&\\
H_{p-QD} &= \hbar g_1 \left(a_+ c_{3+}^\dagger c_{1-} + a_- c_{3-}^\dagger c_{1+}\right) + h.c. && (3.50)\\
&\quad +\hbar g_2 \left(a_+ c_{3-}^\dagger c_{2-} + a_- c_{3+}^\dagger c_{2+}\right) + h.c., && (3.51)
\end{aligned}$$

are the cavity photon Hamiltonian, the QD Hamiltonian describing the Weyl states, and the interaction Hamiltonian describing the photon-QD interaction, respectively. We can safely neglect the vacuum energy $\hbar\omega_c/2$ per mode. The photon-QD coupling constants are given by $\hbar g_1 = \sqrt{\hbar\omega/2\epsilon_0 V_0}\, e \left\langle \Phi^{\kappa=2}_{\frac{3}{2},\pm\frac{1}{2}} \middle| \frac{P}{im_0\omega}\boldsymbol{e}\cdot\boldsymbol{\alpha}+\boldsymbol{e}\cdot\hat{\mathbf{r}} \middle| \Phi^{\kappa=1}_{\frac{1}{2},\mp\frac{1}{2}} \right\rangle$ and $\hbar g_2 = \sqrt{\hbar\omega/2\epsilon_0 V_0}\, e \left\langle \Phi^{\kappa=2}_{\frac{3}{2},\pm\frac{3}{2}} \middle| \frac{P}{im_0\omega}\boldsymbol{e}\cdot\boldsymbol{\alpha}+ \boldsymbol{e}\cdot\hat{\mathbf{r}} \middle| \Phi^{\kappa=1}_{\frac{1}{2},\pm\frac{1}{2}} \right\rangle$, where V_0 is the modal volume. After switching to the electron-hole picture using the new electron and hole operators $c_\pm = c_{3\pm}$ and $v_{j\mp}^\dagger = c_{j\pm}$ for $j = 1, 2$, we obtain

$$\begin{aligned}
H_p &= \hbar\omega_c \left(a_+^\dagger a_+ + a_-^\dagger a_-\right), && (3.52)\\
H_{QD} &= \hbar\omega_3 \left(c_+^\dagger c_+ + c_-^\dagger c_-\right) + \sum_{j=1}^{2} \hbar\omega_j \left(v_{j+}^\dagger v_{j+} + v_{j-}^\dagger v_{j-}\right), && (3.53)\\
H_{int} &= \hbar g_1 \left(a_+ c_+^\dagger v_{1+}^\dagger + a_- c_-^\dagger v_{1-}^\dagger\right) + h.c. && (3.54)\\
&\quad +\hbar g_2 \left(a_+ c_-^\dagger v_{2+}^\dagger + a_- c_+^\dagger v_{2-}^\dagger\right) + h.c. && (3.55)
\end{aligned}$$

where $\hbar\omega_3 - \hbar\omega_2 = \hbar\omega_c + \hbar\delta$ and $\hbar\omega_2 - \hbar\omega_1 = \Delta_S$. Since the interaction between the EM fields and the QDs is off-resonant, we can apply an adiabatic approximation. For that, let us calculate the time evolution of the polarization operators $p_{j\sigma\sigma'}(t) = v_{j\sigma} c_{\sigma'}$ (coherences) by means of the Heisenberg equation of motion, i.e.

$$\frac{\partial p_{j\sigma\sigma'}(t)}{\partial t} = \frac{1}{i\hbar}\left[p_{j\sigma\sigma'}(t), H\right] = \frac{1}{i\hbar}\left[p_{j\sigma\sigma'}(t), H_{QD} + H_{int}\right] \tag{3.56}$$

Since

$$\begin{aligned}
\left[p_{j\sigma\sigma'}, p^{\dagger}_{\lambda j'\lambda'}\right] &= v_{j\sigma}v^{\dagger}_{j'\lambda'}\delta_{\sigma'\lambda} - c^{\dagger}_{\lambda}c_{\sigma'}\delta_{jj'}\delta_{\sigma\lambda'} \\
&= \left(1 - v^{\dagger}_{j'\lambda'}v_{j\sigma}\right)\delta_{\sigma'\lambda} - c^{\dagger}_{\lambda}c_{\sigma'}\delta_{jj'}\delta_{\sigma\lambda'}
\end{aligned} \tag{3.57}$$

and

$$\begin{aligned}
\left[p_{j\sigma\sigma'}, c^{\dagger}_{\lambda}c_{\lambda}\right] &= p_{j\sigma\lambda}\delta_{\sigma'\lambda} \\
\left[p_{j\sigma\sigma'}, v^{\dagger}_{j'\lambda}v_{j'\lambda}\right] &= p_{j'\lambda\sigma'}\delta_{jj'}\delta_{\sigma\lambda}
\end{aligned} \tag{3.58}$$

we obtain

$$\begin{aligned}
i\frac{\partial p_{1\pm\pm}}{\partial t} &= \left(\omega_c + \delta + \frac{\Delta_S}{\hbar}\right)p_{1\pm\pm} \\
&\quad + g_1 a_{\pm}\left(1 - c^{\dagger}_{\pm}c_{\pm} - v^{\dagger}_{1\pm}v_{1\pm}\right) \\
&\quad + g_2 a_{\mp}\left(1 - v^{\dagger}_{2\mp}v_{1\pm}\right),
\end{aligned} \tag{3.59}$$

$$\begin{aligned}
i\frac{\partial p_{2\pm\mp}}{\partial t} &= \left(\omega_c + \delta\right)p_{2\pm\mp} \\
&\quad + g_1 a_{\mp}\left(1 - v^{\dagger}_{1\mp}v_{2\pm}\right) \\
&\quad + g_2 a_{\pm}\left(1 - c^{\dagger}_{\mp}c_{\mp} - v^{\dagger}_{2\pm}v_{2\pm}\right),
\end{aligned} \tag{3.60}$$

where the + (-) sign denotes the components of the circular polarization. Since the states $\left|\Phi^{\kappa=2}_{\frac{3}{2},\pm\frac{1}{2}}\right\rangle$ and $\left|\Phi^{\kappa=2}_{\frac{3}{2},\pm\frac{3}{2}}\right\rangle$ are not resonantly coupled, no coherences $v_{2\pm}v^{\dagger}_{1\mp}$ and $v_{2\pm}v^{\dagger}_{1\mp}$ are created. Therefore they are zero. It is possible to transform to the rotating frame by means of

$\widetilde{p}_{1\pm\pm} = p_{1\pm\pm}e^{-i\omega_c t}$, $\widetilde{p}_{2\pm\mp} = p_{2\pm\pm}e^{-i\omega_c t}$ and $\widetilde{a}_{\pm} = a_{\pm}e^{-i\omega_c t}$, resulting in

$$\begin{aligned} i\frac{\partial p_{1\pm\pm}}{\partial t} &= \left(\delta + \frac{\Delta_S}{\hbar}\right) p_{1\pm\pm} \\ &\quad + g_1 a_{\pm}\left(1 - c_{\pm}^{\dagger}c_{\pm} - v_{1\pm}^{\dagger}v_{1\pm}\right), \qquad (3.61) \\ i\frac{\partial p_{2\pm\mp}}{\partial t} &= \delta p_{2\pm\mp} + g_2 a_{\pm}\left(1 - c_{\mp}^{\dagger}c_{\mp} - v_{2\pm}^{\dagger}v_{2\pm}\right), \qquad (3.62) \end{aligned}$$

where we omitted the tildes. The Heisenberg equations for the polarization operators $p_{1\pm\pm}^{\dagger}$ and $p_{2\pm\mp}^{\dagger}$ can be obtained by taking the Hermitian conjugate. Since in the case of the Faraday effect the photon is off-resonant with the energy difference $\hbar\omega_{21} = \hbar\omega_2 - \hbar\omega_1$, we can apply the adiabatic approximation, which corresponds to setting the time derivatives in the Heisenberg equations to zero, i.e. taking the stationary limit. Then we obtain

$$\begin{aligned} p_{1\pm\pm} &= -\frac{g_1 a_{\pm}\left(1 - c_{\pm}^{\dagger}c_{\pm} - v_{1\pm}^{\dagger}v_{1\pm}\right)}{\left(\delta + \frac{\Delta_S}{\hbar}\right)}, \qquad (3.63) \\ p_{2\pm\mp} &= -\frac{g_2 a_{\pm}\left(1 - c_{\mp}^{\dagger}c_{\mp} - v_{2\pm}^{\dagger}v_{2\pm}\right)}{\delta}. \qquad (3.64) \end{aligned}$$

Inserting this result into the interaction Hamiltonian leads to an effective interaction Hamiltonian of the form

$$\begin{aligned} H_{int}^{eff} &= -\frac{\hbar g_1^2}{\left(\delta + \frac{\Delta_S}{\hbar}\right)} \sum_{\sigma} \left(2a_{\sigma}^{\dagger}a_{\sigma} + 1\right)\left(1 - c_{\sigma}^{\dagger}c_{\sigma} - v_{1\sigma}^{\dagger}v_{1\sigma}\right) \\ &\quad -\frac{\hbar g_2^2}{\delta} \sum_{\sigma} \left(2a_{\sigma}^{\dagger}a_{\sigma} + 1\right)\left(1 - c_{\bar{\sigma}}^{\dagger}c_{\bar{\sigma}} - v_{1\sigma}^{\dagger}v_{1\sigma}\right), \qquad (3.65) \end{aligned}$$

where $\bar{\sigma}$ has the opposite sign of σ. It becomes obvious that if electrons or holes are present, the effective interaction can be suppressed. Most importantly, this suppression of interaction depends on the spin of the present electrons or holes. This is exactly the mechanism for the

Faraday effect due to Pauli exclusion principle. Let us now calculate the time evolution of the photon operator in the rotating frame under the effective interaction Hamiltonian, i.e.

$$\begin{aligned} i\hbar\frac{\partial a_\pm}{\partial t} &= \left[a_\pm, H_{int}^{eff}\right] \\ &= -2a_\pm\left[\left(\frac{\hbar g_1^2}{\delta+\frac{\Delta_S}{\hbar}}\right)\left(1-c_\pm^\dagger c_\pm - v_{1\pm}^\dagger v_{1\pm}\right)\right. \\ &\quad \left.+\left(\frac{\hbar g_2^2}{\delta}\right)\left(1-c_\mp^\dagger c_\mp - v_{2\pm}^\dagger v_{2\pm}\right)\right], \end{aligned} \tag{3.66}$$

resulting in the solution

$$\begin{aligned} a_\pm(t) &= a_\pm(0)\exp\left\{-i\left[\frac{2g_1^2}{\delta+\frac{\Delta_S}{\hbar}}\left(1-c_\pm^\dagger c_\pm - v_{1\pm}^\dagger v_{1\pm}\right)\right.\right. \\ &\quad \left.\left.+\ \frac{2g_2^2}{\delta}\left(1-c_\mp^\dagger c_\mp - v_{2\pm}^\dagger v_{2\pm}\right)\right]t\right\}. \end{aligned} \tag{3.67}$$

This formula is the main result of this section. It shows that the Faraday rotation of the linearly polarized light depends strongly on the presence of electrons and holes due to the Pauli exclusion principle.

3.8 Quantum Teleportation and Quantum Computing with 3D TI QDs

Here we show that the single-photon Faraday rotation can be used to entangle a single photon with either a single e-h pair, a single electron, or a single hole. This entanglement can be used as a resource to implement optically mediated quantum teleportation and quantum computing 3D TI QDs based on the Faraday effect due to the Pauli exclusion principle, where the qubit is defined as either the polarization of a single e-h pair, the spin of a single electron, or the spin of a single hole. The quantum-informational methods for the implementation of quantum teleportation and quantum computing are described in Refs. [103, 104]. We describe here the physical methods for creating the entanglement.

3.8.1 Photon polarization - e-h pair polarization entanglement

Let us consider now the Faraday effect due to an e-h pair on the QD for the level configuration shown in Figure 3.7. The initial state before the photon-QD interaction reads

$$\left|\psi_{\mp 1}(0)\right\rangle = \frac{1}{\sqrt{2}}\left(e^{-i\vartheta_0}a_+^\dagger + e^{i\vartheta_0}a_-^\dagger\right)c_\pm^\dagger v_{2\mp}^\dagger\left|0\right\rangle \tag{3.68}$$

where the photon is linearly polarized at an angle ϑ_0 from the x-axis. If the initial e-h pair is -1 polarized, then the state after time t is given by

$$\begin{aligned}\left|\psi_{-1}(t)\right\rangle &= \frac{1}{\sqrt{2}}\left(e^{-i(\vartheta_0+\vartheta_+)}a_+^\dagger(0) + e^{i(\vartheta_0+\vartheta_-)}a_-^\dagger(0)\right) \\ &\quad \times c_+^\dagger v_{2-}^\dagger\left|0\right\rangle &(3.69)\\ &= \frac{e^{-i\left(\frac{\vartheta_+-\vartheta_-}{2}\right)}}{\sqrt{2}}\left(e^{-i\left(\vartheta_0+\frac{\vartheta_++\vartheta_-}{2}\right)}a_+^\dagger(0)\right. \\ &\quad \left.+\,e^{i\left(\vartheta_0+\frac{\vartheta_++\vartheta_-}{2}\right)}a_-^\dagger(0)\right)c_+^\dagger v_{2-}^\dagger\left|0\right\rangle &(3.70)\end{aligned}$$

with $\vartheta_+(t) = -\frac{2g_2^2}{\delta}t$ and $\vartheta_-(t) = \left(\frac{2g_1^2}{\delta+\frac{\Delta_S}{\hbar}} - \frac{2g_2^2}{\delta}\right)t$, resulting in a Faraday rotation angle of $\vartheta_{-1}(t) = \left[\vartheta_+(t)+\vartheta_-(t)\right]/2 = -\left(\frac{2g_2^2}{\delta} - \frac{g_1^2}{\delta+\frac{\Delta_S}{\hbar}}\right)t$. If the initial e-h pair is $+1$ polarized, then the state after time t is given by

$$\begin{aligned}
|\psi_{+1}(t)\rangle &= \frac{1}{\sqrt{2}}\left(e^{-i(\vartheta_0+\vartheta_+(t))}a_+^\dagger(0)+e^{i(\vartheta_0+\vartheta_-(t))}a_-^\dagger(0)\right)\\
&\quad\times c_-^\dagger v_{2+}^\dagger\left|0\right\rangle \qquad (3.71)\\
&= \frac{e^{-i\left(\frac{\vartheta_+-\vartheta_-}{2}\right)}}{\sqrt{2}}\left(e^{-i\left(\vartheta_0+\frac{\vartheta_++\vartheta_-}{2}\right)}a_+^\dagger(0)\right.\\
&\quad\left.+\,e^{i\left(\vartheta_0+\frac{\vartheta_++\vartheta_-}{2}\right)}a_-^\dagger(0)\right)c_-^\dagger v_{2+}^\dagger\left|0\right\rangle \qquad (3.72)
\end{aligned}$$

with $\vartheta_+(t)=-\left(\frac{2g_1^2}{\delta+\frac{\Delta_S}{\hbar}}-\frac{2g_2^2}{\delta}\right)t$ and $\vartheta_-(t)=\frac{2g_2^2}{\delta}t$, resulting in a Faraday rotation angle of $\vartheta_{+1}(t)=\left[\vartheta_+(t)+\vartheta_-(t)\right]/2=+\left(\frac{2g_2^2}{\delta}-\frac{g_1^2}{\delta+\frac{\Delta_S}{\hbar}}\right)t$. These results are in complete agreement with the result using Fermi's golden rule above.

In addition, the quantum-optical calculation lets us entangle the photon with the electron-hole state on the 3D TI QD. In particular, if we choose the initial state to be

$$|\psi(0)\rangle=\frac{1}{\sqrt{2}}\left(a_+^\dagger+a_-^\dagger\right)\left(c_+^\dagger v_{2-}^\dagger+c_-^\dagger v_{2+}^\dagger\right)\left|0\right\rangle \qquad (3.73)$$

the photon and the e-h pair get fully entangled for $\vartheta_{\mp1}(\tau)=\pm\frac{\pi}{4}$, i.e. after a time $\tau=\pi/4\left(\frac{2g_2^2}{\delta}-\frac{g_1^2}{\delta+\frac{\Delta_S}{\hbar}}\right)$, yielding

$$\begin{aligned}
|\psi(\tau)\rangle &= \frac{1}{\sqrt{2}}\left(e^{-i\frac{\pi}{4}}a_+^\dagger(0)+e^{i\frac{\pi}{4}}a_-^\dagger(0)\right)c_+^\dagger v_{2-}^\dagger \qquad (3.74)\\
&\quad+\frac{1}{\sqrt{2}}\left(e^{-i\left(-\frac{\pi}{4}\right)}a_+^\dagger(0)+e^{i\left(-\frac{\pi}{4}\right)}a_-^\dagger(0)\right)c_-^\dagger v_{2+}^\dagger\left|0\right\rangle
\end{aligned}$$

This state consists of a photon entangled to the e-h pair on the 3D TI QD.

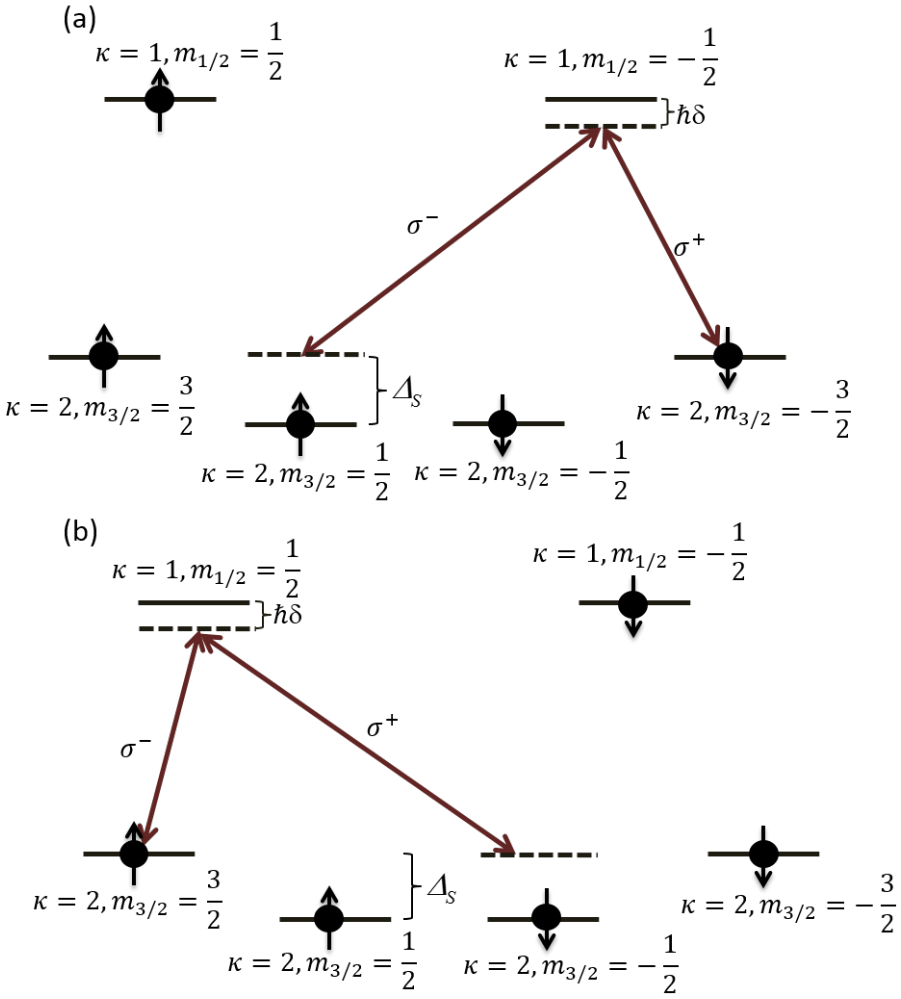
(a)
$\kappa = 1, m_{1/2} = \frac{1}{2}$
$\kappa = 1, m_{1/2} = -\frac{1}{2}$
$\hbar\delta$
σ^-
σ^+
Δ_S
$\kappa = 2, m_{3/2} = \frac{3}{2}$
$\kappa = 2, m_{3/2} = \frac{1}{2}$
$\kappa = 2, m_{3/2} = -\frac{1}{2}$
$\kappa = 2, m_{3/2} = -\frac{3}{2}$
(b)
$\kappa = 1, m_{1/2} = \frac{1}{2}$
$\hbar\delta$
$\kappa = 1, m_{1/2} = -\frac{1}{2}$
σ^-
σ^+
Δ_S
$\kappa = 2, m_{3/2} = \frac{3}{2}$
$\kappa = 2, m_{3/2} = \frac{1}{2}$
$\kappa = 2, m_{3/2} = -\frac{1}{2}$
$\kappa = 2, m_{3/2} = -\frac{3}{2}$

Figure 3.9: This is one possible level configuration that can be used for the implementation of the quantum Faraday rotation, where the quantum information is stored in form of an electron (a) in the spin up state or (b) in the spin down state. (a) A single spin up electron is probed by using off-resonant linearly polarized photon that acquires a positive Faraday rotation angle through virtual excitation of e-h pairs. (b) A single spin down electron is probed by using off-resonant linearly polarized photon that acquires a negative Faraday rotation angle through virtual excitation of e-h pairs.

We consider two possible level configurations due to the electron-hole symmetry in 3D TI QDs:

1. Figure 3.9 shows the first level configuration, in which only one of the states $\left|\Phi^{\kappa=1}_{\frac{1}{2},\pm\frac{1}{2}}\right\rangle$ is populated with an electron.
2. Figure 3.10 shows the second level configuration, in which only one of the states $\left|\Phi^{\kappa=1}_{\frac{1}{2},\pm\frac{1}{2}}\right\rangle$ is populated with a hole.

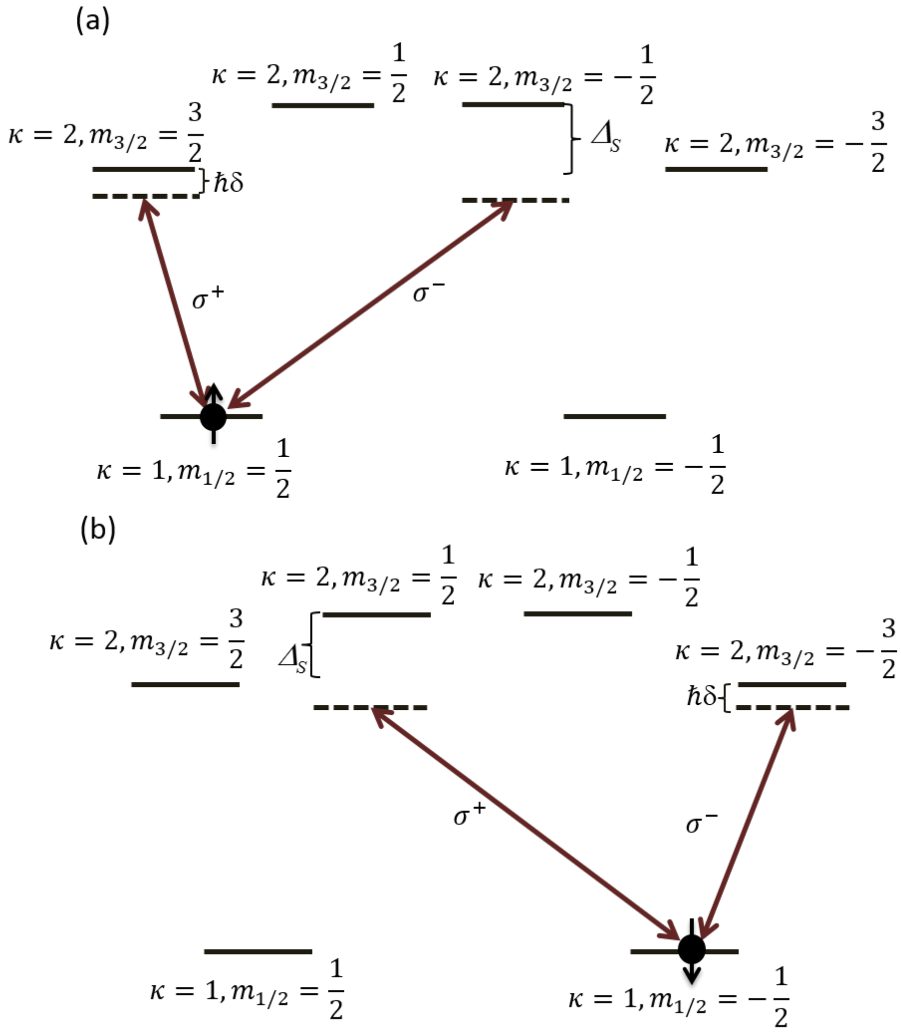
(a)
$\kappa = 2, m_{3/2} = \frac{1}{2}$
$\kappa = 2, m_{3/2} = -\frac{1}{2}$
$\kappa = 2, m_{3/2} = \frac{3}{2}$
Δ_S
$\kappa = 2, m_{3/2} = -\frac{3}{2}$
$\hbar\delta$
σ^+
σ^-
$\kappa = 1, m_{1/2} = \frac{1}{2}$
$\kappa = 1, m_{1/2} = -\frac{1}{2}$
(b)
$\kappa = 2, m_{3/2} = \frac{1}{2}$
$\kappa = 2, m_{3/2} = -\frac{1}{2}$
$\kappa = 2, m_{3/2} = \frac{3}{2}$
Δ_S
$\kappa = 2, m_{3/2} = -\frac{3}{2}$
$\hbar\delta$
σ^+
σ^-
$\kappa = 1, m_{1/2} = \frac{1}{2}$
$\kappa = 1, m_{1/2} = -\frac{1}{2}$

Figure 3.10: This is another possible level configuration that can be used for the implementation of the quantum Faraday rotation, where the quantum information is stored in form of a hole (a) in the spin up state or (b) in the spin down state. (a) A single spin up hole is probed by using off-resonant linearly polarized photon that acquires a positive Faraday rotation angle through virtual excitation of e-h pairs. (b) A single spin down hole is probed by using off-resonant linearly polarized photon that acquires a negative Faraday rotation angle through virtual excitation of e-h pairs.

3.8.2 Photon polarization - electron spin entanglement

Now let us consider the Faraday effect due to a single electron for the level configuration shown in Figure 3.10. Here the electron is in a s-like state. If the initial state is

$$|\psi(0)\rangle = \frac{1}{\sqrt{2}}\left(e^{-i\vartheta_0}a_+^\dagger + e^{i\vartheta_0}a_-^\dagger\right)c_+^\dagger\,|0\rangle \tag{3.75}$$

then state after the interaction is given by

$$\begin{aligned} |\psi(t)\rangle \;&=\; \frac{1}{\sqrt{2}}\Bigg(e^{-i\left(\vartheta_0-\frac{2g_2^2}{\delta}t\right)}a_+^\dagger(0) \\ &\qquad + e^{i\left(\vartheta_0+\frac{2g_1^2}{\delta+\Delta_S}t\right)}a_-^\dagger(0)\Bigg)c_+^\dagger\,|0\rangle \end{aligned} \tag{3.76}$$

resulting in $\vartheta_{+1}(t) = \left(\frac{g_1^2}{\delta+\frac{\Delta_S}{\hbar}} - \frac{g_2^2}{\delta}\right)t$. Conversely, if the initial state is (see Figure 3.10 (b))

$$|\psi(0)\rangle = \frac{1}{\sqrt{2}}\left(e^{-i\vartheta_0}a_+^\dagger + e^{i\vartheta_0}a_-^\dagger\right)c_-^\dagger\,|0\rangle \tag{3.77}$$

then state after the interaction is given by

$$\begin{aligned} |\psi(t)\rangle \;&=\; \frac{1}{\sqrt{2}}\Bigg(e^{-i\left(\vartheta_0-\frac{2g_1^2}{\delta+\frac{\Delta_S}{\hbar}}t\right)}a_+^\dagger(0) \\ &\qquad + e^{i\left(\vartheta_0+\frac{2g_2^2}{\delta}t\right)}a_-^\dagger(0)\Bigg)c_-^\dagger\,|0\rangle \end{aligned} \tag{3.78}$$

resulting in $\vartheta_{-1}(t) = -\left(\frac{g_1^2}{\delta+\frac{\Delta_S}{\hbar}} - \frac{g_2^2}{\delta}\right)t$. This result is also in complete agreement with the Faraday effect obtained above.

Again, the quantum-optical calculation allows us to entangle the photon with the single electron on the 3D TI QD. In particular, if we choose the initial state

$$|\psi(0)\rangle = \frac{1}{\sqrt{2}}\left(a_+^\dagger + a_-^\dagger\right)\left(c_+^\dagger + c_-^\dagger\right)|0\rangle \tag{3.79}$$

then the state after the interaction is fully entangled after a time $\tau = \pi / \left[4 \left(\frac{g_1^2}{\delta + \frac{\Delta_S}{\hbar}} - \frac{g_2^2}{\delta} \right) \right]$, i.e.

$$\begin{aligned} |\psi(\tau)\rangle &= \frac{1}{\sqrt{2}} \left(e^{-i\frac{\pi}{4}} a_+^\dagger(0) + e^{i\frac{\pi}{4}} a_-^\dagger(0) \right) c_+^\dagger \\ &+ \frac{1}{\sqrt{2}} \left(e^{-i\left(-\frac{\pi}{4}\right)} a_+^\dagger(0) + e^{i\left(-\frac{\pi}{4}\right)} a_-^\dagger(0) \right) c_-^\dagger \, |0\rangle \end{aligned} \tag{3.80}$$

This state is a fully entangled electron-photon state.

The Faraday effect due to a single hole for the level configuration shown in Figure 3.9 can be calculated in a similar way. Here the hole is in an s-like state. Other possible configurations include a single electron in a p-like state or a single hole in a p-like state.

Due to the symmetry between positive- and negative-energy solutions, in a 3D TI QD it is possible to define an electron spin qubit in terms of an s-like or a p-like state. At the same time it is possible to define a hole spin qubit in terms of an s-like or a p-like state. This cannot be done in a conventional wide-bandgap semiconductor QD, where the electron is associated with an s-like state and the hole is associated with a p-like state.[106]

For a quantitative description, we can assume a single 3D TI QD embedded in a semiconductor microcavity. The strong and weak interaction can occur between the QD e-h pair and discretized cavity modes at resonance, $\omega_{21} = \omega_c$. The e-h-photon coupling parameter g is given by $g = \left(\pi e^2 f\right)^{1/2} / \left(4\pi\epsilon_r\epsilon_o m_o V_m\right)^{1/2}$, where ϵ_r is the dielectric constants for the cavity material, [?] m_o is the free electron mass, and V_m is the mode volume. The mode volume for a mode of wavelength λ is $V_m \approx (\lambda/2n)^3$, where $n = \sqrt{\epsilon_r}$ (for a GaAs microcavity, $n = 3.31$). Using $\hbar\omega_{21} = 130$ meV, the oscillator strengths for the transition

$\Phi^{\kappa=2}_{\frac{3}{2},+\frac{1}{2}} \longleftrightarrow \Phi^{\kappa=1}_{\frac{1}{2},-\frac{1}{2}}$ and $\Phi^{\kappa=2}_{\frac{3}{2},-\frac{3}{2}} \longleftrightarrow \Phi^{\kappa=1}_{\frac{1}{2},-\frac{1}{2}}$ are obtained, respectively, $f_1 \approx 9$ and $f_2 \approx 27$. This gives us an estimate of $\hbar g_1 \approx 10\mu$eV and $\hbar g_2 \approx 17\mu$eV. For a detuning energy of $\hbar\delta = 100\mu$eV the time it takes to fully entangle the electron spin and the photon polarization is calculated to be of the order of 180 ps. The necessary condition to be in the strong coupling regime is that g must be large compared to both spontaneous emission rate and cavity decay loss rate.[125] Thus, for $Q \geq \omega/g_1 \approx 1.3 \times 10^4$ the 3D TI QD is in the strong coupling regime. For $Q = 10^5$, the photon decay rate is given by $\kappa = \frac{\omega}{2\pi Q} = 3.1 \times 10^9$ s^{-1}. This gives a cavity photon life time of 3 ns.

3.9 Conclusions

We have shown that Weyl fermions can be confined in all three dimensions at the spherically shaped interface between two narrow-bandgap semiconductor alloys, such as the core-bulk heterostructure made of PbTe/Pb$_{0.31}$Sn$_{0.69}$Te. This configuration provides us with the model of a spherical 3D TI QD with tunable size r_0 and potential Δ_0, which allows for complete control over the number of bound interface states. The most important features of 3D TI have been identified in a 3D TI QD, namely the spin locking effect and the Kramers degeneracy. We found that the Weyl states are confined on the surface of the QD, in contrast to the electrons and holes in topologically trivial semiconductor QDs. We showed that due to the large dipole moment of 450 Debye it is possible to reach the strong-coupling regime inside a cavity with a quality factor of $Q \approx 10^4$ in the infrared wavelength regime around

10 μm. Because of the strict optical selection rules, the 3D TI QD gives rise to interesting applications based on the semi-classical and quantum Faraday effect. We found that the 3D TI QD is a good candidate for quantum memory, quantum teleportation, and quantum computing with single spins in 3D TI QDs using infrared light. In particular, a single e-h pair, a single electron or a single hole can be used as a qubit for the implementation of optically mediated quantum computing with 3D TI QDs. Interestingly, we found that due to the symmetry between positive- and negative-energy solutions, in a 3D TI QD it is possible to define an electron spin qubit in terms of an s-like or a p-like state. At the same time it is possible to define a hole spin qubit in terms of an s-like or a p-like state. This cannot be done in a zincblende wide direct-bandgap semiconductor QD, where the electron is associated with an s-like state and the hole is associated with a p-like state.[106]

CHAPTER 4
TOPOLOGICAL INSULATORS WITH BULK GEOMETRY

4.1 Introduction

The 3D TI is a new state of matter on the surface or at the interface of narrow-bandgap materials where topologically protected gapless surface/interface states appear within the bulk insulating gap.[7, 8, 24, 69, 78, 126, 127] These states are characterized by the linear excitation energy of massless Weyl fermions. The spins of the Kramers partners are locked at a right angle to their momenta due to the Rashba spin-orbit coupling,[12] protecting them against perturbation and scattering.[7, 10, 11, 69] Because of the presence of a single Dirac cone with fixed spin direction at the *surface*, the main feature of strong TIs,[23, 128] the materials Bi_2Se_3 and Bi_2Te_3 are currently being widely studied.[129, 78, 127]

The heterostructures of compound semiconductors such as $Bi_{1-x}Sb_x$ and $Pb_{1-x}Sn_xTe$ exhibit a strong topological phase.[11] In $Bi_{1-x}Sb_x$, the L^+ and L^- bands cross at $x = 0.04$. The pure PbTe has inverted bands at the band gap extrema with respect to SnTe. In $Pb_{1-x}Sn_xTe$, initially increasing the concentration of Sn leads to a decreasing band gap. At around $x = 0.35$, the bands cross and the gap reopens for $x > 0.35$ with even parity L^+ band and odd parity L^- band being inverted with respect to each other.[130] The band inversion between PbTe and SnTe results in *interface* states,[131, 132, 133] which can be described by the Weyl equation.[110]

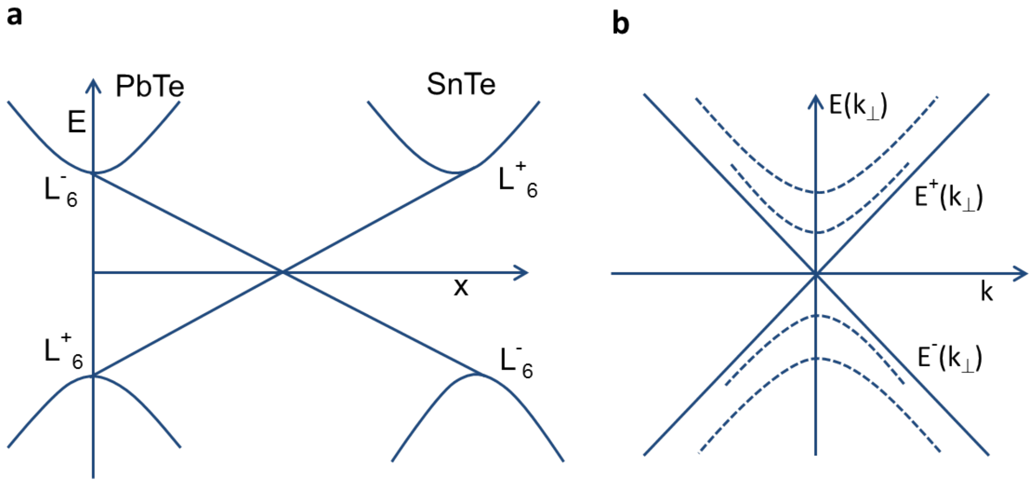

Figure 4.1: (a) Band inversion in between two end members in $Pb_{1-x}Sn_xTe$. (b) Energy spectrum of the inverted contact. The solid lines are Weyl states and dashed lines are additional branches that appear for contact thickness $l > l_o$.

Here we investigate the giant Faraday effect due to Pauli exclusion principle and the strict optical selection rules governing the low energy excitation of electron-hole pairs around a Dirac point in a 3D TI. Due to interference effects, the Faraday rotation angle exhibits oscillations as a function of probe wavelength and thickness of the slab material on either side of the 3D TI double interface of a PbTe/$Pb_{0.31}Sn_{0.69}Te$/PbTe heterostructure. The maxima in the Faraday rotation angle are in the mrad regime. We find that in 3D TIs both interband transitions (between positive and negative energy solutions) and intraband transitions (within the same energy solutions) are allowed. Note that the selection rules obtained here are different from the selection rules in ARPES experiments, which record the number of photoelectrons as a function of kinetic energy and emission angle with respect to the sample surface. A number of experiments have shown the existence of the helical surface states in 3D TI.[129, ?] As an example, we consider the alloy $\mathrm{Pb}_{1-x}\mathrm{Sn}_x\mathrm{Te}$, which has topologically nontrivial interface states under appropriate doping level. Our results are qualitatively valid for all strong 3D TIs. $\mathrm{Pb}_{1-x}\mathrm{Sn}_x\mathrm{Te}$ has a rocksalt type crystal lattice with four non-equivalent L points located in the center of the hexagonal facets on [111] axis. The valence and conduction band edges are derived from the hybridized p-type and s-type orbitals at the L point.[134] Its end species have inverted band character, L^+ character of PbTe band switches to L^- character of SnTe band and vice versa as shown in Figure 4.1. The Brillouin zone has eight hexagonal faces each with center at the L point (see figure4.2). Two faces lying diametrically opposite are equivalent. As a result, the band inversion happens at four distinct Dirac points. The crystal possesses a mirror symmetry. Therefore, it is a distinct class of 3D TI where surface states are protected by mirror symmetry.[135] We choose the z-axis to point in direction of the gradient of the concentration ∇x. At the two band extrema, the low energy Hamiltonian is described by a 3D relativistic Dirac equation whose solutions are localized near the $z = 0$ plane where the band crossing occurs, which defines the interface. Dispersion is nearly linear owing to the large band velocities of $v_\perp = 8 \times 10^5$ m/s and $v_\parallel = 2.24 \times 10^5$ m/s with a small gap.[110] Such properties result in a small localization length l_o of the interface wave functions along the z-axis. Due to the absence of a center of inversion, a Rashba-type spin-orbit coupling is present, which is automatically taken into account through the Dirac equation. We also present the details of our ab-initio calculation of the bandstructure in the supercell Brillouin zone obtained by doubling the lattice parameters in each direction. Analysis of the alloy band structures is usually complicated due to folding of the bands from neighboring Brillouin zones, making it difficult to map the calculated bandstructures onto the bandstructures obtained from momentum-resolving experiments. The analysis is further complicated by the presence of impurity bands inside the normal bulk energy gap. The interface states sometimes overlap with bulk energy states. Therefore, we unfold the band structures along the [111] direction in order to shift the band crossing from the Γ point, as seen in the supercell Brillouin zone, to the L point in the primitive cell Brillouin zone.[136, 137]

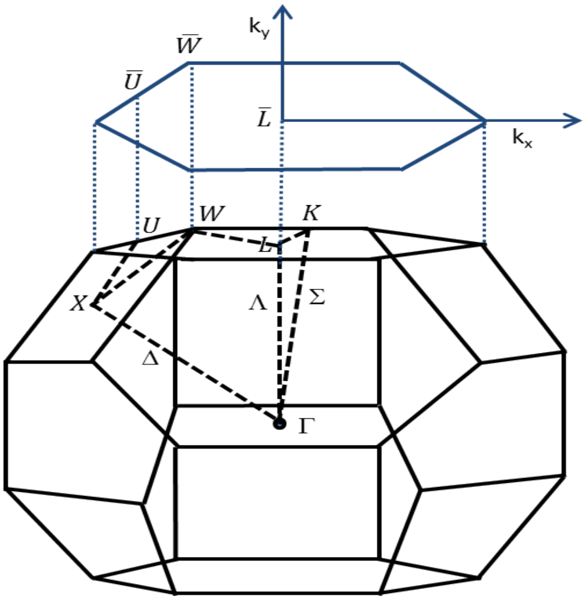

Figure 4.2: Brillouin zone for rocksalt type crystal with space group Fm$\bar{3}$m. There are four inequivalent L points at the center of the faces on the surface of the Brillouin zone. The growth direction is along [111] and is chosen to point along the z-axis. With the appropriate level of doping by Sn atoms in PbTe, band gap goes to zero at L point with a linear excitation energy that traces out a cone in the 2D Fermi surface parallel to the face of Brillouin zone that is perpendicular to the growth direction .

We developed a method of the Faraday rotation of a single photon due to Pauli exclusion principle for a topologically trivial quantum dot[103, 104] and for a 3D TI quantum dot.[138] The proposed method can be used for entangling remote excitons, electron spins, and hole spins. We showed that this entanglement can be used for the implementation of optically mediated quantum teleportation and quantum computing.

Here we investigate the Faraday effect due to the Pauli exclusion principle for a 3D TI double interface of a PbTe/$\mathrm{Pb}_{0.31}\mathrm{Sn}_{0.69}$Te/PbTe heterostructure. This Faraday effect is completely different from the Faraday effect due to an external magnetic field, which was presented in Ref. MacDonald:2012 for a thin film of a 3DTI where a gap was opened by breaking the time reversal symmetry through a magnetic field. When a thin film of topological insulator material is placed between ferromagnets or placed between paramagents with an externally applied magnetic field, the transverse Hall effect is observed due to the presence of the transverse conductivity σ_{xy}. Consequently, the Dirac fermion performs a cyclotron motion acquiring a Berry phase of π due to the Dirac node. The Faraday rotation angle in this case comes from the topological contribution.[127] In our case, as we show in our calculations below, there is no magnetic field and hence $\sigma_{xy} = 0$. Therefore, in our case there is no topological contribution to the Faraday effect.

The Faraday effect presented here arises from the polarization of electron-hole (e-h) pairs that are excited by means of a linearly polarized laser pump beam. A laser probe beam with energy below twice the absolute value of the Fermi energy measured from the Dirac point cannot be absorbed due to the absence of charge carriers in this energy regime. The excitation of the Weyl fermion can happen when a photon has an energy of $\hbar\omega \geq 2E_F$ as shown in the Figure 4.3 **a**. There are no interband transitions with the photon energy less than $2E_F$. A gate voltage can also be applied to shift the Fermi level below the Dirac node. [**3**] Figure 4.3 **b** shows the scheme of the gate-induced shift in the Fermi level. In the Figure photon of energy $\hbar\omega \geq |E_F|$ can excite a Weyl fermion. We call this energy regime the transparency region, in order to avoid confusion with a bandgap in a gapped semiconductor material. When x- and y-linearly polarized e-h pairs are present, a probe beam linearly polarized along the diagonal direction $x + y$ experiences a Faraday rotation on the Poincare sphere as shown in Figure 4.9[139]. The resulting Faraday rotation angle is giant and of the order of mrad. It exhibits oscillations as a function of the slab thickness of the two PbTe layers of the PbTe/$\mathrm{Pb_{0.31}Sn_{0.69}Te}$/PbTe heterostructure containing two interfaces (see Figure 4.8). The $\mathrm{Pb_{0.31}Sn_{0.69}Te}$ is 10 nm thick in order to introduce a gap for three out of the four L-points, as described below. The Faraday effect results then only from the excitation of e-h pairs at a single L-point.

The paper is organized as follows. In Sec. 4.2 we present the analytical derivation of the Weyl solution of the Dirac equation that describes the level crossing at the L point. Using the Rashba spin-orbit Hamiltonian, we derive the helicity operator for 3D topological insulators in Sec. 4.3. Sec. 4.4 is devoted to the evaluation of the optical transition matrix elements. In order to obtain a quantitative result for the optical transition matrix elements, we perform a bandstructure calculation of the alloy $\mathrm{Pb}_{1-x}\mathrm{Sn}_x\mathrm{Te}$ in Sec. 4.5. The Sec. 4.6 is devoted to the explicit derivation of the Faraday rotation effect and calculation of the Faraday rotation angle in the PbTe/$\mathrm{Pb_{0.31}Sn_{0.69}Te}$/PbTe heterostructure.

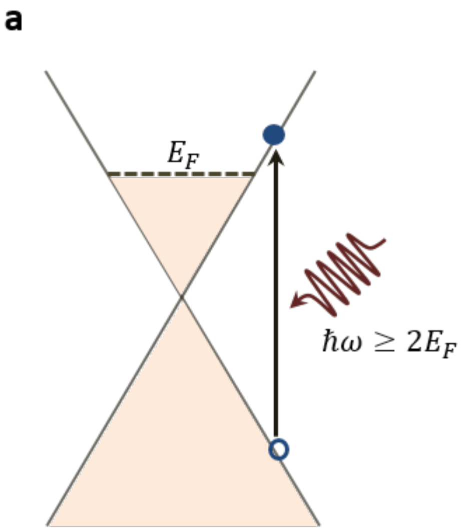

Figure 4.3: Transparency region for the optical excitation of the Weyl fermion. The light yellow color (online) represents the filled Fermi sea of the electrons. The zero energy is defined by the apex of the Dirac cone. **a** With the photon energy of $\hbar\omega \geq 2E_F$ a Weyl fermion can be excited. There are no transitions for a photon energy below $2E_F$. The Fermi level is measured from the zero of the energy. **b** The Fermi level can be shifted below the Dirac node by applying a gate voltage $V_g \geq E_F$. Then a Weyl fermion can be excited with a photon energy of $\hbar\omega \geq |E_F|$.

4.2 Model based on Dirac equation

The energy spectrum of $\mathrm{Pb}_{1-x}\,\mathrm{Sn}_x\mathrm{Te}$ near the $L_6^{\mp}$ band crossing is described within the $\mathbf{k}\cdot\mathbf{p}$ perturbation theory by the two-band Dirac Hamiltonian[107]

$$H=\begin{pmatrix} \Delta(z) & v_{\|}\sigma_z\hat{p}_z+v_{\perp}\boldsymbol{\sigma}_{\perp}\cdot\hat{\mathbf{p}}_{\perp} \\ v_{\|}\sigma_z\hat{p}_z+v_{\perp}\boldsymbol{\sigma}_{\perp}\cdot\hat{\mathbf{p}}_{\perp} & -\Delta(z) \end{pmatrix}, \tag{4.1}$$

where $\boldsymbol{\sigma}$ are the Pauli matrices, $\hat{\mathbf{p}}=-i\hbar\boldsymbol{\nabla}$ is the momentum operator and $\Delta(z)=\varepsilon_g\left(z\right)/2$ is the gap energy parameter with symmetry $\Delta\left(z\right)=-\triangle\left(-z\right)$. $\boldsymbol{\sigma}_{\perp}=(\sigma_x,\sigma_y)$ and $\hat{\mathbf{p}}_{\perp}=(\hat{p}_x,\hat{p}_y)$ denote the Pauli matrices and momenta in the interface plane, respectively. The transverse and longitudinal velocities are determined by $v_{\perp}=P_{\perp}/m_0$ and $v_{\|}=P_{\|}/m_0$, where $P_{\perp}$ and $P_{\|}$ are the transverse and longitudinal Kane interband matrix elements, respectively. $m_0=9.10938188\times10^{-31}$ kg is the free electron mass. The inhomogeneous structure is synthesized by changing the composition along one of the [111] axes, whose symmetry breaking leads to a single Dirac cone in the chosen direction,[140] thereby recovering the Z_2 strong topological insulator phase. The direction of the gradient of the concentration $\boldsymbol{\nabla}x$ defines our z-axis. After the unitary transformation of the Hamiltonian $H=UH'U^{\dagger}$ using

$$U=\frac{1}{\sqrt{2}}\begin{pmatrix} 1 & i \\ i & 1 \end{pmatrix}, \tag{4.2}$$

the time-independent Dirac equation $H'\Phi_{\pm}^{'} = (\varepsilon - \varphi(z))\,\Phi_{\pm}^{'}$ can be written as

$$\begin{pmatrix} 0 & i\Delta + v_{\parallel}\sigma_z\hat{p}_z + v_{\perp}\boldsymbol{\sigma}_{\perp}\cdot\hat{\mathbf{p}}_{\perp} \\ -i\Delta + v_{\parallel}\sigma_z\hat{p}_z + v_{\perp}\boldsymbol{\sigma}_{\perp}\cdot\hat{\mathbf{p}}_{\perp} & 0 \end{pmatrix}$$

$$\times \begin{pmatrix} {\phi'}^{L^-} \\ {\phi'}^{L^+} \end{pmatrix} = (\varepsilon - \varphi(z)) \begin{pmatrix} {\phi'}^{L^-} \\ {\phi'}^{L^+} \end{pmatrix} \tag{4.3}$$

where ${\phi'}^{L^-}$ and ${\phi'}^{L^+}$ are the two-component spinors of the L^- and the L^+ band, respectively. The potential $\varphi(z)$ (work function) describes the variation of the gap center. For simplicity we consider the case $\varphi(z) = 0$. From Eq. (4.3), the two-component spinor ${\phi'}^{L^{\pm}}$ satisfies

$$\left(p^2 + U_{\pm}(z, \sigma_z) - \varepsilon^2\right){\phi'}^{L^{\pm}} = 0 \tag{4.4}$$

where $U_{\pm}(z, \sigma_z) = \Delta^2 \pm \hbar v_{\parallel}\sigma_z\frac{\partial\Delta}{\partial z}$. In its origin, the linear Weyl spectrum $\varepsilon_o^{\pm}(k_{\perp}) = \pm\hbar v_{\perp}k_{\perp}$at $k_{\perp} = 0$ is approximately equal to the soliton spectrum in the 1D Peierl's insulator. This implies that $\Delta(z)$ can be chosen to be $\Delta(z) = \Delta(\infty)\tanh(z/l)$. Interface states are localized along the z-axis with the localization length $l_o = \hbar v_{\parallel}/\Delta(\infty)$. For $l_o < l$, additional branches with finite mass appear. There are several solutions at $\varepsilon^2 > \Delta^2(\infty)$ which are localized at the contact. For $l_o > l$, only Weyl solutions exist. We focus on the case when $l_o > l$. Then we have only zero-energy solutions, which correspond to the Weyl states and are given by [**?**]

$$\Phi_{\pm}^{'} = C \begin{pmatrix} \pm e^{-\frac{i\theta}{2}} \\ 0 \\ 0 \\ e^{\frac{i\theta}{2}} \end{pmatrix} e^{-\frac{1}{\hbar v_{\|}}\int\limits_{0}^{z}\Delta\left(z^{'}\right)dz^{'}+i\mathbf{k}_{\perp}\cdot\mathbf{r}} \tag{4.5}$$

where C is a normalization constant, $\mathbf{k}_{\perp} = (k_x,\, k_y,\, 0)$ and $e^{\mp i\theta} = \frac{k_x \mp i k_y}{k_\perp}$. These solutions have eigenenergies $\varepsilon_o^{\pm}\left(k_\perp\right) = \pm\hbar v_\perp k_\perp$. For $\Delta\left(z\right)$ to vanish at the inverted contact, it can be seen from Eq. (4.3) that ${\phi'}_{\pm}^{L^-}$ and ${\phi'}_{\pm}^{L^+}$ must have only non-zero spin down and spin up components, respectively. Each spinor at $L^{\mp}$ band can be represented with the spin up states from the L^- band and spin down states from the L^+ band for both the positive and the negative energies. The motion of the particle at the inverted contact is separated into free motion in the xy-plane and confinement along the z-axis. A remarkable property of Eq. (4.3) is the presence of the zero mode (Weyl mode) localized around $z = 0$. It is this mode that has a locked spin structure. In order to understand the direction in which the 4-spinors point, we have to transform the solutions back to the original basis of the Hamiltonian in Eq. (4.1). After the back transformation $\Phi_{\pm} = U\Phi_{\pm}^{'}$, the Weyl solutions are

$$\Phi_{\pm} = Ce^{\pm i\frac{\pi}{4}} \begin{pmatrix} \pm e^{-i\frac{(\theta\pm\pi/2)}{2}} \\ \pm e^{i\frac{(\theta\pm\pi/2)}{2}} \\ e^{-i\frac{(\theta\mp\pi/2)}{2}} \\ e^{i\frac{(\theta\mp\pi/2)}{2}} \end{pmatrix} e^{-\frac{1}{\hbar v_{\|}}\int\limits_{0}^{z}\Delta(z^{'})dz^{'}+i\mathbf{k}_{\perp}\cdot\mathbf{r}} \tag{4.6}$$

where C is a normalization constant. These solutions have eigenenergies $\varepsilon_o^{\pm}(k_\perp) = \pm\hbar v_\perp k_\perp$ and are *helical.* At this time, it is useful to introduce the notation

$$\Phi_\pm = \begin{pmatrix} \phi_\pm^{L^-} \\ \\ \phi_\pm^{L^+} \end{pmatrix} = \begin{pmatrix} \chi_\pm^{L^-} \\ \\ \chi_\pm^{L^+} \end{pmatrix} F(\mathbf{r}) = \chi_\pm F(\mathbf{r}), \tag{4.7}$$

where $\chi_\pm$ is the four-spinor consisting of the two-spinors $\chi_\pm^{L^-}$ and $\chi_\pm^{L^+}$ are two-spinors, and $F(\mathbf{r}) = Ce^{-\frac{1}{\hbar v_\parallel}\int\limits_0^z \Delta(z')dz' + i\mathbf{k}_\perp\cdot\mathbf{r}}$. We define $F(z) = e^{-\frac{1}{\hbar v_\parallel}\int\limits_0^z \Delta(z')dz'}$.

4.3 Helicity operator

We show in this section that it is possible to clearly identify the positive and negative energy solutions by means of a spin helicity operator. In the representation shown in Eq. (4.7), the spin directions reveal themselves clearly: the spins of the two-spinors $\chi_\pm^{L^-}$ and $\chi_\pm^{L^+}$ point perpendicular to $\mathbf{k}_\perp$ owing to the $\mp\pi/2$ shifts. For an asymmetric scalar potential V applied to a semiconductor heterostructure, the inversion symmetry is broken, which leads to the Rashba spin-orbit coupling.[12, 139] Here in the case of the interface of a 3D TI we have antisymmetric potentials $V^\mp = \pm\Delta$, which correspond to the diagonal elements of the Hamiltonian H and whose signs depend on the band $L^\mp$. This results in a band-dependent Rashba spin-orbit coupling. For the positive (negative) solutions the Rashba spin-orbit coupling has the form $H_R = \mp\lambda_R \boldsymbol{\sigma}\cdot(\boldsymbol{p}\times\boldsymbol{\nabla}V^\mp) = \mp\lambda_R\boldsymbol{\nabla}V^\mp\cdot(\boldsymbol{\sigma}\times\boldsymbol{p})$, (($-$) sign for positive energy solutions and ($+$) sign for negative energy solutions), where $\lambda_R \geq 0$ is the Rashba spin-orbit coupling constant. It is to be noted that in both cases each spin $S^{(\mp)}$ is perpendicular both to the momentum and to the potential gradient direction, i.e. the z-axis (see Figure 4.4). Our findings are consistent with the spin density functional calculations (DFT).[141]

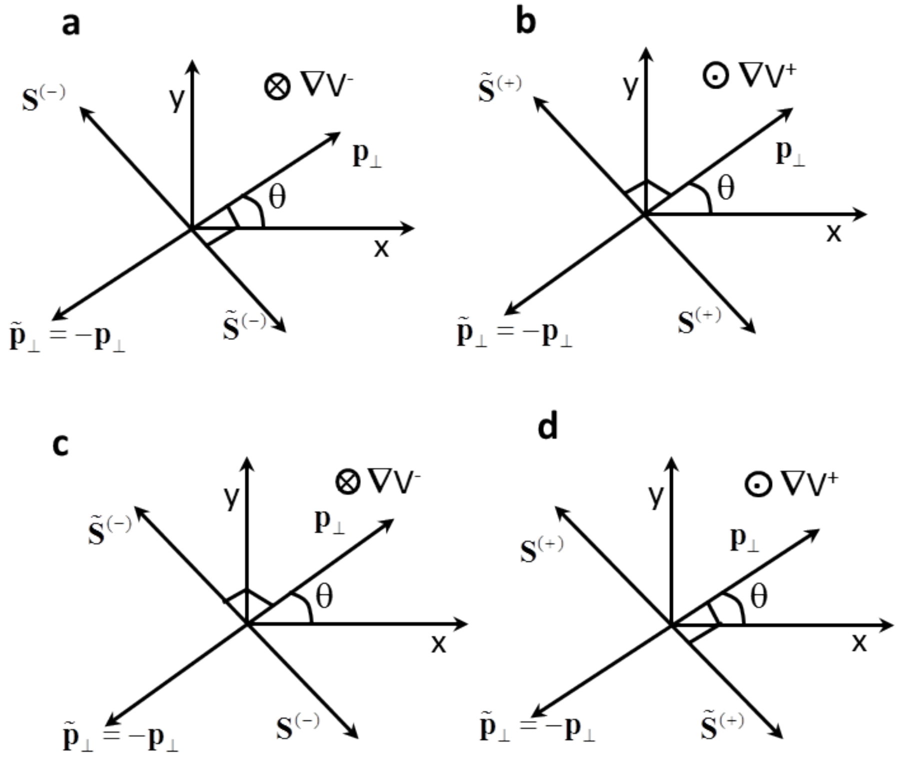
a
$\mathbf{S}^{(-)}$
y
$\otimes \nabla V^-$
$\mathbf{p}_\perp$
θ
x
$\tilde{\mathbf{p}}_\perp = -\mathbf{p}_\perp$
$\tilde{\mathbf{S}}^{(-)}$
b
$\tilde{\mathbf{S}}^{(+)}$
y
$\odot \nabla V^+$
$\mathbf{p}_\perp$
θ
x
$\tilde{\mathbf{p}}_\perp = -\mathbf{p}_\perp$
$\mathbf{S}^{(+)}$
c
$\tilde{\mathbf{S}}^{(-)}$
y
$\otimes \nabla V^-$
$\mathbf{p}_\perp$
θ
x
$\tilde{\mathbf{p}}_\perp = -\mathbf{p}_\perp$
$\mathbf{S}^{(-)}$
d
$\mathbf{S}^{(+)}$
y
$\odot \nabla V^+$
$\mathbf{p}_\perp$
θ
x
$\tilde{\mathbf{p}}_\perp = -\mathbf{p}_\perp$
$\tilde{\mathbf{S}}^{(+)}$

Figure 4.4: Effect of Rashba spin-orbit coupling. Spin vector $\boldsymbol{S}^{(-)}$ ($\tilde{\boldsymbol{S}}^{(-)}$) in the L^- band and spin vector $\boldsymbol{S}^{(+)}$ ($\tilde{\boldsymbol{S}}^{(+)}$) in the L^+ band are perpendicular to both the z-axis and $\boldsymbol{p}_\perp$ ($\tilde{\boldsymbol{p}}_\perp$) for Weyl interface states (Weyl Kramers partner states). (a) and (b) ((c) and (d)) correspond to positive (negative) eigenenergy.

In order to determine the Kramers partners explicitly, we rotate the phase of each of the two-spinor wavefunction by an angle π in the 2D interface plane, yielding $\phi_{\pm}^{L^-}(\theta + \pi) =$

$e^{\mp i\frac{\pi}{4}}\begin{pmatrix} -e^{-i\frac{(\theta\mp\pi/2)}{2}} \\ -e^{i\frac{(\theta\mp\pi/2)}{2}} \end{pmatrix} F^*(\mathbf{r})$ and $\phi_{\pm}^{L^+}(\theta+\pi) = e^{\mp i\frac{\pi}{4}}\begin{pmatrix} \pm e^{-i\frac{(\theta\pm\pi/2)}{2}} \\ \pm e^{i\frac{(\theta\pm\pi/2)}{2}} \end{pmatrix} F^*(\mathbf{r})$. Their spin and momentum direction are flipped by an angle π (Figure 4.4). This provides a theoretical hallmark of Kramers partners in 3D TI.

Helical properties of solutions given by Eq. (4.6) apply to all 3D TIs. In the case of free neutrinos in 3D space, the standard helicity operator $\hat{h}_n = -\left(1/\left|p_\perp\right|\right)\boldsymbol{\sigma}\cdot\boldsymbol{p}$ for the spin $\mathbf{S} = \hbar\boldsymbol{\sigma}/2$ can be used. Similarly, in the case of graphene the helicity for the pseudospin is given by $\hat{h}_g = -\left(1/\left|p_\perp\right|\right)\boldsymbol{\sigma}\cdot\boldsymbol{p}$. However, in the case of 3D TI this definition is not useful, because the spin points perpendicular to the momentum. Therefore, since we know that the Rashba spin-orbit coupling is responsible for the helicity in 3D TIs, we define the 3D TI helicity operator as

$$\begin{aligned} \hat{h}_{\mathrm{TI}} &= \left(1/\left|p_\perp\right|\right)\begin{pmatrix} \left(\boldsymbol{\sigma}_\perp\times\boldsymbol{p}_\perp\right)\cdot\hat{\boldsymbol{z}} & 0 \\ 0 & -\left(\boldsymbol{\sigma}_\perp\times\boldsymbol{p}_\perp\right)\cdot\hat{\boldsymbol{z}} \end{pmatrix} \\ &= \left(1/\left|p_\perp\right|\right)\beta\left(\boldsymbol{\sigma}_\perp\times\boldsymbol{p}_\perp\right)\cdot\hat{\boldsymbol{z}} \end{aligned} \tag{4.8}$$

where $\boldsymbol{\sigma}_\perp = \{\sigma_x, \sigma_y\}$ is the 2D vector of Pauli matrices in the xy-plane and $\beta = \begin{pmatrix} 1 & 0 \\ 0 & -1 \end{pmatrix}$ is a Dirac matrix. Note that the $+$ and $-$ signs in front of the diagonal terms are due to the direction of $\boldsymbol{\nabla}V^{\mp}$ and thus a direct consequence of the Rashba spin-orbit coupling. The eigenfunctions of the operator $\hat{h}_{\mathrm{TI}}$ are the 4-spinor wavefunctions given by the Eq. (4.6) with the eigenvalues $(+1)$ for the positive energy solution and (-1) for the negative energy solution, i.e. $\hat{h}_{\mathrm{TI}}\Phi_\pm = (\pm 1/2)\,\Phi_\pm$. $\hat{h}_{\mathrm{TI}}$ commutes with the Hamiltonian in Eq. (4.1). This provides the possibility to write an effective 2D Hamiltonian for the Weyl fermions on the surface of 3D topological insulators, i.e.

$$H_{2D} = \hbar v \begin{pmatrix} (\boldsymbol{\sigma}_\perp \times \boldsymbol{k}_\perp) \cdot \hat{\boldsymbol{z}} & 0 \\ 0 & -(\boldsymbol{\sigma}_\perp \times \boldsymbol{k}_\perp) \cdot \hat{\boldsymbol{z}} \end{pmatrix} \tag{4.9}$$

This effective 2D Hamiltonian can be reduced to two Weyl Hamiltonians of the form $H_{2D}^{2\times2} = \pm\hbar v \left(\boldsymbol{\sigma}_\perp \times \boldsymbol{k}_\perp\right) \cdot \hat{\boldsymbol{z}}$. It is important to note that both 2-spinors of $\chi_\pm$, the 2-spinor $\chi_\pm^{L^-}$ of the L^- band and the 2-spinor $\chi_\pm^{L^+}$ of the L^+ band have the same helicity, in contrast to the commonly used Weyl Hamiltonians $H_W(\mathbf{k}) = \pm\hbar v \boldsymbol{\sigma}\cdot\mathbf{k}$. The reason for this is that the two 2-spinors are coupled through the mass term $\Delta(z)$ in z-direction, as given in the 3D Hamiltonian in Eq. (4.1).

4.4 Optical transition matrix elements

We calculate the low-energy transitions around the L valley that is lifted up along the z-direction from the other three L valleys. With the proper choice of uniform strain, composition and layer width, there exist practically gapless helical states for the [111] valley inside the gapped states of the oblique valleys.[140] In unstrained $\mathrm{Pb}_{1-x}\mathrm{Sn}_x\mathrm{Te}$, band inversion occurs simultaneously at four L points and the phase is topologically trivial. For most experiments, in a structure with a layer of thickness d $\approx$ 10 nm between the two interfaces in a PbTe/$\mathrm{Pb}_{0.31}\mathrm{Sn}_{0.69}$Te/PbTe heterostructure, dispersion of the [111] valley states can be assumed to be gapless while the states in the oblique valleys are gapped.[140] The interface can be modeled with the bulk of $\mathrm{Pb}_{0.31}\mathrm{Sn}_{0.69}$Te and PbTe with bandgaps of, respectively,

-0.187 and 0.187 eV, so that Weyl fermions are generated at the two interfaces. Here, the bandgap formula provided in Ref. Grassie:1985 was used. It is to be noted that localized spin states of 2D Weyl fermions in 3D TI are solutions of the $\mathbf{k}\cdot\mathbf{p}$ Hamiltonian given in Eq. (4.1).

Now we proceed to calculate the optical selection rules for the excitation of electron-hole pairs, keeping in mind that the Dirac equation provides an effective description of the two-band system consisting of the $L^{\mp}$ bands. The $\mathbf{k}\cdot\mathbf{p}$ Hamiltonian contains also a quadratic term in the momenta,[107] namely

$$H_q = \begin{pmatrix} \frac{(p_z+eA_z)^2}{2m_{\parallel}^{-}} + \frac{(\mathbf{p}_{\perp}+e\mathbf{A}_{\perp})^2}{2m_{\perp}^{-}} & 0 \\ 0 & \frac{(p_z+eA_z)^2}{2m_{\parallel}^{+}} + \frac{(\mathbf{p}_{\perp}+e\mathbf{A}_{\perp})^2}{2m_{\perp}^{+}} \end{pmatrix}, \tag{4.10}$$

where $m_{\parallel}^{\mp}$ and $m_{\perp}^{\mp}$ are the longitudinal and transverse effective masses of the $L^{\mp}$ bands, respectively. Through minimal coupling the quadratic term leads to a linear term in the momentum, which we need to take into account. Hence, in the presence of electromagnetic radiation, the total Hamiltonian for the Dirac particle is given by

$$\begin{aligned} H_{tot} &= v_{\parallel}\alpha_z\left(\hat{p}_z + eA_z\right) + v_{\perp}\boldsymbol{\alpha}_{\perp}\cdot\left(\hat{\mathbf{p}} + e\mathbf{A}_{\perp}\right) + \beta\Delta(z) + (e/m)\mathbf{A}\cdot\mathbf{p} \\ &= \begin{pmatrix} \Delta(z) + e\left(\frac{p_zA_z}{m_{\parallel}^{-}} + \frac{\mathbf{p}_{\perp}\cdot\mathbf{A}_{\perp}}{m_{\perp}^{-}}\right) & v_{\parallel}\sigma_z\left(\hat{p}_z + eA_z\right) + v_{\perp}\boldsymbol{\sigma}_{\perp}\cdot\left(\hat{\mathbf{p}} + e\mathbf{A}_{\perp}\right) \\ v_{\parallel}\sigma_z\left(\hat{p}_z + eA_z\right) + v_{\perp}\boldsymbol{\sigma}_{\perp}\cdot\left(\hat{\mathbf{p}} + e\mathbf{A}_{\perp}\right) & -\Delta(z) + e\left(\frac{p_zA_z}{m_{\parallel}^{+}} + \frac{\mathbf{p}_{\perp}\cdot\mathbf{A}_{\perp}}{m_{\perp}^{+}}\right) \end{pmatrix} \end{aligned} \tag{4.11}$$

where $A = (A_z,\ \boldsymbol{A}_{\perp})$ is the vector potential, $\boldsymbol{\alpha} = (\alpha_z,\ \boldsymbol{\alpha}_{\perp})$ and β are the Dirac matrices $\boldsymbol{\alpha}_i = \begin{pmatrix} 0 & \boldsymbol{\sigma}_i \\ \boldsymbol{\sigma}_i & 0 \end{pmatrix}$, $\beta = \begin{pmatrix} I & 0 \\ 0 & -I \end{pmatrix}$, and $\mathbf{E} = \partial\mathbf{A}/\partial t$ in the Coulomb gauge. We identify the interaction Hamiltonian as

$$H_{int} = ev_{\|}\alpha_z A_z + ev_{\perp}\boldsymbol{\alpha}_{\perp}\cdot\boldsymbol{A}_{\perp} + (e/m)\mathbf{A}\cdot\mathbf{p} \tag{4.12}$$

$$= \begin{pmatrix} e\left(\frac{p_z A_z}{m_{\|}^{-}} + \frac{\mathbf{p}_{\perp}\cdot\mathbf{A}_{\perp}}{m_{\perp}^{-}}\right) & ev_{\|}\sigma_z A_z + ev_{\perp}\boldsymbol{\sigma}_{\perp}\cdot\mathbf{A}_{\perp} \\ ev_{\|}\sigma_z A_z + ev_{\perp}\boldsymbol{\sigma}_{\perp}\cdot\mathbf{A}_{\perp} & e\left(\frac{p_z A_z}{m_{\|}^{+}} + \frac{\mathbf{p}_{\perp}\cdot\mathbf{A}_{\perp}}{m_{\perp}^{+}}\right) \end{pmatrix}.$$

It will turn out that only interband transitions contribute for a 2D interface, whereas both interband and intraband transitions contribute in the case of a 3D TI quantum dot as shown in [138]. It is important to note that $v_{\|} = P_{\|}/m_0$ and $v_{\perp} = P_{\perp}/m_0$ include the Kane interband matrix elements $\mathbf{P} = \left\langle u^{\mp}_{\mathbf{k_f}} \left| \hat{\mathbf{P}} \right| u^{\pm}_{\mathbf{k_I}} \right\rangle$, where $u^{\mp}_{\mathbf{k}}$ are the Bloch's functions for the $L^{\mp}$ bands. This means that the interband transitions are governed by the interband Hamiltonian $H_{inter} = ev_{\|}\alpha_z A_z + ev_{\perp}\boldsymbol{\alpha}_{\perp}\cdot\boldsymbol{A}_{\perp}$, where the Dirac $\boldsymbol{\alpha}$- matrices couple the L^{-} band with the L^{+} band. The Hamiltonian $H_{intra} = (e/m)\mathbf{A}\cdot\mathbf{p}$ accounts for intraband transitions with $\hat{\mathbf{p}}$ operating on the envelope wavefunctions only. H_{intra} is proportional to the identity in 4-spinor space and therefore couples the L^{-} band to itself and the L^{+} band to itself. Thus the interband Hamiltonian H_{inter} and the intraband Hamiltonian H_{intra} are not equivalent in this description. On the one hand, H_{inter} gives rise to interband transitions because it contains the Kane interband matrix elements $P_{\perp}$ and $P_{\|}$. On the other hand, H_{intra} gives rise to intraband transitions because the term $(e/m)\mathbf{A}\cdot\mathbf{p}$ operates on the envelope wavefunctions.

We start with calculating the interband matrix elements which are given by the off diagonal elements of the interaction Hamiltonian. We identify $j_z = ev_{\|}\Psi^{\dagger}\alpha_z\Psi$ and $\mathbf{j}_{\perp} = ev_{\perp}\Psi^{\dagger}\boldsymbol{\alpha}_{\perp}\Psi$ as the longitudinal and transverse relativistic current densities, respectively[108].

Therefore, the evaluation of the optical transition matrix elements is reduced to calculating the matrix elements of α_i.

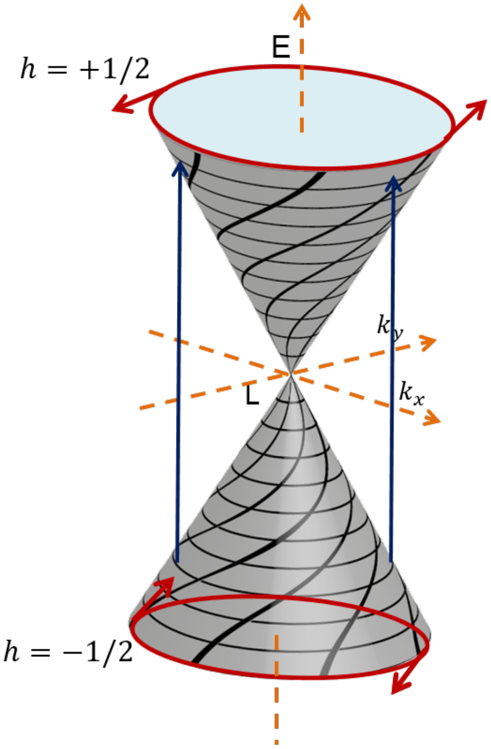

Figure 4.5: The interband transitions for the spin selection rules in 3D TIs. The Dirac cone represents the component of the Weyl states. The interband transitions occur between positive and negative energy solutions. The helicity of the band is represented by $h = +1/2$ ($h = -1/2$) for the positive energy solution (negative energy solution).

The optical transition matrix elements involve the integral over the envelope functions and the periodic part of the Bloch functions. The integral over the envelope function can be carefully separated out from the remaining part, similarly to the case of wide-bandgap semiconductor materials.[142] The idea is to separate the slowly varying envelope part from the rapidly varying periodic part of the total wavefunction. For that we need to first replace the position vector by $r = r' + R_m$, where R_m is a lattice vector and r' is a vector within one unit cell. Writing the vector potential $\mathbf{A} = (A_{x0}, A_{y0}, A_{z0})e^{i\mathbf{q}\cdot\mathbf{r}}$ and taking advantage of the periodicity $u_{\mathbf{k}}^{L^{\pm}}(r' + R_m) = u_{\mathbf{k}}^{L^{\pm}}(r')$ and the fact that $\phi_{\pm}^{L^{\pm}}(r' + R_m) \approx \phi_{\pm}^{L^{\pm}}(R_m)$, we obtain

$$\begin{aligned}
\langle \Phi_f \left| H_{int} \right| \Phi_I \rangle \approx\ & \frac{e}{m_0} \sum_m \left| F(z) \right|^2 e^{i(q+k_{\mathrm{I}}-k_{\mathrm{f}})\cdot R_m} \\
& \times \sum_i A_{i0} \int\limits_{\Omega} u_{k_{\mathrm{f}}}^{L^{-}*}(r') \hat{P}_i u_{k_{\mathrm{I}}}^{L^{+}}(r') \\
& \times e^{i(q+k_{\mathrm{I}}-k_{\mathrm{f}})\cdot r'} d^3 r' \\
& \times \left(\chi_{\mathrm{f}}^{L^{-}} \sigma_i \chi_I^{L^{+}} + \chi_f^{L^{+}} \sigma_i \chi_I^{L^{-}} \right)
\end{aligned} \tag{4.13}$$

for an optical transition from the initial state $|\Phi_I\rangle$ to the final state $|\Phi_f\rangle$. Ω is the volume of the unit cell. By applying the secular approximation to the term with the exponential function $e^{i(q+k_{\mathrm{I}}-k_{\mathrm{f}})\cdot R_m}$, we obtain $k_{\mathrm{f}} = q + k_{\mathrm{I}}$, which ensures momentum conservation in the plane of the interface. Using the normalization $\int_{-\infty}^{\infty} \left| F(z) \right|^2 dz = 1$, the optical matrix element is well approximated by

$$\begin{aligned}
\langle \Phi_f \left| H_{int} \right| \Phi_I \rangle \approx\ & \frac{e}{m_0} \sum_i A_{i0} \int\limits_{\Omega} u_{k_{\mathrm{f}}}^{L^{-}*}(r') \hat{P}_i u_{k_{\mathrm{I}}}^{L^{+}}(r') d^3 r' \\
& \times \left(\chi_{\mathrm{f}}^{L^{-}} \sigma_i \chi_I^{L^{+}} + \chi_f^{L^{+}} \sigma_i \chi_I^{L^{-}} \right) \\
=\ & e A_{z0} v_{\parallel} \left\langle \chi_f \left| \alpha_z \right| \chi_I \right\rangle \\
& + e A_{x0} v_{\perp} \left\langle \chi_f \left| \alpha_x \right| \chi_I \right\rangle \\
& + e A_{y0} v_{\perp} \left\langle \chi_f \left| \alpha_y \right| \chi_I \right\rangle .
\end{aligned} \tag{4.14}$$

Note that in contrast to semiconductor quantum wells where the overlap between electron and hole envelope wavefunctions is smaller than 1 in general, here the overlap between Weyl envelope wavefunctions is $\int_{-\infty}^{\infty} |F(z)|^2 \, dz = 1$. We assume that the wavelength of incoming photon is small compared to the lattice constant. This means we can use the dipole approximation: $\mathbf{A} \approx (A_{x0}, A_{y0}, A_{z0})$. Since there is no net momentum transfer the directions of the initial and final momentum vectors are the same; i.e. we consider only vertical transitions. For the α matrix elements we obtain the following interband matrix elements:

$$\langle \chi_+ | \alpha_x | \chi_- \rangle = 4i \sin\theta \qquad \langle \chi_+ | \alpha_y | \chi_- \rangle = -4i \cos\theta, \tag{4.15}$$

These transitions are vertical. The z-component of the matrix element of $\boldsymbol{\alpha}$ vanishes.

The Kane interband matrix element can be calculated explicitly. The periodic function $u_{\mathbf{k}}(\mathbf{r})$ can be written as $u_{\mathbf{k}}^{L^\pm} = \sum\limits_{\mathbf{G}} a_{L^\pm}(\mathbf{G}) e^{i\mathbf{G}\cdot\mathbf{r}}$, where $\mathbf{G}$ is the reciprocal lattice vector and $a_{L^\pm}(\mathbf{G})$ are the expansion cofficients for the $L^\pm$ bands. The Kane interband matrix elements can be evaluated as

$$\begin{aligned} \int\limits_{\Omega} u_{\mathbf{k}_\mathrm{f}}^{L^- *} \hat{\mathbf{P}} u_{\mathbf{k}_\mathrm{I}}^{L^+} d^3r = \sum_{\mathbf{G}_\mathrm{f}, \mathbf{G}_\mathrm{I}} \int\limits_{\Omega} e^{-i(\mathbf{G}_\mathrm{f} - \mathbf{G}_\mathrm{I})\cdot\mathbf{r}} d^3r \\ \times a_{L^-}^* (\mathbf{G}_\mathrm{f}) \, \mathbf{G}_\mathrm{I} a_{L^+} (\mathbf{G}_\mathrm{I}) \end{aligned} \tag{4.16}$$

For the vertical transitions $k_f \approx k_I$ and $\int\limits_{\Omega} e^{-i(\mathbf{G}_\mathrm{f} - \mathbf{G}_\mathrm{I})\cdot\mathbf{r}} d^3r = \delta(\mathbf{G}_\mathrm{f} - \mathbf{G}_\mathrm{I})$, we obtain

$$\int\limits_{\Omega} u_{\mathbf{k}}^{L^- *} \hat{\mathbf{P}} u_{\mathbf{k}}^{L^+} d^3r = \sum_{\mathbf{G}} a_{L^-}^*(\mathbf{G}) \mathbf{G} \, a_{L^+}(\mathbf{G}). \tag{4.17}$$

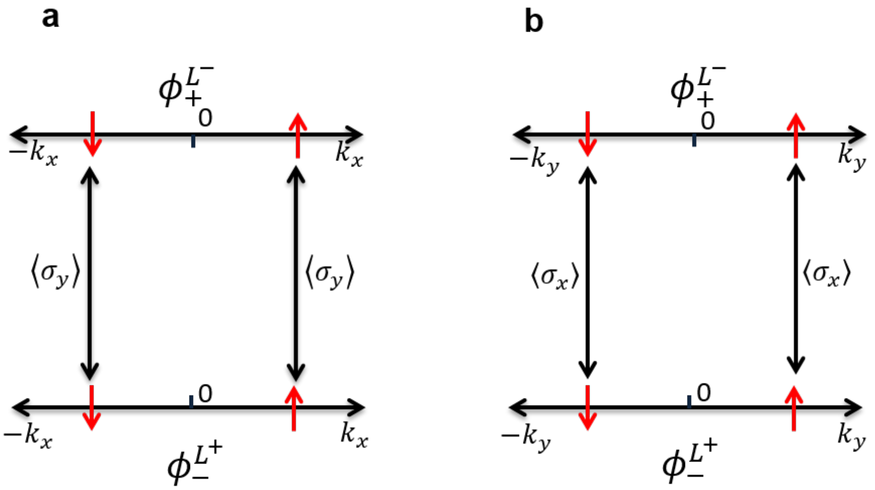
a
$\phi_+^{L^-}$
0
$-k_x$
k_x
$\langle\sigma_y\rangle$
$\langle\sigma_y\rangle$
0
$-k_x$
k_x
$\phi_-^{L^+}$
b
$\phi_+^{L^-}$
0
$-k_y$
k_y
$\langle\sigma_x\rangle$
$\langle\sigma_x\rangle$
0
$-k_y$
k_y
$\phi_-^{L^+}$

Figure 4.6: Spin selection rules in 3D TIs. The states are labeled with $\phi_{\pm}^{L^{\pm}}$. The transitions are vertical conserving the spin's direction. The direction of the momentum is shown along x-axis (a) in which case the polarization of the light couples the spin pointing along y-axis and along y-axis (b) in which case the polarization of the light couples the spin pointing along x-axis. In each case the spin points perpendicular to the momentum (see Figure 4.5).

The diagonal matrix elements of the interaction Hamiltonian give rise to the intraband transitions. As stated above, the intraband matrix elements operate on the envelope functions only and thus couple to the L^- band to itself and L^+ band to itself. In the electric dipole approximation the transitions within the same energy solutions are absent. The intraband matrix elements for the transitions occurring between the positive and negative energy solutions are given by

$$\begin{aligned} \langle \Phi_+ | \hat{\mathbf{e}}.\mathbf{p} | \Phi_- \rangle &= \left[\left\langle \chi_+^{L^-} \middle| \chi_-^{L^-} \right\rangle + \left\langle \chi_+^{L^+} \middle| \chi_-^{L^+} \right\rangle \right] \\ &\quad \times \langle F(\mathbf{r}) | \hat{\mathbf{e}}.\mathbf{p} | F(\mathbf{r}) \rangle , \end{aligned} \tag{4.18}$$

where the Bloch's functions are already integrated to unity. From the Eqs. (4.6) and (4.7), it is seen that the 2-component spinors for the same band corresponding to different energy solutions are orthogonal to each other: $\left\langle \chi_+^{L^-} \middle| \chi_-^{L^-} \right\rangle = 0$ and $\left\langle \chi_+^{L^+} \middle| \chi_-^{L^+} \right\rangle = 0$. This implies that $\langle \Phi_+ | \hat{\mathbf{e}}.\mathbf{p} | \Phi_- \rangle = 0$. This is, indeed, different from the case of wide bandgap semiconductor materials where we usually have both intraband and interband transitions.

In Figure 4.6 we show the possible transitions allowed by the spin selection rules. In each case transitions happen between the L^+ and L^- components of the positive and negative energy solutions. Since we use the dipole approximation initial and final momentum point in same direction and have the same magnitude; i.e. the transitions are vertical. If the momentum vector in one of the bands points along the x-axis, according the Eq. (4.15), the polarization of the photon couples to the spin pointing along y-axis. If the momentum vector in one of the bands points along the y-axis, the polarization of the photon couples to the spin pointing along x-axis. In each case the spin's direction is conserved.

4.5 Bandstructure calculation

In order to observe the band linearity at the crossing, it is important to calculate the complete bandstructures of $Pb_{1-x}Sn_xTe$, which also provides the cofficients of the periodic part of Bloch functions that appear in the selection rules. Figure 4.7 shows the calculations of the complete bulk bandstructures of $Pb_{1-x}Sn_xTe$ at 37.5% doping by Sn impurities in a supercell Brillouin zone using density functional theory within PAW approximation as implemented in VASP.[61, 143, 144] We unfold the bandstructures along the Γ to L point in the first Brillouin zone using unfolding recipes.[136]

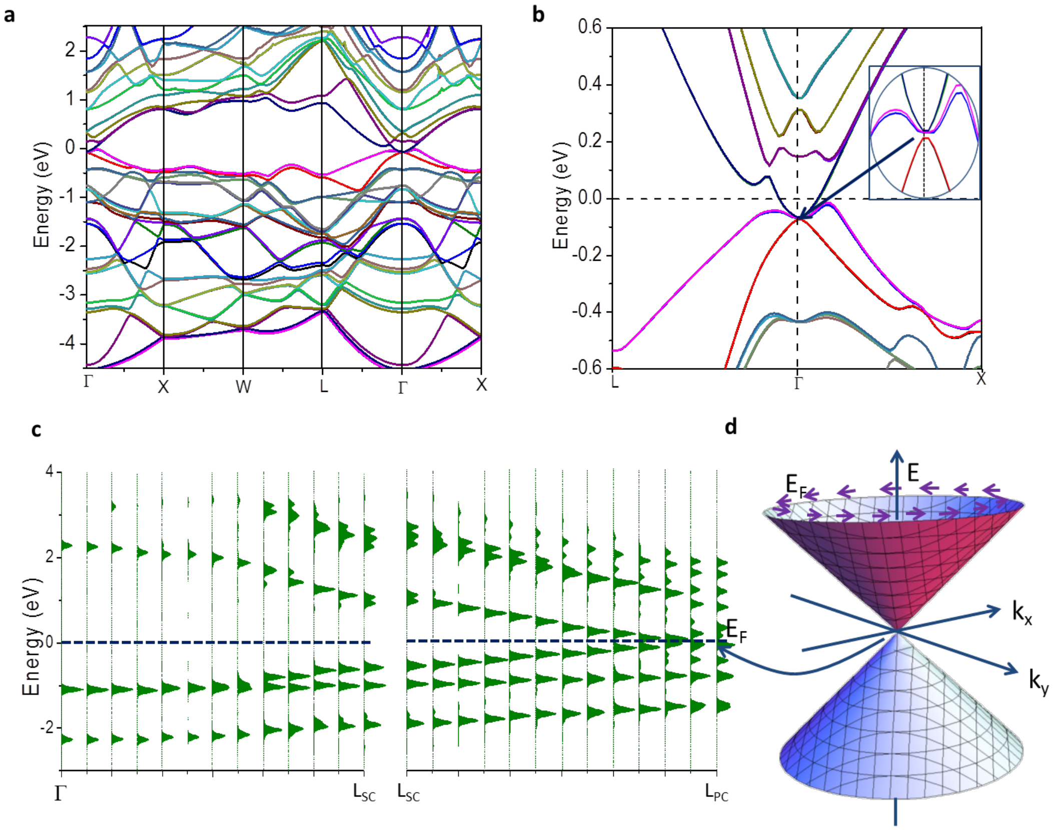

Figure 4.7: Bulk bandstructure of Pb$_{1-x}$Sn$_x$Te at $x = 0.375$ doping level including spin-orbit coupling. The crossing has been reported around $x = 0.35$. In the supercell Brillouin zone bands are folded from the neighboring Brillouin zones into the first Brillouin zone [(a) and (b)]. A small band gap of 1.8 meV appears at the Γ point of the supercell Brillouin zone, which corresponds to the band gap minimum at the L point in the primitive cell Brillouin zone after unfolding, as shown in **c**. L_{SC} and L_{PC} are L points in the supercell Brillouin zone and the primitive cell Brillouin zone, respectively. The solid green color peaks in (c) denotes the spectral functions. Bands of opposite parity nearly cross at around 67 meV below the Fermi level at the L point where a single Dirac point is observed (d).

The unfolded bandstructure is equivalent to the folded bandstructure in terms of the magnitude of band separation as required by the energy conservation law. The point L_{PC} in the unfolded bandstructure is a mirror image of the point Γ in the folded bandstructure, therefore, bands appear with the same dispersion as they were before unfolding. In the unfolded bandstructures, bands around the L point are almost linear, which is best described by Weyl fermions. The Dirac point appears at 67 meV below the Fermi level at the L point. The valence band maximum is derived from the p orbitals of Pb and Sn hybridized with the s orbital of Te and the conduction band minimum is derived from the s orbitals of Pb and Sn hybridized with the p orbital of Te. They have opposite parity, thus making interband transitions allowed. As measured in the experiment, the anisotropy in the crystal structure gives velocity components as $v_{\perp} = 4.2 \times 10^5$ m/s and $v_{\parallel} = 1.7 \times 10^5$ m/s.[135]

The localization length l_o for the Weyl states along z-axis can be obtained using our calculated band gap of 350 meV including spin-orbit coupling for PbTe. Using the band velocity, $v_{\parallel} = 1.7 \times 10^5$ m/s, we obtain $l_o = 0.32$ nm. This length measures the characteristic scale of the confinement of Weyl states along z-axis at the interface.

4.6 Faraday Effect for 3D TIs

In Refs. Leuenberger:2005,Leuenberger:2006,Seigneur:2011,Gonzalez:2010,Seigneur:2010 it has been shown that the single-photon Faraday rotation can be used for quantum spin memory and quantum teleportation and quantum computing with wide-bandgap semiconductor QDs. The conditional Faraday rotation can be used for optical switching of classical information[145]. A single-photon Mach-Zehnder interferometer for quantum networks based on the single-photon Faraday effect has been proposed in Ref. Seigneur:2008. In Ref. Berezovsky a single spin in a wide-bandgap semiconductor QD was detected using the Faraday rotation. It is evident from the calculation above that we have strict optical selection rules for the x and y polarization states of the photons. We show below that these strict optical selection rules give rise to a giant Faraday effect due to Pauli exclusion principle for 3D TIs using our continuum eigenstates.

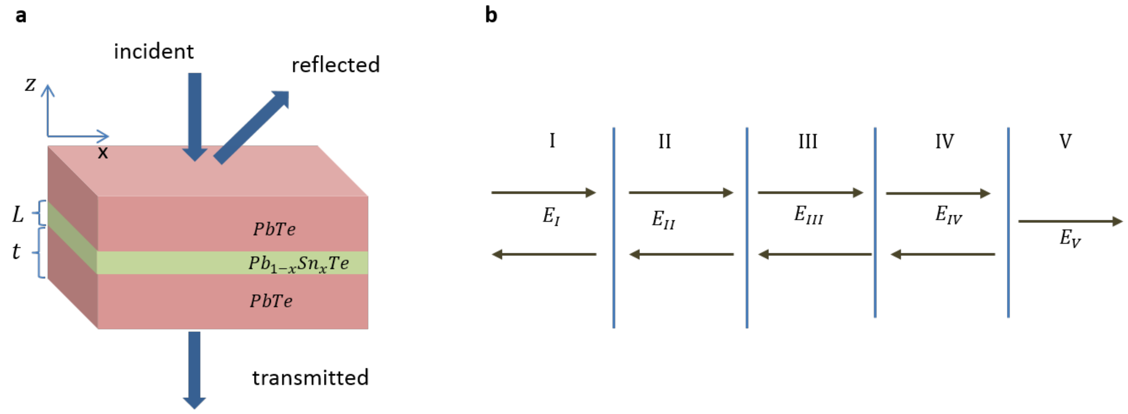

Figure 4.8: **a**. A slab of thickness $d = 10$ nm of 3D TI material $\mathrm{Pb}_{1-x}\mathrm{Sn}_x\mathrm{Te}$ is sandwiched by PbTe with thickness t. This structure can have Weyl fermions at the interface with zero bandgap at one of the L point in the Brillouin zone while the rest of the L points have non-zero bandgaps due to the interactions between the L valleys of the two interfaces. **b**. Solutions inside and outside the material can be found by dividing the geometry into five different regions, I, II, III, IV and V with the fields E_I, E_{II}, E_{III}, E_{IV} and E_V,

Let us consider the PbTe/$\mathrm{Pb_{0.31}Sn_{0.69}Te}$/PbTe heterostructure shown in Figure 4.8. A laser pump beam excites e-h pairs at the two interfaces between $\mathrm{Pb_{0.31}Sn_{0.69}Te}$ and PbTe. It is important to understand the working scheme of the driving fields and a dynamics of the hot carriers in the excited states so that maximum Faraday effect can be achieved in an experiment. The e-h pairs pumped by the driving field relax mainly through the electron-phonon interaction before they recombine. On a time scale of several hundred ps, the electrons and holes cool down after the driving field is turned off[**?**]. Due to the presence of the strong spin-orbit coupling in 3D TI, the induced spin polarization relaxes on a time scale of the momentum scattering. As calculated in Ref. [**?**], the spin polarization decays rapidly within a time of the order of T_2 =0.01–0.1 ps, which results in a loss of spin coherence. Consequently, it is very difficult to measure the Faraday effect after the pump pulse is turned off. To circumvent the problem of fast spin decoherence, we suggest to use both the pump and the probe fields simultaneously, thereby maintaining the coherence of the induced spin polarization in the excited states. Therefore, the probe field experiences a response from the spin polarized carriers. We use an off-resonant probe field with detuning energy of around 10 meV.

Let us write the light-matter interaction Hamiltonian as $H_{int} = ev\boldsymbol{\alpha} \cdot \boldsymbol{A}$, which contains the interband term only because the intaband term is zero, as shown in Sec. 4.4. Without loss of generality, the anisotropy coming from the band velocity can be introduced back into the solutions at a later time. Since the incident light is a plane wave with wave vector $\mathbf{q}$ and frequency ω and the electric field component is $E = -\partial\boldsymbol{A}/\partial t$, the interaction

Hamiltonian reads

$$H_{int} = \frac{ePE_0}{im_0\omega}\left(e^{i(\mathbf{q}\cdot\mathbf{r}-\omega t)} - e^{-i(\mathbf{q}\cdot\mathbf{r}-\omega t)}\right)\boldsymbol{e}\cdot\boldsymbol{\alpha} \tag{4.19}$$

where $P = m_0 v$ is the Kane interband matrix element. The transition rate can be calculated using Fermi's golden rule,

$$\begin{aligned} W_{fI} &= \frac{2\pi}{\hbar}\left(\frac{eE_0P}{m_0\omega}\right)^2 \left|\langle\Phi_f|\,\boldsymbol{e}\cdot\boldsymbol{\alpha}\,|\Phi_I\rangle\right|^2 \\ &\quad\times n_I(t)\left[1-n_f(t)\right]\delta\left(\varepsilon_f-\varepsilon_I\mp\hbar\omega\right) \end{aligned} \tag{4.20}$$

where $n_{I,f}$ is the population distribution function for the initial and final states, ε_F is the Fermi energy, $|\Phi_I\rangle$ denotes the initial Weyl state, $|\Phi_f\rangle$ denotes the final Weyl state, and the - sign in front of $\hbar\omega$ corresponds to absorption and the + sign to emission. Thus, the absorption of energy per spin state is $\mathcal{P} = \hbar\omega\sum_{I,f} W_{fI}$. Comparing with the total power $\mathcal{P} = 2\sigma_1\mathcal{A}E_0^2$ dissipated in the system area $\mathcal{A}$, where $\sigma = \sigma_1 + i\sigma_2$ is the complex conductivity, and including absorption and emission, it follows that the real part of the conductivity is

$$\begin{aligned} \sigma_1 &= \frac{\pi e^2P^2}{\mathcal{A}m_0^2\omega}\sum_{I,f}\left|\langle\Phi_f|\,\boldsymbol{e}\cdot\boldsymbol{\alpha}\,|\Phi_I\rangle\right|^2 \\ &\quad\times\left[n_I(t)-n_f(t)\right]\delta\left(\varepsilon_f-\varepsilon_I-\hbar\omega\right) \end{aligned} \tag{4.21}$$

which can be written in terms of the oscillator strengths $f_{fI} = \left(\frac{2P^2}{\hbar m_0\omega_{fI}}\right)\left|\langle\Phi_f|\,\boldsymbol{e}\cdot\boldsymbol{\alpha}\,|\Phi_I\rangle\right|^2$,

$$\sigma_1(\omega) = \frac{\pi e^2}{2m_0\mathcal{A}}\sum_{fI} f_{fI}\left[n_I(t)-n_f(t)\right]\delta\left(\varepsilon_f-\varepsilon_I-\hbar\omega\right) \tag{4.22}$$

Using the Kramers-Kronig relations $\sigma_2(\omega)$ can be obtained. It is important to note that $\sigma_1(\omega)$ is equivalent to the imaginary part of the dieletric function, $\epsilon(\omega)$. The physical significance of $\sigma_1(\omega)$ and $\sigma_2(\omega)$ appear in different way, $\sigma_1(\omega)$ being for the dissipiation while $\sigma_2(\omega)$ for the polarization.

We calculate now the Faraday rotation angle due to Pauli exclusion principle between the initial and final continuum states. In order to this, a strong π-pulse of the laser pump beam is used to excite e-h pairs. The direction of the polarization can be along $x-$and $y-$axis. The dynamics of the excitation of e-h pairs can be described by the optical Bloch equations [**?**]. Due to the large screening the exciton binding energies in perpendicular and parallel directions are small, i.e. $E_{b\perp} = 143$ μeV and $E_{b\|} = 1.68$ meV.[146] Therefore, we can safely neglect the Coulomb interaction. Then the time dependences of the polarization $P_{\mathbf{k}}$ and the electron population distribution $n_{e,\mathbf{k}}$ for the state $\mathbf{k}$ are given by

$$\frac{dP_{\mathbf{k}}}{dt} = i\varepsilon_g P_{\mathbf{k}} + i(n_{e,\mathbf{k}} + n_{h,\mathbf{k}} - 1)\omega_{R,\mathbf{k}}, \tag{4.23}$$

$$\frac{dn_{e,\mathbf{k}}}{dt} = -2Im(\omega_{R,\mathbf{k}} P^*_{\mathbf{k}}), \tag{4.24}$$

where $\varepsilon_g = \varepsilon_{e,\mathbf{k}} + \varepsilon_{h,\mathbf{k}}$ $\varepsilon_{e,\mathbf{k}}$ and $\varepsilon_{h,\mathbf{k}}$ are the electron and hole kinetic energies, respectively, in the state $\mathbf{k}$, and $\omega_{R,\mathbf{k}}$ is the Rabi frequency. An equation similar to Eq. (4.24) can be written for the hole distribution function $n_{h,\mathbf{k}}$. It is to be noted that $n_{h,\mathbf{k}} = n_{e,\mathbf{k}}$. In the rotating frame approximation, $P_{\mathbf{k}}(t) = \tilde{P}(t)e^{-i\varepsilon_g t}$ and $\omega_{R,\mathbf{k}}(t) = \omega_{o,\mathbf{k}} e^{-i\varepsilon_g t}$. Using this Eqs. (5.4) and (4.24) yield $d\tilde{\eta}_{\mathbf{k}}/dt = 2(n_{e,\mathbf{k}} - 1)\omega_{o,\mathbf{k}}$ and $\tilde{n}_{e,\mathbf{k}} = -2\omega_o\tilde{\eta}$, where $\tilde{\eta} = (\tilde{P} - \tilde{P}^*)/2i$. These two equations can be solved for $n_{e,\mathbf{k}}$. We obtain, $n_{e,\mathbf{k}} = \frac{1}{2}\left[1 - \cos(2\omega_{o,\mathbf{k}} t)\right]$. A similar solution can be obtained for $n_{h,\mathbf{k}}$. For $2\omega_{o,\mathbf{k}} t = m\pi$, $n_{e,\mathbf{k}} = 1$ if m is an odd integer, $n_{e,\mathbf{k}} = 0$ if m is an even integer, and $n_{e,\mathbf{k}} = 1/2$ if m is an odd half-integer. A strong π-pulse excites the maximum number of electrons so that $n_{e,\mathbf{k}} \approx 1$ with $2\omega_{o,\mathbf{k}}t \approx \pi$. In the absence of Coulomb interaction the Rabi frequency can be written as $\omega_{o,\mathbf{k}} = d_{fI}\mathcal{E}\cos\theta/\hbar$, where d_{fI} is a transitions dipole moment, $\mathcal{E}$ is the strength of the electric field and θ is the direction of polarization.

It is useful to estimate the value of the Rabi frequency. The amplitude of the electric field can be calculated as $|E_S| = \sqrt{2\mathcal{S}n/A\epsilon_o c}$, where $\mathcal{S}$ is the power of the laser, n is the index of refraction of the medium through which the light propagates and A is the area of the aperture of the laser source. A laser power of 0.5 mW with an area of the aperture of $10\,\mu m^2$ in a medium with $n = 5.8$ (for $\mathrm{Pb_{0.68}Sn_{0.32}Te}$ at room temperature) can produce an electric field of 4.67×10^5 V/m. Using $v_\perp = 4.2 \times 10^5$ m/s and the matrix elements from Eq. (4.15), we obtain a maximum Rabi frequency of $\omega_{o,max} = 5.89 \times 10^{12}$/s which occurs for $\theta = 0$ or π. During the pump beam a laser probe beam is incident on the double interface within the transparency region. The polarization of this probe beam experiences the Faraday rotation that we compute in the following.

The time dependence of the population becomes, $n_{e,\mathbf{k}} = \frac{1}{2}\left[1 - \cos\left(\frac{2d_{fI}\mathcal{E}\cos\theta t}{\hbar}\right)\right]$. The pump pulse duration, T_p, can be calculated using as $T_p = \pi\frac{\hbar}{2d_{fI}\mathcal{E}}$. Probe and pump pulses are illuminated simultaneously to circumvent the problem of decoherence of spin polarization, as described above. Therefore, the probe pulse experiences the response from the average spin coherent population distribution excited by the pump pulse. If the probe pulse has the duration of $T_r = T_p$, the average population distribution is calculated as, $\bar{n}_{e,\mathbf{k}} = \frac{1}{T_p}\int_0^{T_p} n_{e,\mathbf{k}}\,dt$ which gives $\bar{n}_{e,\mathbf{k}} = \frac{1}{2} - \frac{1}{2}\frac{1}{\pi\cos\theta}\sin(\pi\cos\theta)$. Since, $n_{v,\mathbf{k}} - n_{c,\mathbf{k}} = 1 - 2n_{e,\mathbf{k}}$, for $n_{v,\mathbf{k}} = n_I(t)$ and

$n_{c,\mathbf{k}} = n_f(t)$, the average of the net population distribution is $\overline{n_I(t) - n_f(t)} = \frac{1}{\pi\mathrm{cos}\theta}\mathrm{sin}(\pi\mathrm{cos}\theta)$. If the probe pulse has the duration of $T_r = T_p/10$ and lasts from the time $0.9T_p$ to the time T_p of the pump pulse, the average population distribution is $\bar{n}_{e,\mathbf{k}} = \frac{1}{T_r}\int_{0.9T_p}^{T_p} n_{e,\mathbf{k}}\ dt$, which gives $\bar{n}_{e,\mathbf{k}} = \frac{1}{2} - \frac{1}{2}\frac{10}{\pi\mathrm{cos}\theta}\mathrm{sin}(\pi\mathrm{cos}\theta) + \frac{1}{2}\frac{10}{\pi\mathrm{cos}\theta}\mathrm{sin}(0.9\pi\mathrm{cos}\theta)$. Thus, we obtain $\overline{n_I(t) - n_f(t)} = \frac{10}{\pi\mathrm{cos}\theta}\left[\mathrm{sin}(\pi\mathrm{cos}\theta) - \mathrm{sin}(0.9\pi\mathrm{cos}\theta)\right]$. These average populations give rise to the Faraday rotation of the probe field polarization.

Now we proceed to describe the Faraday effect due to the 2D Weyl fermions living at the interface of the 3D topological insulators. The difference in the phase accumulated for the x and y polarization of the light as it passes through the material is measured by the Faraday rotation angle, which is solely due to the difference in response of surface carriers to the x and y polarized light. This response of the surface carriers at the two interfaces between $\mathrm{Pb}_{0.31}\mathrm{Sn}_{0.69}\mathrm{Te}$ and PbTe is given by the optical conductivity tensor σ_{ij}, $i = x, y$, $j = x, y$, which can be calculated by means of Eq. (5.6). The interband matrix element, $|\langle\Phi_f|\,\boldsymbol{e}\cdot\boldsymbol{\alpha}\,|\Phi_I\rangle|^2$, for the linear polarization of light in x and y direction can be written as

$$\begin{aligned} |\langle\Phi_f|\,\boldsymbol{e}\cdot\boldsymbol{\alpha}\,|\Phi_I\rangle|^2 &= \Big[|\langle\Phi_f|\,\alpha_x\,|\Phi_I\rangle|^2 \\ &\quad +2\,\langle\Phi_I|\,\alpha_x\,|\Phi_f\rangle\,\langle\Phi_f|\,\alpha_y\,|\Phi_I\rangle \\ &\quad +|\langle\Phi_f|\,\alpha_y\,|\Phi_I\rangle|^2\Big]. \end{aligned} \tag{4.25}$$

The first and last terms of the RHS in Eq. (4.25) are the matrix elements that give rise to σ_{xx} and σ_{yy}, respectively, in x and y directions. The middle term gives rise toσ_{xy}. Using Eq. (4.25) and the average population distribution $\overline{n_I(t) - n_f(t)}$ after pumping using a linearly polarized light in x direction in Eq. (5.6), one can solve for σ_{xx} , σ_{yy} and σ_{xy}. The summation can be changed into the integration over the momentum space area, $\sum\limits_{fI} \longrightarrow \left[1/\Omega_{\mathbf{k}} \left(2\pi\right)^2\right] \int k\, dk \int d\theta$, $0 \leq \theta \leq 2\pi$, where $\Omega_{\mathbf{k}}$ is the cross sectional area of the Brillouin zone. Using $d\varepsilon = \hbar v_F dk$, k-space integration can be written as $\int k\, dk = [1/\hbar^2 v_F^2] \int \varepsilon d\varepsilon$, where $v_F = P/m_0$ is the Fermi velocity. As discussed above, here we calculate the conductivity tensors for two examples of pulse duration: $T_r = T_p$ and $T_r = T_p/10$. We obtain that $\sigma_{1xy} = 0$. This signifies that there is no transverse Hall effect with this type of population distribution. If the polarization of the pump pulse is in y direction the transverse conductivity is still zero. $\sigma_{1xx}\left(\omega\right)$ and $\sigma_{1yy}\left(\omega\right)$ are calculated as follows: using Eq. (5.6), we obtain

$$
\begin{aligned}
\sigma_{1xx}\left(\omega\right) &= \frac{16\pi e^2}{\omega_{fI}\hbar^2 \left(2\pi\right)^2} \int\limits_{2|E_F|}^{\infty} \int\limits_{0}^{2\pi} \varepsilon d\varepsilon \delta\left(\varepsilon_f - \varepsilon_I - \hbar\omega\right) \\
&\quad \times \overline{n_I(t) - n_f(t)} \sin^2\theta d\theta, \qquad (4.26) \\
\sigma_{1yy}\left(\omega\right) &= \frac{16\pi e^2}{\omega_{fI}\hbar^2 \left(2\pi\right)^2} \int\limits_{2|E_F|}^{\infty} \int\limits_{0}^{2\pi} \varepsilon d\varepsilon \delta\left(\varepsilon_f - \varepsilon_I - \hbar\omega\right) \\
&\quad \times \overline{n_I(t) - n_f(t)} \cos^2\theta d\theta. \qquad (4.27)
\end{aligned}
$$

Using the population distribution $\overline{n_I(t) - n_f(t)}$ obtained for $T_r = T_p$, Eqs. (4.26) and (4.27) yield $\sigma_{1xx}\left(\omega\right) = \sigma_{oxx}\Theta(\omega - 2\left|E_F\right|/\hbar)$ and $\sigma_{1yy}\left(\omega\right) = \sigma_{oyy}\Theta(\omega - 2\left|E_F\right|/\hbar)$ with $\sigma_{oxx} = 2.707\, e^2/\hbar$ and $\sigma_{oyy} = 0.725\, e^2/\hbar$. Using the population distribution $\overline{n_I(t) - n_f(t)}$ obtained for $T_r = T_p/10$, Eqs. (4.26) and (4.27) yield $\sigma_{1xx}\left(\omega\right) = \sigma_{oxx}\Theta(\omega - 2\left|E_F\right|/\hbar)$ and $\sigma_{1yy}\left(\omega\right) = \sigma_{oyy}\Theta(\omega - 2\left|E_F\right|/\hbar)$ with $\sigma_{oxx} = 0.926\, e^2/\hbar$and $\sigma_{oyy} = -2.952\, e^2/\hbar$. These results can be compared with the conductivity tensors obtained in case of a graphene sheet in Ref. Ferreira:2011. The difference here is that we have use the population distribution obtained by solving the optical Bloch equations, whereas in Ref. Ferreira:2011 the Fermi Dirac distribution function has been used.

Using Kramers-Kronig relation, $\sigma_2(\omega)$ can be calculated from $\sigma_1(\omega)$ according to

$$\sigma_2(\omega) = -\frac{2}{\pi}\mathcal{P}\int_0^\infty \frac{\omega\sigma_1\left(\omega^{'}\right)}{\omega^{'2}-\omega^2}\,d\omega^{'}, \tag{4.28}$$

where $\mathcal{P}$ denotes the Cauchy principle part of the integral. The measurement of the Faraday rotation angle is performed with the probe pulse with frequency in the transparency region. In the experiment, the probe pulse has an energy of $2\hbar\omega_F - \hbar\delta$, where $\hbar\omega_F$ is the Fermi energy and $\hbar\delta$ is the detuning energy. Therefore the width of the transparency region is given by $2\hbar\omega_F$. Thus, the Eq. (4.28) can be evaluated for $\hbar\omega \leq 2\hbar\omega_F$. There are poles at $\omega^{'} = \pm\omega$. Using $\sigma_{1xx}(\omega)$, Eq. (4.28) gives

$$\begin{aligned}\sigma_{2xx}(\omega) \quad &= \quad -\frac{2\sigma_{oxx}}{\pi}\lim_{\eta\to 0}\left[\int_0^{\omega-\eta}\frac{\omega\Theta(\omega^{'}-2\omega_F)}{\omega^{'2}-\omega^2}\,d\omega^{'}\right.\\ &\qquad \left.+\int_{\omega+\eta}^{\infty}\frac{\omega\Theta(\omega^{'}-2\omega_F)}{\omega^{'2}-\omega^2}\,d\omega^{'}\right],\end{aligned} \tag{4.29}$$

where η is an infinitesimal positive quantity. Since $\hbar\omega < 2\hbar\omega_F$, the first integral in Eq. (4.29) is zero. After evaluating the second integral we get

$$\sigma_{2xx}(\omega) = i\sigma_{oxx} + \frac{2\sigma_{oxx}}{\pi}\,\mathrm{arctan\,h}\left(\frac{2\omega_F}{\omega}\right) \tag{4.30}$$

We are in the transparency region for the probe pulse, which means $\frac{2\omega_F}{\omega} > 1$. The functionarctan h (z) can be then expanded in terms of a Maclaurin series at infinity, i.e. $\mathrm{arctan\,h}\,(\mathrm{z}) = -\frac{i\pi}{2} +$

$\sum_{n=1}^{\infty}\frac{z^{-2n+1}}{2n-1}$. Consequently, Eq. (4.30) yields

$$\sigma_{2xx}\left(\omega\right)=\frac{2\sigma_{oxx}}{\pi}\sum_{n=1}^{\infty}\frac{1}{2n-1}\left(\frac{2\omega_F}{\omega}\right)^{-2n+1}. \tag{4.31}$$

Similarly we obtain

$$\sigma_{2yy}\left(\omega\right)=\frac{2\sigma_{oyy}}{\pi}\sum_{n=1}^{\infty}\frac{1}{2n-1}\left(\frac{2\omega_F}{\omega}\right)^{-2n+1}. \tag{4.32}$$

As shown in Ref. Buczko:2012, there are interface bound states (IBS) localized at two decoupled interface states of a PbTe/Pb$_{1-x}$Sn$_x$Te/PbTe heterostructure with $d = 10$ nm grown in the [111] direction. It has been shown that the L-valley in [111] direction remains gapless while gaps are opened in the oblique L valleys due to the coupling of the IBS from the opposite interface states. Here we calculate the Faraday rotation angle produced by the Weyl fermions at the two interfaces with gapless L valley. We consider a structure with a slab of thickness d of 3D TI material Pb$_{1-x}$Sn$_x$Te sandwiched by PbTe with thickness t, as shown in Figure 4.8a. We choose the thickness of the slab to be $d = 10$ nm. A probe pulse linearly polarized along the $x + y$-direction and propagating along z-direction travels perpendicularly to the two interfaces. This probe pulse is partially reflected and partially transmitted at the boundaries. Solutions inside and outside the material can be solved by dividing the space into five different regions as shown in Figure 4.8b, where E_I, E_{II}, E_{III}, E_{IV} and E_V,are the fields in the region I, II, III, IV and IV, respectively. The solutions are

$$\mathbf{E}_I = \begin{bmatrix} E_{ax} \\ E_{ay} \end{bmatrix} e^{ik_I z} + \begin{bmatrix} E_{bx} \\ E_{by} \end{bmatrix} e^{-ik_I z}, \tag{4.33}$$

$$\mathbf{E}_{II} = \begin{bmatrix} E_{cx} \\ E_{cy} \end{bmatrix} e^{ik_{II} z} + \begin{bmatrix} E_{dx} \\ E_{dy} \end{bmatrix} e^{-ik_{II} z}, \tag{4.34}$$

$$\mathbf{E}_{III} = \begin{bmatrix} E_{ex} \\ E_{ey} \end{bmatrix} e^{ik_{III} z} + \begin{bmatrix} E_{fx} \\ E_{fy} \end{bmatrix} e^{-ik_{III} z}, \tag{4.35}$$

$$\mathbf{E}_{IV} = \begin{bmatrix} E_{gx} \\ E_{gy} \end{bmatrix} e^{ik_{II} z} + \begin{bmatrix} E_{hx} \\ E_{hy} \end{bmatrix} e^{-ik_{II} z}, \tag{4.36}$$

$$\mathbf{E}_V = \begin{bmatrix} E_{ix} \\ E_{iy} \end{bmatrix} e^{ik_I z}, \tag{4.37}$$

where $E_{\alpha x}$ ($E_{\alpha y}$), $\alpha = a, b, c, d, e, f, g, h, i$, are the x (y) components of the field amplitudes in regions I through V. k_I, k_{II} and k_{III} are the wave vectors in air (region I), in PbTe (region II and IV) and in $\text{Pb}_{1-x}\text{Sn}_x\text{Te}$ (region III), respectively. The incident probe pulse is polarized along the $x + y$-axis. Therefore $E_{ax} = E_{ay}$. For simplicity, we assume that the wave vectors within the material $\text{Pb}_{1-x}\text{Sn}_x\text{Te}$ and PbTe do not differ significantly and thus $k_{II} \approx k_{III}$.

Our geometry has a dimension of length $2t + d$ with top, bottom, and interface surfaces being parallel to the plane of polarization. Rotation of the polarization on the Poincare sphere is due to the charge carriers at the interfaces, which are excited by the pump pulse with energy at least twice the Dirac point energy measured from the Fermi level (see Figure 4.3). The accumulation of the phase difference is only due to surface carriers that come from the difference in the optical conductivity tensor for the x and y polarization of the light. There is no contribution to the phase shift in the polarization from the bulk. However, the index of refraction of the bulk leads to interference effects due to reflection and transmission at the boundaries. The Maxwell equations to be solved are given by[147]

$$\begin{aligned} \frac{\partial^2 E_i}{\partial z^2} &= i\omega\mu_o \left[\delta\left(z-t\right)+\delta\left(z-t-d\right)\right] \sum_{j=x,\,y} \sigma_{ij} E_j \\ &\quad + \omega^2 \epsilon_r \mu_o E_i, \end{aligned} \tag{4.38}$$

where μ_o is the permeability of the free space and ϵ_r is the dielectric constant of the material in the bulk. It is important to note that the delta functions ensure that the optical conductivity tensor originates only from the interface carriers. The optical conductivity tensor that enters Maxwell's equations is the imaginary part of $\sigma\left(\omega\right)$, i.e. $\sigma_2\left(\omega\right)$ [see Eqs. (4.31) and (4.32)], which gives rise to the dispersion of the incident light inside the material. The boundary conditions are determined by the continuity of the tangential components of the electric field and their derivatives at the boundaries of the materials at $z=0$, $z=t$, $z=t+d$ and $z=2t+d$. The details of matching of the fields at the boundaries are shown in Appendix A. The transmission amplitudes for x and y components of the electric field are calculated to be $T_{x,y}=E_{ix,iy}/E_a=\left|T_{x,y}\right|e^{i\theta_{x,y}}$, where $\left|T_{x,y}\right|$ is the transmission amplitude and $\theta_{x,y}$ are the Faraday rotation angles for the light polarized in x and y direction. T_x and T_y are given by

$$\begin{aligned} T_x &= 4k_I k_{II} e^{-ik_I(2t+d)} \\ &\quad / \Big\{ (k_I + k_{II}) e^{-ik_{II}t} \left[\alpha(k_{II}A_x + C_x) \right. \\ &\quad \left. + \beta(k_{II}B_x + D_x) \right] + (k_I - k_{II}) e^{ik_{II}t} \\ &\quad \times \left[\alpha(k_{II}A_x - C_x) + \beta(k_{II}B_x - D_x) \right] \Big\} \end{aligned} \tag{4.39}$$

$$\begin{aligned} T_y &= 4k_I k_{II} e^{-ik_I(2t+d)} \\ &\quad / \Big\{ (k_I + k_{II}) e^{-ik_{II}t} \left[\alpha(k_{II}A_y + C_y) \right. \\ &\quad \left. + \beta(k_{II}B_y + D_y) \right] + (k_I - k_{II}) e^{ik_{II}t} \\ &\quad \times \left[\alpha(k_{II}A_y - C_y) + \beta(k_{II}B_y - D_y) \right] \Big\} \end{aligned} \tag{4.40}$$

where $A_x(A_y)$, $B_x(B_y)$, $C_x(C_y)$ and $D_x(D_y)$ are the $x(y)$ components of the parameters A, B, C and D, respectively (see Appendix A). After solving Eqs. 4.39 and 4.40 for θ_x and θ_y, we write the Faraday rotation angle as $\theta_F = (\theta_x - \theta_y)/2$. The useful quantity, the total transmittance$\top$, which measures the energy of the electromagnetic field inside the material, can be defined as $\top = \left(|T_x|^2 + |T_y|^2\right)/2$.

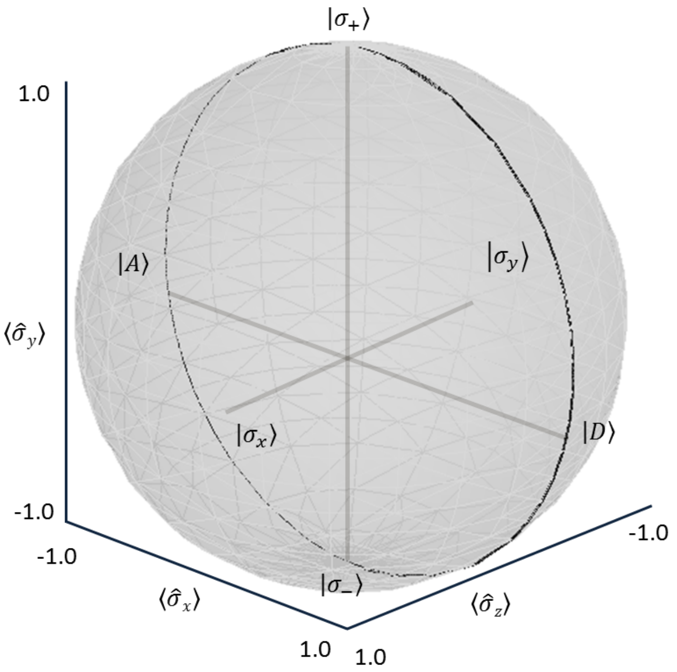

$|\sigma_+\rangle$
1.0
$|A\rangle$
$|\sigma_y\rangle$
$\langle\hat{\sigma}_y\rangle$
$|\sigma_x\rangle$
$|D\rangle$
-1.0
-1.0
-1.0
$\langle\hat{\sigma}_x\rangle$
$|\sigma_-\rangle$
$\langle\hat{\sigma}_z\rangle$
1.0
1.0

Figure 4.9: Illustration of the diagonal, $|D\rangle$ and anti-diagonal, $|A\rangle$ polarization in a Poincare sphere. $\langle\hat{\sigma}_x\rangle$, $\langle\hat{\sigma}_y\rangle$ and $\langle\hat{\sigma}_z\rangle$ are the expectation values of the Pauli matrices $\sigma_x = \begin{pmatrix} 0 & 1 \\ 1 & 0 \end{pmatrix}$, $\sigma_y = \begin{pmatrix} 0 & -i \\ i & 0 \end{pmatrix}$ and $\sigma_z = \begin{pmatrix} 1 & 0 \\ 0 & -1 \end{pmatrix}$, respectively. $|\sigma_x\rangle$ and $|\sigma_y\rangle$ represent the x- and y-polarization states and $|\sigma_+\rangle$ and $|\sigma_-\rangle$ represent the left and right circular polarization states of the photon .

From the bandstructure calculation we obtain that the Fermi level lies around 67 meV below the Dirac point. Therefore, we choose a transparency energy gap of $\hbar\omega_{cv} = 2\,|E_F|$, which is 134 meV in our calculation. A linearly polarized probe pulse with detuning energy of $\hbar\delta = 10$ meV, pulse duration of 1 ps and bandwidth of $\hbar\gamma = 4$ meV can be used. In Figs. 4.10 **a** and **b** we show the transmittance and the Faraday rotation angle for $T_r = T_p$. In Figs. 4.10 **c** and **d** the transmittance and the Faraday rotation for $T_r = T_p/10$ are shown. For the transmittance and the Faraday rotation angle as a function of thickness t the wavelength is chosen to be $\lambda = 9.97\ \mu m$. For the transmittance and the Faraday rotation angle as a function of wavelength λ the thickness of PbTe layers is taken to be $t = 1.720\ \mu m$. It is seen from the figures that the Faraday rotation angle follows exactly the transmittance. In particular, the maxima of the Faraday rotation angle occur at the maxima of the transmittance, which corresponds the case of nearly reflectionless slab in optics. There are two cases when reflection turns to zero. The first case is given by the half-wave condition when $w = m\lambda/2n$, n is an integer and $n_1 = n_2$. The second case is given by the quarter-wave condition when $w = (2m+1)\,\lambda/4n$, $n = \sqrt{n_1 n_2}$, where w is the total length of the slab, m is an integer, n, n_1 and n_2 are the indices of refraction of a slab of material and of the materials on either side of the slab, respectively. In our case the half-wave condition is met. Therefore, the resonances are seen (Figure 4.10**b** and d) inside the material at half-integer multiples of the probe wavelength divided by the index of refraction of the material, which is $n = 5.8$. Of course, Figure 4.10 exhibits a slight deviation from zero reflection at maxima due to the presence of multiple interfaces. The Faraday rotation angle obtained using a wide-bandgap semiconductor quantum dot is usually small compared to this result. [120]

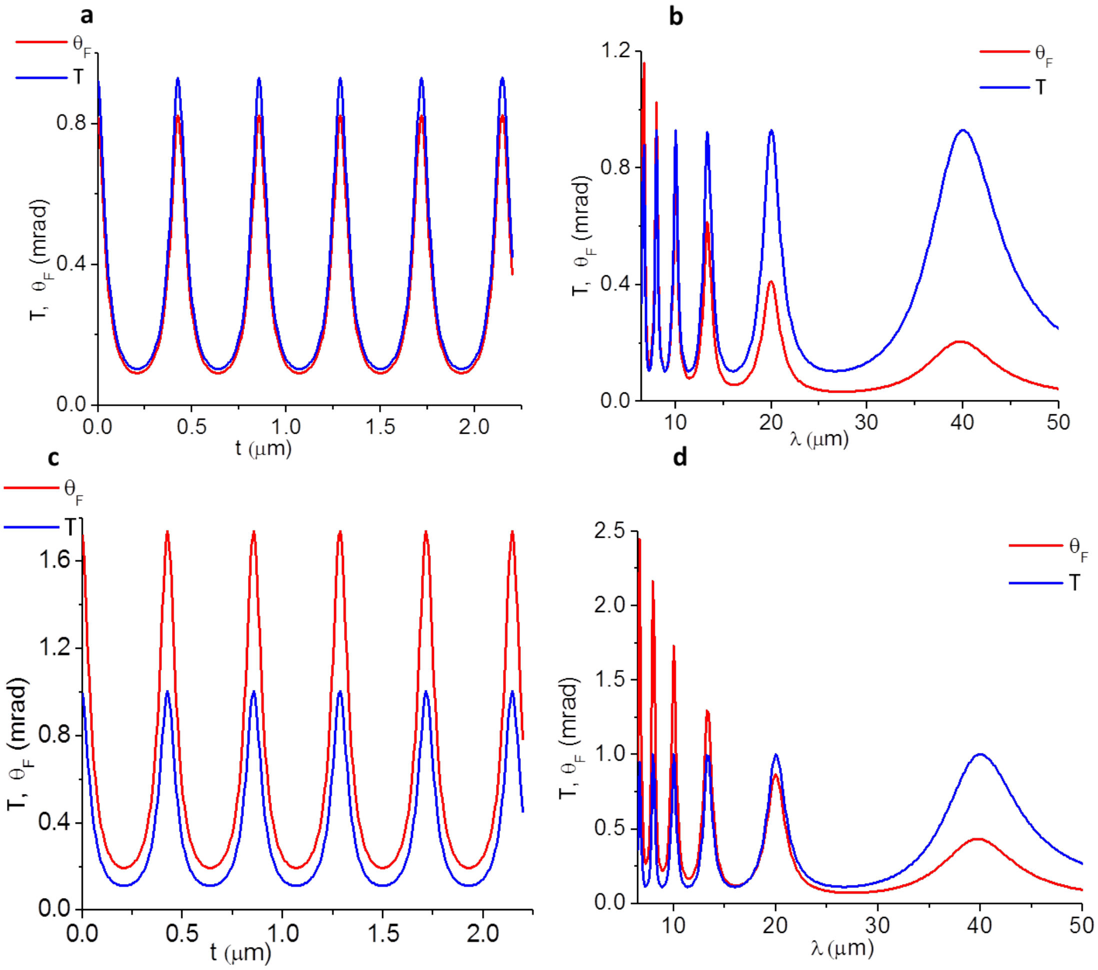

Figure 4.10: Transmittance and the Faraday rotation angle are plotted as a function of thickness t and wavelength λ for the geometry shown in Figure 4.8. In **a** and **b** we choose $T_r = T_p = 1$ ps, while in **c** and **d** we choose $T_r = T_p/10 = 1$ ps. For **a** and **c** the wavelength is $\lambda = 9.97\,\mu m$, which corresponds to a detuning energy of 10 meV. For **b** and **d** the thickness is $t = 1.72\,\mu m$. The width of the transparency region of the excitation of Weyl fermion is 134 meV, as calculated from the bandstructure as shown in Figure 4.7.

4.7 Conclusion

We have calculated the optical transitions for the Weyl interface fermions in 3D TI at the L point using the Dirac Hamiltonian. The spin selection rules for the optical transitions are very strict. The interaction Hamiltonian that comes from the quadratic part of the $\mathbf{k}.\ \mathbf{p}$ is included in the calculation and is shown to have zero contribution to the transition dipole moment.

We demonstrate the effect of the strict optical selection rules by considering the Faraday effect due to Pauli exclusion principle in a pump-probe setup. Our calculations show that the Faraday rotation angle exhibits oscillations as a function of probe wavelength and thickness of the slab material on either side of the 3D TI double interface of a PbTe/$\mathrm{Pb_{0.31}Sn_{0.69}Te}$/PbTe heterostructure. The maxima in the Faraday rotation angle are in the mrad regime.

CHAPTER 5
TRANSMISSION FROM THE MULTILAYER OF THREE DIMENSIONAL TOPOLOGICAL INSULATORS: A TRANSFER MATRIX METHOD

5.1 Introduction

In chapter II we described the change in frequency dependent dielectric function due to the Pauli exclusion principle. Depending on the density of the the excitation of the free electron-hole pairs in the semiconductor, there was a gradual shift in the dielectric function of the semiconductor that altered the dielectric environment of the plasmons excited at the metal-dielectric interface. The consequence was that the plasmons resonance peak shifted up to 125 nm at a density of the order of $10^{22}/\text{cm}^3$. In this process, change in the absorption can be understood from the dynamics of the photoexcited carriers. The incident light creates electron-hole pairs in the semiconductor, some of which recombine through various mechanisms such as Auger, radiative, and Shockley-Read-Hall processes. The incident photons excite carriers in the picosecond regime. The Auger and radiative recombination processes typically last from nanoseconds to microseconds.[1] Therefore, the photoexcited electron-hole pairs accumulate in the conduction and valence bands, which leads to a change in the absorption and/or refraction above and below the fundamental bandgap.[148] In ref [3] the Q value of the nanocavity is dynamically controlled in the range from 30000 to 12000 within picoseconds. This is possible due to the free carrier plasma effect that alters the index of refraction of the silicon-based photonic crystals. The change in the absorption happens on the same timescale as the duration of the optical pump pulse in the pump and probe technique.

The above-mentioned effects show that the photoexcited carriers in the bulk and nanostructures of semiconductor lead to many interesting phenomena. In Ref. [149], the transmissivity of electromagnetic waves through a stack of monolayer graphene sheets separated by dielectric slabs at low-terahertz frequencies has been reported. Such multilayer structures possess a series of bandpass and band-stop regions. In a breakthrough work of Nair et al.[6], it has been found that a single sheet of graphene absorbs 2.3% of incident white light. This is precisely the value of $\pi\alpha$, where α is the fine structure constant, showing that the graphene's optical properties are determined by α. This intriguing result is due to the 2D nature and the gapless spectrum of the surface carriers. A single sheet of graphene is atomically thin and thus does not carry as many carriers as bulk materials. When a beam of laser light with energy $\hbar\omega \geq 2E_F$ hits a 2D sheet of graphene, it excites electron-hole pairs. Here ω is the frequency of the laser light and E_F is the Fermi energy at Dirac point. Consequently, if the photon energy is kept constant, then the density of the excited carriers in graphene is small compared to the excited carriers density in the semiconductor bulk crystal. Therefore, a significant fraction of photons is transmitted through graphene.

Now, it is interesting to investigate similar effects on 2D surfaces of 3D topological insulators where the Weyl fermions are excited on the 2D surfaces/interfaces. Since the

Weyl fermions live on the surface, as in graphene, here also we expect that a significant number of photons passes through the sheet without absorption. Here we present our results that solve the general problem of transmission and reflection coefficients for many layers of 3D TI materials stacked on top of each other. Consider a 3D TI multilayer system with ABABAB... stacking style as shown in Figure. 5.1. The structure can be carefully engineered with PbTe/$\mathrm{Pb}_{0.31}\mathrm{Sn}_{0.69}$Te/PbTe interfaces grown perpendicular to the $x\,y$ plane, i.e. along the z-direction. In such a structure Weyl fermions are generated at each interface by means of a laser pulse with energy $\hbar\omega \geq 2\,|E_F|$. It is possible to tune the Fermi level using a gate voltage V_g as shown in Figure 5.2, so that a transparency regime can be reached in a controlled way. When $\hbar\omega \geq 2\,|E_F|$, there is absorption. Transmission close to unity is expected for $\hbar\omega < 2\,|E_F|$, i.e. when the incoming photon energy is below the Fermi energy.

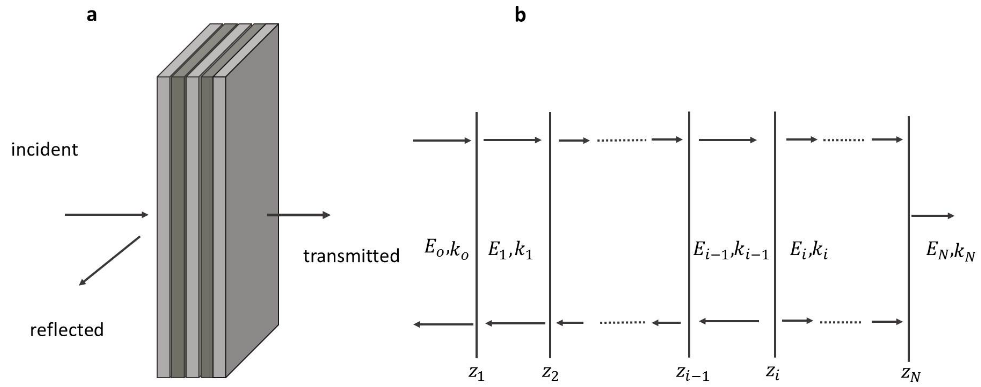

Figure 5.1: **a**, 3D TI layers stacked on top of each other to make a multilayer heterostructure consisting of PbTe/Pb$_{0.31}$Sn$_{0.69}$Te/PbTe. There are Weyl fermions at each interface that give rise to the large value of the surface conductivity. **b**, The multilayer system can be solved by using a transfer matrix method. In each layer there is a reflected and a transmitted field. The interface conductivity is modeled to be proportional to a delta function, which corresponds to the trapping of the Weyl fermions at each interface.

5.2 Transfer matrix method

Let z_1, z_2,.... z_N be the positions of the interfaces along the z-axis and E_1, E_2 .... E_{N-1} be the total electric fields in the layer regions with the corresponding wave vectors k_o, k_1, k_2.......k_{N-1} and k_N as shown in Figure 5.1 **a**. E_o and E_N are the incident and transmitted fields in the system with wave vectors k_o and k_N, respectively. The width of each layer is given by $d_i = z_i - z_{i-1}$. The polarization vector lies in the xy-plane. The component of the fields in the region just behind the $(i-1)^{th}$ and the ith interfaces can be written as

$$E_{i-1} = \begin{bmatrix} A_{i-1,\,x} \\ A_{i-1,\,y} \end{bmatrix} e^{ik_{i-1}z} + \begin{bmatrix} B_{i-1,\,x} \\ B_{i-1,\,y} \end{bmatrix} e^{-ik_{i-1}z}, \tag{5.1}$$

$$E_{i} = \begin{bmatrix} A_{i,\,x} \\ A_{i,\,y} \end{bmatrix} e^{ik_{i}z} + \begin{bmatrix} B_{i,\,x} \\ B_{i,\,y} \end{bmatrix} e^{-ik_{i}z}, \tag{5.2}$$

where $A_{i,\,x}$ and $A_{i,\,y}$ are, respectively, the x and y amplitudes of the right moving i^{th} field and $B_{i,\,x}$ and $B_{i,\,y}$ are, respectively, the x and y amplitudes of the left moving i^{th} field. The conductivity at each interface can be modeled to be proportional to a delta function that explicitly enters Maxwell's equations, as given by the Eq. 3.18. The boundary conditions are determined by the continuity of the tangential components of the electric field and their derivatives at each interface. The continuity of the field at z_i yields

$$a_o a_{i-1} A_{i-1,\,x} + a_o B_{i-1,\,x} = a_i A_{i,\,x} + B_{i,\,x}, \tag{5.3}$$

where $a_o = e^{i(k_i - k_{i-1})z_i}$, $a_i = e^{2ik_i z_i}$ and $a_{i-1} = e^{2ik_{i-1}z_i}$. The continuity of the derivatives of the field at z_i can be obtained by integrating the Eq. 3.18 and is given by

$$a_o a_{i-1} A_{i-1,\,x} k_{i-1} - a_o B_{i-1,\,x} k_{i-1} = a_i k_i^{'} A_{i,\,x} - k_i^{'} B_{i,\,x}, \tag{5.4}$$

where $k_i^{'} = k_i + \omega\mu_o \begin{bmatrix} \sigma_{1xx} \\ \sigma_{1yy} \end{bmatrix}$ is the effective wave vector in the medium. μ_o is the permeability of the free space. From Eq. 5.3 and 5.4 we obtain

$$\begin{bmatrix} A_{i-1} \\ B_{i-1} \end{bmatrix} = T_{i-1,\,i} \begin{bmatrix} A_{i} \\ B_{i}, \end{bmatrix} \tag{5.5}$$

where $T_{i-1,\,i} = \begin{bmatrix} T_{11} & T_{12} \\ T_{21} & T_{22} \end{bmatrix}$ is the transfer matrix across the ith interface and its elements are given by $T_{11} = \frac{a_i\left(k_{i-1}+k_i^{'}\right)}{2a_{i-1}a_o k_{i-1}}$, $T_{12} = \frac{a_i\left(k_{i-1}-k_i^{'}\right)}{2a_{i-1}a_o k_{i-1}}$, $T_{21} = \frac{a_i\left(k_{i-1}-k_i^{'}\right)}{2a_o k_{i-1}}$ and $T_{22} = \frac{\left(k_{i-1}+k_i^{'}\right)}{2a_o k_{i-1}}$. The matrix $T_{i-1,\,i}$ takes us across the ith interface.

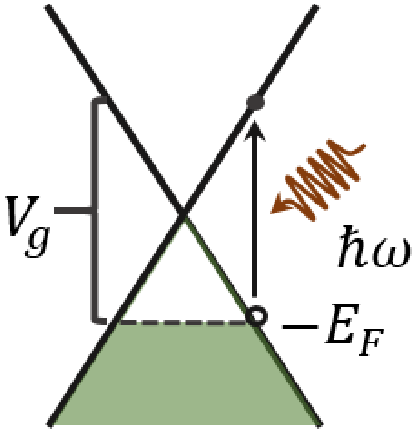

Figure 5.2: A gate voltage V_g can be applied to shift the Fermi level in a controlled way.

In the layer region, the transfer matrix is a diagonal matrix and is simply a propagator that takes us from the $(i-1)^{th}$ interface to the ith interface. The total transfer matrix across all the N layers is equal to the product of all the transfer matrices from the layer regions and across the interfaces, and is given by

$$T_{0,\,N} = T_{0,\,1}T_1T_{1,\,2}........T_{N-1}T_{N-1,\,N} = \begin{bmatrix} T_{11}^{0,\,N} & T_{12}^{0,\,N} \\ T_{21}^{0,\,N} & T_{22}^{0,\,N} \end{bmatrix}, \tag{5.6}$$

where $T_i = \begin{bmatrix} e^{ik_i d_i} & 0 \\ 0 & e^{ik_i d_i} \end{bmatrix}$ is the propagator from the $(i-1)^{th}$ interface to the ith interface. Using Eq. 5.6, we can write

$$\begin{bmatrix} A_o \\ B_o \end{bmatrix} = T_{o,\,N} \begin{bmatrix} A_N \\ B_N \end{bmatrix}. \tag{5.7}$$

The reflection coefficient $r_{o,\,N}$ and the transmission coefficient $t_{o,\,N}$ for the stack of N 3D TI layers can be written in terms of the matrix elements of the transfer matrix as $r_{o,\,N} = \frac{T_{21}^{0,\,N}}{T_{11}^{0,\,N}}$ and $t_{o,\,N} = \frac{1}{T_{11}^{0,\,N}}$. Transmittance and reflectance are given by $T_{tr} = |r_{o,\,N}|^2$ and $R_{ref} = |t_{o,\,N}|^2$, respectively.

5.3 Transmission through 3D TI multilayers

As an example, consider the ABA... stacking consisting of PbTe/Pb$_{0.31}$Sn$_{0.69}$Te/PbTe. Such heterostructures can be engineered with $d_i \approx 10$ nm. The wave vector in the alternate region is the same, i.e. $k_i = k_{i+2}$. We can define the unit cell of a AB stack, which has a transfer matrix of the form of $T_1 T_{12} T_2 T_{23}$. It repeats itself $N/2$ times in a system with N interface. To model such a system, it is essential to calculate the conductivity tensor that accounts for the response of the carriers to the incoming photons at the interfaces. It is important to note that there is no contribution to the conductivity tensor from the bulk carriers in our model.

If the incoming photon energy is larger than twice the Fermi energy, the photon is absorbed and that leads to a decrease in the transmittance. The real part of σ accounts for the absorption. Therefore, the absorption can be calculated by means of the equation

$$\sigma_1 = \frac{\pi e^2 P^2}{V m_0^2 \omega} \sum_{I,f} \left| \langle \Phi_f | \boldsymbol{e} \cdot \boldsymbol{\alpha} \, | \Phi_I \rangle \right|^2 \times \left[n_I(t) - n_f(t) \right] \delta \left(\varepsilon_f - \varepsilon_I - \hbar\omega \right). \tag{5.8}$$

Using the matrix elements given in chapter 5 section 5.4, and transforming the summation as $\sum\limits_{fI} \longrightarrow \left[1/\Omega_{\mathbf{k}} \left(2\pi\right)^2 \right] \int k\, dk \int d\theta$, $0 \le \theta \le 2\pi$, we obtain

$$\sigma_{1xx} = \frac{4e^2}{\pi \hbar^2 \omega_{fI}} \int_0^{2\pi} d\theta \sin^2\theta \int_{2|E_F|}^{\infty} \varepsilon d\varepsilon \delta(E_f - E_I - \hbar\omega), \tag{5.9}$$

$$\sigma_{1xx} = \sigma_{1yy} = 4\frac{e^2}{\hbar^2} \theta \left(\omega - 2\omega_F \right) \tag{5.10}$$

where the integration was performed above $2\,|E_F|$.

σ_2 accounts the dispersion of the photons. Therefore, while calculating σ_2 the above integration can be performed below the Fermi level. Using the Kramers-Kronig transformation relation, σ_{2xx} and σ_{2yy} can be calculated as

$$\sigma_{2xx} = \sigma_{2yy} = 4\frac{e^2}{\hbar^2} \left[i + \frac{2}{\pi} \arctan \left(\frac{2\omega_F}{\omega} \right) \right]. \tag{5.11}$$

Let us take the Fermi energy to be $2\hbar\omega_F = 350$ meV. This is also the bandgap of PbTe. We further assume that wavelength of incoming photon is in the telecommunication regime. Taking $\lambda = 10\ \mu m$, (123 meV) we obtain that $\sigma_{2xx} = \sigma_{2yy} = 2.2784 \times 10^{-4}$ S and $\sigma_{1xx} = \sigma_{1yy} = 9.752 \times 10^{-4}$ S. Using these values, we calculate the transmittance from 75 unit cells (AB stacking). Each unit cell is repeated periodically.

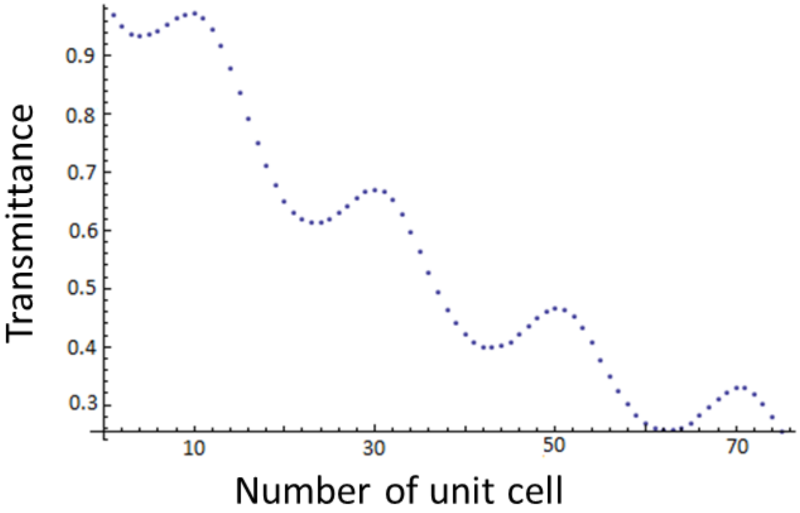

Figure 5.3: Transmittance plotted as a function of the number of unit cell (number of AB stacking). Transmittance decreases as the number of interface layers increases. Each layer has a width of $d \approx 10$ nm along the growth direction.

Figure 5.3 shows the plot of transmittance as a function of the number of AB stacks in the multilayer structure. The transmittance decreases as the number of layer increases. It indicates that a large number of layers in the multilayer stacking are needed for the complete absorption of the photon. This can be understood from the fact that the density of the carriers available for absorbing photons at each interface is small. Therefore, the photons travel through many layers before they are completely absorbed by the carriers at the interfaces. This is also the case in graphene and is posing a challenge in making devices where strong absorption is required.

In conclusion, we calculated the conductivity for the Weyl fermions at the interface of the heterostructure consisting of PbTe/Pb$_{1-x}$Sn$_x$Te/PbTe. The result for the transmittance through a single interface of PbTe/Pb$_{1-x}$Sn$_x$Te/PbTe shows that each interface absorbs photons only weakly. The transmittance through 75 interfaces shows that there is still a transmission of about 30% of the total number of incident photons.

CHAPTER 6
TWO DIMENSIONAL LAYERED MATERIALS

6.1 Introduction

One of the most recent focused topics in physics, chemistry, and engineering is the understanding of material properties of a single layer of 2D materials such as MoS_2 and engineering them to design low power electronic and optoelectronic devices. One of the most important questions is whether it would be possible to realize metallic, semiconducting, and insulating phases of matter in a single 2D sheet of MoS_2 without combining multiple materials of each phase. The atomically thin MoS_2 single sheet is sensitive to external control. Theoretical studies predict that, owing to its lower symmetry, strain engineering can be used to tune the MoS_2 bandgap, which can in turn modulate the electrical and optical properties. Application of strain in a single sheet of MoS_2 leads to transition from direct to indirect bandgap. The electronic structure modification of MoS_2 in a recent experiment has been found to be possible by strain engineering.[150]

In this chapter, we present an approach to continuously tune the electrical and optical properties of single layer MoS_2 FET from semiconducting regime to insulating regime using an external control. Dr. Khondaker's group performed experiments on MoS_2 based on this novel approach and we provided the theoretical explanation of the experimental results. The main idea of the approach is to treat a single sheet of MoS_2 with oxygen plasma (O_2:Ar mixture of 20:80) for different exposure time. In the experiment, the mobility, current, and resistance of a single layer MoS_2 FET were found to vary exponentially by up to four orders of magnitude. In addition, photoluminescence was changed from high intensity to complete quenching as the plasma exposure time increases. Raman studies confirmed that there is a formation of MoO_3 peaks with the creation of Mo-O bonds. During the exposure to oxygen plasma, the energetic oxygen molecules knock out the sulfur atoms from MoS_2 and create MoO_3 rich defect regions, which are insulating. As the plasma exposure time increases, the MoO_3 defect regions increases inside MoS_2. To confirm this, we performed density functional theory (DFT) calculations and showed that MoO_3 is stable inside MoS_2.

6.2 Electrical property tuning of MoS_2 single sheet

6.2.1 Results from the experiments

Figs. 6.1 (a) and 6.1 (b) show optical micrograph and atomic force microscopy (AFM) topography images of a single layer flake on a Si/SiO_2 substrate. The flake is 0.9 nm thick, corresponding to a single layer.[151, 152] This was also confirmed by Raman spectroscopy, as shown in Figure 6.1 (c). Two modes E^1_{2g} and A_{1g} corresponding to in plane and out of plane vibrations of Mo and S atoms with difference of 19.28 / cm were observed. Figure 6.1

(d) shows the mobility of the device after different plasma exposure time. The drain current at all gate voltages was found to decrease with increasing oxygen plasma exposure time.

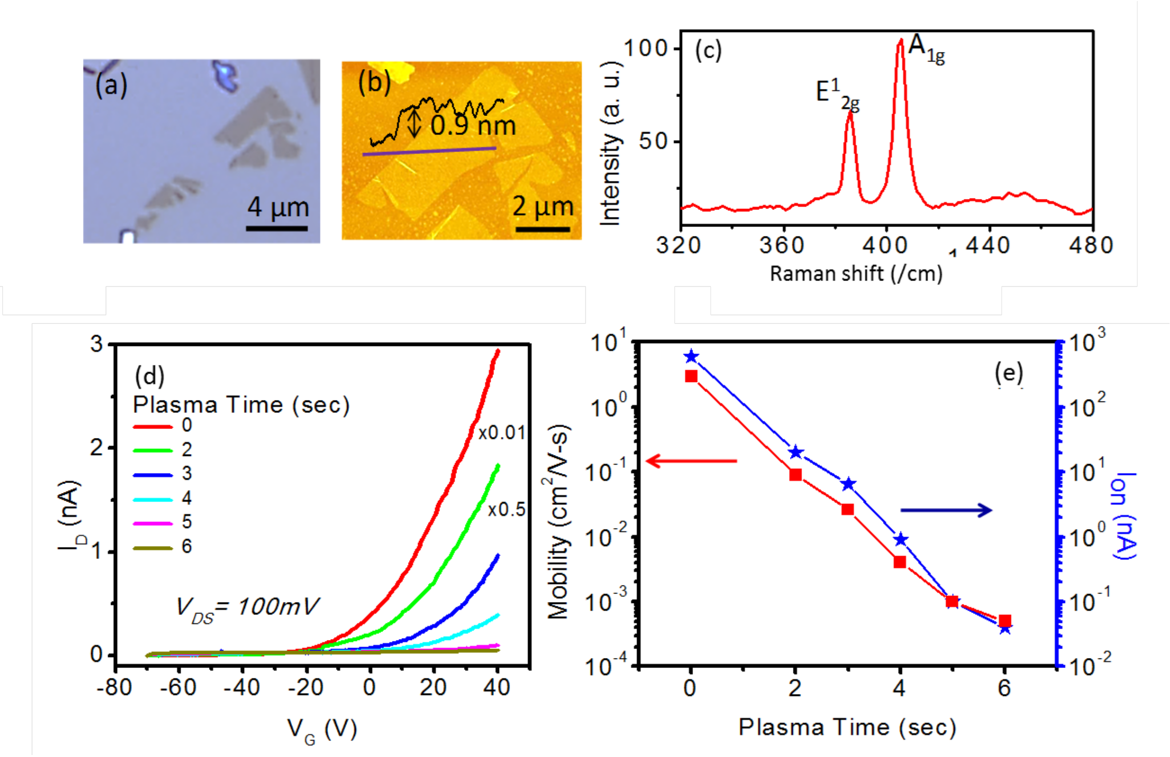

Figure 6.1: (a) and (b) Optical micrograph and AFM image of a single layer MoS_2 flake exfoliated on Si/SiO_2 substrate. (c) Raman spectrum of the single layer MoS_2. (d) Gate dependence of the source drain current (ID) after different plasma exposure time. (e) Effect of plasma exposure on the on-current (at $V_G = 40$ V) and mobility of the single layer MoS_2 device (These results were obtained by Dr. Khandaker's group).

The current at a gate voltage of $V_G = 40$ V is shown in Figure 6.1 (e) in a semi-log scale. The drain current was 285 nA for the fabricated sample, which decreased exponentially with time to a value of less than 20 pA after only a total of 6 s plasma exposure time. The mobility of the device after each plasma exposure is also calculated from the I_D-V_G curves in Figure 6.1 (d), and is plotted in Figure 6.1 (e) in a semi-log scale. The mobility also drops exponentially from 6 cm^2 /Vs for the fabricated sample to 4x10^{-4} cm^2 /Vs after the 6 s plasma exposure.

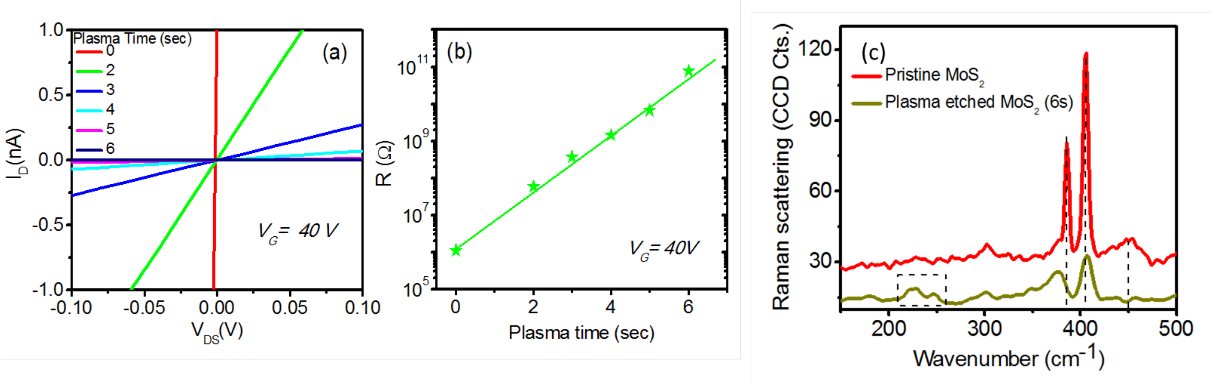

Figure 6.2: (a) I_D vs V_{DS} characteristics curve for the single layer MoS$_2$ device after different plasma exposure time. (b) Resistance of the device as a function of plasma exposure time. The green line is the linear fit of the logarithmic resistance as a function of exposure duration. (c) Raman spectra of pristine MoS$_2$ (red) and plasma etched MoS$_2$ (green) obtained with a 532 nm excitation wavelength.

Figure 6.2 (a) shows the I_D vs V_{DS} graph of the device at V_G = 40 V for different plasma exposure time. It is observed that at all exposure times, the I_D vs V_{DS} curves are linear around the zero bias representing Ohmic behavior from which we can measure the resistance. Figure6.2 (b) shows the dependence of resistance with respect to plasma exposure time. The resistance increased up to five orders of magnitude with increasing plasma exposure. The logarithmic plot in Figure 6.2 (b) demonstrates that the resistance increases exponentially upon plasma exposure. Similar changes in resistance were also observed for other gate voltages. This can be described by an effective medium model that shows the exponential increase in the resistance as a function of plasma exposure time and leads to the gradual increase of the tunnel barrier raised by the effective medium semiconductor (EMSC) material made of MoS_2 and strain-inducing MoO_3 rich defect regions.

Raman spectroscopy can be used to confirm the formation of different phases of the material during the plasma treatment in the experiment. In Figure 6.2 Raman spectra of a same single layer MoS_2 flake before (red curve) and after 6 s of oxygen plasma treatment (green curve) is shown. The pristine MoS_2 flake has two Raman modes at E_{2g}^1 (~385 cm^{-1}) and A_{1g} (~410 cm^{-1}) which diminish in amplitude after exposure of the flake to plasma. The appearance of other peaks in the range of 150-400 cm^{-1} indicates the formation of Mo-O bonds in the system.

6.2.2 Theoretical calculation

In order to understand the above experimental results, we present our calculations based on density functional theory (DFT) as implemented in the atomistic tool kit (ATK) program. A 2D layer of MoS_2 has Mo atoms sandwiched by the S atoms with honeycomb lattice structure as shown in Figure 6(a). Two (0001) MoS_2 layers bind weakly through van der Waals interaction, making mechanical exfoliation along the c direction possible. In contrast, MoO_3 has orthorhombic layered structure with separate layers stacked along the b direction. A single sheet of MoO_3 consists of bilayers with both sides terminated with O atoms, as shown in Figure 6(b). The interlayer is bridged by O atoms along the [100] direction. Due to the O atom termination of the single sheet of MoO_3 on both sides, there is a weak van der Waals bond that connects two sheets, as in the case of MoO_3, but along the [010] direction.

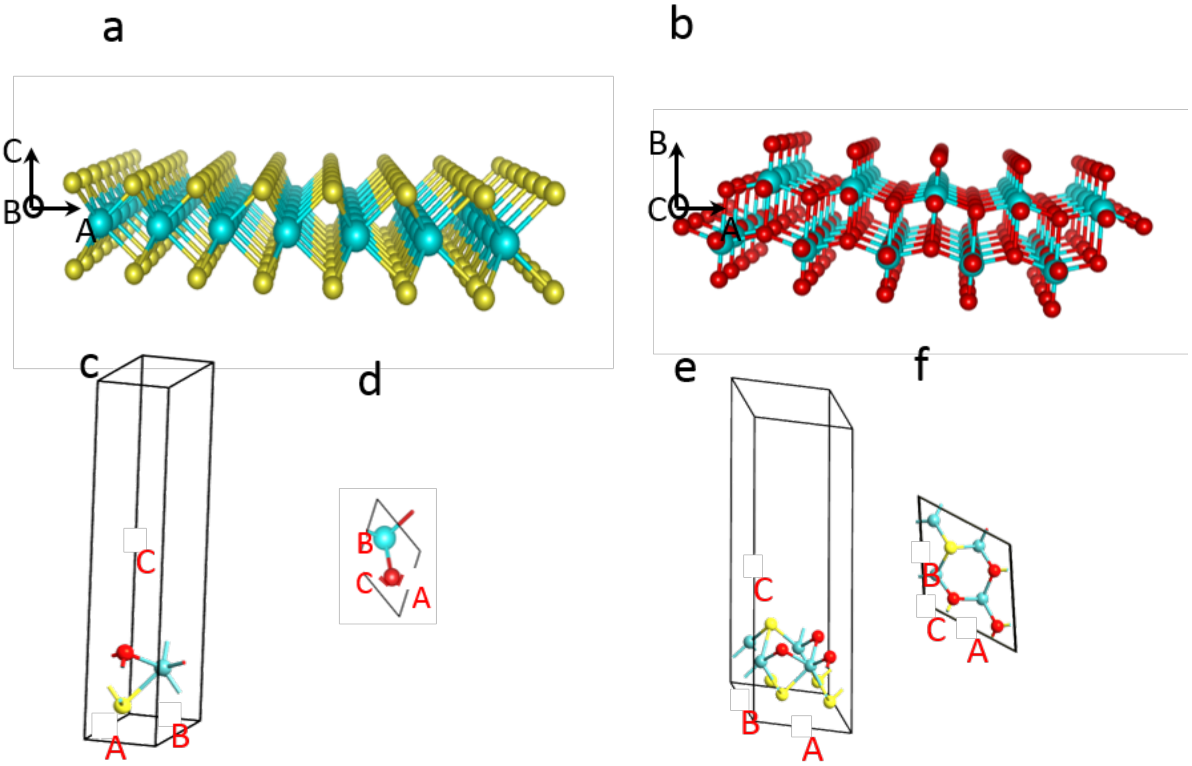

Figure 6.3: A single sheet of (a) MoS_2 and (b) MoO_3. (c) Side and (d) top view of the optimized structure of MoS_2 with a single O atom (red) replaced by a single S atom (yellow) in the unit cell. (e) Top and (e) side view of the optimized structure of MoS_2 with three S atoms replaced by three O atoms in a 2x2 supercell, where it is evident that the covalent bonds form between one of the Molybdenum atoms (cyan) and the three O atoms forming a stable MoO_3 defect .

The introduction of MoO_3 defects in a single layer of MoS_2 results in significant lattice distortions. Our results show that MoO_3 rich defect regions can be created when oxygen is introduced and that MoO_3 defects are stable inside MoS_2, which is in line with the Raman spectra shown in Figure 6.2. Figs. 6.3 (c), (d), (e) and (f) show the change in lattice structures in the MoS_2 2D sheet when few oxygen O (red) atoms replace the covalently bonded S (yellow online) atoms. First we replace one S atom by an O atom in the 2D unit cell and optimize the structure (Figure 6c). We find that the original plane of MoS_2 is distorted and the O atom is shifted by a distance of 0.32 Å along the c direction after optimization. In addition, the O atom covalently bonds with the Mo (grey online) atom by forming a molybdenum oxysulphide (MoOS). We then replace three S atoms by three O atoms within a 2x2 supercell (doubling the lattice constant of the unit cell along the a and b directions). Figs. 6 (e) and (f) show the configuration from the side and top view, respectively. As O atoms form bonds with the Mo atom, the original plane of the S atoms is distorted. After optimization, it is evident that the covalent bonds form between one of the Mo atoms and the three O atoms, providing evidence for the stable configuration containing a MoO_3 defect. The formation of MoO_3 is in agreement with the experimental data from the Raman spectroscopy. This structural deformation leads to an increase of resistance and decrease of mobility. Thus, the DFT analysis shows an evidence about the presence of MoO_3 defects along with their surrounding lattice distortions due to oxygen plasma.

The DFT analysis presented in Figure 6.3 shows conclusive evidence about the presence of MoO_3 defects along with their surrounding lattice distortions due to oxygen plasma. It is clear that the effect of the plasma treatment on the structure of the MoS_2 layer is not homogeneous, it forms regions with variable concentration of MoO_3 defect regions in MoS_2 and forms a complex network of heterojunctions that affect the electron transport.

For a qualitative description of the effect of such complex network on resistance, we adopt the approximation of an effective medium, which regards the plasma-treated material as an EMSC (see Appendix C). For simplicity, we assume the EMSC has a homogeneous structure whose work function depends on plasma exposure time (τ). Thus we effectively have a heterostructure of EMSC-MoS_2. The electron transport through EMSC-MoS_2 interface is determined by the respective band bending and the built-in potential $\triangle\phi$, which depends on the concentration of defects and, therefore, depends on the plasma exposure time. It is natural to assume that with an increasing concentration of defects the built-in potential evolves towards its limiting value characterizing MoS_2-MoO_3 interface ($\tau \rightarrow \infty$). Thus the maximal value of $\triangle\phi$ can be estimated using Anderson's rule:

$$\triangle\phi_{max} = \phi_{MoO_3} - \phi_{MoS_2} \approx 2\,eV \tag{6.1}$$

where $\phi_{MoO_3} \approx 4.9$ eV and $\phi_{MoS_2} \approx 6.9$ eV are respective work functions. The values of ϕ_{MoO_3} and ϕ_{MoS_2} reported in the literature vary noticeably but in any case $\triangle\phi_{max} > 1$ eV can be expected. Such strong built-in potential results in great increase of resistance $R_{max}/R(0) = exp\{\triangle\phi_{max}/k_B T\} \sim 10^{12}$, k_B where is the Boltzmann constant and T is temperature (see Appendix C for details). This is well above the values of $\sim 10^4$ measured in the experiment and suggests that our final EMSC is not a crystalline MoO_3 sheet, in agreement with physical characterization. Rather, our experiment suggests that $\triangle\phi$ varies with plasma exposure time and should have values: $0 \leq \triangle\phi(\tau) \ll \triangle\phi_{max}$. Taking this circumstance into account we can expand $\triangle\phi(\tau)$ in series with respect to τ and keeping only the linear term we present $\triangle\phi(\tau) = \alpha\tau$, where α is the rate at which the barrier increases. Thus we obtain

$$ln\left(R\left(\tau\right)/R\left(0\right)\right) \sim \frac{\alpha\tau}{k_B T} \tag{6.2}$$

for the dependence of resistance on the plasma exposure time. It is interesting to note that the result obtained from this rather simple model is in excellent agreement with our experimental results shown in Figure 6.2 (b), with $\alpha = 6\times10^{-2}eV/s^{-1}$. This calculation also suggests that with longer oxygen plasma exposure the work function of the exposed region increases. For the same reason the mobility and on-current decreases with plasma exposure time.

6.3 Photoluminescence tuning of MoS_2 single sheet

The result from the experimental observation using Raman spectroscopy (Figure 6.2) provided a clue for the formation of MoO_3 rich defect regions in a single sheet of MoS_2. When an energetic oxygen plasma reacts with the MoS_2 molecule, due to high kinetic energy, plasma knocks out sulfur atoms bonded with molybdenum atom and replaces them with oxygen atoms. The reaction follows $2MoS_2+7O_2 \longrightarrow MoO_3+4SO_2$.[153] The oxidation state of Mo in MoO_3 is Mo^{6+}, which has been confirmed in X-ray photoelectron microscopy (XPS).[154] The oxygen plasma oxidizes the surface of MoS_2, thereby forming a metal trioxide bonding in the 2D sheet. The excessive supply of the energetic oxygen plasma can oxidizes both Mo and S, leading to a complete structural distortion of the lattice in all direction. Here we show theoretical and experimental evidence of quenching of the PL after the single-layer of MoS_2 is treated for few seconds with oxygen plasma. The results presented here underline the importance of studying the effect of external control on MoS_2 monolayers and the great impact of oxygen plasma treatment on the material properties of the monolayers.

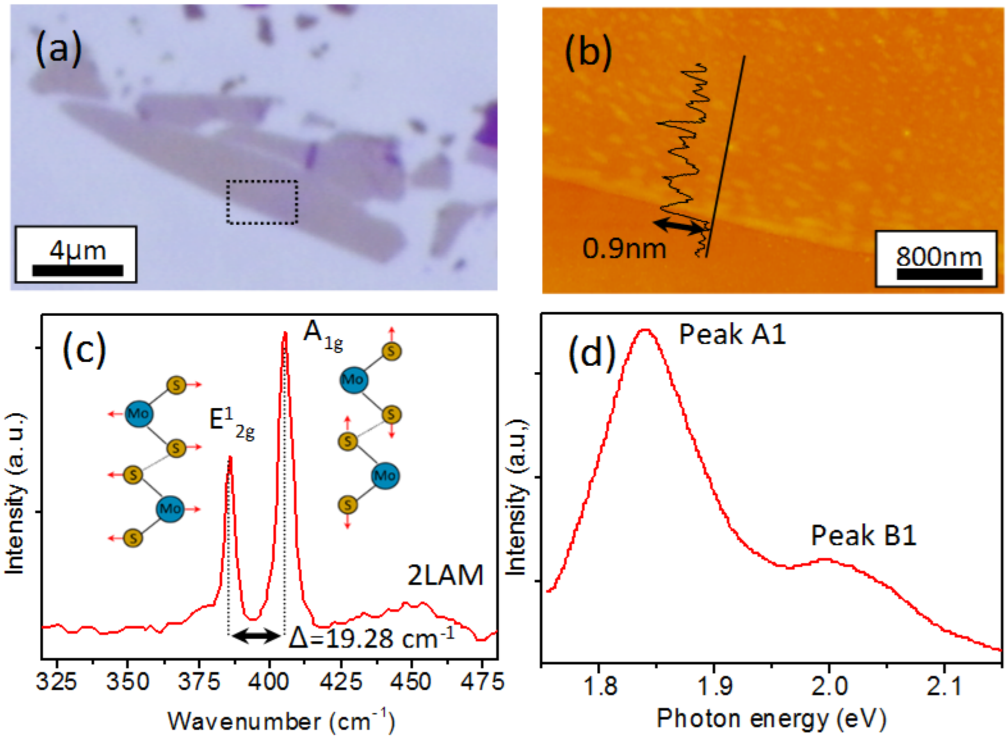

Figure 6.4: Single-layer MoS_2 characterization. (a) Optical, (b) AFM image and height profile, (c) Raman spectrum, (d) photoluminescence (PL) spectrum of exfoliated single-layer MoS_2 on Si/SiO_2 substrate.

The measurements were performed on a single-layer MoS_2 which was mechanically exfoliated onto a Si/SiO_2 (250nm) substrate from bulk MoS_2. The optical and atomic force microscopy (AFM) images of the single-layer MoS_2 are presented in Figs. 6.4 (a) and (b), respectively. The height of the single-layer MoS_2 is estimated at 0.9 nm [Figure 1(b)]. Raman spectroscopy (performed on the flake at room temperature using an excitation wavelength at 532 nm) was used to further confirm the number of layers in the MoS_2 flake [Figure 1(c)]. The resulting spectrum presents two prominent peaks corresponding to the in-plane E^1_{2g} and out-of-plane A^{1g} vibration of MoS_2 [Figure 6.4(c) inset], and the position difference of these two dominant Raman peaks (D) was found to be 19.3 cm^{-1}. This corresponds to the response of a single-layer of MoS_2. Figure 6.4 (d) shows the PL profile of single-layer MoS_2 with the strong PL peak (peak A1) at 1.84 eV arising from the direct recombination of photo-generated electron-hole pairs with higher luminescence quantum efficiency in the single-layer MoS_2, while the weak shoulder peak (peak B1) at 2.02 eV is attributed to the energy split of the valence band spin-orbital coupling of MoS_2 occurring in presence of the Si/SiO_2 substrate.

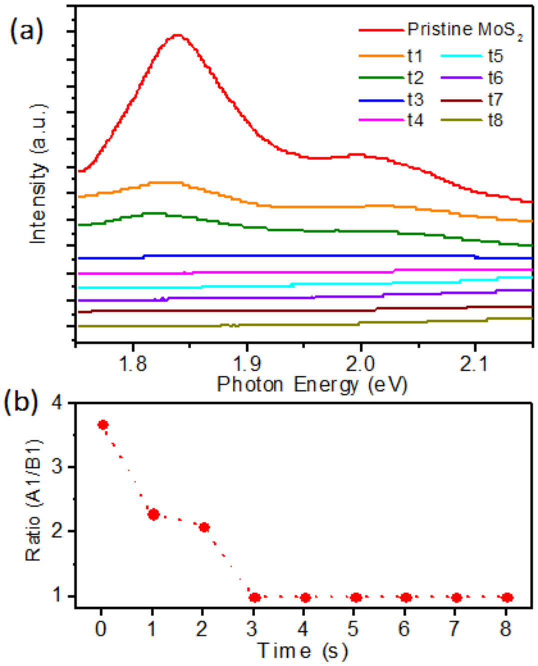

Figure 6.5: (a) PL spectrum of single-layer MoS_2 as function of plasma-treated time. PL spectra of pristine flake shows strong response of the monolayer (red) and gradual PL quenching appears after treatment (t1 to t8). (b) PL intensity ratio (peak A1/peak B1) is plotted with respect to exposure time.

Figure 6.5 shows the effect of oxygen plasma exposure time on the PL of single-layer MoS_2. For the pristine MoS_2, the intensity of A1 and B1 peak is 31.3 CCD cts and 8.5 CCD cts, respectively as seen in Figure 6.5 (a). The intensity of the PL significantly weakens after t1 exposure and is fully quenched after t3 [Figure 6.5(a)]. Hence by comparing the intensity ratio A1/B1 in the PL spectra as a function of plasma exposure time, we show in Figure 6.5 (b) that the highest PL ratio, with a value of 3.7, was observed in pristine single-layer MoS_2, and gradually decreased to 2.3 and 2.1, at t1 and t2, respectively. After t3, we observed the full quenching of PL. Emitted radiation in PL is caused by the radiative recombination in the sample upon photo-excitation. Radiative recombination is most effective in direct bandgap semiconductors, such as MoS_2, as it only requires the electron to recombine with the hole to transition back to its equilibrium level. We postulate that lattice distortions forming as a result of oxygen plasma treatment strongly impede the electron-hole recombination rate in the defected MoS_2 flake due to a conversion to an indirect bandgap material, leading to total quenching at t3.

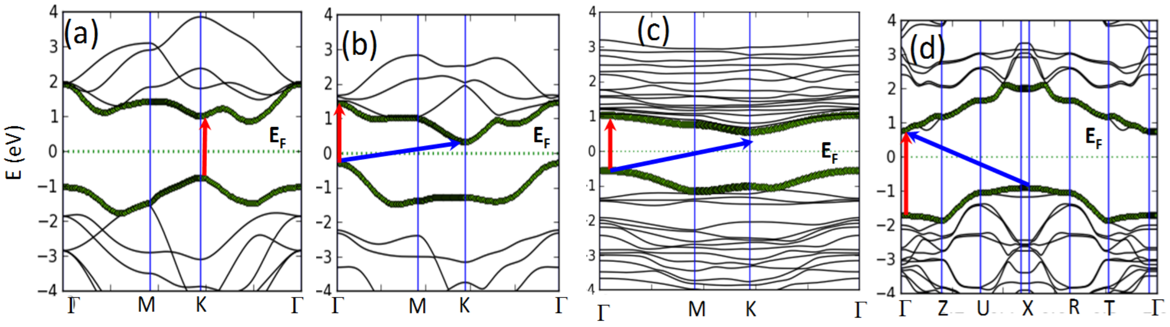

Figure 6.6: Band structure of (a) pristine single-layer MoS_2, (b) single-layer MoS_2 with one S atom replaced by one O atom, (c) single-layer MoS_2 with three S atoms replaced by three O atoms, and (d) a single-layer of MoO_3. Single layer of MoS_2 has direct bandgap at K point (a). The replacement of an S atom by an O atom changes the positions of the band extrema (b,c). The d-bands of MoS2 at the band extrema are more hole type at the K point (a). The red arrows indicate the direct bandgap and blue arrows indicate the indirect bandgap .

In order to understand the quenching of the photoluminescence peak of the MoS_2 sheet after the plasma treatment, we performed density functional theory (DFT) calculations to determine the bandstructure of pristine monolayer MoS_2, monolayer MoS_2 with O defects, and a monolayer MoS_2 with a MoO_3 defect and MoO_3 along the high symmetry lines in the first Brillouin zone Figure 6.6. Note that bulk MoO_3 and a single-layer of MoO_3 have similar bandstructures. In a pristine single-layer of MoS_2, when one S atom is replaced by an O atom, the conduction band minimum (CBM) remains at the K point (as in pristine MoS_2 single-layer) but the the valence band maximum (VBM) shifts to the Γ point from the K point, which leads to the indirect bandgap of metal oxysulphide (MoO_xS_y). Indirect bandgap is also obtained when three S atoms are replaced by three O atoms. From the calculated bandstructures of MoO_3, it is seen that MoO_3 is a wide bandgap semiconductor with an indirect bandgap. It is to be noted that DFT underestimates the bandgap, sometimes substantially. The single sheet of pristine MoS_2 has a direct bandgap of 1.8 eV and pristine MoO_3 has an indirect bandgap of 3.2 eV.[154] It is plausible to assume that the bandgap of MoS_2 single sheet increases with defects from 1.8 eV for 0% MoO_3 defect concentration to 3.2 eV for 100 % MoO_3 concentration.[155] Note that Kohn-Sham eigenstates resulting from the DFT calculation are accurate in the sense that they provide the accurate distribution of electron density and provide accurate results for the type of bandgap.[156] Our results for the bandstructures show that pristine MoS_2 has direct bandgap and all other configurations have indirect bandgap, which explains the quenching of the photoluminescence after oxygen plasma treatment. Therefore, the radiative recombination must be assisted by electron-phonon scattering inside the first Brillouin zone, which leads to a substantial reduction in the photoluminescence intensity.

CHAPTER 7
CONCLUSIONS

The free electron-hole pairs generation in semiconductor and topological insulator materials is interesting from both the scientific and the engineering point of view. A variety of applications in semiconductor technology rely on electron-hole pair generation and their recombination. In devices based on electronics, optoelectronics, and spintronics, excited electron-hole pairs are generated using controlled electrical and light signal. Generated carriers can be properly engineered to be utilized for semiclassical computation, quantum information processing, and quantum memory. The electron-hole pair polarization can be more interesting for the scientific and engineering aspects in 3D TIs as there are exotic states living on the surfaces which are protected from backscattering. Using nanostructures of such materials, one can amplify the effect coming from the surfaces that may lead to opportunities in engineering electron-hole pair polarization selection rules for applications in nanotechnology.

In this thesis we focused on the generation of electron-hole pairs and their utilization for a variety of the applications. We presented plasmon resonance peak shifts due to the change in dielectric environment in a silver core TiO_2 nanoshell. By calculating electronic and optical properties, we showed that it is possible to dynamically control the shift by varying the dielectric function of TiO_2. Generation of electron-hole pairs leads to a change in absorption due to Pauli blocking and lack of carriers for certain transitions. The magnitude of the change depends on the densities of excited electron-hole pairs. Using the mechanism of the dynamic control over the plasmon resonances, we proposed the concept of a light controlled plasmon switch that can be much faster than conventional electronic switches.

We developed nice applications of electron-hole pair polarization selection rules in 3D TIs for quantum memory and quantum information processing. Our approach is based on solutions of the low energy Dirac Hamiltonian around the Dirac point in 3D TI material $Pb_{1-x}Sn_xTe$. We presented a model of spherically shaped 3D TI QD from two narrow-bandgap semiconductor alloys. The interface was modeled using a simple delta potential.This model provided the number of bound states which can be tuned using the strength of delta potential. A unique feature of 3D TI is that there is a particle-hole symmetry in the energy spectrum, which provided us the opportunity to utilize efficiently the 3D TI QD for quantum memory and quantum information processing. 3D TI QD has strict optical selection rules. We found that the 3D TI QD is a good candidate for quantum memory, quantum teleportation, and quantum computing with single spins in 3D TI QDs using infrared light. In particular, a single e-h pair, a single electron, or a single hole can be used as a qubit for the implementation of optically mediated quantum computing with 3D TI QDs. Interestingly, we found that due to the symmetry between positive- and negative-energy solutions, in a 3D TI QD it is possible to define an electron spin qubit in terms of an s-like or a p-like state. At the same time it is possible to define a hole spin qubit in terms of an s-like or a p-like state.

This cannot be done in a zincblende wide direct-bandgap semiconductor QDs, where the electron is associated with an s-like state and the hole is associated with a p-like state. Our calculations predict that the semiclassical Faraday effect can be observed in a slab of 3D TI material. We consider the Faraday effect due to Pauli exclusion principle in a pump-probe setup using a 3D TI double interface of a PbTe/$Pb_{0.31}Sn_{0.69}$/PbTe heterostructure. For that we calculate the optical conductivity tensor of this heterostructure, which we use to solve Maxwell's equations. The Faraday rotation angle exhibits oscillations as a function of probe wavelength and thickness of the heterostructure. The maxima in the Faraday rotation angle are of the order of milirads.

In addition, we also presented theoretical and experimental evidences of electrical and optical properties tuning in 2D layered materials such as MoS_2 via oxygen plasma treatment. When a single sheet of MoS_2 was treated with energetic oxygen plasma, due to surface oxidation, MoO_3 rich defect regions are formed inside MoS_2 sheet. This leads to an exponential decrease in mobility, current, and resistance. We provided theoretical explanations of this mechanism using DFT calculations.

APPENDIX A
FERMION DOUBLING THEOREM IN 3D TI QD

A.1 Calculation of the Wronskian

The Wronskian of the functions $\mathcal{I}_\kappa\left(z\right)$ and $\mathcal{K}_\kappa\left(z\right)$ is defined as [157]

$$W_\kappa\left[\mathcal{I}_\kappa\left(z\right),\mathcal{K}_\kappa\left(z\right)\right]=\mathcal{I}_\kappa\left(z\right)\mathcal{K}_\kappa^{'}\left(z\right)-\mathcal{I}_\kappa^{'}\left(z\right)\mathcal{K}_\kappa\left(z\right), \tag{A.1}$$

where the prime denotes the derivative of the function. For independent solutions, it is to be noted that Wronskian is proportional to $1/p\left(x\right)$ in a Sturm-Liouville type equation $\frac{d}{dx}\left[p\left(x\right)\frac{dy}{dx}\right]+g\left(x\right)y=0$. Therefore, Wronskians in the text are calculated to be

$$\begin{aligned} W_\kappa\left[\mathcal{I}_\kappa\left(z\right),\mathcal{K}_\kappa\left(z\right)\right] &= -\frac{1}{z^2}, && \text{(A.2)}\\ W_{\kappa-1}\left[\mathcal{I}_{\kappa-1}\left(z\right),\mathcal{K}_{\kappa-1}\left(z\right)\right] &= -\frac{1}{z^2}. && \text{(A.3)} \end{aligned}$$

A.2 Limiting form of Bessel functions

The limiting forms of modified Bessel functions for $z\to 0$ are given by

$$\left.\begin{array}{r} I_\kappa\left(z\right)=\frac{1}{\Gamma(\kappa+1)}\left(\frac{z}{2}\right)^\kappa \\ K_\kappa\left(z\right)=\frac{\Gamma(\kappa)}{2}\left(\frac{2}{z}\right)^\kappa \end{array}\right\}\text{ as } z\to 0 \tag{A.4}$$

The modified spherical Bessel functions can be written in terms of modified Bessel functions as

$$\mathcal{I}_\kappa\left(z\right)=\left(\sqrt{\frac{\pi}{2z}}\right)I_{\kappa+\frac{1}{2}}\left(z\right),\ \mathcal{K}_\kappa\left(z\right)=\left(\sqrt{\frac{2}{\pi z}}\right)K_{\kappa+\frac{1}{2}}\left(z\right) \tag{A.5}$$

Therefore, the function

$$F\left(z\right)=\left[z\mathcal{I}_\kappa\left(z\right)\mathcal{K}_\kappa\left(z\right)\right]\left[z\mathcal{I}_{\kappa-1}\left(z\right)\mathcal{K}_{\kappa-1}\left(z\right)\right] \tag{A.6}$$

has the limiting form $F(z) = \frac{1}{4\kappa^2-1}$ as $z \to 0$.

The asymptotic expansion ($z \to \infty$) of the modified Bessel functions are given by

$$\begin{array}{c} I_\kappa(z) = \frac{e^z}{\sqrt{2\pi z}} \left\{ 1 - \frac{4\kappa^2-1}{8z} + \frac{\left(4\kappa^2-1\right)\left(4\kappa^2-9\right)}{2!(8z^2)} - \ldots \right\} \\ K_\kappa(z) = \sqrt{\frac{\pi}{2z}} e^{-z} \left\{ 1 + \frac{4\kappa^2-1}{8z} + \frac{\left(4\kappa^2-1\right)\left(4\kappa^2-9\right)}{2!(8z^2)} - \ldots \right\} \end{array} . \tag{A.7}$$

A.3 The fermion doubling theorem

Nielsen and Ninomiya investigated Weyl fermions on a crystal.[112, 113, 114] They formulated a no-go theorem, called the fermion doubling theorem, requiring that Weyl nodes in a crystal always exist in pairs of opposite chirality. The reason for this theorem is that the number of Weyl fermions in the first Brillouin zone must be conserved. This conservation law can be checked by calculating the Berry flux in the first Brillouin zone.

It is important to note that the fermion doubling theorem is only valid for continuum states. Therefore it does not apply to the bound eigenstates of the 3D TI QD, which have a discrete eigenspectrum. Below we give arguments for the validity of the fermion doubling theorem in the continuum limit, which corresponds to the asymptotic limit when the 3D TI QD radius r_o becomes infinite.

A typical calculation of the Berry curvature $\mathcal{B}_n(\mathbf{k}) = \nabla_{\mathbf{k}} \times \mathcal{A}_n(\mathbf{k})$ considers a single band Bloch state $u_{n\mathbf{k}}(\mathbf{r})e^{i\mathbf{k}\cdot\mathbf{r}}$, which gives rise to the Berry connection $\mathcal{A}_n(\mathbf{k}) = i\int_\Omega d^3r\ u^*_{n\mathbf{k}}(\mathbf{r})$ $\nabla_{\mathbf{k}} u_{n\mathbf{k}}(\mathbf{r})$.[158] As long as the nth band does not touch or cross any other band, the Berry flux is zero, i.e. $\nabla_{\mathbf{k}} \cdot \mathcal{B}_n(\mathbf{k}) = 0$. However, if there is a band crossing, this situation changes drastically due to the monopole at the crossing point. Using $\mathbf{k} \cdot \mathbf{p}$ approximation, around the crossing point in the first Brillouin zone the Berry connection becomes $\mathcal{A}_{\pm}(\mathbf{k}) = i \left\langle \chi_{\pm} \right| \nabla_{\mathbf{k}} \left| \chi_{\pm} \right\rangle$, where $\chi_{\pm}$ is the four-spinor of the solution $\Phi_{\pm} = \chi_{\pm} F(\mathbf{r})$ of Eq. (4.1).[109] Assuming a very large QD, where quantum confinement can be neglected, the four-spinor reads

$$\chi_{\pm} = \begin{pmatrix} \pm e^{-i\frac{(\varphi \pm \pi/2)}{2}} \\ \pm e^{i\frac{(\varphi \pm \pi/2)}{2}} \\ e^{-i\frac{(\varphi \mp \pi/2)}{2}} \\ e^{i\frac{(\varphi \mp \pi/2)}{2}} \end{pmatrix} \tag{A.8}$$

where $e^{\mp i\varphi} = \frac{k_x \mp i k_y}{k_\perp}$ and the position-dependent function is given by $F(\mathbf{r}) = C e^{-\frac{1}{\hbar v_\parallel}\int_0^z \Delta(z')dz'}$ $e^{i\mathbf{k}_\perp \cdot \mathbf{r}}$, where C is the normalization constant. In order to capture the Berry curvature apart from the azimuthal angle φ we need to add the dependence on the polar angle θ. At the same time, we perform the gauge transformations $e^{\pm i\varphi}$ to shift the singularity of the Berry curvature to the south pole. This means we calculate the Berry curvature with respect to the normalized 4-spinors

$$
\begin{aligned}
\chi_{C,+} &= \frac{1}{\sqrt{2}}\begin{pmatrix} e^{-i\frac{\pi}{4}}\cos\frac{\theta}{2} \\ e^{i\left(\varphi+\frac{\pi}{4}\right)}\sin\frac{\theta}{2} \\ e^{i\frac{\pi}{4}}\cos\frac{\theta}{2} \\ e^{i\left(\varphi-\frac{\pi}{4}\right)}\sin\frac{\theta}{2} \end{pmatrix}, \\
\chi_{C,-} &= \frac{1}{\sqrt{2}}\begin{pmatrix} -e^{-i\left(\varphi-\frac{\pi}{4}\right)}\sin\frac{\theta}{2} \\ e^{-i\frac{\pi}{4}}\cos\frac{\theta}{2} \\ e^{-i\left(\varphi+\frac{\pi}{4}\right)}\sin\frac{\theta}{2} \\ -e^{i\frac{\pi}{4}}\cos\frac{\theta}{2} \end{pmatrix}
\end{aligned}
\tag{A.9}
$$

The Berry connection is then given by

$$
\mathcal{A}_{\pm}(\mathbf{k}) = i\left\langle \chi_{C,\pm}\right| \nabla_{\mathbf{k}} \left|\chi_{C,\pm}\right\rangle = \mp\frac{(1-\cos\theta)}{2k\sin\theta}\mathbf{e}_{\varphi} \tag{A.10}
$$

where $\mathbf{e}_{\varphi}$ is the unit vector pointing in φ-direction. Thus, we obtain the Berry phase

$$
\gamma_{\pm} = \oint \mathcal{A}_{\pm}(\mathbf{k}) \cdot d\mathbf{k} = \mp\pi(1-\cos\theta) \tag{A.11}
$$

and the Berry curvature

$$
\mathcal{B}_{\pm}(\mathbf{k}) = \mp\frac{1}{2k^2}\mathbf{e}_{k} \tag{A.12}
$$

Note that the Berry curvature for the 4-spinor is the same as the Berry curvature of a 2-spinor (see Refs. Shankar). For a loop on the 2D surface where $\theta = \pi/2$, we get $\gamma_{\pm} = \mp\pi$, which gives rise to the topological phase shift seen in Shubnikov-de Haas oscillations for the surface of 3D topological insulators.[159] From $\triangle(1/k) = \mp 4\pi\delta^{(3)}(\mathbf{k})$ and $\nabla(1/k) = \mp\frac{1}{k^2}\mathbf{e}_k$

it follows that the Berry curvature is the solution of the equation

$$\nabla_{\mathbf{k}} \cdot \mathcal{B}_{\pm}(\mathbf{k}) = \mp 4\pi g \delta^{(3)}(\mathbf{k}) \tag{A.13}$$

where $g = \mp 1/2$ is the strength of the Dirac monopole for positive and negative helicity of the 4-spinor, which is identical to the result for 2-spinors (see Refs. Shankar and Nakahara).

In order to understand the helicity of the Weyl fermions at the interface, we have shown in Ref. Paudel&Leuenberger that the helicity operator is given by

$$\hat{h}_{\mathrm{TI}} = (1/|p_{\perp}|) \begin{pmatrix} (\boldsymbol{\sigma}_{\perp} \times \boldsymbol{p}_{\perp}) \cdot \hat{\boldsymbol{z}} & 0 \\ 0 & -(\boldsymbol{\sigma}_{\perp} \times \boldsymbol{p}_{\perp}) \cdot \hat{\boldsymbol{z}} \end{pmatrix} \tag{A.14}$$

which commutes with the Hamiltonian in Eq. (4.1) and yields $\hat{h}_{\mathrm{TI}}\Phi_{\pm} = (\pm 1/2)\,\Phi_{\pm}$, where the + sign denotes the positive helicity of positive-energy solutions and the - sign denotes the negative helicity of negative-energy solutions. This provides the possibility to write an effective 2D Hamiltonian for the Weyl fermions on the surface of 3D topological insulators, i.e.

$$H_{2D} = \hbar v \begin{pmatrix} (\boldsymbol{\sigma}_{\perp} \times \boldsymbol{k}_{\perp}) \cdot \hat{\boldsymbol{z}} & 0 \\ 0 & -(\boldsymbol{\sigma}_{\perp} \times \boldsymbol{k}_{\perp}) \cdot \hat{\boldsymbol{z}} \end{pmatrix} \tag{A.15}$$

This effective 2D Hamiltonian can be reduced to two Weyl Hamiltonians of the form $H_{2D}^{2x2} = \pm\hbar v\,(\boldsymbol{\sigma}_{\perp} \times \boldsymbol{k}_{\perp}) \cdot \hat{\boldsymbol{z}}$. It is important to note that both 2-spinors of $\chi_{\pm}$, the 2-spinor $\chi_{\pm}^{L^-}$ of the L^- band and the 2-spinor $\chi_{\pm}^{L^+}$ of the L^+ band have the same helicity, in contrast to the commonly used Weyl Hamiltonians $H_W(\mathbf{k}) = \pm\hbar v \boldsymbol{\sigma}\cdot\mathbf{k}$. The reason for this is that the two 2-spinors are coupled through the mass term $\Delta(z)$ in z-direction, as given in the 3D Hamiltonian in Eq. (4.1).

In order to satisfy the fermion doubling theorem,[112, 113, 114] usually the Dirac cones on the opposite side of the slab of a 3D topological insulator are identified as the fermion doublers. In the case of the 3D IT QD, for $r_o \to \infty$, i.e. in the continuum limit, the Berry curvature in $\mathbf{k}$-space for a 2D interface, given by Eq. (A.12), determines the Weyl nodes that need to satisfy the fermion doubling theorem. Hence, according to Ref. [160], we can adopt the mapping of the two opposite surfaces of a 3D slab of TI onto the northern and southern hemispheres of a sphere. We then identify the pairs of Dirac cones with opposite helicity as the ones located on the antipodal points on the surface of the sphere defined by the QD, as shown in Figure A.1. Note that in both cases, the slab and the QD, the pairs of Dirac cones map into each other through the parity transformation, which in general reverses the helicity. We can identify a current on the surface of the sphere flowing along a latitude. The parity transformation then maps one latitude on the northern hemisphere with one type of helicity to its partner latitude on the southern hemisphere with the opposite helicity. These arguments show that the fermion doubling theorem is satisfied for a 3D TI QD in the continuum limit.

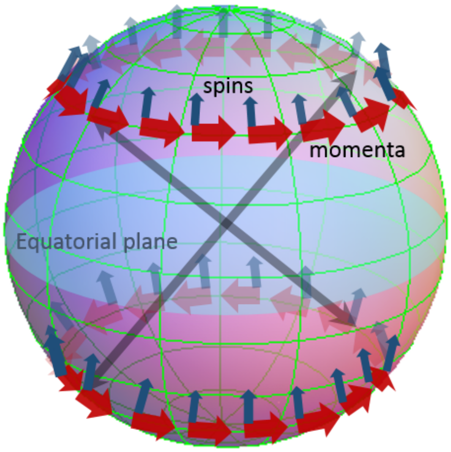

Figure A.1: Two antipodal points on the surface of the sphere defined by the QD are identified as the Dirac cones of opposite helicity. One point lies on the northern hemisphere, while its antipodal point lies on the southern hemisphere. The currents flowing along the latitudes can be imagined as angular momentum states of a 3D TI QD in the continuum limit. At the antipodal points momenta (red arrows) point in opposite $\hat{\varphi}$ direction to each other while spins (blue arrows) point in the same $\hat{\theta}$ direction, where $\hat{\theta}$ and $\hat{\varphi}$ are the spherical angular unit vectors. Hence, they have opposite chirality. This satisfies the fermion doubling theorem.

APPENDIX B
BOUNDARY CONDITIONS IN 3D TI SLAB

B.1 Solutions of the Maxwell Equations and the Boundary Conditions

The continuity of the tangential components of the electric field at $z = 0$, $z = t$, $z = t + d$ and $z = 2t + d$ leads to

$$\begin{bmatrix} E_a \\ E_a \end{bmatrix} + \begin{bmatrix} E_{bx} \\ E_{by} \end{bmatrix} = \begin{bmatrix} E_{cx} \\ E_{cy} \end{bmatrix} + \begin{bmatrix} E_{dx} \\ E_{dy} \end{bmatrix}, \tag{B.1}$$

$$\begin{aligned} \begin{bmatrix} E_{cx} \\ E_{cy} \end{bmatrix} e^{ik_{II}t} + \begin{bmatrix} E_{dx} \\ E_{dy} \end{bmatrix} e^{-ik_{II}t} = \begin{bmatrix} E_{ex} \\ E_{ey} \end{bmatrix} e^{ik_{II}t} \\ + \begin{bmatrix} E_{ex} \\ E_{ey} \end{bmatrix} e^{-ik_{II}t}, \end{aligned} \tag{B.2}$$

$$\begin{aligned} \begin{bmatrix} E_{ex} \\ E_{ey} \end{bmatrix} e^{ik_{II}(t+d)} + \begin{bmatrix} E_{fx} \\ E_{fy} \end{bmatrix} e^{-ik_{II}(t+d)} \\ = \begin{bmatrix} E_{gx} \\ E_{gy} \end{bmatrix} e^{ik_{II}(t+d)} + \begin{bmatrix} E_{hx} \\ E_{hy} \end{bmatrix} e^{-ik_{II}(t+d)}, \end{aligned} \tag{B.3}$$

$$\begin{aligned} \begin{bmatrix} E_{gx} \\ E_{gy} \end{bmatrix} e^{ik_{II}(2t+d)} + \begin{bmatrix} E_{hx} \\ E_{hy} \end{bmatrix} e^{-ik_{II}(2t+d)} \\ = \begin{bmatrix} E_{ix} \\ E_{iy} \end{bmatrix} e^{ik_{I}(2t+d)}. \end{aligned} \tag{B.4}$$

Similarly the continuity of derivative of the electric fields at $z = 0$, $z = t$, $z = t + d$ and $z = 2t + d$ yields

$$ik_I \begin{bmatrix} E_a \\ E_a \end{bmatrix} - ik_I \begin{bmatrix} E_{bx} \\ E_{by} \end{bmatrix} = ik_{II} \begin{bmatrix} E_{cx} \\ E_{cy} \end{bmatrix} - ik_{II} \begin{bmatrix} E_{dx} \\ E_{dy} \end{bmatrix}, \tag{B.5}$$

$$\begin{aligned} ik_{II} \begin{bmatrix} E_{cx} \\ E_{cy} \end{bmatrix} e^{ik_{II}t} - ik_{II} \begin{bmatrix} E_{dx} \\ E_{dy} \end{bmatrix} e^{-ik_{II}t} &= ik_{II} \begin{bmatrix} E_{ex} \\ E_{ey} \end{bmatrix} e^{ik_{II}t} - ik_{II} \begin{bmatrix} E_{fx} \\ E_{fy} \end{bmatrix} e^{-ik_{II}t} \\ &+ i\omega\mu_o \begin{bmatrix} \sigma_{xx}(E_{ex}e^{ik_{II}t} - E_{fx}e^{-ik_{II}t}) + \sigma_{xy}(E_{ey}e^{ik_{II}t} - E_{fy}e^{-ik_{II}t}) \\ \sigma_{yx}(E_{ex}e^{ik_{II}t} - E_{fx}e^{-ik_{II}t}) + \sigma_{yy}(E_{ey}e^{ik_{II}t} - E_{fy}e^{-ik_{II}t}) \end{bmatrix}, \end{aligned} \tag{B.6}$$

$$\begin{aligned} ik_{II} \begin{bmatrix} E_{ex} \\ E_{ey} \end{bmatrix} e^{ik_{II}(t+d)} - ik_{II} \begin{bmatrix} E_{fx} \\ E_{fy} \end{bmatrix} e^{-ik_{II}(t+d)} &= ik_{II} \begin{bmatrix} E_{gx} \\ E_{gy} \end{bmatrix} e^{ik_{II}(t+d)} - ik_{II} \begin{bmatrix} E_{hx} \\ E_{hy} \end{bmatrix} e^{-ik_{II}(t+d)} \\ &+ i\omega\mu_o \begin{bmatrix} \sigma_{xx}(E_{gx}e^{ik_{II}(t+d)} - E_{hx}e^{-ik_{II}(t+d)}) + \sigma_{xy}(E_{gy}e^{ik_{II}(t+d)} - E_{hy}e^{-ik_{II}(t+d)}) \\ \sigma_{yx}(E_{gx}e^{ik_{II}(t+d)} - E_{hx}e^{-ik_{II}(t+d)}) + \sigma_{yy}(E_{gy}e^{ik_{II}(t+d)} - E_{gy}e^{-ik_{II}(t+d)}) \end{bmatrix}, \end{aligned} \tag{B.7}$$

$$ik_{II} \begin{bmatrix} E_{gx} \\ E_{gy} \end{bmatrix} e^{ik_{II}(2t+d)} - ik_{II} \begin{bmatrix} E_{hx} \\ E_{hy} \end{bmatrix} e^{-ik_{II}(2t+d)} = ik_I \begin{bmatrix} E_{ix} \\ E_{iy} \end{bmatrix} e^{ik_I(2t+d)}. \tag{B.8}$$

The response of the top and bottom surfaces of the $\mathrm{Pb}_{1-x}\mathrm{Sn}_x\mathrm{Te}$ slab to the field depends on the transition matrix elements on the corresponding surfaces. Since, the transition matrix elemets for both of the surfaces are same, we have $\sigma_{t,ij} = \sigma_{t+L,ij}$. The off diagonal elements σ_{xy} and σ_{xy} of the magneto-optical tensors σ_{ij} are calculated to be zero. The algebric Eqs. B.1 to B.8 can be solved for each of the amplitude of component field in each region interm of the incident filed. The solutions for the transmitted field are given by

$$\begin{bmatrix} E_{ix} \\ \\ E_{iy} \end{bmatrix} = \frac{4k_I k_{II} e^{-ik_I(2t+d)}}{X\left[\alpha(k_{II}A+C)+\beta(k_{II}B+D)\right]+Y\left[\alpha(k_{II}A-C)+\beta(k_{II}B-D)\right]} \begin{bmatrix} E_a \\ \\ E_a \end{bmatrix},$$

where $\alpha = \frac{k_{II}+k_I}{4k_{II}}$, $\beta = \frac{k_{II}-k_I}{4k_{II}}$, $X = (k_I + k_{II})e^{-ik_{II}t}$, $Y = (k_I - k_{II})e^{ik_{II}t}$,

$$A = 2e^{-ik_{II}(t+d)} - \frac{2i\omega\mu_o \sin k_{II}d}{k_{II}} \begin{bmatrix} \sigma_{xx} \\ \\ \sigma_{yy} \end{bmatrix} e^{-ik_{II}t}, \tag{B.10}$$

$$B = 2e^{ik_{II}(t+d)} + \frac{2i\omega\mu_o \sin k_{II}d}{k_{II}} \begin{bmatrix} \sigma_{xx} \\ \\ \sigma_{yy} \end{bmatrix} e^{ik_{II}t}, \tag{B.11}$$

$$\begin{aligned} C = {} & e^{-ik_{II}(t+d)} \left(k_{II} + \omega\mu_o \begin{bmatrix} \sigma_{xx} \\ \\ \sigma_{yy} \end{bmatrix} \right) \left(2 + \frac{\omega\mu_o}{k_{II}} \begin{bmatrix} \sigma_{xx} \\ \\ \sigma_{yy} \end{bmatrix} \right) \\ & - \frac{\omega\mu_o}{k_{II}} e^{-ik_{II}(t+d)} \begin{bmatrix} \sigma_{xx} \\ \\ \sigma_{yy} \end{bmatrix} \left(-k_{II} - \omega\mu_o \begin{bmatrix} \sigma_{xx} \\ \\ \sigma_{yy} \end{bmatrix} \right), \end{aligned} \tag{B.12}$$

$$\begin{aligned} D = {} & -\frac{\omega\mu_o}{k_{II}} e^{ik_{II}(t-d)} \begin{bmatrix} \sigma_{xx} \\ \\ \sigma_{yy} \end{bmatrix} \left(k_{II} + \omega\mu_o \begin{bmatrix} \sigma_{xx} \\ \\ \sigma_{yy} \end{bmatrix} \right) \\ & - e^{-ik_{II}(t+d)} \left(-k_{II} - \omega\mu_o \begin{bmatrix} \sigma_{xx} \\ \\ \sigma_{yy} \end{bmatrix} \right) \left(2 + \frac{\omega\mu_o}{k_{II}} \begin{bmatrix} \sigma_{xx} \\ \\ \sigma_{yy} \end{bmatrix} \right). \end{aligned} \tag{B.13}$$

APPENDIX C

2D LAYERED MATERIALS: EXPERIMENTAL AND THEORETICAL METHODS

C.1 Experimental method

The electron transport measurements of the MoS_2 device were performed in a probe station at ambient condition using a Keithley 2400 source meter and a DL instruments 1211 current preamplifier interfaced with LabView program. The measurements were performed for the pristine flake before and after each oxygen plasma treatment. The plasma treatment on the MoS_2 devices was carried out using a commercial (Plasma Etch, PE-50) plasma chamber at a power of 100 W operating at 50 kHz. During plasma exposure, the pressure within the plasma chamber was held at 250 – 350 mTorr and a gas mixture of Oxygen (20%) and Argon (80%) flow at a constant rate of 15 sccm (sccm - standard cubic centimeters per minute). For the first exposure, the samples were exposed for 2 s and subsequently they were exposed at 1 s interval and the electron transport measurements were repeated.

C.2 Theoretical method

Theoretical calculation: Density functional theory calculations (DFT) were performed to investigate the stability of MoOS and MoO_3 defects inside a single layer of MoO_3. For that we performed DFT calculations for a single layer of MoS_2, a single layer of MoO_3, a single layer of MoS_2 with MoOS defects, and a single layer of MoS_2 with MoO_3 defects. In each of the cases we considered a mesh of 9x9x1 k-points in the Brillouin zone. For MoO_3 sheet, we considered 9x1x9 k-points. The ion-electron interaction is described by the projected augmented wave (PAW) method and the exchange-correlation energy is calculated using the Perdew, Burke and Ernzerhof (PBE) approximation within the framework of the generalized gradient approximation (GGA). The grid point cutoff of 415 eV is used and a maximum force of 0.1 eV/Åon each atom is reached during the optimization process in all cases.

C.3 Theoretical calculation of resistance

We considered the plasma-treated material as an effective-medium semiconductor (EMSC). This is shown in Figure C.1, where the right side Figure shows that the intact MoS_2 underneath the gold electrode formed a heterojunction with EMSC. The current through a heterojunction with a relatively high built-in potential has a form similar to the Shockley diode equation

$$I = I_S \left(e^{eV/nk_BT} - 1 \right) \approx I_S \frac{eV}{nk_BT}, \tag{C.1}$$

where V is the applied voltage, k_B is the Boltzmann constant, T is the temperature, and n is the ideality factor (n accounts the imperfection of the junctions). The dependence on the band mismatch at the heterojunction enters this equation through the saturation current

$$I_S (\Delta\phi) \approx AT^2 \exp\left(-\frac{\Delta\phi}{k_BT} \right), \tag{C.2}$$

where $A = em^* k_B^2 / 2\pi^2 \hbar^3$ is the Richardson constant. In order to define an effective resistance of the heterojunction, we consider the limit of small applied voltage, $V \lll V_T = nk_BT/e \approx 0.2$ V (for $T = 400$ KT and $n = 1$) and we obtain as $I = V/R(\Delta\phi)$, where

$R(\Delta\phi) = V_T/I_S(\Delta\phi)$. Thus we find $\ln[R(\Delta\phi)] = C + \frac{\Delta\phi}{k_B T}$. This formula provides the dependence of total resistance in the case when the junction under consideration gives the main contribution.

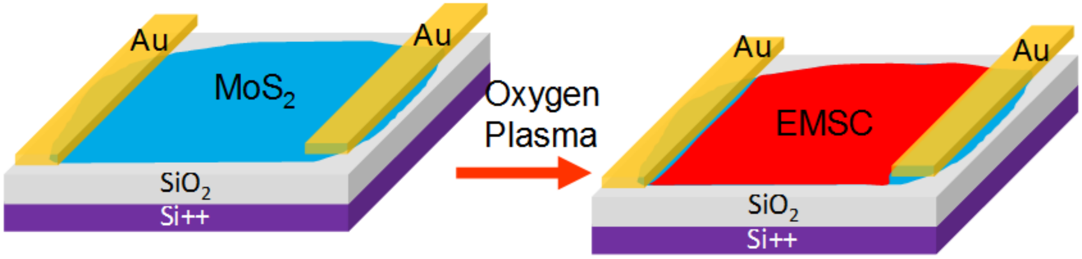
Au
Au
MoS2
SiO2
Si++
Oxygen
Plasma
Au
Au
EMSC
SiO2
Si++

Figure C.1: Schematic of MoS_2–EMSC heterojunction when treated with oxygen plasma.

LIST OF REFERENCES

[1] S. Sundaram and E. Mazur, "Inducing and probing non-thermal transitions in semiconductors using femtosecond laser pulses," *Nat. Mater.*, vol. 1, pp. 217–224, DEC 2002.

[2] T. Suzuki and R. Shimano, "Cooling dynamics of photoexcited carriers in Si studied using optical pump and terahertz probe spectroscopy," *Phys. Rev. B*, vol. 83, FEB 23 2011.

[3] J. Kim, H. Son, D. J. Cho, B. Geng, W. Regan, S. Shi, K. Kim, A. Zettl, Y.-R. Shen, and F. Wang, "Electrical Control of Optical Plasmon Resonance with Graphene," *Nano Lett.*, vol. 12, pp. 5598–5602, NOV 2012.

[4] F. Rana, "Electron-hole generation and recombination rates for Coulomb scattering in graphene," *Phys. Rev. B*, vol. 76, OCT 2007.

[5] T. Ando, "Anomaly of optical phonon in monolayer graphene," *J. Phys. Soc. Jpn.*, vol. 75, DEC 2006.

[6] R. R. Nair, P. Blake, A. N. Grigorenko, K. S. Novoselov, T. J. Booth, T. Stauber, N. M. R. Peres, and A. K. Geim, "Fine structure constant defines visual transparency of graphene," *Science*, vol. 320, p. 1308, JUN 6 2008.

[7] M. Z. Hasan and C. L. Kane, "Colloquium: Topological insulators," *Rev. Mod. Phys.*, vol. 82, pp. 3045–3067, NOV 8 2010.

[8] M. Hajlaoui, E. Papalazarou, J. Mauchain, G. Lantz, N. Moisan, D. Boschetto, Z. Jiang, I. Miotkowski, Y. P. Chen, A. Taleb-Ibrahimi, L. Perfetti, and M. Marsi, "Ultrafast Surface Carrier Dynamics in the Topological Insulator Bi_2Te_3," *Nano Lett.*, vol. 12, pp. 3532–3536, JUL 2012.

[9] D. Hsieh, Y. Xia, L. Wray, D. Qian, A. Pal, J. H. Dil, J. Osterwalder, F. Meier, G. Bihlmayer, C. L. Kane, Y. S. Hor, R. J. Cava, and M. Z. Hasan, "Observation of Unconventional Quantum Spin Textures in Topological Insulators," *Science*, vol. 323, pp. 919–922, FEB 13 2009.

[10] C. Kane and E. Mele, "Z(2) topological order and the quantum spin Hall effect," *Phys. Rev. Lett.*, vol. 95, SEP 30 2005.

[11] L. Fu and C. L. Kane, "Topological insulators with inversion symmetry," *Phys. Rev. B*, vol. 76, JUL 2007.

[12] Y. bychkov and E. Rashba, "Properties of a 2d electron-gas with lifted spectral degeneracy," *J. Exp. Theor. Phys. Lett.*, vol. 39, no. 2, pp. 78–81, 1984.

[13] P. B. Johnson and R. W. Christy, "Optical constants of the noble metals," *Phys. Rev. B*, vol. 6, pp. 4370–4379, Dec 1972.

[14] A. Vial and T. Laroche, "Comparison of gold and silver dispersion laws suitable for FDTD simulations," *Appl. Phys. B: Lasers and Optics*, vol. 93, pp. 139–143, OCT 2008.

[15] K. VonKlitzing, G. Dorda, and M. Pepper, "New method for high-accuracy determination of the fine-structure constant based on quantized hall resistance," *Phys. Rev. Lett.*, vol. 45, no. 6, pp. 494–497, 1980.

[16] S. M. G. Prange, R. E., *The Quantum Hall Effect*. Springer, New York, 1987.

[17] D. Thouless, M. Kohmoto, M. Nightingale, and M. Dennijs, "Quantized hall conductance in a two-dimensional periodic potential," *Phys. Rev. Lett.*, vol. 49, no. 6, pp. 405–408, 1982.

[18] A. Ludwig, M. Fisher, R. Shankar, and G. Grinstein, "Integer quantum hall transition - an alternative approach and exact results," *Phys. Rev. B*, vol. 50, pp. 7526–7552, SEP 15 1994.

[19] D. N. Sheng, Z. Y. Weng, L. Sheng, and F. D. M. Haldane, "Quantum spin-hall effect and topologically invariant Chern numbers," *Phys. Rev. Lett.*, vol. 97, JUL 21 2006.

[20] B. A. Bernevig, T. L. Hughes, and S.-C. Zhang, "Quantum spin Hall effect and topological phase transition in HgTe quantum wells," *Science*, vol. 314, pp. 1757–1761, DEC 15 2006.

[21] M. Koenig, S. Wiedmann, C. Bruene, A. Roth, H. Buhmann, L. W. Molenkamp, X.-L. Qi, and S.-C. Zhang, "Quantum spin hall insulator state in HgTe quantum wells," *Science*, vol. 318, pp. 766–770, NOV 2 2007.

[22] F. Haldane, "Model for a quantum hall-effect without Landau-levels - condensed-matter realization of the parity anomaly," *Phys. Rev. Lett.*, vol. 61, pp. 2015–2018, OCT 31 1988.

[23] J. E. Moore and L. Balents, "Topological invariants of time-reversal-invariant band structures," *Phys. Rev. B*, vol. 75, MAR 2007.

[24] D. Hsieh, D. Qian, L. Wray, Y. Xia, Y. S. Hor, R. J. Cava, and M. Z. Hasan, “A topological Dirac insulator in a quantum spin Hall phase,” *Nature*, vol. 452, pp. 970–U5, APR 24 2008.

[25] Y. Xia, D. Qian, D. Hsieh, L. Wray, A. Pal, H. Lin, A. Bansil, D. Grauer, Y. S. Hor, R. J. Cava, and M. Z. Hasan, “Observation of a large-gap topological-insulator class with a single Dirac cone on the surface,” *Nature Phys.*, vol. 5, pp. 398–402, JUN 2009.

[26] P. Zhang and M. W. Wu, “Hot-carrier transport and spin relaxation on the surface of topological insulator,” *Phys. Rev. B*, vol. 87, FEB 26 2013.

[27] N. P. Butch, K. Kirshenbaum, P. Syers, A. B. Sushkov, G. S. Jenkins, H. D. Drew, and J. Paglione, “Strong surface scattering in ultrahigh-mobility Bi_2Se_3 topological insulator crystals,” *Phys. Rev. B*, vol. 81, JUN 1 2010.

[28] J. N. Coleman, M. Lotya, A. O’Neill, S. D. Bergin, P. J. King, U. Khan, K. Young, A. Gaucher, S. De, R. J. Smith, I. V. Shvets, S. K. Arora, G. Stanton, H.-Y. Kim, K. Lee, G. T. Kim, G. S. Duesberg, T. Hallam, J. J. Boland, J. J. Wang, J. F. Donegan, J. C. Grunlan, G. Moriarty, A. Shmeliov, R. J. Nicholls, J. M. Perkins, E. M. Grieveson, K. Theuwissen, D. W. McComb, P. D. Nellist, and V. Nicolosi, “Two-Dimensional Nanosheets Produced by Liquid Exfoliation of Layered Materials,” *Science*, vol. 331, pp. 568–571, FEB 4 2011.

[29] V. Nicolosi, M. Chhowalla, M. G. Kanatzidis, M. S. Strano, and J. N. Coleman, “Liquid Exfoliation of Layered Materials,” *Science*, vol. 340, pp. 1420+, JUN 21 2013.

[30] Q. H. Wang, K. Kalantar-Zadeh, A. Kis, J. N. Coleman, and M. S. Strano, “Electronics and optoelectronics of two-dimensional transition metal dichalcogenides,” *Nat. Nanotechnol.*, vol. 7, pp. 699–712, NOV 2012.

[31] A. Splendiani, L. Sun, Y. Zhang, T. Li, J. Kim, C.-Y. Chim, G. Galli, and F. Wang, “Emerging Photoluminescence in Monolayer MoS_2,” *Nano Lett.*, vol. 10, pp. 1271–1275, APR 2010.

[32] P. Hohenberg and W. Kohn, “Inhomogeneous electron gas,” *Phys. Rev.*, vol. 136, pp. B864–B871, Nov 1964.

[33] Y. Wang and J. Perdew, “Correlation hole of the spin-polarized electron-gas, with exact small-wave-vector and high-density scaling,” *Phys. Rev. B*, vol. 44, pp. 13298–13307, DEC 15 1991.

[34] D. R. Bohren, C. F. Huffmann, *Absorption and scattering of light by small particles.* New York: Wiley-Interscience, 2010.

[35] R. H. Ritchie, “Plasma losses by fast electrons in thin films,” *Phys. Rev.*, vol. 106, pp. 874–881, Jun 1957.

[36] B. Hecht, H. Bielefeldt, L. Novotny, Y. Inouye, and D. Pohl, “Local excitation, scattering, and interference of surface plasmons,” *Phys. Rev. Lett.*, vol. 77, pp. 1889–1892, AUG 26 1996.

[37] J. Pendry, “Applied physics - Playing tricks with light,” *Science*, vol. 285, pp. 1687–1688, SEP 10 1999.

[38] K. Kneipp, Y. Wang, H. Kneipp, L. Perelman, I. Itzkan, R. Dasari, and M. Feld, “Single molecule detection using surface-enhanced Raman scattering (SERS),” *Phys. Rev. Lett.*, vol. 78, pp. 1667–1670, MAR 3 1997.

[39] W. Barnes, A. Dereux, and T. Ebbesen, “Surface plasmon subwavelength optics,” *Nature*, vol. 424, pp. 824–830, AUG 14 2003.

[40] H. A. Atwater, “The promise of plasmonics,” *Sci. Am.*, vol. 296, pp. 56–63, APR 2007.

[41] D. Pacifici, “Plasmonics - A shifting perspective,” *Nature Photon.*, vol. 1, pp. 689–690, DEC 2007.

[42] B. Fluegel, A. Mascarenhas, D. W. Snoke, L. N. Pfeiffer, and K. West, “Plasmonic all-optical tunable wavelength shifter,” *Nature Photon., Year = 2007, Volume = 1, Number = 12, Pages = 701-703, Month = DEC, DOI = 10.1038/nphoton.2007.229, ISSN = 1749-4885, Unique-ID = ISI:000251282800012,.*

[43] P. J. Reece, “Plasmonics - Finer optical tweezers,” *Nature Photon., Year = 2008, Volume = 2, Number = 6, Pages = 333-334, Month = JUN, DOI = 10.1038/nphoton.2008.88, ISSN = 1749-4885, Unique-ID = ISI:000256881800003,.*

[44] A. N. Grigorenko, N. W. Roberts, M. R. Dickinson, and Y. Zhang, “Nanometric optical tweezers based on nanostructured substrates,” *Nature Photon., Year = 2008, Volume = 2, Number = 6, Pages = 365-370, Month = JUN, DOI = 10.1038/nphoton.2008.78, ISSN = 1749-4885, ResearcherID-Numbers = Roberts, Nicholas/A-5769-2010, ORCID-Numbers = Roberts, Nicholas/0000-0002-4540-6683, Unique-ID = ISI:000256881800014,.*

[45] M. L. Juan, M. Righini, and R. Quidant, “Plasmon nano-optical tweezers,” *Nature Photon., Year = 2011, Volume = 5, Number = 6, Pages = 349-356, Month = JUN, DOI = 10.1038/NPHOTON.2011.56, ISSN = 1749-4885, ResearcherID-Numbers = Juan, Mathieu/C-6331-2008, ORCID-Numbers = Juan, Mathieu/0000-0002-2740-8001, Unique-ID = ISI:000291089000013,.*

[46] D. E. Chang, A. S. Sorensen, P. R. Hemmer, and M. D. Lukin, “Quantum optics with surface plasmons,” *Phys. Rev. Lett.*, vol. 97, AUG 4 2006.

[47] D. E. Chang, A. S. Sorensen, E. A. Demler, and M. D. Lukin, “A single-photon transistor using nanoscale surface plasmons,” *Nature Physics*, vol. 3, pp. 807–812, NOV 2007.

[48] J. N. Caspers, N. Rotenberg, and H. M. van Driel, “Ultrafast silicon-based active plasmonics at telecom wavelengths,” *Opt. Express*, vol. 18, pp. 19761–19769, SEP 13 2010.

[49] E. Prodan, P. Nordlander, and N. Halas, “Electronic structure and optical properties of gold nanoshells,” *Nano Lett.*, vol. 3, pp. 1411–1415, OCT 2003.

[50] P. Nordlander, C. Oubre, E. Prodan, K. Li, and M. Stockman, “Plasmon hybridizaton in nanoparticle dimers,” *Nano Lett.*, vol. 4, pp. 899–903, MAY 2004.

[51] J. Krenn, M. Salerno, N. Felidj, B. Lamprecht, G. Schider, A. Leitner, F. Aussenegg, J. Weeber, A. Dereux, and J. Goudonnet, “Light field propagation by metal micro- and nanostructures,” *J. Mircosc. (Oxf)*, vol. 202, pp. 122–128, APR 2001. 6th International Conference on Near-field Optics and Related Techniques, Unit Twente, Enschede, Netherlands, AUG 27-31, 2000.

[52] S. Maier, P. Kik, and H. Atwater, “Optical pulse propagation in metal nanoparticle chain waveguides,” *Phys. Rev. B*, vol. 67, MAY 15 2003.

[53] S. Maier, P. Kik, H. Atwater, S. Meltzer, E. Harel, B. Koel, and A. Requicha, “Local detection of electromagnetic energy transport below the diffraction limit in metal nanoparticle plasmon waveguides,” *Nat. Mater.*, vol. 2, pp. 229–232, APR 2003.

[54] M. Abb, P. Albella, J. Aizpurua, and O. L. Muskens, “All-Optical Control of a Single Plasmonic Nanoantenna-ITO Hybrid,” *Nano Lett.*, vol. 11, pp. 2457–2463, JUN 2011.

[55] Y. Chen, P. Lodahl, and A. F. Koenderink, “Dynamically reconfigurable directionality of plasmon-based single photon sources,” *Phys. Rev. B*, vol. 82, AUG 6 2010.

[56] J. Zhu, “Spatial dependence of the local field enhancement in dielectric shell coated silver nanospheres,” *Appl. Surf. Sci.*, vol. 253, pp. 8729–8733, AUG 31 2007.

[57] J. Pascual, J. Camassel, and H. Mathieu, “Fine-structure in the intrinsic absorption-edge of TiO_2,” *Phys. Rev. B*, vol. 18, no. 10, pp. 5606–5614, 1978.

[58] G. Acket and J. Volger, “On electron mobility and donor centres in reduced and lithium-doped rutile (TiO_2),” *Physica*, vol. 32, no. 10, pp. 1680–&, 1966.

[59] Y. Liu and R. Claus, “Blue light emitting nanosized TiO_2 colloids,” *J. Am. Chem. Soc.*, vol. 119, pp. 5273–5274, JUN 4 1997.

[60] G. Rothenberger, J. Moser, M. Gratzel, N. Serpone, and D. Sharma, "Eharge carrier trapping and recombination dynamics in small semiconductor particles," *J. Am. Chem. Soc.*, vol. 107, pp. 8054–8059, DEC 25 1985.

[61] G. Kresse and J. Furthmuller, "Efficient iterative schemes for ab initio total-energy calculations using a plane-wave basis set," *Phys. Rev. B*, vol. 54, pp. 11169–11186, OCT 15 1996.

[62] M. Kbotek and P. Feibelman, "Ion desorption by core-hole auger decay," *Phys. Rev. Lett.*, vol. 40, no. 14, pp. 964–967, 1978.

[63] S. Kowalczyk, F. Mcfeely, L. LEY, V. Gritsyna, and D. Shirley, "electronic-structure of srtio3 and some simple related oxides (MgO, Al_2O_3, SrO, TiO_2)," *Solid State Commun.*, vol. 23, no. 3, pp. 161–169, 1977.

[64] K. Glassford and J. Chelokowsky, "Structural and electronic-properties of titanium-dioxide," *Phys. Rev. B*, vol. 46, pp. 1284–1298, JUL 15 1992.

[65] S. Mo and W. Ching, "Eelectronic and optical-properties of 3 phases of titanium-dioxide - rutile, anatase, and brookite,"

[66] N. Smith, "Photoelectron energy spectra and band structures of noble metals," *Phys. Rev. B*, vol. 3, no. 6, p. 1862, 1971.

[67] M. Cardona and G. Harbeke, "Optical properties and band structure of wurtzite-type crystals and rutile," *Phys. Rev.*, vol. 137, no. 5A, p. 1467, 1965.

[68] D. vonderLinde, K. SokolowskiTinten, and J. Bialkowski, "Laser-solid interaction in the femtosecond time regime," *Appl. Surf. Sci*, vol. 109, pp. 1–10, FEB 1997. Proceedings of Symposium H on Laser Processing of Surfaces and Thin Films of the 1996 E-MRS Spring Conference, STRASBOURG, FRANCE, JUN 04-07, 1996.

[69] J. E. Moore, "The birth of topological insulators," *Nature*, vol. 464, pp. 194–198, MAR 11 2010.

[70] Y. L. Chen, J. G. Analytis, J. H. Chu, Z. K. Liu, S. K. Mo, X. L. Qi, H. J. Zhang, D. H. Lu, X. Dai, Z. Fang, S. C. Zhang, I. R. Fisher, Z. Hussain, and Z. X. Shen, "Experimental Realization of a Three-Dimensional Topological Insulator, Bi_2Te_3," *Science*, vol. 325, pp. 178–181, JUL 10 2009.

[71] P. Roushan, J. Seo, C. V. Parker, Y. S. Hor, D. Hsieh, D. Qian, A. Richardella, M. Z. Hasan, R. J. Cava, and A. Yazdani, "Topological surface states protected from backscattering by chiral spin texture," *Nature*, vol. 460, pp. 1106–U64, AUG 27 2009.

[72] Z. Alpichshev, J. G. Analytis, J. H. Chu, I. R. Fisher, Y. L. Chen, Z. X. Shen, A. Fang, and A. Kapitulnik, “STM Imaging of Electronic Waves on the Surface of Bi2Te3: Topologically Protected Surface States and Hexagonal Warping Effects,” *Phys. Rev. Lett.*, vol. 104, JAN 8 2010.

[73] D. Pesin and A. H. MacDonald, “Spintronics and pseudospintronics in graphene and topological insulators,” *Nat. Mater.*, vol. 11, pp. 409–416, MAY 2012.

[74] V. Edelstein, “Spin polarization of conduction electrons induced by electric-current in 2-dimensional asymmetric electron-systems,” *Solid State Commun.*, vol. 73, pp. 233–235, JAN 1990.

[75] J. Wunderlich, B. Kaestner, J. Sinova, and T. Jungwirth, “Experimental observation of the spin-Hall effect in a two-dimensional spin-orbit coupled semiconductor system,” *Phys. Rev. Lett.*, vol. 94, FEB 4 2005.

[76] L. Fu and C. L. Kane, “Superconducting proximity effect and Majorana fermions at the surface of a topological insulator,” *Phys. Rev. Lett.*, vol. 100, MAR 7 2008.

[77] I. Zutic, J. Fabian, and S. Das Sarma, “Spintronics: Fundamentals and applications,” *Rev. Mod. Phys.*, vol. 76, pp. 323–410, APR 2004.

[78] D. Hsieh, Y. Xia, D. Qian, L. Wray, J. H. Dil, F. Meier, J. Osterwalder, L. Patthey, J. G. Checkelsky, N. P. Ong, A. V. Fedorov, H. Lin, A. Bansil, D. Grauer, Y. S. Hor, R. J. Cava, and M. Z. Hasan, “A tunable topological insulator in the spin helical Dirac transport regime,” *Nature*, vol. 460, pp. 1101–U59, AUG 27 2009.

[79] P. J. Leek, J. M. Fink, A. Blais, R. Bianchetti, M. Goeppl, J. M. Gambetta, D. I. Schuster, L. Frunzio, R. J. Schoelkopf, and A. Wallraff, “Observation of Berry’s phase in a solid-state qubit,” *Science*, vol. 318, pp. 1889–1892, DEC 21 2007.

[80] H.-T. He, G. Wang, T. Zhang, I.-K. Sou, G. K. L. Wong, J.-N. Wang, H.-Z. Lu, S.-Q. Shen, and F.-C. Zhang, “Impurity Effect on Weak Antilocalization in the Topological Insulator Bi2Te3,” *Phys. Rev. Lett.*, vol. 106, APR 21 2011.

[81] H. Peng, K. Lai, D. Kong, S. Meister, Y. Chen, X.-L. Qi, S.-C. Zhang, Z.-X. Shen, and Y. Cui, “Aharonov-Bohm interference in topological insulator nanoribbons,” *Nat. Mater.*, vol. 9, pp. 225–229, MAR 2010.

[82] J. J. Cha, K. J. Koski, and Y. Cui, “Topological insulator nanostructures,” *Phys. Status Solidi-RRL*, vol. 7, pp. 15–25, FEB 2013.

[83] H. Peng, W. Dang, J. Cao, Y. Chen, D. Wu, W. Zheng, H. Li, Z.-X. Shen, and Z. Liu, “Topological insulator nanostructures for near-infrared transparent flexible electrodes,” *Nature Chem.*, vol. 4, pp. 281–286, APR 2012.

[84] D. Kong and Y. Cui, "Opportunities in chemistry and materials science for topological insulators and their nanostructures," *Nature Chem.*, vol. 3, pp. 845–849, NOV 2011.

[85] S. Cho, D. Kim, P. Syers, N. P. Butch, J. Paglione, and M. S. Fuhrer, "Topological Insulator Quantum Dot with Tunable Barriers," *Nano Lett.*, vol. 12, pp. 469–472, JAN 2012.

[86] C. Simon, M. Afzelius, J. Appel, A. B. de la Giroday, S. J. Dewhurst, N. Gisin, C. Y. Hu, F. Jelezko, S. Kroll, J. H. Muller, J. Nunn, E. S. Polzik, J. G. Rarity, H. De Riedmatten, W. Rosenfeld, A. J. Shields, N. Skoeld, R. M. Stevenson, R. Thew, I. A. Walmsley, M. C. Weber, H. Weinfurter, J. Wrachtrup, and R. J. Young, "Quantum memories," *Eur. Phys. J. D*, vol. 58, pp. 1–22, MAY 2010.

[87] R.-B. Liu, W. Yao, and L. J. Sham, "Quantum computing by optical control of electron spins," *Adv. Phys.*, vol. 59, no. 5, pp. 703–802, 2010.

[88] M. Kroutvar, Y. Ducommun, D. Heiss, M. Bichler, D. Schuh, G. Abstreiter, and J. Finley, "Optically programmable electron spin memory using semiconductor quantum dots," *Nature*, vol. 432, pp. 81–84, NOV 4 2004.

[89] A. Ebbens, D. Krizhanovskii, A. Tartakovskii, F. Pulizzi, T. Wright, A. Savelyev, M. Skolnick, and M. Hopkinson, "Optical orientation and control of spin memory in individual InGaAs quantum dots," *Phys. Rev. B*, vol. 72, AUG 2005.

[90] H. J. Krenner, C. E. Pryor, J. He, and P. M. Petroff, "A semiconductor exciton memory cell based on a single quantum nanostructure," *Nano Lett.*, vol. 8, pp. 1750–1755, JUN 2008.

[91] D. Brunner, B. D. Gerardot, P. A. Dalgarno, G. Wuest, K. Karrai, N. G. Stoltz, P. M. Petroff, and R. J. Warburton, "A Coherent Single-Hole Spin in a Semiconductor," *Science*, vol. 325, pp. 70–72, JUL 3 2009.

[92] M. Atature, J. Dreiser, A. Badolato, A. Hogele, K. Karrai, and A. Imamoglu, "Quantum-dot spin-state preparation with near-unity fidelity," *Science*, vol. 312, pp. 551–553, APR 28 2006.

[93] A. Imamoglu, D. Awschalom, G. Burkard, D. DiVincenzo, D. Loss, M. Sherwin, and A. Small, "Quantum information processing using quantum dot spins and cavity QED," *Phys. Rev. Lett.*, vol. 83, pp. 4204–4207, NOV 15 1999.

[94] C. Piermarocchi, P. Chen, L. Sham, and D. Steel, "Optical RKKY interaction between charged semiconductor quantum dots," *Phys. Rev. Lett.*, vol. 89, OCT 14 2002.

[95] T. Calarco, A. Datta, P. Fedichev, E. Pazy, and P. Zoller, "Spin-based all-optical quantum computation with quantum dots: Understanding and suppressing decoherence," *Phys. Rev. A*, vol. 68, JUL 2003.

[96] B. D. Gerardot, D. Brunner, P. A. Dalgarno, P. Ohberg, S. Seidl, M. Kroner, K. Karrai, N. G. Stoltz, P. M. Petroff, and R. J. Warburton, “Optical pumping of a single hole spin in a quantum dot,” *Nature*, vol. 451, pp. 441–444, JAN 24 2008.

[97] A. N. Vamivakas, C. Y. Lu, C. Matthiesen, Y. Zhao, S. Falt, A. Badolato, and M. Atatuere, “Observation of spin-dependent quantum jumps via quantum dot resonance fluorescence,” *Nature*, vol. 467, pp. 297–300, SEP 16 2010.

[98] A. Greilich, D. R. Yakovlev, A. Shabaev, A. L. Efros, I. A. Yugova, R. Oulton, V. Stavarache, D. Reuter, A. Wieck, and M. Bayer, “Mode locking of electron spin coherences in singly charged quantum dots,” *Science*, vol. 313, pp. 341–345, JUL 21 2006.

[99] E. Stinaff, M. Scheibner, A. Bracker, I. Ponomarev, V. Korenev, M. Ware, M. Doty, T. Reinecke, and D. Gammon, “Optical signatures of coupled quantum dots,” *Science*, vol. 311, pp. 636–639, FEB 3 2006.

[100] L. Robledo, J. Elzerman, G. Jundt, M. Atature, A. Hoegele, S. Faelt, and A. Imamoglu, “Conditional dynamics of interacting quantum dots,” *Science*, vol. 320, pp. 772–775, MAY 9 2008.

[101] D. Kim, S. G. Carter, A. Greilich, A. S. Bracker, and D. Gammon, “Ultrafast optical control of entanglement between two quantum-dot spins,” *Nature Phys.*, vol. 7, pp. 223–229, MAR 2011.

[102] A. N. Vamivakas, Y. Zhao, C.-Y. Lu, and M. Atatuere, “Spin-resolved quantum-dot resonance fluorescence,” *Nature Phys.*, vol. 5, pp. 198–202, MAR 2009.

[103] M. Leuenberger, M. Flatte, and D. Awschalom, “Teleportation of electronic many-qubit states encoded in the electron spin of quantum dots via single photons,” *Phys. Rev. Lett.*, vol. 94, MAR 18 2005.

[104] M. Leuenberger, “Fault-tolerant quantum computing with coded spins using the conditional Faraday rotation in quantum dots,” *Phys. Rev. B*, vol. 73, FEB 2006.

[105] C. Y. Hu, A. Young, J. L. O’Brien, W. J. Munro, and J. G. Rarity, “Giant optical Faraday rotation induced by a single-electron spin in a quantum dot: Applications to entangling remote spins via a single photon,” *Phys. Rev. B*, vol. 78, AUG 2008.

[106] J. Singh, *Electronic and Optoelectronic Properties of Semiconductor Structures.* Cambridge University Press, Cambridge, 2003.

[107] B. S. G. Nimtz, *Narrow Gap Semiconductors.* Springer, Berlin, 1983.

[108] J. J. Sakurai, *Advanced Quantum Mechanics.* Pearson Education, 2007.

[109] H. P. Paudel and M. N. Leuenberger, "Giant Faraday effect due to Pauli exclusion principle in 3D topological insulators," *J. Phys: Condens. Matter.*, vol. 26, FEB 26 2014.

[110] B. Volkov and O. Pankratov, "Two-dimensional massless electrons in an inverted contact," *J. Exp. Theor. Phys. Lett.*, vol. 42, no. 4, pp. 178–181, 1985.

[111] D.-H. Lee, "Surface states of topological insulators: The dirac fermion in curved two-dimensional spaces," *Phys. Rev. Lett.*, vol. 103, p. 196804, Nov 2009.

[112] H. Nielsen and M. Ninomiya, "A no-go theorem for regularizing chiral fermions," *Phys. Lett. B*, vol. 105, no. 2-3, pp. 219–223, 1981.

[113] H. Nielsen and M. Ninomiya, "Absence of neutrinos on a lattice .I. proof by homotopy-theory," *Nucl. Phys. B*, vol. 185, no. 1, pp. 20–40, 1981.

[114] H. Nielsen and M. Ninomiya, "Absence of neutrinos on a lattice .II. intuitive topological proof," *Nucl. Phys. B*, vol. 193, no. 1, pp. 173–194, 1981.

[115] G. Bastard, *Wave Mechanics Applied to Semiconductor.* Wiley, New York, 1991.

[116] B. V. E. Rosencher, *Optoelectronics.* Cambridge University Press, Cambridge, 2004.

[117] G. Gonzalez, M. N. Leuenberger, H. Seigneur, and W. V. Schoenfeld, "Theory of a Scalable Electron-Spin Based Quantum Network Inside a Photonic Crystal," *J. Comput. Theor. Nanos.*, vol. 7, pp. 1651–1672, SEP 2010.

[118] H. P. Seigneur, G. Gonzalez, M. N. Leuenberger, and W. V. Schoenfeld, "Dynamics of Entanglement between a Quantum Dot Spin Qubit and a Photon Qubit inside a Semiconductor High-Q Nanocavity," *Adv. Math. Phys.*, 2010.

[119] H. P. Seigneur, M. N. Leuenberger, and W. V. Schoenfeld, "Single-photon Mach-Zehnder interferometer for quantum networks based on the single-photon Faraday effect," *J. Appl. Phys.*, vol. 104, JUL 1 2008.

[120] J. Berezovsky, M. H. Mikkelsen, O. Gywat, N. G. Stoltz, L. A. Coldren, and D. D. Awschalom, "Nondestructive optical measurements of a single electron spin in a quantum dot," *Science*, vol. 314, pp. 1916–1920, DEC 22 2006.

[121] M. S. Z. M. O. Scully, *Quantum Optics.* Cambridge University Press, Cambridge, 2001.

[122] J. Reithmaier, G. Sek, A. Loffler, C. Hofmann, S. Kuhn, S. Reitzenstein, L. Keldysh, V. Kulakovskii, T. Reinecke, and A. Forchel, "Strong coupling in a single quantum dot-semiconductor microcavity system," *Nature*, vol. 432, pp. 197–200, NOV 11 2004.

[123] T. Stievater, X. Li, D. Steel, D. Gammon, D. Katzer, D. Park, C. Piermarocchi, and L. Sham, “Rabi oscillations of excitons in single quantum dots,” *Phys. Rev. Lett.*, vol. 87, SEP 24 2001.

[124] T. Takagahara, *Quantum Coherence, Correlation and Decoherence in Semiconductor Nanostructures.* Academic Press, San Diego, 2003.

[125] M. Fox, *Quantum Optics: An Introduction.* Oxford University Press, 2006.

[126] I. Knez, R.-R. Du, and G. Sullivan, “Evidence for Helical Edge Modes in Inverted InAs/GaSb Quantum Wells,” *Phys. Rev. Lett.*, vol. 107, SEP 19 2011.

[127] H. Zhang, C.-X. Liu, X.-L. Qi, X. Dai, Z. Fang, and S.-C. Zhang, “Topological insulators in $\mathrm{Bi_2Se_3}, Bi_2\mathrm{Te_3}$ and $\mathrm{Sb_2Te_3}$ with a single Dirac cone on the surface,” *Nature Phys.*, vol. 5, pp. 438–442, JUN 2009.

[128] L. Fu, C. L. Kane, and E. J. Mele, “Topological insulators in three dimensions,” *Phys. Rev. Lett.*, vol. 98, MAR 9 2007.

[129] Y. L. Chen, J. G. Analytis, J. H. Chu, Z. K. Liu, S. K. Mo, X. L. Qi, H. J. Zhang, D. H. Lu, X. Dai, Z. Fang, S. C. Zhang, I. R. Fisher, Z. Hussain, and Z. X. Shen, “Experimental Realization of a Three-Dimensional Topological Insulator, $\mathrm{Bi_2Te_3}$,” *Science*, vol. 325, pp. 178–181, JUL 10 2009.

[130] J. Dimmock, M. I., and A. Strauss, “Band structure and laser action in $\mathrm{Pb}_xSn_{1-x}\mathrm{Te}$,” *Phys. Rev. Letts.*, vol. 16, no. 26, p. 1193, 1966.

[131] O. Pankratov, “Electronic-properties of band-inverted heterojunctions - supersymmetry in narrow-gap semiconductors,” *Semicond. Sci. Technol.*, vol. 5, pp. S204–S209, MAR 1990. International conf on narrow-gap semiconductors and related materials, Gaithersburg, MD, Jun 12-15, 1989.

[132] V. Korenman and H. Drew, “Subbands in the gap in inverted-band semiconductor quantum-wells,” *Phys. Rev. B*, vol. 35, pp. 6446–6449, APR 15 1987.

[133] D. Agassi and V. Korenman, “Interface states in band-inverted semiconductor heterojunctions,” *Phys. Rev. B*, vol. 37, pp. 10095–10106, JUN 15 1988.

[134] X. Gao and M. S. Daw, “Investigation of band inversion in (Pb,Sn)Te alloys using ab initio calculations,” *Phys. Rev. B*, vol. 77, JAN 2008.

[135] S.-Y. Xu, C. Liu, N. Alidoust, M. Neupane, D. Qian, I. Belopolski, J. D. Denlinger, Y. J. Wang, H. Lin, L. A. Wray, G. Landolt, B. Slomski, J. H. Dil, A. Marcinkova, E. Morosan, Q. Gibson, R. Sankar, F. C. Chou, R. J. Cava, A. Bansil, and M. Z. Hasan, “Observation of a topological crystalline insulator phase and topological phase transition in Pb1-xSnxTe,” *Nature Commun.*, vol. 3, NOV 2012.

[136] V. Popescu and A. Zunger, "Extracting E versus (k)over-right-arrow effective band structure from supercell calculations on alloys and impurities," *Phys. Rev. B*, vol. 85, FEB 2 2012.

[137] W. Ku, T. Berlijn, and C.-C. Lee, "Unfolding First-Principles Band Structures," *Phys. Rev. Lett.*, vol. 104, MAY 28 2010.

[138] H. P. Paudel and M. N. Leuenberger, "Three-dimensional topological insulator quantum dot for optically controlled quantum memory and quantum computing," *Phys. Rev. B*, vol. 88, AUG 22 2013.

[139] J. Z. Salvail, M. Agnew, A. S. Johnson, E. Bolduc, J. Leach, and R. W. Boyd, "Full characterization of polarization states of light via direct measurement," *Nature Photon.*, vol. 7, pp. 316–321, APR 2013.

[140] R. Buczko and L. Cywinski, "PbTe/PbSnTe heterostructures as analogs of topological insulators," *Phys. Rev. B*, vol. 85, MAY 29 2012.

[141] Y. Zhao, Y. Hu, L. Liu, Y. Zhu, and H. Guo, "Helical States of Topological Insulator Bi_2Se_3," *Nano Lett.*, vol. 11, pp. 2088–2091, MAY 2011.

[142] P. Y. Yu and M. Cardona, *Fundamentals of Semiconductors: Physics and Material Properties.* 3rd edition, Springer, Berlin, 2005.

[143] G. Kresse and J. Hanfer, "Norm-conserving and ultrasoft pseudopotentials for first-row and transition-elements," *J. Phys: Condens. Matter.*, vol. 6, pp. 8245–8257, OCT 3 1994.

[144] P. Blochl, "Projector augmented-wave method," *Phys. Rev. B*, vol. 50, pp. 17953–17979, DEC 15 1994.

[145] A. V. Thompson, H. Seigneur, M. N. Leuenberger, and W. V. Schoenfeld, "Optical Switching Based on the Conditional Faraday Effect With Electron Spins in Quantum Dots," *IEEE J. Quant. Electron.*, vol. 45, pp. 637–645, MAY-JUN 2009.

[146] J. Murphy, M. Beard, A. Norman, S. Ahrenkiel, J. Johnson, P. Yu, O. Micic, R. Ellingson, and A. Nozik, "PbTe colloidal nanocrystals: Synthesis, characterization, and multiple exciton generation," *J. Am. Chem. Soc.*, vol. 128, pp. 3241–3247, MAR 15 2006.

[147] A. Ferreira, J. Viana-Gomes, Y. V. Bludov, V. Pereira, N. M. R. Peres, and A. H. Castro Neto, "Faraday effect in graphene enclosed in an optical cavity and the equation of motion method for the study of magneto-optical transport in solids," *Phys. Rev. B*, vol. 84, DEC 1 2011.

[148] Z. G. Yu, S. Krishnamurthy, and S. Guha, "Photoexcited-carrier-induced refractive index change in small bandgap semiconductors," *J. Opt. Soc. Am. B: Opt. Phys.*, vol. 23, pp. 2356–2360, NOV 2006.

[149] C. S. R. Kaipa, A. B. Yakovlev, G. W. Hanson, Y. R. Padooru, F. Medina, and F. Mesa, "Enhanced transmission with a graphene-dielectric microstructure at low-terahertz frequencies," *Phys. Rev. B*, vol. 85, JUN 5 2012.

[150] K. He, C. Poole, K. F. Mak, and J. Shan, "Experimental Demonstration of Continuous Electronic Structure Tuning via Strain in Atomically Thin MoS_2," *Nano Lett.*, vol. 13, pp. 2931–2936, JUN 2013.

[151] M. Buscema, M. Barkelid, V. Zwiller, H. S. J. van der Zant, G. A. Steele, and A. Castellanos-Gomez, "Large and Tunable Photothermoelectric Effect in Single-Layer MoS_2," *Nano Lett.*, vol. 13, pp. 358–363, FEB 2013.

[152] H. Wang, L. Yu, Y.-H. Lee, Y. Shi, A. Hsu, M. L. Chin, L.-J. Li, M. Dubey, J. Kong, and T. Palacios, "Integrated Circuits Based on Bilayer MoS_2 Transistors," *Nano Lett.*, vol. 12, pp. 4674–4680, SEP 2012.

[153] B. C. Windom, W. G. Sawyer, and D. W. Hahn, "A Raman Spectroscopic Study of MoS_2 and MoO_3: Applications to Tribological Systems," *Tribol. Lett.*, vol. 42, pp. 301–310, JUN 2011.

[154] N. Brown, N. Cui, and A. McKinley, "An XPS study of the surface modification of natural MoS_2 following treatment in an RF-oxygen plasma," *Appl. Surf. Sci.*, vol. 134, pp. 11–21, SEP 1998.

[155] J. Perdew, J. Chevary, S. Vosko, K. Jackson, M. Pederson, D. Singh, and C. Fiolhais, "Atoms, molecules, solids, and surfaces - applications of the generalized gradient approximation for exchange and correlation," *Phys. Rev. B*, vol. 46, pp. 6671–6687, SEP 15 1992.

[156] D. Segev, A. Janotti, and C. G. Van de Walle, "Self-consistent band-gap corrections in density functional theory using modified pseudopotentials," *Phys. Rev. B*, vol. 75, JAN 2007.

[157] D. Miller, "Handbook of Mathematical FFunctions - Abramowitz, M and Stegun, IA," *Manag. Sci.*, vol. 14, no. 6, p. B404, 1968.

[158] M. P. Marder, *Condensed Matter Physics.* 2nd edition, Wiley, New York, 2010.

[159] M. Veldhorst, M. Snelder, M. Hoek, T. Gang, V. K. Guduru, X. L. Wang, U. Zeitler, W. G. van der Wiel, A. A. Golubov, H. Hilgenkamp, and A. Brinkman, "Josephson supercurrent through a topological insulator surface state," *Nat. Mater.*, vol. 11, pp. 417–421, MAY 2012.

[160] D.-H. Lee, “Surface States of Topological Insulators: The Dirac Fermion in Curved Two-Dimensional Spaces,” *Phys. Rev. Lett.*, vol. 103, NOV 6 2009.